

Modelling the beam and circumsolar radiation under cloud-free conditions in desert environment

Yehia Abdelmaksoud Abdalla Eissa

▶ **To cite this version:**

Yehia Abdelmaksoud Abdalla Eissa. Modelling the beam and circumsolar radiation under cloud-free conditions in desert environment. Ocean, Atmosphere. Ecole Nationale Supérieure des Mines de Paris, 2015. English. NNT : 2015ENMP0009 . tel-01168647

HAL Id: tel-01168647

https://pastel.hal.science/tel-01168647

Submitted on 26 Jun 2015

HAL is a multi-disciplinary open access archive for the deposit and dissemination of scientific research documents, whether they are published or not. The documents may come from teaching and research institutions in France or abroad, or from public or private research centers.

L'archive ouverte pluridisciplinaire **HAL**, est destinée au dépôt et à la diffusion de documents scientifiques de niveau recherche, publiés ou non, émanant des établissements d'enseignement et de recherche français ou étrangers, des laboratoires publics ou privés.

ParisTech
INSTITUT DES SCIENCES ET TECHNOLOGIES
PARIS INSTITUTE OF TECHNOLOGY

MINES ParisTech

École doctorale n° 432 : “Science des Métiers de l’Ingénieur”

Doctorat ParisTech

T H È S E

pour obtenir le grade de docteur délivré par

l’École nationale supérieure des mines de Paris

Spécialité “ Energétique et Procédés ”

présentée et soutenue publiquement par

Yehia Abdelmaksoud Abdalla EISSA

le 01 juin 2015

Modelling the beam and circumsolar radiation under cloud-free conditions in desert environment

Modélisation des rayonnements direct et circumsolaire par ciel clair en environnement désertique

Directeur de thèse : **Lucien WALD**
Co-encadrement de la thèse : **Philippe BLANC**

Jury

M. Thierry RANCHIN, Professeur, MINES ParisTech	Président
M. Stéphane ALFARO, Professeur, Université de Paris-Est Créteil	Rapporteur
M. Richard PEREZ, Professeur, State University of New York at Albany	Rapporteur
M. Philippe BLANC, Docteur, MINES ParisTech	Examinateur
M. Malik CHAMI, Professeur, Université Pierre et Marie Curie	Examinateur
M. Hosni GHEDIRA, Docteur, Masdar Institute, Abu Dhabi	Examinateur
M. Armel OUMBE, Docteur, Total New Energies	Examinateur
M. Lucien WALD, Professeur, MINES ParisTech	Examinateur
Mme. Marion SCHROEDTER-HOMSCHEIDT, Docteur, German Aerospace Center (DLR)	Invitée

T H È S E

MINES ParisTech
O.I.E. – Centre Observation, Impacts, Energie
CS 10207 – 06904 Sophia Antipolis cedex, France

to Ismail, Howida and Madiha

Acknowledgments

Firstly, I thank God for his blessings upon me through which I was able to finish this work.

I am grateful for having Lucien Wald as the director of my thesis. His guidance in the development of the thesis along with his advice (not only with regards to the thesis) are very greatly appreciated. I also thank him for involving me in the SUSIE and MISRA projects. The interactions with all the scientists active in these projects have been great, and the outcomes of the research of these projects are beneficial for the development of solar powered plants in my home country, Egypt.

It has been a pleasure having Philippe Blanc as the co-supervisor of my thesis. I deeply thank him for his encouragement and support throughout the course of this work. I am also thankful for his help with matters not related to the thesis.

I thank all the members of the jury for their time and interesting remarks. I am fortunate to have had a jury made up from such a panel of experts: Thierry Ranchin, Stéphane Alfaro, Richard Perez, Philippe Blanc, Malik Chami, Hosni Ghedira, Armel Oumbe, Lucien Wald and Marion Schroedter-Homscheidt.

The research leading to this thesis has received funding from Total New Energies in the framework of the PREDISOL project, and I thank Total New Energies for that. I also thank Masdar Institute, Hosni Ghedira in particular, for facilitating my role in the collaboration between Masdar Institute, MINES ParisTech and Total.

I, of course, express my sincerest gratitude to all my family members for their support throughout the course of my PhD, specifically: Howida, Madiha, Noura, Eiman, Salwa and Tarek. Abdelmaksoud, my late father, I appreciate the way you raised me. Ismail, my son who was born half way through the PhD and the light of my life, was a very powerful source of encouragement to complete this work.

I am very glad to have spent time at the Centre Observation, Impacts, Energy (O.I.E.) of MINES ParisTech. All members are fun to be around and would not hesitate to help in any way they can, including: Lionel Menard, Mark Bengulescu, William Wandji-Nyamsi, Youva Aoun, Benoit Gschwind, Isabelle Blanc, Sandra Hassan, Pierre Massip, Khai-Minh Ngo, Mirielle Lefevre and Jean Dubranna.

I am also glad to have spent time at the Research Center for Renewable Energy Mapping and Assessment of Masdar Institute, and I thank all the members of the center.

Table of contents

Chapter 1 - Introduction **1**

1.1. Motivation **1**

1.2. State of the research **5**

1.3. Objective and research questions **8**

1.4. Methodology **9**

1.5. Layout of the thesis **10**

Chapitre 2 – Résumé étendu **11**

2.1. Introduction **11**

2.2. Les bases théoriques **13**

2.2.1. Les différentes composantes du rayonnement solaire atteignant la surface de la Terre *13*

2.2.2. Paramétrisation de la luminance diffuse *15*

2.3. Lieu géographique d'étude et mesures *in-situ* **16**

2.3.1. Lieu géographique d'étude *16*

2.3.2. Les mesures in-situ *16*

2.4. Modélisation des rayonnements directs et circumsolaires **19**

2.4.1. Les propriétés optiques des aérosols *20*

2.4.2. Paramétrisation des modèles de transfert radiatif libRadtran et SMARTS *22*

2.5. La modélisation des rayonnements directs et circumsolaire : modèles et résultats **25**

2.5.1. La modélisation des éclairements spectraux direct et circumsolaire à 670 nm *25*

2.5.2. Proposition d'une méthode pour la modélisation des éclairements totaux direct et circumsolaire *27*

2.5.3. Modélisation empirique des éclairements totaux direct et circumsolaire *28*

2.6. Applicabilité du modèle proposé à un autre site de type désertique **31**

2.7. Conclusions et perspectives **35**

Chapter 3 - Basics **37**

3.1. Sun-Earth geometry **37**

3.2. The solar radiation at top of atmosphere **39**

3.3. Radiative transfer in the atmosphere **40**

3.3.1. Scattering, multiple scattering and absorption *40*

3.3.2. The radiative transfer equation *42*

3.4. The solar radiation components reaching the surface of the Earth **45**

3.5. Parameterization of the diffuse radiance **50**

Chapter 4 - Study area and ground measurements **53**

4.1. Study area **53**

4.2. Solar irradiance ground measurements **55**

4.3. AERONET measurements **57**

4.4. Beam and circumsolar radiance ground measurements 58
4.5. Comparisons between SAM and AERONET observations 61
4.6. The data sets available over the study area 66
Chapter 5 - Modelling the beam and circumsolar radiation 68
5.1. The aerosol optical properties 68
5.1.1. Sensitivity of the radiance 68
5.1.2. The aerosol optical depth 71
5.1.3. The aerosol single scattering albedo 74
5.1.4. The aerosol phase function 75
5.1.5. Discussion on the aerosol optical properties 77
5.2. Parameterizations of the radiative transfer models 78
5.2.1. libRadtran 78
5.2.2. SMARTS 80
Chapter 6 - Modelling the beam and circumsolar radiation: results and model 83
6.1. Modelling the monochromatic beam and circumsolar irradiances at 670 nm using libRadtran 84
6.1.1. Results of modelling the monochromatic beam irradiance 85
6.1.2. Results of modelling the monochromatic circumsolar irradiance using the Henyey-Greenstein phase function 86
6.1.3. Results of modelling the monochromatic circumsolar irradiance using the OPAC library aerosol optical properties 87
6.1.4. Results of modelling the monochromatic circumsolar irradiance using the two term Henyey-Greenstein phase function 88
6.2. Modelling the monochromatic beam and circumsolar irradiances at 670 nm using SMARTS 89
6.2.1. Results of modelling the monochromatic beam irradiance 90
6.2.2. Results of modelling the monochromatic circumsolar irradiance by user-defined aerosol optical properties 91
6.2.3. Results of modelling the monochromatic circumsolar irradiance using the 'DESERT_MAX' aerosol properties 92
6.3. Discussion on the modelled monochromatic beam and circumsolar irradiances 92
6.4. Proposed method for modelling the broadband beam and circumsolar irradiances using libRadtran 95
6.4.1. Modelling the broadband beam and circumsolar irradiances using libRadtran 96
6.4.2. Validations of the modelled broadband beam and circumsolar irradiances using libRadtran 98
6.4.3. Empirical model to estimate the broadband beam and circumsolar irradiances 102
6.5. Discussion 114
Chapter 7 - Applicability of the model to another site 117

7.1. The study area and ground measurements 117
7.2. Validation of the model developed in Abu Dhabi over Tamanrasset 119
7.2.1. Validation of the broadband beam irradiance over Tamanrasset 119
7.2.2. Validation of the circumsolar ratio, and the broadband beam and circumsolar irradiances over Tamanrasset 120
7.3. Refitting the coefficients of the model over Tamanrasset 124
7.3.1. Validations of the modelled broadband beam and circumsolar irradiances using libRadtran 124
7.3.2. Empirical model to estimate the broadband beam and circumsolar irradiances 127
7.4. Validation of the model developed in Tamanrasset over Abu Dhabi 136
7.4.1. Validation of the broadband beam irradiance over Abu Dhabi 137
7.4.2. Validation of the circumsolar ratio, and the broadband beam and circumsolar irradiances over Abu Dhabi 138
7.5. Discussion 141
Chapter 8 - Conclusions and perspectives 143
References 146
Nomenclature 152
List of figures 155
List of tables 160

Chapter 1 - Introduction

1.1. Motivation

During the past decade an exponential increase in the installed capacity of solar powered plants, including solar photovoltaics (PV) and concentrated solar technologies (CST), has taken place. CST systems include both concentrated solar thermal electric (CSTE) and concentrated photovoltaic (CPV) systems, but the current installed capacity of CSTE systems far exceeds that of CPV. The total global operational capacity of solar PV systems increased from 4 GW in 2004 to 100 GW in 2012, while that of CSTE increased from 0.354 GW in 2004 to 2.55 GW in 2012. The CPV installed capacity was reported as 0.1 GW in 2012 (REN21, 2013).

Even though the solar technologies utilize the same renewable energy source to generate electricity, *i.e.* the surface downwelling solar radiation, they have different principles in operation. Solar PV systems produce electricity based on the direct photovoltaic conversion of sunlight into electricity (Parida *et al.*, 2011; Singh, 2013). The resource of interest is the solar radiation incident on the plane of the PV modules, *i.e.* the global tilted irradiance (GTI), which comprises the diffuse (or scattered) radiation from the whole sky incident on the plane, the direct (or beam) radiation incident on the plane and the ground reflected radiation incident on the plane (Gueymard, 2009; Perez *et al.*, 1990a). The irradiance is the radiant flux per unit area, having SI units of W m^{-2}.

In contrast, CSTE plants operate from the heat generated from the solar radiation. While tracking the solar disc the broadband direct radiation incident from the Sun on a plane normal to the Sun, *i.e.* the direct normal irradiance (DNI), is concentrated by a reflecting material onto a focal plane, a line or point. A fluid present in the tubes at the focal plane is then heated, which generates steam to run a steam turbine or a Stirling engine to generate electricity (Kuravi *et al.*, 2013; Lee *et al.*, 2009; Richter *et al.*, 2009). The ISO states: "d*irect irradiance is the quotient of the radiant flux on a given plane receiver surface received from a small solid angle centered to the sun's disk to the area of that surface. If the plane is perpendicular to the axis of the solar angle, direct normal solar irradiance is received*" (ISO-9488, 1999).

CSTE systems are more attractive in regions with modest cloud coverage exhibiting high DNI during most days. These conditions could be met in the so-called sunbelt region, which is generally found at latitudes between 10° and 40° north or south (Schillings *et al.*, 2004). Interest of CSTE systems in the Middle East and North Africa (MENA) region is presently increasing. Saudi Arabia has ambitious plans to install 25 GW from CSTE systems by 2032 (Griffiths, 2013). Other countries of the MENA region are also partly targeting CSTE systems to reach their targets of electricity production from renewable energy sources (Brand and Zingerle, 2011; Bryden, *et al.*, 2013). Fig. 1.1 shows a picture of the 0.1 GW CSTE power plant Shams 1, located in Madinat Zayed, Abu Dhabi, United Arab Emirates (UAE) (Al

Jaber, 2013). This plant uses parabolic troughs to concentrate the direct solar radiation on to the focal plane.



Fig. 1.1: Picture of the parabolic troughs of Shams 1, a CSTE power plant located in the UAE. © Yehia Eissa, 2012.

The third technology, CPV, is a combination of the two aforementioned technologies (Kurtz, 2012). In CPV systems lenses concentrate the DNI onto a small area of multijunction PV cell, obtaining higher efficiency than standard PV cells. The CPV systems have a spectral response different than that of the broadband irradiance measurements and they require a tracking system as only the direct radiation is effective.

All CST systems directly or indirectly convert the DNI into electricity. They have different optical characteristics corresponding to different solid angle apertures centered to the position of the Sun, where the solid angle apertures are generally defined by the opening (or aperture) half-angle. This variety of aperture half-angles may pose a challenge because pyrheliometers and radiometers meant to measure the DNI may have different solid angle apertures, generally larger than those of CST systems. The problem with the ISO definition of the DNI is that the *small solid angle* is not specified. The World Meteorological Organization (WMO, 2010) recommends aperture half-angles ranging from 2.5° and 5° for DNI measuring systems.

Due to the variety of the aperture half-angles of CST systems and DNI measurement devices, the assessment of the solar resource for CST systems is more challenging than just directly measuring the DNI. Table 1.1 lists the aperture half-angles of common pyrheliometers and CST systems.

Table 1.1: Aperture half-angles of current pyrheliometers and CST systems (adapted from Blanc *et al.*, 2014).

Pyrheliometer/CST system	**Aperture half-angle (°)**
Parabolic trough – CSTE	< 0.8
Solar tower – CSTE	< 1.8
Linear Fresnel – CSTE	~ 1
Dish-Stirling – CSTE	< 1.6
Different CPV technologies	~ 1.8 to 3.6
Abbott, silver disk – pyrheliometer	2.9
Eko, MS-56 – pyrheliometer	2.5
Eppley, AHF (Cavity) – pyrheliometer	2.5
Eppley, NIP – pyrheliometer	2.9
Eppley, sNIP – pyrheliometer	2.5
Hukseflux, DR01, DR02 – pyrheliometer	2.5
Kipp and Zonen, CH1, CHP1, SHP1 – pyrheliometer	2.5
Kipp and Zonen L-F (Linke-Feussner) – pyrheliometer	5.1
Middleton, DN5, DN5-E – pyrheliometer	2.5

Most CST systems have an aperture half-angle larger than the angular radius (or half-angle) of the Sun but smaller than that of pyrheliometers. The aperture half-angle of the current pyrheliometers is one order of magnitude greater than the half-angle of the Sun as observed from the surface of the Earth. For an observer at ground level, the half-angle of the Sun is 0.266° (4.64 mrad) ± 1.7% (Emilio *et al.*, 2012; Jilinski *et al.*, 1998). This implies that the ground measured DNI includes both the DNI received from the solar disc (DNI_S) and that from a larger circumsolar region, *i.e.* the circumsolar normal irradiance (CSNI), which depends on the corresponding half-angle. Fig. 1.2 exhibits the size of the solar disc with respect to a corresponding half-angle of 2.5°. Assuming the response of the pyrheliometer is a Heaviside function (*i.e.* a full response between [0°, 2.5°]), then all of the radiation incident from the Sun and the circumsolar region (up to 2.5° from the center of the Sun) is measured by the pyrheliometer.

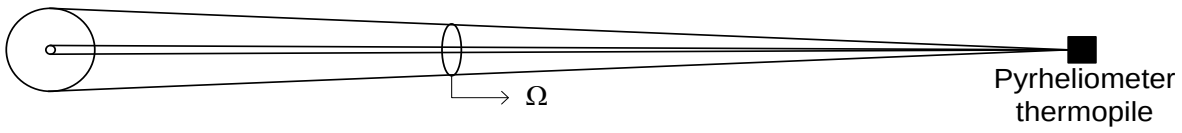
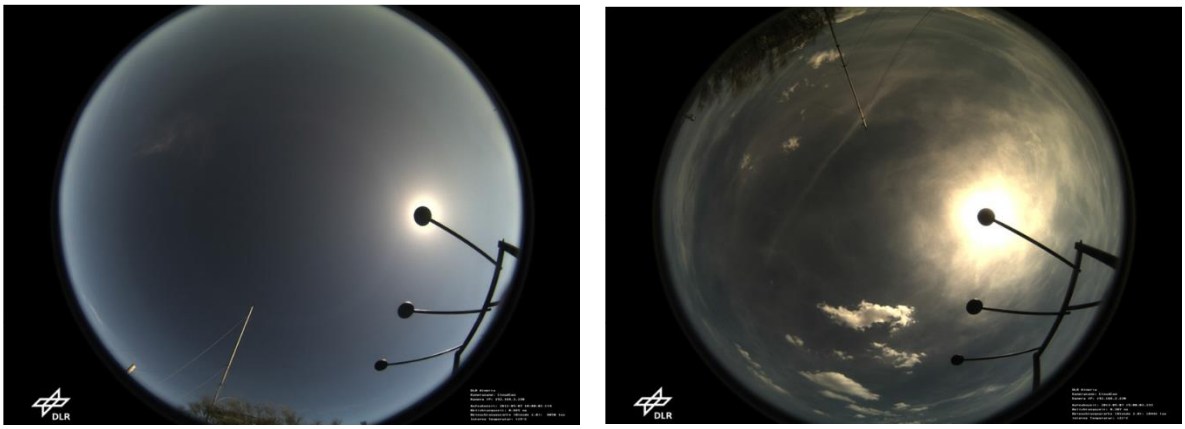


Fig. 1.2: The radiation intercepted by a pyrheliometer normal to the Sun. The small disc on the left represents the solar disc and the large disc on the left represents the circumsolar region having a half-angle of 2.5°. The solid angle Ω is explained further in Sect. 3.3.2.

The circumsolar region, also known as the solar aureole, is the bright region surrounding the solar disc (Fig. 1.3). Forward scattering by molecules, aerosols and particular cloud coverage, *e.g.* ice crystals

such as cirrus, transfer part of the energy from the exact direction of the Sun to the circumsolar region (Blanc *et al.*, 2014; Noring *et al.*, 1991; Reinhardt *et al.*, 2014; Thomalla *et al.*, 1983; Wilbert *et al.*, 2013). Hence, the angular distribution of the sky radiance in the circumsolar region depends on the optical state of the atmosphere, where the radiance is the radiant flux per unit area and per unit solid angle. The azimuthally averaged angular distribution of the radiance from the center of the solar disc is called the solar radiance profile. The solar radiance profile normalized with respect to its central intensity reading is named the sunshape. There is no clear cutoff to the outer limit of the circumsolar region, as it is user-defined, depending on the largest solid angle aperture considered for a given study (Buie *et al.*, 2003; Neumann *et al.*, 2002). Standard pyrheliometers have a non-null sensitivity up to a half-angle between ~ [4°, 5°]. Therefore, in this work the half-angle of the circumsolar region is set to 6°, where the CSNI could be computed at any half-angle smaller than that.



(a) (b)

Fig. 1.3: The circumsolar region under clear sky conditions (a) and cirrus cloud conditions (b). The solar disc is shaded by the shading ball (Wilbert *et al.*, 2012a).

The CSNI could be computed from the solar radiance profile, excluding the solar disc region (*cf.* Sect. 3.4). Knowledge of the CSNI would be valuable in predicting the radiation incident within the aperture of a CST system (Gueymard, 2010). The sunshape is also required to compute the intercept factor, *i.e.* the fraction of incident rays on the aperture that are intercepted by the receiver, which is important for the optimization of the collector optics and receiver geometry (Gueymard, 2010; Rabl and Bendt, 1982; Wilbert *et al.*, 2013). The circumsolar ratio (CSR) is commonly used to characterize the circumsolar radiation. It is defined as the ratio of the CSNI to the sum of the CSNI and DNI_S (Buie *et al.*, 2003).

Besides this current difficulty, another challenge for the resource assessment of CST systems is that measurement campaigns of the solar radiance profile have been performed in a very few locations worldwide and for short periods of time (Neumann *et al.*, 2002; Noring *et al.*, 1991; Wilbert *et al.*, 2013). Measurements from AERONET (AERosol RObotic NETwork) include the almucantar sky radiance, but they are only provided at angles greater than 2.5° from the center of the solar disc (Holben

et al., 1998). Therefore, models to reproduce the sunshape and estimate the circumsolar radiation need to be developed.

More accurate predictions and economic analyses of performances of CST systems imply improved assessments of the resource (Rabl and Bendt, 1982). Standard DNI measurements can be used in an initial assessment of a project feasibility and site selection. In the absence of *in situ* measurements the DNI may be estimated by means of clear-sky models (Gueymard, 2012; Ineichen, 2006). As an example, the McClear model (Lefevre *et al.*, 2013), which is a physical model based on the radiative transfer model (RTM) libRadtran (Mayer and Kylling, 2005; Mayer *et al.*, 2012), predicts the DNI_S under cloud-free skies using atmospheric composition data from the MACC (Monitoring Atmospheric Composition and Climate) project (Benedetti *et al.*, 2009; Inness *et al.*, 2013; Schroedter-Homscheidt *et al.*, 2013). This model usually provides very accurate estimates. It is not always the case. Though validations of the DNI over the UAE exhibited good results, there was an underestimation by McClear because i) it does not consider the CSNI and ii) due to errors in the composition of the atmosphere (Eissa *et al.*, 2015).

Standard DNI measurements or modelled values alone are not sufficient for project development of CST systems. Notably, a better understanding of the circumsolar radiation received at the surface of the Earth along with the standard DNI measurements or modelled values is required in order to provide an improved assessment of the solar resource for CST systems.

1.2. State of the research

Scientific literature on accurate assessments of the beam and circumsolar radiation has developed since the 1970s.

Shaw and Deehr (1974) submitted a report to the Environmental Protection Agency of the United States on the relationship between circumsolar radiance and atmospheric aerosols. However, in their report the circumsolar region was defined up to 30° away from the center of the Sun, and due to instrument limitations the measurement instrument only recorded the radiance after 10° away from the center of the solar disc (Shaw and Deehr, 1974).

During the period 1976 to 1981, solar radiance profile measurements were collected across 11 locations in the United States by the Lawrence Berkeley Laboratory (LBL) (Noring *et al.*, 1991). Using a dedicated telescope, profiles were measured up to 3.2° from the center of the solar disc (Grether *et al.*, 1978). In the Reduced Data Base (RDB), which is available online for public access (http://rredc.nrel.gov/solar/old_data/circumsolar/), broadband solar radiance profile measurements are available with an angular displacement of 0.025° (0.44 mrad) in the solar disc region and 0.075° (1.31 mrad) in the circumsolar region up to 3.2°. Also available are DNI measurements (for an aperture half-angle of 2.5°), measurements of the GHI, *i.e.* the broadband global irradiance received on a

horizontal plane, and measurements of the GNI, *i.e.* the broadband global irradiance received in a direction normal to the Sun.

Thomalla *et al.* (1983) used an RTM to estimate the broadband CSNI under different atmospheric conditions, clear to turbid cloud-free and cloudy conditions. They tested four types of aerosol models (urban, continental, marine and desert) and it is clear from their work that the CSNI is non-negligible. Let $CSR(\alpha)$ denote the broadband circumsolar ratio for an aperture half-angle of α, defined as:

$$CSR(\alpha) = \frac{CS_n(\delta_S, \alpha)}{CS_n(\delta_S, \alpha) + B_n^{Sun}} \tag{1.1}$$

where CS_n is the broadband CSNI in the interval $[\delta_S, \alpha]$, δ_S is the angular radius of the Sun corrected with respect to the Sun-Earth distance, and B_n^{Sun} is the DNI_S. For a solar zenith angle θ_S of 30°, α = 5° and an aerosol optical depth (AOD) at 550 nm set to 0.4 the $CSR(\alpha)$ ranged from 0.013 to 0.084 for the four aerosol types. For the same inputs but θ_S = 70° the $CSR(\alpha)$ increased to range from 0.030 to 0.186. Thomalla *et al.* only reported the results for a maximum AOD of 0.4, which is not representative of several desert regions. One year of AOD retrievals at the desert environment of Masdar Institute, Abu Dhabi, UAE, reveals that 45% of the AOD at 550 nm in cloud-free conditions exceed the value 0.4.

Several parametric models have been developed to estimate the distribution of broadband radiance across the whole sky vault, *e.g.* the all-weather model of Perez *et al.* (1993), the anisotropic sky radiance model of Brunger and Hooper (1993) and the all sky model of Igawa *et al.* (2004). The main drawback of the sky models is that they do not provide accurate estimations of the radiance in the circumsolar region, as such models were only validated 12° to 15° away from the center of the Sun (Ineichen *et al.*, 1994).

Attempts for modelling the sunshape and CSNI are available in the literature, *e.g.* Buie *et al.* (2003), Neumann *et al.* (2002) and Rabl and Bendt (1982). Using the LBL RDB solar radiance profile measurements, Rabl and Bendt proposed an average sunshape profile for improved assessments of the circumsolar effects on solar concentrators, while Buie *et al.* propose an empirical model to reproduce the sunshape of a given $CSR(\alpha)$. Neumann *et al.* conducted a statistical analysis of 2300 measurements of profiles of solar radiance collected in Cologne, Germany (1450 measurement), Odeillo, France (500 measurements) and Almeria, Spain (350 measurements). The measurement system, designed by the German Aerospace Agency (DLR), was comprised of a high-resolution 12-bit digital camera, where the solar and circumsolar images of the Sun were recorded at a 0.0037° (0.065 mrad) resolution and up to an angular extent of 1.72° (30 mrad). As a result, six average sunshape profiles were proposed to improve the assessment of CST systems.

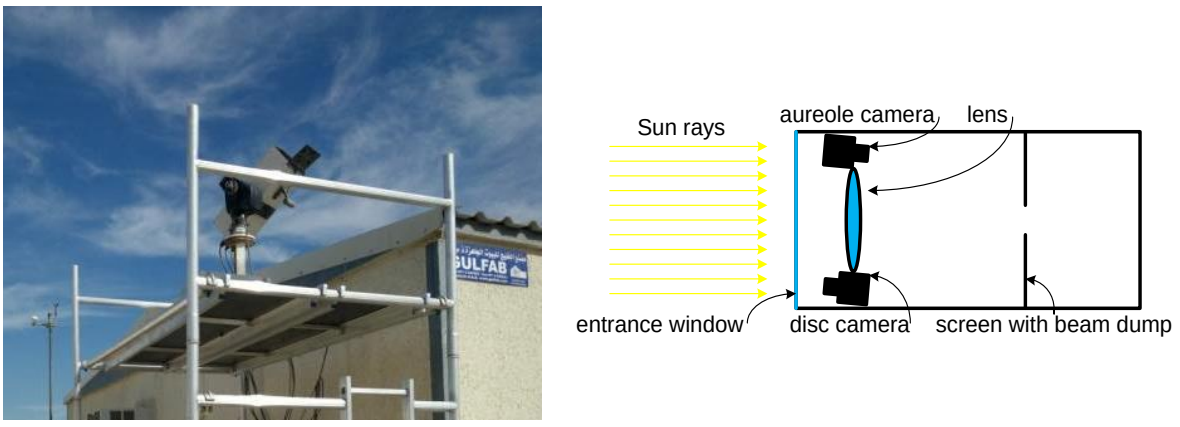
The drawback of the Buie *et al.* approach is that the *CSR* needs to be known beforehand to reproduce the sunshape, while the drawback of the Rabl and Bendt and Neumann *et al.* approaches is that the

average sunshape for different locations may vary significantly (Wilbert *et al.*, 2013). In addition, their analyses were based on measurements collected in Europe and the United States, which exhibit different climates than those in the MENA region.

More recent and still ongoing campaigns have measured or are measuring the monochromatic solar radiance profile, through the Sun and aureole measurement system (SAM) manufactured by Visidyne Inc. (http://www.visidyne.com/). Having a field of view of ≈ 0.015°, the SAM instrument measures the solar radiance profile up to 8° from the center of the solar disc (DeVore *et al.*, 2012b). The SAM instrument is currently installed in 9 stations across the globe:

1. Institute of Experimental Meteorology, Obninsk, Russia,
2. ARM, Southern Great Plains, Oklahoma, USA,
3. NASA GSFC, Greenbelt, Maryland, USA,
4. Visidyne, Burlington, Massachusetts, USA,
5. PSA/DLR, Tabernas, Almeria, Spain,
6. Masdar Institute, Abu Dhabi, UAE,
7. CNRS, Odeillo, France,
8. K.A.CARE, Riyadh, Saudi Arabia,
9. K.A.CARE, Jeddah, Saudi Arabia.

The system is comprised of 2 cameras. One directly measures the radiance within the solar disc. The solar aureole image is formed on a screen with a beam dump for the solar disc region and this image is captured by the other camera facing the screen (*cf.* Fig. 1.4). The SAM instrument only measures the monochromatic radiance at 670 nm with a full spectral width at half-maximum of 10 nm. Other spectral filters exist at 440 nm and 870 nm.



(a) (b)

Fig. 1.4: A picture of the SAM instrument in Abu Dhabi (image from: http://www.visidyne.com/SAM/SAM_DATA_MAS_files/image002.jpg) (a) and a schematic of the SAM instrument modified after Wilbert *et al.* (2012a) (b).

A gap exists between the solar disc radiance and the solar aureole radiance to avoid superimposition of the solar disc radiance scattered on the screen with the image of the circumsolar region on that screen (Wilbert *et al.*, 2013). DeVore *et al.* (2012b) suggest that radiance measurements less than 0.64° measured by the solar aureole camera are noisy and should be excluded. Wilbert *et al.* (2013) propose a method to fill the gap in the SAM measurements using a power-law fit.

Concerning CST applications, the SAM measurements which are monochromatic radiances are not directly applicable as CSTE systems are sensitive to the broadband measurements while CPV systems are sensitive to a specific range of the solar spectrum. Wilbert *et al.* (2013) propose a method to convert the monochromatic measurements of the profile of solar radiance into broadband profiles through the use of a modified version of the RTM SMARTS (Simple Model of the Atmospheric Radiative Transfer of Sunshine) (Gueymard, 1995, 2001) using the following inputs: monochromatic AOD, total column content in water vapor, aerosol single scattering albedo (SSA) and phase function (PFCN), asymmetry parameter, atmospheric pressure, and ozone concentration. The aerosol SSA is the ratio of the attenuation due to scattering effects of aerosols to the attenuation due to both scattering and absorption effects of aerosols. The aerosol PFCN is a measure of the angular distribution of the scattered energy due to aerosol effects. The asymmetry parameter is a measure of the preferred scattering direction, approaching +1 for very strong forward scattering and −1 for very strong backward scattering. In the context of this work, the term *aerosol optical properties* refers to the AOD, aerosol SSA and aerosol PFCN.

Upon availability of such inputs, the CSNI may be computed from the modelled profile of the diffuse solar radiance. The DNI_S may be accurately modelled by RTMs, using accurate AOD and observations of the total column content in water vapor as the main inputs. The main drawback of RTMs from an operational point of view is that they are computationally expensive. Therefore, a fast model to estimate the DNI_S and CSNI would be valuable for the resource assessment of CST systems.

1.3. Objective and research questions

The objective of this PhD thesis is to contribute to an improved assessment of the beam and circumsolar radiation under cloud-free conditions in a desert environment. The thesis attempts to answer the following research questions:

i. What are the key aerosol optical properties required under cloud-free conditions in a desert environment for an accurate estimate of the beam and circumsolar radiation?
ii. Can a fast and accurate model be developed to estimate the beam and circumsolar radiation (for a defined aperture angle) using observables which are more frequently available than aerosol optical properties?

iii. If such a model can be devised, is it applicable over other desert areas under cloud-free conditions or is it limited to the site for which it was developed?

A desert environment is of interest because the countries in the MENA region, where the environment is mostly dominated by desert surroundings, have set ambitious plans to install CST systems in the upcoming years. Also, in desert environments the circumsolar radiation could be significant under turbid cloud-free skies, implying that information of the CSNI and DNI_S is essential for an improved assessment of the DNI (Blanc *et al.*, 2014; Thomalla *et al.*, 1983).

1.4. Methodology

The following methodology was devised to fulfill the objective of this thesis.

The main study area was selected to be in the UAE for a number of reasons. It is a desert environment with frequent turbid but cloud-free skies. It has several measuring instruments which are valuable in the context of this thesis. The ground measurements include: the GHI, the diffuse horizontal irradiance (DHI), and the DNI from a rotating shadowband irradiometer (RSI); the AOD, aerosol SSA, aerosol PFCN, and almucantar radiance, all at several wavelengths from the AERONET station; and the monochromatic solar and circumsolar radiance from the SAM instrument. A detailed description of the measurements and their quality checks will be presented.

A sensitivity analysis will then be conducted to identify the main variables affecting the modelling of the beam and circumsolar radiation. After selecting the variables of significance two RTMs will be exploited to model the monochromatic DNI_S and CSNI at 670 nm. The monochromatic values are modelled at 670 nm because the SAM reference measurements are monochromatic measurements at that specific wavelength. The two tested RTMs will be SMARTS (Gueymard, 1995, 2001) and libRadtran (Mayer and Kylling, 2005; Mayer *et al.*, 2012). The validations will be split into two parts, namely the monochromatic DNI_S and the monochromatic CSNI.

Following this test, the most accurate RTM will be selected to model the broadband DNI_S and CSNI. As no reference broadband DNI_S and CSNI are available, the modelled values will be indirectly validated with respect to broadband DNI measurements for a defined aperture half-angle. Ideally the modelled DNI_S should exhibit an underestimation when compared to the reference DNI, while the DNI_S + CSNI should exhibit no bias with respect the reference DNI.

Assuming the validation results of the modelled broadband DNI_S and CSNI are satisfactory then a fast model to estimate such values from observables which are more frequently available than the aerosol optical properties will be developed. This model will be validated in a similar manner, but with observations which were not included in the development of the model.

Assuming that the validation results and the development of the model are satisfactory, the same methodology will be applied to another location in the MENA region which also has a desert environment. This would highlight as to whether the model could be applied globally to other desert regions or not.

1.5. Layout of the thesis

Chapter 2 is written in French and summarizes the content of the thesis to the attention of the French-reading persons.

Chapter 3 will start by covering the definitions of the angles describing the position of the Sun. Then a background on the extraterrestrial solar radiation is presented, followed by the radiative transfer in the atmosphere and the components of the solar radiation received at the surface of the Earth. The equations to compute the irradiances of interest and the diffuse radiance in the very near vicinity of the solar disc are also presented.

Chapter 4 describes the study area and the ground measurements used in this thesis.

Chapter 5 discusses the sensitivity of the CSNI and DNI_S to the aerosol optical properties. The two RTMs exploited herein, *i.e.* SMARTS and libRadtran, and their inputs are presented.

Chapter 6 presents the validations of the monochromatic and broadband CSNI and DNI_S, the fast model to estimate the CSNI and DNI_S and its validations.

Chapter 7 deals with the applicability of the model to other desert areas. The methodologies described in Chapters 5 and 6 are repeated over another desert site in the MENA region.

Finally, Chapter 8 presents the conclusions of this thesis along with the future prospects.

Chapitre 2 – Résumé étendu

2.1. Introduction

Les mesures de l'éclairement direct total en incidence normale (en anglais, *direct normal irradiance*, et abrégé DNI par la suite), par des pyrhéliomètres ou des systèmes pyranométriques équivalents comprennent non seulement l'éclairement provenant de l'angle solide du disque solaire (DNI_S) mais aussi l'éclairement provenant d'une région angulaire circumsolaire plus large. Cet éclairement est appelé l'éclairement circumsolaire en incidence normale (*circumsolar normal irradiance*, abrégé en CSNI). Ces instruments pyranométriques peuvent avoir des caractéristiques optiques différentes les uns des autres, qui conduisent à des ouvertures angulaires différentes, généralement définies en première approximation par le demi-angle d'ouverture. L'organisation météorologique mondiale (*World Meteorological Organization*, WMO, 2010) recommande pour la mesure du DNI par les pyrhéliomètres, un demi-angle d'ouverture compris entre 2.5° et 5°, soit un ordre de grandeur plus grand que le demi-angle du disque solaire. Les technologies à concentration solaire (*concentrated solar technologies*, CST), comprenant les systèmes de production électrique par conversion thermodynamique du rayonnement solaire concentré (*concentrated solar thermal electric*, CSTE) ou par conversion photovoltaïque du rayonnement solaire concentré (*concentrated photovoltaic*, CPV), permettent, indirectement ou directement, la conversion du DNI en électricité. L'analyse de la ressource solaire pour de tels systèmes CST doit porter une attention particulière au fait que leurs ouvertures angulaires sont généralement plus petites que celles des pyrhéliomètres ou autres instruments pyranométriques mesurant le DNI (Blanc *et al.*, 2014).

La région circumsolaire, aussi dénommée l'auréole solaire, correspond à la région angulaire particulièrement brillante autour du disque solaire. La tendance à la prodiffusion –diffusion en avant– du rayonnement solaire incident due aux molécules, aérosols et aux éléments constitutifs des nuages, notamment les nuages de cristaux de glaces comme les cirrus, entraîne un transfert d'une partie de l'énergie provenant du disque solaire vers la région circumsolaire (Blanc *et al.*, 2014 ; Noring *et al.*, 1991 ; Reinhardt *et al.*, 2014 ; Thomalla *et al.*, 1983 ; Wilbert *et al.*, 2013). Par conséquent, la distribution angulaire de la luminance du ciel dans la région angulaire dépend de l'état optique de l'atmosphère. Le profil de luminance solaire est défini comme la moyenne azimutale de la distribution angulaire de la luminance à partir de la position angulaire du centre du Soleil. Une fois normalisé par sa valeur pour le centre du Soleil, ce profil est défini par le terme anglais de *sunshape*. Il n'y a pas de limite clairement définie de demi-angle d'ouverture maximale pour la région circumsolaire puisque cette limite dépend du demi-angle d'ouverture de l'instrument de mesure ou du moyen de conversion considéré (Buie *et al.*, 2003; Neumann *et al.*, 2002). Blanc et *al.* (2014) recommandent pour l'analyse de la ressource solaire pour les technologies CST de considérer non seulement la mesure du DNI associée à la donnée du demi-angle d'ouverture de l'instrument mais aussi les informations disponibles

sur le *sunshape* et la distribution de la luminance circumsolaire, qui peuvent être par exemple, le ratio du circumsolaire (*circumsolar ratio*, CSR) pour différents demi-angles d'ouverture. Le CSR est défini comme le rapport du CSNI sur la somme du DNI_S et du CSNI.

Des campagnes de mesure de profil de luminance solaire ont eu lieu pour très peu d'endroits dans le monde et ce pour de courtes périodes de temps (Neumann *et al.*, 2002 ; Noring *et al.*, 1991 ; Wilbert *et al.*, 2013). Les mesures provenant du réseau de photomètres solaires AERONET (*AERosol RObotic NETwork*) comprennent notamment, en plus des données d'épaisseur optiques des aérosols, des luminances du ciel de type *almucantar*[1]. Cependant l'échantillonnage angulaire de ces luminances ne débute qu'à 2.5° du centre du disque solaire (Holben *et al.*, 1998). Par conséquent, des modèles de prédiction du rayonnement circumsolaire doivent être développés. L'objectif de la thèse est de contribuer à l'amélioration de la connaissance des composantes directe et circumsolaire du rayonnement solaire, en se limitant aux situations de ciel clair – *i.e.* sans nuage – en milieu désertique. La thèse tente d'apporter des réponses aux questions de recherche suivantes :

i. Quelles sont les propriétés optiques clés des aérosols pour une estimation précise des rayonnements directs et circumsolaires en milieu désertique, sous condition de ciel clair ?
ii. Peut-on développer un modèle précis et rapide pour estimer ces rayonnements pour un demi-angle d'ouverture donné, utilisant des observables ou des mesures qui sont plus couramment disponibles que les données relatives aux propriétés optiques des aérosols ?
iii. Le cas échéant, ce modèle sera-t-il utilisable, sous condition de ciel clair, pour d'autres régions désertiques que celle à partir duquel il a été développé ?

L'environnement désertique revêt un intérêt particulier car les pays des régions du Moyen Orient et d'Afrique du Nord (*Middle East and North Africa*, MENA), effectivement largement dominés par des environnements désertiques, ont des objectifs ambitieux de réalisation de systèmes de type CST pour les années à venir (Brand et Zingerle, 2011 ; Bryden *et al.*, 2013 ; Griffiths, 2013). Par ailleurs, pour de tels environnements désertiques, le rayonnement circumsolaire peut être particulièrement important compte tenu des nombreuses situations de ciel turbide sans nuage : dans de telles situations, des informations sur le CSNI, le DNI_S ou le CSR sont cruciales pour une estimation de la ressource solaire en DNI (Blanc *et al.*, 2014 ; Thomalla *et al.*, 1983).

Ce chapitre est organisé en sept sous-sections :

- la section 2.2 est dédiée à l'exposé des bases théoriques pour évaluer les éclairements direct et diffus d'intérêt dans la région circumsolaire ;
- la section 2.3 présente la zone géographique d'étude ainsi que les moyens de mesures au sol utilisés lors de la thèse ;

[1] *Echantillonnage angulaire en azimut de la luminance du ciel pour une hauteur angulaire constante correspondant à l'élévation angulaire du Soleil au-dessus de l'horizon.*

- la section 2.4 propose une analyse de sensibilité du CSNI et du DNI_S vis à vis des propriétés optiques des aérosols et des entrées des modèles de transfert radiatif ;
- la section 2.5 présente le modèle de calcul rapide proposé pour l'évaluation du CSNI et du DNI_S et sa validations ;
- la section 2.6 traite de l'applicabilité du modèle à d'autres régions désertiques ;
- enfin, la section 2.6 présente les conclusions de la thèse ainsi que ses perspectives.

2.2. Les bases théoriques

2.2.1. Les différentes composantes du rayonnement solaire atteignant la surface de la Terre

Les équations permettant d'établir les éclairements DNI_S, DNI, CSNI ainsi que le CSR sont présentées pour une longueur d'onde donnée. Le DNI_S monochromatique peut être calculé à partir de la luminance monochromatique du ciel (Blanc *et al.*, 2014 ; Buie *et al.*, 2003 ; Wilbert *et al.*, 2013):

$$B_{n,\lambda}^{Sun} = \int_0^{2\pi} \int_0^{\delta_S} L_\lambda(\xi, \varphi_n) \cos(\xi) \sin(\xi) d\xi d\varphi_n \quad (2.1)$$

où L_λ est la luminance monochromatique du ciel, ξ est l'angle de diffusion[2], φ_n est l'angle d'azimut dans le plan normal à la direction du Soleil et δ_S est le rayon angulaire du disque solaire tenant compte de la variation de la distance Terre-Soleil. Pour de petits angles de diffusion ξ dans les régions circumsolaire et du disque solaire, l'écart à l'unité de cos(ξ) peut être négligé. De plus, en faisant l'hypothèse raisonnable, sous condition de ciel clair, d'une symétrie radiale de la luminance du ciel au voisinage du centre du Soleil, l'équation (2.1) se simplifie :

$$B_{n,\lambda}^{Sun} = 2\pi \int_0^{\delta_S} L_\lambda(\xi) \sin(\xi) d\xi \quad (2.2)$$

De même, le DNI monochromatique pour un demi-angle d'ouverture α incluant le CSNI correspondant est donné par la relation suivante :

$$B_{n,\lambda}(\alpha) = 2\pi \int_0^{\alpha} L_\lambda(\xi) \sin(\xi) d\xi \quad (2.3)$$

Pour une meilleure représentation du DNI mesuré par un pyrhéliomètre, la fonction de pénombre de l'instrument doit être considérée dans l'équation (2.3). La fonction de pénombre – aussi appelée la fonction d'acceptance – correspond, pour une direction donnée, à la fraction du rayonnement incident atteignant le capteur du pyrhéliomètre (Blanc *et al.*, 2014 ; Gueymard, 1995). Pour des pyrhéliomètres ayant une ouverture circulaire, cette fonction de pénombre peut être décrite en première approximation par trois demi-angles : le demi-angle de pente ε_S (*slope angle*), le demi-angle limite ε_L (*limit angle*) et le demi-angle d'ouverture α. Le demi-angle de pente est défini comme le demi-angle en deçà duquel la fonction de pénombre peut être considérée comme étant égale à l'unité. A l'inverse, le demi-angle limite

[2] *L'angle de diffusion correspond à la distance angulaire entre la zone angulaire considérée et la position centrale du disque solaire.*

est défini comme le demi-angle au-delà duquel la fonction de pénombre peut être considérée comme nulle. Le demi-angle d'ouverture est approximativement la moyenne des deux demi-angles ε_S et ε_L.

Connaissant ces demi-angles, le DNI monochromatique mesuré par un pyrhéliomètre peut s'écrire :

$$B_{n,\lambda}(\varepsilon_L) = 2\pi\int_0^{\varepsilon_L} p(\xi)L_\lambda(\xi)\sin(\xi)d\xi \tag{2.4}$$

où la fonction de pénombre $p(\xi)$ est égale à 1 pour $\xi < \varepsilon_S$ et égale à 0 pour $\xi > \varepsilon_L$.

Le CSNI monochromatique s'écrit alors :

$$CS_{n,\lambda}(\delta_S, \varepsilon_L) = 2\pi\int_{\delta_S}^{\varepsilon_L} p(\xi)L_\lambda(\xi)\sin(\xi)d\xi \tag{2.5}$$

Dans le cas où seul le demi-angle d'ouverture α est connu, la fonction de pénombre est alors prise comme une fonction rectangulaire pour laquelle les trois demi-angles sont confondus. Dans ce cas, on peut écrire :

$$CS_{n,\lambda}(\delta_S, \alpha) = 2\pi\int_{\delta_S}^{\alpha} L_\lambda(\xi)\sin(\xi)d\xi \tag{2.6}$$

En supposant que $\varepsilon_S > \delta_S$, les grandeurs monochromatiques CSNI, DNI et DNI_S sont liées :

$$B_{n,\lambda}(\varepsilon_L) = CS_{n,\lambda}(\delta_S, \varepsilon_L) + B_{n,\lambda}^{Sun} \tag{2.7}$$

Le ratio circumsolaire monochromatique CSR est alors :

$$CSR_\lambda(\varepsilon_L) = \frac{CS_{n,\lambda}(\delta_S, \varepsilon_L)}{CS_{n,\lambda}(\delta_S, \varepsilon_L) + B_{n,\lambda}^{Sun}} \tag{2.8}$$

Lorsque seul le demi-angle d'ouverture α est défini, on a :

$$B_{n,\lambda}(\alpha) = CS_{n,\lambda}(\delta_S, \alpha) + B_{n,\lambda}^{Sun} \tag{2.9}$$

et

$$CSR_\lambda(\alpha) = \frac{CS_{n,\lambda}(\delta_S, \alpha)}{CS_{n,\lambda}(\delta_S, \alpha) + B_{n,\lambda}^{Sun}} \tag{2.10}$$

Les précédentes équations établies pour une longueur d'onde donnée s'étendent simplement au cas des éclairements et luminances totales, c'est-à-dire intégrés sur l'ensemble du spectre.

L'éclairement total GHI peut ainsi s'écrire :

$$G = \int_0^{2\pi}\int_0^{\pi/2} L(\theta,\varphi)\cos(\theta)\sin(\theta)d\theta d\varphi \tag{2.11}$$

où θ et φ correspondent respectivement à l'angle zénithal et l'angle azimutal d'une portion élémentaire du ciel.

L'éclairement total diffus DHI s'écrit :

$$D = \int_0^{2\pi} \int_0^{\pi/2} L(\theta,\varphi)\cos(\theta)\sin(\theta)(1-(\xi(\theta,\varphi) < \alpha))d\theta d\varphi \quad (2.12)$$

Les éclairements totaux GHI, DHI et DNI sont liés par l'expression suivante :

$$G = B_n(\alpha)\cos(\theta_S) + D \quad (2.13)$$

où θ_S est l'angle zénithal solaire.

Idéalement, le DHI ne doit pas intégrer la part du diffus provenant de la région circumsolaire correspondant à l'ouverture angulaire pour les mesures de DNI.

Dans les sections 2.5 et 2.6, un indice empirique, appelé indice de clarté du ciel (*sky clearness index*) et noté *SC*, est utilisé. Proposé par Perez et al. (1993), il est défini par :

$$SC = \left[(D + B_n)/D + 1.041\theta_S{}^3\right] / \left[1 + 1.041\theta_S{}^3\right] \quad (2.14)$$

où θ_S est en radian.

2.2.2. Paramétrisation de la luminance diffuse

Afin de modéliser la composante diffuse de la luminance du ciel dans le voisinage du disque solaire, il est essentiel de connaître les variables de l'état de l'atmosphère qui l'affectent. En négligeant les effets de la diffusion multiple dans la région circumsolaire (Box et Deepak, 1978 ; Dubovik *et al.*, 2000 ; Kocifaj et Gueymard, 2011 ; Thomalla *et al.*, 1983), la luminance diffuse vue par un observateur à la surface de la Terre peut être approchée par la relation suivante (Dubovik et King, 2000 ; Liou, 2002 ; Wilbert *et al.*, 2013) :

$$L_\lambda(\xi) = E_{0,n,\lambda}\, m \exp(-\tau_\lambda m) P_\lambda(\xi)\omega_\lambda \tau_\lambda / (4\pi) \quad (2.15)$$

où $E_{0,n,\lambda}$ est l'éclairement monochromatique extraterrestre en incidence normale (Wald, 2007) et m est la masse d'air corrigée de la pression (Kasten et Young, 1989 ; Remund *et al.*, 2003 ; Rigollier *et al.*, 2000). Les autres variables régissant la luminance diffuse dans la région circumsolaire sont :

- la fonction monochromatique de phase (*phase function*, PFCN) de diffusion qui représente la distribution angulaire de l'énergie diffusée ;
- l'albédo monochromatique de simple diffusion (*single scattering albedo*, SSA) qui représente la fraction d'énergie atténuée par diffusion ;
- l'épaisseur monochromatique optique des aérosols (*aerosol optical depth*, AOD) qui représente l'atténuation relative à l'interaction du rayonnement avec les aérosols dans l'atmosphère.

2.3. Lieu géographique d'étude et mesures *in-situ*

2.3.1. Lieu géographique d'étude

La thèse s'intéresse à l'environnement désertique sans nuage. Les Emirats Arabes Unis (EAU), avec ses régions désertiques et sa très faible occurrence nuageuse, correspondent à ce type d'environnement. De plus, les EAU présentent souvent des situations sans nuage mais des ciels turbides, dues aux émissions naturelles et anthropogéniques de poussières et de sables en suspension (Gherboudj et Ghedira, 2014) : cette région est donc particulièrement intéressante pour la thèse qui est focalisée sur les éclairements directs et circumsolaires.

Masdar City est une ville nouvelle, située dans l'émirat d'Abu Dhabi, EAU. L'environnement de *Masdar City* peut être qualifié de désertique, d'urbain et de proche-côtier. L'altitude de la ville est de seulement 7 m ; ses coordonnées géographiques sont 24.4200° N et 54.613° E.

Enfin, point particulièrement intéressant dans le contexte de cette thèse, des mesures d'éclairement solaire incident au sol – ou mesures pyranométriques –, de caractéristiques des aérosols et de luminance du disque solaire et de la région circumsolaire sont disponibles sur un site de mesures *in-situ* de *Masdar City*.

2.3.2. Les mesures in-situ

Plus précisément :

- les mesures pyranométriques d'éclairement diffus et global – l'éclairement direct étant calculé avec l'équation (2.13) – sont effectuées par un capteur pyranométrique à bande d'ombrage rotatif (*rotating shadowband irradiometer*, RSI) ;
- les mesures des caractéristiques des aérosols sont effectuées par un photomètre solaire CIMEL CE-318 appartenant au réseau AERONET ;
- les mesures de luminances du disque solaire et de la région circumsolaire sont effectuées par un système spécifique nommé *Sun and Aureole Measurement* (SAM) (DeVore *et al.*, 2012a).

La période de temps pendant laquelle les trois instruments ont fonctionné en même temps s'étend de juin 2012 à mai 2013.

Le RSI est composé d'une photodiode à silicium LI-COR LI-200 et d'un anneau d'ombrage en rotation. Ce pyranomètre possède une sensibilité spectrale limitée à l'intervalle de 400 nm à 1100 nm, et a fait l'objet d'un étalonnage avec un pyranomètre de première classe de type thermopile, le *Eppley Precision Spectral Pyranometer (PSP)*, dans des conditions d'éclairage naturel (http://www.licor.com/env/products/light/pyranometers). La société CSP Services, qui a installé la station de mesure RSI, a procédé en outre à un étalonnage supplémentaire de ce dernier avec des mesures pyranomètriques de type thermopile de grande qualité sur le site de la *Plataforma Solar de Almeria* (PSA) en Espagne. Elle a ensuite pris soin de vérifier que cet étalonnage était effectivement valable pour des sites dans la région du Moyen-Orient et d'Afrique du Nord (Geuder *et al.*, 2014).

Toutes les mesures passent positivement le test de qualité décrit par Roesch *et al.* (2011a, b). La température ambiante (T_{amb}) et l'humidité relative (*relative humidity*, RH) ont été aussi relevées de manière concomitante par une station de mesure CS215 de *Campbell Scientific*.

Un des problèmes du RSI est que, contrairement à un pyrhéliomètre, l'ouverture angulaire correspondant aux mesures de DNI n'est pas explicitement définie. Wilbert *et al.* (2012b) proposent les caractéristiques d'ouverture angulaire suivantes : $\varepsilon_S = 1.1°$, $\alpha = 2.86°$ et $\varepsilon_L = 4.6°$.

Pour la station AERONET, le photomètre solaire CIMEL CE-318 de demi-angle d'ouverture de 0.6° (Holben *et al.*, 1998) collecte des mesures monochromatiques d'éclairement direct en incidence normale au niveau du sol qui sont ensuite converties en propriétés optiques des aérosols, disponibles publiquement sur http://aeronet.gsfc.nasa.gov. Issues de l'algorithme d'estimation *Direct Sun Algorithm* (DSA) dans sa version 2, ces propriétés optiques des aérosols comprennent l'épaisseur optique des aérosols (AOD) pour huit longueurs d'onde, l'angle zénithal solaire et le contenu total de la colonne d'air en vapeur d'eau. Seul le niveau de traitement « *Level 2.0* » a été considéré : pour ce niveau de traitement, les estimations des propriétés optiques des aérosols ne sont pas contaminées par la présence de nuage dans l'ouverture du photomètre solaire et ont subi des tests drastiques de qualité.

L'algorithme *Inversion* dans sa version 2 d'AERONET permet en outre, notamment pour *Masdar City* :

- des profils monochromatiques de luminance de type *almucantar* pour des angles de diffusion ξ de ±3°; ±3.5°; ±4°; ±5°; ±6° et pour quatre longueurs d'onde (1020 nm, 870 nm, 675 nm et 440 nm). La luminance *almucantar* est disponible pour d'autres angles de diffusion plus importants mais qui sortent du champ d'étude de la thèse, focalisée sur la région circumsolaire. La luminance *almucantar* pour la longueur d'onde particulière 675 nm présente un intérêt particulier car elle correspond quasiment à celle fournie par l'instrument SAM, à 670 nm ;
- toujours pour ces quatre longueurs d'onde, l'algorithme *Inversion* dans sa version 2 d'AERONET permet l'estimation des AOD monochromatiques $\tau_{a,\lambda}$, des SSA monochromatiques $\omega_{a,\lambda}$, des PFCN monochromatiques des aérosols $P_{a,\lambda}(\xi)$ et de facteurs monochromatiques d'asymétrie d'aérosols g_λ (Dubovik et King, 2000 ; Holben *et al.*, 1998).

Les luminances du disque solaire et de la région circumsolaire sont acquises 4 à 5 fois par minute par l'instrument SAM installé sur le site de *Masdar City* (DeVore *et al.*, 2012a). Cet instrument mesure verticalement et horizontalement ces luminances pour des angles de diffusion de ± 8°. Il s'agit de luminances monochromatiques pour la longueur d'onde centrale de 670 nm et une largeur totale à mi-hauteur de 10 nm. L'instrument comprend deux caméras. La première mesure directement la luminance provenant du disque solaire. Une image de l'auréole solaire est ensuite formée sur un écran avec un système d'atténuation du rayonnement issu du disque solaire, et acquise par la deuxième caméra. La résolution angulaire des mesures de luminances est de 0.0217° pour le site de *Masdar City*. Afin d'éviter des phénomènes de diffusion de la luminance du disque solaire venant parasiter les mesures de

luminance circumsolaire, il y a un trou dans l'échantillonnage angulaire entre 0.26° et 0.52°, environ (Wilbert *et al.*, 2013). De plus, DeVore *et al.* (2012b) suggèrent que les mesures de luminance circumsolaire pour des angles de diffusion inférieurs à 0.64° sont bruitées et ne doivent pas être utilisées.

Les erreurs relatives de la luminance du disque solaire sont estimées à moins de 1 % pour des épaisseurs optiques des aérosols inférieures à 0.6. Pour les luminances circumsolaires, ces erreurs relatives sont estimées entre 5 % et 15 % (Stair et DeVore, 2012).

Une série de tests de qualité des mesures issues de SAM a été définie lors de la thèse afin de ne garder que les mesures de grande qualité. Ainsi, sur les 244609 mesures de luminances issues de SAM, 191818 ont passé la série de tests de qualité, soit une proportion de 78.4 %.

Comme indiqué précédemment, SAM et le photomètre solaire d'AERONET produisent tous les deux des mesures de luminances dans la région circumsolaire et d'AOD, pour la longueur d'onde 670 nm. La comparaison de ces séries de mesure permet de détecter et d'enlever, le cas échéant, des mesures aberrantes car non cohérentes entre les deux instruments.

Afin de comparer les luminances *almucantar* d'AERONET et les profils horizontaux de luminance de SAM correspondant au même instant à plus ou moins une minute près, ces derniers ont été préalablement agrégées angulairement pour correspondre aux mesures du photomètre solaire CIMEL 318 qui a un demi-angle d'ouverture de 0.6°. Globalement, les mesures de luminance entre les deux instruments sont en accord, avec une erreur quadratique moyenne de 18 % (rapportée à la moyenne des mesures AERONET), un biais relatif de 0 % et un coefficient de détermination R^2 élevé, de 0.894. Il est à noter que les mesures issues d'AERONET correspondent à la longueur d'onde 675 nm alors que celles de SAM correspondent à 670 nm. Cet état de fait induit de légères différences.

Cette légère différence de sensibilité spectrale a été corrigée en utilisant la relation d'Ångström (Ångström, 1964) pour effectuer la comparaison entre les mesures d'AOD produites par SAM et par AERONET. Par ailleurs, l'élimination des mesures incohérentes entre les deux instruments tient compte des précisions des algorithmes d'estimation d'AOD de SAM et d'AERONET qui sont, respectivement de ± 0.03 (DeVore *et al.*, 2012a) et de ± 0.01 pour des longueurs d'onde supérieures à 440 nm (Holben *et al.*, 1998). Ainsi, toutes les mesures concomitantes d'AOD monochromatique différant en valeur absolue de plus de 0.03 entre les deux instruments ont été éliminées. En définitive, l'erreur quadratique moyenne relative entre les deux séries de mesures concomitantes d'AOD est de 6 % et le coefficient de détermination (R^2) est de 0.998. Cependant, le biais relatif est de 5 %, indiquant une très nette surestimation des AOD par SAM, comparés aux AOD mesurés par AERONET. En effet, le photomètre solaire d'AERONET présente un demi-angle d'ouverture de 0.6° : cela signifie que le rayonnement circumsolaire du bord du disque solaire à l'angle de diffusion de 0.6° est intercepté par l'instrument. Ainsi, le rayonnement direct mesuré par le photomètre solaire pour l'estimation de l'AOD est plus grand que celui de SAM, ce dernier correspondant au disque solaire seulement (DeVore *et al.*, 2012a). Il

s'ensuit une sous-estimation systématique des mesures d'AOD d'AERONET comparées à celles de SAM.

Le tableau 2.1 liste les différents jeux de données utilisés dans les sections suivantes :

Tableau 2.1: Les différents jeux de données disponibles pour la thèse sur le site d'Abu Dhabi (EAU).

Jeu de données	**Période temporelle**	**Nombre de données**	**Types de mesures**
DS1	juin 2012 à mai 2013	10285	▪ RSI : DNI, DHI et GHI ; ▪ CS215 : T_{amb} et RH ; ▪ AERONET DSA *(Level 2.0)* : les AOD monochromatiques (1020 nm, 870 nm, 675 nm et 440 nm) et le contenu total de la colonne d'air en vapeur d'eau.
DS2	juin 2012 à avril 2013	3723	▪ RSI : DNI, DHI et GHI ; ▪ CS215 : T_{amb} et RH ; ▪ AERONET DSA (*Level 2.0)* : les AOD monochromatiques (1020 nm, 870 nm, 675 nm et 440 nm) et le contenu total de la colonne d'air en vapeur d'eau ; ▪ SAM : AOD monochromatique (670 nm), et les profils horizontaux, verticaux et moyennés en azimut de la luminance monochromatique du ciel à 670 nm.
DS3	juin 2012 à mai 2013	1068	▪ RSI : DNI, DHI et GHI ; ▪ CS215 : T_{amb} et RH ; ▪ AERONET *Inversion* (*Level 2.0*) : les PFCN et les facteurs d'asymétrie monochromatiques (1020 nm, 870 nm, 675 nm, and 440 nm) ; ▪ AERONET DSA (*Level 2.0)* : les AOD monochromatiques (1020 nm, 870 nm, 675 nm, and 440 nm) et le contenu total de la colonne d'air en vapeur d'eau, moyennés sur plus ou moins 16 min autour de chaque instant de mesures AERONET *Inversion* (*Level 2.0*).
DS4	juin 2012 à mai 2013	491	Identique à DS3 avec en plus, pour des temps concomitants, les SSA monochromatiques issus de AERONET *Inversion* (*level 2.0*)
DS5	juin 2012 à avril 2013	425	Identique à DS4 avec, en plus, pour des temps concomitants : AOD monochromatique (670 nm), et les profils horizontaux, verticaux et moyennés en azimut de la luminance monochromatique du ciel à 670 nm issus de SAM.

2.4. Modélisation des rayonnements directs et circumsolaires

Dans cette section, les variables affectant les rayonnements directs et circumsolaires sont analysés afin de répondre à la première question de recherche : « *Quels sont les propriétés optiques clés des aérosols*

pour une estimation précise des rayonnements directs et circumsolaires en milieu désertique, sous condition de ciel clair ? ». Par la suite, sont présentées les paramétrisations des modèles de transfert radiatif libRadtran (Mayer et Kylling, 2005; Mayer *et al.*, 2012) et SMARTS (*Simple Model of the Atmospheric Radiative Transfer of Sunshine*) (Gueymard, 1995, 2001) utilisés pour évaluer ces rayonnements directs et circumsolaires.

2.4.1. Les propriétés optiques des aérosols

Les termes $E_{0,n,\lambda}$ et m de l'équation (2.15) sont bien définis et peuvent être calculés avec une précision suffisante. Par conséquent, les incertitudes de la modélisation de la luminance monochromatique diffuse circumsolaire sont liées aux incertitudes relatives aux variables suivants : τ_λ, $P_\lambda(\xi)$ et ω_λ. Pour mener l'étude de sensibilité, une atmosphère essentiellement dominée par les aérosols est considérée, de telle sorte que la variabilité de la luminance diffuse soit uniquement due à celles des propriétés optiques des aérosols (Dubovik et King, 2000). Dans une telle atmosphère, l'équation (2.15) peut s'écrire :

$$L_\lambda(\xi) = f(P_{a,\lambda}(\xi), \omega_{a,\lambda}, \tau_{a,\lambda}) \tag{2.16}$$

Le jeu de données DS4 a été utilisée par l'analyse de sensibilité. Seules les mesures de $\tau_{a,\lambda}$, $P_{a,\lambda}(\xi)$ et $\omega_{a,\lambda}$ pour la longueur d'onde 675 nm ont été utilisées. L'étude de sensibilité a été menée en ne considérant qu'une variable à la fois, et en considérant les autres comme constantes. L'écart type temporel de chacune des variables a été évalué. Pour chacune des 491 mesures de DS4, l'erreur absolue relative de la luminance monochromatique à 675 nm a été évaluée pour chaque variable dans l'intervalle $[-1\sigma, +1\sigma]$, où σ correspond à l'écart type temporel correspondant. Puisque la PFCN monochromatique des aérosols $P_{a,\lambda}$ est fonction de l'angle de diffusion ξ, l'étude de sensibilité a été conduite pour les trois valeurs de ξ inférieur à 6°, disponibles par AERONET : 0°, 1.71° et 3.93°.

Sur la zone d'étude en question, le SSA monochromatique $\omega_{a,\lambda}$ a la plus petite influence sur le calcul de la luminance monochromatique correspondante. L'erreur relative maximale est proche de 2 % lorsque le SSA monochromatique varie de ± 1σ pour les 491 valeurs de référence de DS4. En effet, l'écart type temporel rapporté à la moyenne de $\omega_{a,\lambda}$ est de 2 % et la dépendance de la luminance monochromatique au SSA monochromatique est simplement linéaire. A l'inverse, l'AOD monochromatique $\tau_{a,\lambda}$ a la plus grande influence sur le calcul de la luminance monochromatique. Les erreurs relatives dépassent 100 % pour certains cas, lorsque l'AOD monochromatique varie de ± 1σ pour les 491 valeurs de référence. Enfin, les erreurs absolues relatives pour des variations de ± 1σ de la PFCN $P_{a,\lambda}$ pour les trois angles de diffusion est de 43 %.

La principale variable affectant le calcul du DNI_S est l'AOD. Cependant, pour la longueur d'onde 670 nm, une sous-estimation de 5 % des valeurs d'AOD issues d'AERONET par rapport à celle issues de SAM a été constatée. Ce biais est trop important pour être négligé. C'est la raison pour laquelle une régression affine des AOD d'AERONET a été effectuée par rapport à celles de SAM avec les mesures de l'ensemble DS2. Pour cela, cet ensemble a été scindé en deux sous-ensembles de manière aléatoire :

- 80 % des données ont été utilisées effectivement pour la régression ;
- 20 % des données ont été réservées comme sous-ensemble de test, pour l'évaluation des erreurs résiduelles après régression.

La correction des AOD d'AERONET par régression affine par rapport à celles de SAM est la suivante :

$$\tau_{a,\lambda}(\mathrm{SAM}) = 0.992\,\tau_{a,\lambda}(\mathrm{AERONET}) + 0.016 \tag{2.17}$$

Sur le sous-ensemble de test, la comparaison entre les AOD d'AERONET corrigées par l'équation (2.17) et celles de SAM montre que le biais est alors de 0 %, que l'erreur quadratique moyenne relative est de 3 % et que le coefficient de détermination R^2 est de 0.998. Ces résultats sur un sous-ensemble indépendant, montre que cette correction peut être appliquée, pour ce lieu, sur des instants de mesure différents de ceux de DS2.

Dans le modèle libRadtran, la PFCN $P_{a,\lambda}$ est définie par une série tronquée de ses moments de Legendre. Une représentation fidèle du pic de cette dernière pour de faibles angles de diffusion (prodiffusion) est très importante pour une estimation précise de la luminance monochromatique diffuse dans la région circumsolaire. La représentation de $P_{a,\lambda}$ la plus simple et la plus courante est celle de Henyey-Greenstein (HG) qui est complètement déterminée par la seule donnée du facteur d'asymétrie g (Henyey et Greenstein, 1941 ; Liou, 2002) :

$$P_{HG}(\xi, g) = (1-g^2)/(1+g^2-2g\cos(\xi))^{1.5} \tag{2.18}$$

Cependant, la PFCN HG ne permet pas de reproduire correctement les PFCN présentant des pics de prodiffusion très prononcés (Liou, 2002). Irvine (1965) et Kattawar (1975) ont proposé une fonction de phase composée de deux fonctions de type HG (*two term HG*, TTHG) :

$$P_{TTHG}(\xi, c_1, c_2, c_3) = c_1 P_{HG}(\xi, c_2) + (1-c_1) P_{HG}(\xi, c_3) \tag{2.19}$$

où c_1, c_2 et c_3 sont trois paramètres définissant entièrement la fonction TTHG.

Aucun article n'a été trouvé proposant une application directe de ces fonctions de type TTHG pour le calcul du rayonnement solaire dans des conditions de ciel clair turbide. La PFCN de type TTHG peut être décomposée en une série de polynômes de Legendre comme suit :

$$P_{TTHG}(\xi, c_1, c_2, c_3) = \sum_{l=0}^{\infty} (2l+1)(c_1 {c_2}^l + (1-c_1){c_3}^l)\, p_l(\cos(\xi)) \tag{2.20}$$

où $(c_1 {c_2}^l + (1-c_1){c_3}^l)$ correspond au $l^{\text{ième}}$ moment de Legendre et p_l est $l^{\text{ième}}$ polynôme de Legendre.

Dans ce travail, les mesures de PFCN $P_{a,\lambda}$ d'AERONET ont été utilisées pour déterminer à chaque instant de mesure, les trois paramètres de l'équation (2.19) en utilisant pour cela la méthode de régression non-linéaire au sens des moindres carrés Levenberg-Marquardt (Marquardt, 1963).

En conclusion, pour répondre à la première question de recherche concernant la modélisation de la luminance diffuse circumsolaire, les variables $\tau_{a,\lambda}$, $P_{a,\lambda}(\xi)$ and $\omega_{a,\lambda}$ sont effectivement les plus influentes, même si leurs effets ne sont pas identiques. Sur la zone d'étude, le SSA $\omega_{a,\lambda}$ peut être considéré constant car les effets sur la luminance diffuse de sa variabilité temporelle sont très faibles, nettement moins importants que ceux induits par $\tau_{a,\lambda}$ et $P_{a,\lambda}(\xi)$. Ce sont ces deux dernières variables qui doivent être déterminés très précisément. Concernant le DNI_S monochromatique, la variable la plus importante est l'AOD monochromatique correspondant. Cependant, la mesure d'AOD par AERONET, présentant une nette surestimation, doit être corrigée pour une estimation précise du DNI_S. Une telle correction par régression affine est proposée par l'équation (2.17).

2.4.2. Paramétrisation des modèles de transfert radiatif libRadtran et SMARTS

Les entrées de libRadtran sont les suivantes :

- l'angle zénithal solaire θ_S, calculé par l'algorithme SG2 de Blanc et Wald (2012) ;
- la longueur d'onde λ souhaitée pour les calculs des luminances ou des éclairements monochromatiques ;
- l'AOD $\tau_{a,\lambda}$ à la longueur d'onde définie par (ii), et évalué en utilisant la loi d'Ångström sur les mesures d'AOD d'AERONET ;
- pour le lieu et la période d'étude considérés, le profil atmosphérique (*i.e.* les profils verticaux de température, de pression, de densité et de volume des mélanges gazeux). Le profil « *mid-latitude summer* » proposé par Anderson *et al.* (1986) a été choisi ;
- le contenu total en vapeur d'eau issu d'AERONET DSA *Level 2.0* ;
- l'altitude au-dessus du niveau de la mer du site considéré : 7 m;
- le solveur choisi pour la résolution des équations de transfert radiatif : DISORT ;
- la valeur moyenne pour le SSA des aérosols $\omega_{a,\lambda}$ à la longueur d'onde définie par (ii) a été utilisée ;
- les moments de Legendre calculés à partir des PFCN des aérosols $P_{a,\lambda}$ à la longueur d'onde définie par (ii) et issues d'AERONET *Inversion* ;
- la définition des angles zénithaux θ des éléments de ciel considérés sur l'intervalle $[\theta_S - 6°, \theta_S + 6°]$ par pas de 0.0217° ;
- la définition des angles azimutaux φ des éléments de ciel considérés sur l'intervalle $[\varphi_S - 6°, \varphi_S + 6°]$ par pas de 0.0217° ;
- l'éclairement monochromatique hors atmosphère *atlas_plus_modtran ;*
- le jour de l'année (i.e. de 1 à 365) afin de corriger les éclairements hors-atmosphère de la distance Terre-Soleil ;
- le nombre de directions pour lesquelles la luminance est effectivement calculée par DISORT (*streams*) : 16 ;

Pour libRadtran, si seul le facteur d'asymétrie est défini –et pas les moments de Legendre–, la fonction HG est alors utilisée. Par ailleurs, si les paramètres de SSA et de PFCN ne sont pas définis en entrée, ils peuvent être évalués automatiquement en précisant le type d'aérosol dans la librairie OPAC (Hess *et al.*, 1998 ; Mayer et Kylling, 2005).

Pour le code de transfert radiatif SMARTS, les entrées sont organisées en 17 « *cartes* » (Gueymard, 2006). Dans l'ordre, ces 17 « *cartes* » sont les suivants :

- Carte 1 - COMNT : commentaires ;
- Carte 2 - ISPR: pression atmosphérique au niveau du site.
  ISPR=2 : variable déterminée par la latitude du point considéré, l'altitude du sol au-dessus du niveau de la mer et l'élévation du site de mesure au-dessus du sol;
- Carte 3 - IATMOS : profil atmosphérique.
  IATMOS=1 : correspond au profil choisi ici : 'MLS' « *mid-latitude summer* » (comme pour libRadtran) ;
- Carte 4 - IH2O: contenu total en vapeur d'eau.
  IH2O=0 : variable renseignée par les mesures d'AERONET DSA *Level 2.0* ;
- Carte 5 - IO3: contenu total en ozone.
  IO3=1 : paramètre choisi par défaut compte tenu du profil atmosphérique choisi ;
- Carte 6 - IGAS: absorption gazeuse et la pollution atmosphérique.
  IGAS=1 : paramètre défini par défaut ;
- Carte 7 - qCO2: concentration volumique en dioxyde de carbone.
  valeur par défaut qCO2 = 370 (ppmv) ;
- Carte 7a - ISPCTR: éclairement monochromatique hors atmosphère.
  ISPCTR=4 correspondant au fichier MODTRAN « Spctrm_4.dat », le plus proche de celui utilisé par libRadtran ;
- Carte 8 - AEROS: modèle d'aérosol.
  AEROS='DESERT_MAX'
  ou, selon les cas,
  AEROS='USER'
  - Carte 8a – ALPHA1, ALPHA2, OMEGL, GG : paramètres des aérosols.
    ALPHA1 : exposant d'Ångström pour des longueurs d'onde inférieures à 500 nm ;
    ALPHA2 : exposant d'Ångström pour des longueurs d'onde supérieure à 500 nm ;
    OMEGL : SSA total des aérosols ω_a ;
    GG : facteur d'asymétrie total g.
    Les paramètres d'Ångström ALPHA1 et ALPHA2 sont calculés à partir de la loi d'Ångström appliquée aux mesures d'AOD monochromatiques d'AERONET. Par ailleurs, SMARTS nécessite un SSA ω_a et un facteur d'asymétrie g totaux et non pas

monochromatiques. Ces paramètres totaux n'étant pas disponibles avec les mesures *in-situ*, les mesures de facteurs monochromatiques d'asymétrie et la valeur moyenne de SSA à 670 nm issues d'AERONET *Inversion* ont été utilisées ;

- Carte 9 - ITURB: turbidité.
  ITURB=5 : AOD à 550 nm
  - Carte 9a : l'AOD $\tau_{a,\lambda=550\ nm}$ à 550 nm est défini à partir de la loi d'Ångström appliqué aux AOD monochromatiques d'AERONET ;
- Carte 10 - IALBDX : albédo du sol.
  IALBDX = -1 : albédo total.
  - Carte 10a – RHOX : albédo total de type lambertien et pris par défaut à 0.3.
- Carte 11 - WLMN, WLMX, SUNCOR, SOLARC
  WLMN, WLMX : valeur minimale et maximale des longueurs d'onde considérées pour les calculs de transfert radiatif. Ces extrema ont été définis respectivement à 280 nm et 4000 nm ;
  SUNCOR : facteur de correction liée à la distance Terre-Soleil calculé par l'algorithme SG2 de Blanc et Wald (2012) ;
  SOLARC : constante solaire (*i.e.* moyenne annuelle de l'éclairement solaire hors atmosphère en incidence normale) définie à 1367 W m^{-2} ;
- Carte 12 - IPRT: paramètre permettant de définir le type de sortie « totale » ou « monochromatique » de SMARTS
  IPRT=0 pour un calcul des éclairements totaux.
  IPRT=3 pour un calcul des éclairements monochromatiques
  - Carte 12a - WPMN, WPMX, INTVL : valeurs minimales, maximales et pas des longueurs d'onde (nm) pour le calcul des éclairements monochromatiques. Pour un calcul à la longueur d'onde 670 nm uniquement, WPMN= WPMN=670 et INTVL=1 ;
- Carte 13 - ICIRC: option de SMARTS pour le calcul des éclairements circumsolaires.
  ICIRC=1
  - Carte 13a - SLOPE, APERT, LIMIT: respectivement ldemi-angle de pente ε_S, demi-angle d'ouverture α et demi-angle limite ε_L du pyrhéliomètre considéré ;
- Carte 14 - ISCAN: option non utilisée permettant le calcul d'éclairement sur des domaines spectraux, avec des sensibilités monochromatiques spécifiques. ISCAN=0 ;
- Carte 15 - ILLUM: option pour le calcul des éclairements lumineux, non utilisée ici. ILLUM=0 ;
- Carte 16 - IUV: option pour le calcul des éclairements dans le domaine de l'UV, non utilisée ici. IUV=0 ;
- Carte 17 - IMASS: option pour la détermination de la position du Soleil et de la masse de l'air *m*.
  IMASS=0

- Carte 17a - ZENIT, AZIM: respectivement angle zénithal θ_S et angle azimutal φ_S du Soleil établi par l'algorithme SG2.

Une comparaison absolument équitable entre libRadtran et SMARTS n'est pas possible pour deux raisons. Premièrement, contrairement à libRadtran, SMARTS ne permet pas de définir exactement l'AOD monochromatique pour une longueur d'onde donnée : la seule possibilité consiste à déterminer l'AOD soit à 500 nm, soit à 550 nm. Deuxièmement, SMARTS ne permet pas de définir explicitement des PFCN des aérosols comme le permet libRadtran avec la série tronquée de moments de Legendre.

2.5. La modélisation des rayonnements directs et circumsolaire : modèles et résultats

La deuxième question de recherche est abordée dans cette section : « *Peut-on développer un modèle précis et rapide pour estimer ces rayonnements pour un demi-angle d'ouverture donné, utilisant des observables ou des mesures qui sont plus couramment disponibles que les données relatives aux propriétés optiques des aérosols ?* ».

Dans un premier temps, les performances des deux modèles de transfert radiatifs libRadtran et SMARTS pour modéliser les éclairements spectraux DNI_S et le CSNI à 670 nm, sont analysées avec les différentes entrées présentées ci-dessus. Ensuite, le modèle de transfert radiatif le plus précis est utilisé pour estimer les éclairements totaux DNI_S et CSNI. Enfin, un modèle simplifié paramétrique est proposé pour approcher ces éclairements totaux DNI_S et CSNI issus du modèle de transfert radiatif.

2.5.1. La modélisation des éclairements spectraux direct et circumsolaire à 670 nm

Le tableau 2.2 présente les résultats de comparaison des DNI_S monochromatiques produits par libRadtran et SMARTS avec les mesures *in-situ* d'AOD. Les différences entre les deux modèles sont négligeables ; le biais minime entre ces deux modèles peut être éventuellement expliqué par l'utilisation de la loi d'Ångström appliquée à l'AOD monochromatique à 550 nm pour calculer l'AOD à 670 nm. Une autre cause possible de ce biais est liée à la correction des AOD issues d'AERONET, qui a été établie à 670 nm et appliquée à 550 nm, sans avoir été validée.

Pour les deux modèles, le biais relatif entre les mesures et les résultats du modèle, est du même ordre : 1 %. Compte tenu de la précision des mesures issues de SAM estimée à moins de 1 % pour des AOD inférieurs à 0.6, on peut conclure que les deux modèles permettent une modélisation très précise du DNI_S monochromatique.

Tableau 2.2: Comparaison des estimations de DNI_S monochromatique à 670 nm avec les mesures *in-situ* issues de SAM (DS2) (EQM : erreur quadratique moyenne).

Modèle de transfert radiatif	**Nombre de données**	**Moyenne** $W\,m^{-2}\,\mu m^{-2}$	**Biais** $W\,m^{-2}\,\mu m^{-2}$	%	**EQM** $W\,m^{-2}\,\mu m^{-2}$	%	**R^2**
libRadtran	3723	863.9	+4.6	+1	46.9	5	0.972
SMARTS	3723	863.9	+8.5	+1	46.7	5	0.974

La modélisation du CSNI monochromatique pour l'intervalle angulaire [δ = 0.64°, α = 6°] est très fortement dépendante des propriétés optiques des aérosols. Les différences dans les résultats de modélisation par les deux modèles de transfert radiatif pour différentes propriétés des aérosols sont présentées dans le tableau 2.3. Tous les critères statistiques des modélisations du CSNI monochromatique sont très nettement améliorés lorsque les fonctions de type TTHG sont utilisées pour décrire les PFCN des aérosols. Cependant, même avec de telles fonctions, on constate toujours une large sous-estimation du CSNI monochromatique de -19 %. Ce biais peut être partiellement dû aux PFCN monochromatiques $P_{a,\lambda}$ des aérosols mesurées par AERONET *Inversion*. En effet, le photomètre solaire d'AERONET présente un demi-angle d'ouverture de 0.6° qui est relativement important devant le rayon angulaire du Soleil de 0.266°± 1.7% ou devant le demi-angle maximal de 6° considéré pour la région circumsolaire. De plus, pour des angles de diffusion de moins de 6°, les PFCN monochromatiques d'AERONET ne sont déterminées que pour trois angles de diffusion : 0°, 1.71° et 3.93°. Enfin, pour la période considérée sur le site AERONET d'étude, les données de PFCN pour les deux premiers angles de diffusion sont le résultat d'extrapolation : les valeurs de luminance almucantar dont les PFCN sont issues ne sont faites, sur ce site, que pour des angles de diffusion supérieurs à 3°. Il s'agit d'une limitation d'AERONET *Inversion*. Cependant, considérant la précision de l'ordre de 15 % des mesures de luminance de SAM, on peut conclure que l'utilisation de fonctions de type TTHG et de leurs moments de Legendre pour décrire les PFCN des aérosols avec libRadtran permet une modélisation remarquablement précise du CSNI monochromatique sur le lieu d'étude.

Tableau 2.3: Comparaison des estimations de CSNI monochromatique à 670 nm avec les mesures *in-situ* issues de SAM (DS5) (EQM : erreur quadratique moyenne).

Modèle de transfert radiatif	**Propriétés optiques des aérosols utilisées**	**Nombre de données**	**Moyenne** W m^{-2} µm^{-2}	**Biais** W m^{-2} µm^{-2}	%	**EQM** W m^{-2} µm^{-2}	%	**R^2**
libRadtran	AOD à 670 nm ; SSA moyen ; PFCN de type HG	DS5 ; 425	84.3	−63.8	−76	68.2	81	0.721
SMARTS	AOD à 550 nm ; SSA moyen ; facteur d'asymétrie moyen	DS5 ; 425	84.3	−61.6	−73	66.6	79	0.694
libRadtran	AOD à 670 nm ; aérosol de type « *desert type* » d'OPAC	DS5 ; 425	84.3	−26.0	−31	31.7	38	0.719
SMARTS	AOD à 550 nm ; aérosol de type « *DESERT_MAX* »	DS5 ; 425	84.3	−39.0	−46	45.5	54	0.570
libRadtran	AOD à 670 nm ; SSA moyen ; PFCN de type TTHG	DS5 ; 425	84.3	−15.7	−19	18.8	22	0.891

2.5.2. Proposition d'une méthode pour la modélisation des éclairements totaux direct et circumsolaire

Le modèle de transfert radiatif libRadtran permet effectivement une modélisation précise du DNI_S monochromatique. De même, lorsque les PFCN des aérosols sont représentées par des fonctions de type TTHG, libRadtran offre une excellente modélisation du CSNI monochromatique, bien meilleure que celle avec des fonctions de type HG ou encore que celles proposée à la fois par libRadtran et SMARTS avec des propriétés optiques typiques des aérosols issues de librairies prédéfinies.

C'est la raison pour laquelle, le modèle de transfert radiatif libRadtran a été choisi pour la modélisation du DNI_S et du CSNI total avec des entrées similaires à celles utilisées pour la modélisation monochromatique. Les différences principales entre les modélisations monochromatiques et totales avec libRadtran sont les suivantes : i) utilisation de la méthode de *k-distribution* et l'approximation *correlated-k* de Kato *et al.* (1999) pour le calcul des éclairements totaux, et ii) détermination des propriétés optiques des aérosols pour différentes longueurs d'onde en utilisant l'option *aerosol_files* offerte par libRadtran. Ces propriétés optiques des aérosols ($\tau_{a,\lambda}$, $\omega_{a,\lambda}$, et $P_{a,\lambda}$) sont déterminées pour quatre longueurs d'onde (1020 nm, 870 nm, 675 nm et 440 nm) par l'algorithme AEROSOL *Inversion*.

En utilisant la série de mesures *in-situ* DS3, la comparaison entre le DNI_S total évalué par libRadtran et le DNI mesuré par le RSI montre des erreurs très faibles. Ainsi, l'EQM relative est-elle de 5 %, le biais relatif de 1 % et le coefficient de détermination R^2 de 0.992. La surestimation de 1 % pour l'ensemble des mesures – plus prononcée pour les valeurs d'éclairement élevées – est inattendue : en effet, on s'attendrait plutôt à une sous-estimation de DNI_S de libRadtran comparé au DNI du RSI, puisque ce dernier inclue une part du rayonnement circumsolaire. Cependant, ce biais est compris dans l'incertitude des mesures de RSI elles-mêmes, de l'ordre de ± 4 %.

On peut penser à plusieurs causes possibles pour ce léger biais de surestimation du DNI_S de libRadtran. Cela peut être partiellement dû aux données d'entrées utilisées par libRadtran : l'interpolation des propriétés optiques des aérosols pour différentes longueurs d'onde à partir des mesures d'AERONET peut induire des erreurs de modélisation, *in fine*. De plus, la correction par régression affine des AOD monochromatiques d'AERONET a été établie et validée uniquement à 670 nm mais appliquée directement aux autres longueurs d'onde. Une autre cause possible réside dans un problème d'étalonnage du RSI, notamment vis-à-vis de la température, bien que cet étalonnage ait été mené deux fois : une fois par le fabriquant de la photodiode et une fois par CSP Services.

La comparaison du DNI de libRadtran – correspondant à la somme du DNI_S et du CSNI pour l'intervalle angulaire [0°, 4.6°] – avec celui mesuré par le RSI met en évidence une forte surestimation par libRadtran avec un biais relatif de +5 %. L'EQM relative est de 7 % et le coefficient de détermination R^2 est de 0.994. L'augmentation du biais entre les deux comparaisons, celle avec le DNI_S et celle avec le DNI de libRadtran, est de 17.4 W m^{-2}, de 5.1 W m^{-2} à 22.5 W m^{-2}. Cet incrément positif était bien entendu attendu puisque le DNI de libRadtran est le résultat du DNI_S augmenté des valeurs positives de

CSNI. Cependant, on peut noter une légère augmentation du coefficient de détermination lorsque le CSNI est ajouté, montrant ainsi une contribution positive du CSNI modélisé par libRadtran dans la représentation de la variabilité temporelle du DNI. Ceci est aussi corroboré par l'écart type des erreurs de modélisation du DNI de libRadtran de 21 W m^{-2}, plus faible que celle du DNI_S seul de 23.7 W m^{-2}.

2.5.3. Modélisation empirique des éclairements totaux direct et circumsolaire

Le CSR de libRadtran calculé à partir de ses modélisations du DNI_S et du CSNI peut être modélisé empiriquement par une fonction de l'indice de clarté du ciel *SC*. Le diagramme de dispersion du CSR en fonction de *SC* est présenté par la figure 2.1. Comme expliqué par Perez *et al.* (1993), les faibles valeurs de *SC* correspondent aux ciels turbides tandis que les fortes valeurs de *SC* indiquent des ciels très clairs : les valeurs de CSR évoluent de manière cohérente, avec de fortes valeurs lorsque l'indice *SC* est faible et *vice-versa*.

Au lieu de déterminer un modèle de régression pour toute la gamme des indices *SC*, un modèle de régression plus précis a été établi en considérant trois intervalles pour les indices *SC* : $SC < 1.74$, $1.74 \leq SC \leq 5.09$ et $SC > 5.09$. Une régression au sens des moindres carrés avec une fonction de type puissance a été choisie pour les deux premiers intervalles tandis qu'une simple fonction affine est suffisante pour le dernier intervalle. Aucune contrainte de continuité n'a été imposée entre les modèles pour chacun des intervalles. La figure 2.1 présente les trois modèles de régression ainsi que les bornes à 95 % des mesures et des modèles, superposés au diagramme de dispersion. Les bornes à 95 % associées aux modèles correspondent à la variabilité de ces derniers vis-à-vis d'une série d'échantillons, tirés aléatoirement, des mesures utilisées par les régressions au sens des moindres carrés. Ces bornes sont très petites, indiquant une excellente stabilité des modèles de régression et donc une bonne estimation du CSR.

Les trois modèles de régression sont les suivants :

$$CSR(\varepsilon_L) = o_1 SC^{\rho_1} + v_1 \qquad \text{pour } SC < 1.74 \qquad (2.21)$$

$$CSR(\varepsilon_L) = o_2 SC^{\rho_2} \qquad \text{pour } 1.74 \leq SC \leq 5.09 \qquad (2.22)$$

$$CSR(\varepsilon_L) = o_3 SC + v_3 \qquad \text{pour } SC > 5.09 \qquad (2.23)$$

Le tableau 2.4 donne les valeurs des coefficients o_1, o_2, o_3, ρ_1, ρ_2, v_1, v_2 et v_3.

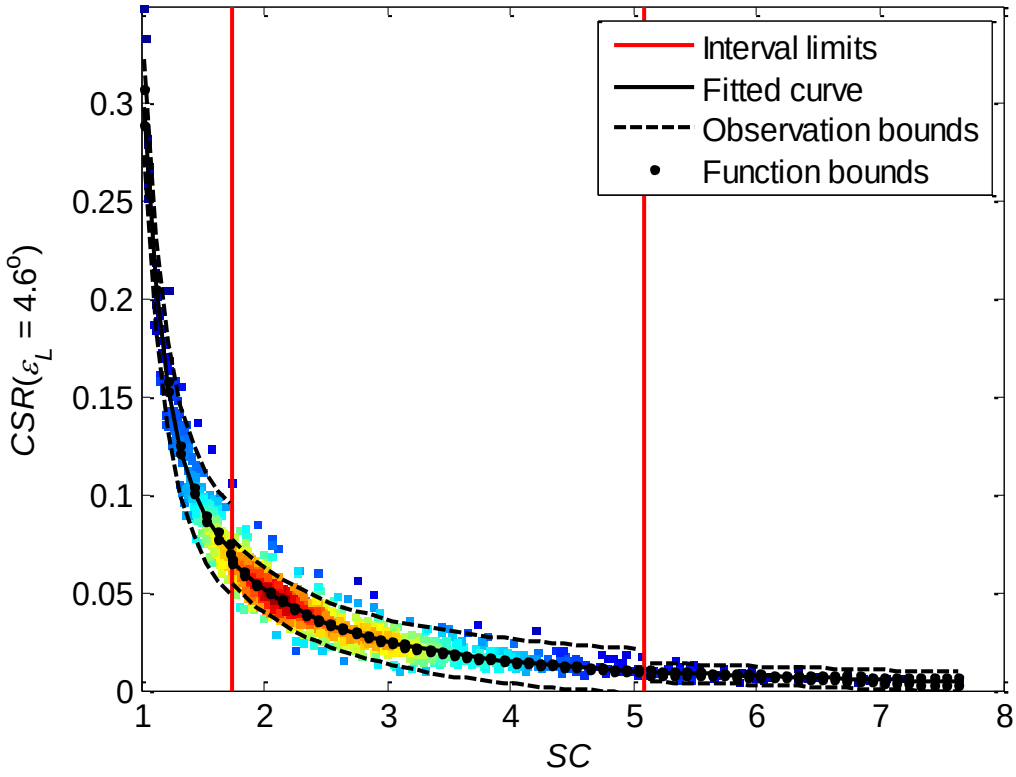


Figure 2.1: diagramme de dispersion entre le CSR modélisé par libRadtran pour un angle limite de 4.6° ($CSR(\varepsilon_L = 4.6°)$) et l'indice de clarté du ciel (SC), associé aux bornes à 95 % des observations. Les limites des trois intervalles pour la modélisation sont représentées en rouge. Pour chacun de ces intervalles, sont représentées la modélisation ainsi que les bornes à 95 % associées.

Tableau 2.4: Les coefficients des équations (2.21) à (2.23), leurs intervalles de confiance (IC) à 95 % et les moyennes des erreurs absolues (MEA) du CSR modélisé pour chacun des trois intervalles.

Intervalle	o_i	ρ_i	v_i	**MEA**
	95 % IC	95 % IC	95 % IC	**CSR**
$SC < 1.74$	0.2753	−4.902	0.05343	0.010
$i = 1$	[0.2659, 0.2847]	[−5.353, −4.452]	[0.04675, 0.06011]	
$1.74 \leq SC \leq 5.09$	0.1779	−1.788	N/A	0.005
$i = 2$	[0.1700, 0.1859]	[−1.845, −1.732]		
$SC > 5.09$	−0.00200	N/A	0.01954	0.002
$i = 3$	[−0.00312, −0.00088]		[0.01294, 0.02614]	

La validation de chacune des fonctions de régression est basée sur une validation croisée de type LOOCV (*leave-one-out cross validation*). En définitive, les erreurs de modélisation du CSR reportées dans le tableau 2.4 correspondent, pour chaque intervalle, à la moyenne des erreurs absolues (MEA). Le tableau 2.4 reporte aussi, pour chaque intervalle, l'intervalle de confiance à 95 % de chacun des coefficients des modèles de régression. Les MEA sont significativement plus faibles pour le deuxième

intervalle (MEA de 0.005) et le troisième intervalle (MEA de 0.002). On note que les intervalles de confiance à 95 % associés aux coefficients sont faibles, sauf peut-être pour le troisième intervalle, à cause d'un relativement faible nombre de mesures pour ce dernier.

Le modèle empirique proposé n'est cependant valide pour que le demi-angle d'ouverture du RSI. Les demi-angles d'ouverture de la plupart des systèmes de conversion par concentration solaire sont nettement plus petits. Les coefficients des équations (2.21) à (2.23) peuvent être alors ré-établis pour modéliser des ratios de CSR avec d'autres demi-angles d'ouverture avec *SC*, calculé à partir du DHI et du DNI du RSI.

Une procédure similaire a été appliquée pour déterminer, avec l'aide de libRadtran, les modèles de régression du CSR pour les trois intervalles de *SC*, en faisant varier le demi-angle d'ouverture de 0.4° à 5° par pas de 0.2°. Ainsi, est-il possible de déterminer le CSR pour tout demi-angle d'ouverture compris entre 0.4° et 5°.

Le CSNI correspondant au CSR établi pour un tel demi-angle d'ouverture α dans l'intervalle [0.4°, 5°] est calculé comme suit :

$$CS_n(\delta = 0°, \alpha) = \frac{CSR(\alpha) B_n^{Sun}}{1 - CSR(\alpha)} \tag{2.24}$$

Le DNI_S est déterminé par l'équation suivante:

$$B_n^{Sun} = B_n^{RSI} - CS_n(\delta = 0°, \varepsilon_L = 4.6°) \approx B_n^{RSI} - CS_n(\delta = 0°, \alpha = 2.86°) \tag{2.25}$$

où B_n^{RSI} correspond au DNI mesuré par le RSI.

La validation de ce modèle a été aussi établie par une validation croisée de type LOOCV. L'erreur absolue maximale du CSR modélisé est de 0.015, pour des valeurs de *SC* faible (premier intervalle), et lorsque le demi-angle d'ouverture α est égal à 5°.

Les coefficients des équations (2.21) à (2.23) en fonction du demi-angle d'ouverture α, sont déterminés par les polynômes d'ordre 6 suivants :

$$o_1 = -4.254\,\mathrm{e}^{-6}\,\alpha^6 - 1.987\,\mathrm{e}^{-4}\,\alpha^5 + 4.505\,\mathrm{e}^{-3}\,\alpha^4 - 3.407\,\mathrm{e}^{-2}\,\alpha^3 + 1.095\,\mathrm{e}^{-1}\,\alpha^2 - 2.944\,\mathrm{e}^{-2}\,\alpha + 4.390\,\mathrm{e}^{-3} \tag{2.26}$$

$$\rho_1 = 8.047\,\mathrm{e}^{-5}\,\alpha^6 - 1.076\,\mathrm{e}^{-3}\,\alpha^5 + 1.050\,\mathrm{e}^{-2}\,\alpha^4 - 8.125\,\mathrm{e}^{-2}\,\alpha^3 + 3.040\,\mathrm{e}^{-1}\,\alpha^2 - 7.735\,\mathrm{e}^{-2}\,\alpha - 5.758 \tag{2.27}$$

$$\nu_1 = -8.853\,\mathrm{e}^{-6}\,\alpha^6 + 9.154\,\mathrm{e}^{-5}\,\alpha^5 + 1.462\,\mathrm{e}^{-5}\,\alpha^4 - 3.663\,\mathrm{e}^{-3}\,\alpha^3 + 1.676\,\mathrm{e}^{-2}\,\alpha^2 - 3.563\,\mathrm{e}^{-3}\,\alpha + 4.440\,\mathrm{e}^{-4} \tag{2.28}$$

$$o_2 = -1.393\,\mathrm{e}^{-5}\,\alpha^6 + 1.850\,\mathrm{e}^{-4}\,\alpha^5 - 3.037\,\mathrm{e}^{-4}\,\alpha^4 - 7.126\,\mathrm{e}^{-3}\,\alpha^3 + 4.483\,\mathrm{e}^{-2}\,\alpha^2 - 8.604\,\mathrm{e}^{-3}\,\alpha + 9.833\,\mathrm{e}^{-4} \quad (2.29)$$

$$\rho_2 = -1.897\,\mathrm{e}^{-5}\,\alpha^6 + 4.410\,\mathrm{e}^{-4}\,\alpha^5 - 4.043\,\mathrm{e}^{-3}\,\alpha^4 + 1.785\,\mathrm{e}^{-2}\,\alpha^3 - 3.254\,\mathrm{e}^{-2}\,\alpha^2 + 2.900\,\mathrm{e}^{-3}\,\alpha - 1.742 \quad (2.30)$$

$$o_3 = -4.935\,\mathrm{e}^{-7}\,\alpha^6 + 8.189\,\mathrm{e}^{-6}\,\alpha^5 - 5.965\,\mathrm{e}^{-5}\,\alpha^4 + 2.669\,\mathrm{e}^{-4}\,\alpha^3 - 7.698\,\mathrm{e}^{-4}\,\alpha^2 + 2.406\,\mathrm{e}^{-4}\,\alpha - 4.127\,\mathrm{e}^{-5} \quad (2.31)$$

$$\nu_3 = 3.164\,\mathrm{e}^{-6}\,\alpha^6 - 6.258\,\mathrm{e}^{-5}\,\alpha^5 + 4.881\,\mathrm{e}^{-4}\,\alpha^4 - 2.359\,\mathrm{e}^{-3}\,\alpha^3 + 7.161\,\mathrm{e}^{-3}\,\alpha^2 - 2.062\,\mathrm{e}^{-3}\,\alpha + 3.349\,\mathrm{e}^{-4} \quad (2.32)$$

où le demi-angle d'ouverture α est défini en degré.

Une autre validation du modèle a été menée en utilisant les calculs de CSR, CSNI et DNI_S issus de libRadtran avec le jeu de mesures DS3 pris comme référence. Les erreurs sur les ratios de CSR (EQM relative de 16 %, biais relatif de -1 % et coefficient de détermination R^2 de 0.964), de CSNI (EQM relative de 18 %, biais relatif de -5 % et coefficient de détermination R^2 de 0.726) et de DNI_S (EQM relative de 7 %, biais relatif de -5 % et coefficient de détermination R^2 de 0.994) sont globalement faibles. La sous-estimation de 5 % du DNI_S a déjà été constatée et discutée précédemment.

De plus, le modèle d'évaluation du DNI_S a été validé spécifiquement avec le jeu de données DS1 qui présente l'avantage d'avoir des mesures *in-situ* qui correspondent à un intervalle plus important d'angles zénithaux solaires et qui n'ont pas été utilisées pour l'établissement des différents modèles empiriques. L'EQM relative est de 8 %, le biais relatif est de -5 % et le coefficient de détermination R^2 est de 0.976. La similarité de ces résultats avec ceux obtenus pour le jeu de données DS3 démontre la capacité du modèle empirique à estimer les éclairements directs et circumsolaires pour des instants autres que ceux utilisés pour son établissement.

En conclusion pour cette section, une réponse a été apportée à la deuxième question de recherche : un modèle précis et rapide, de type empirique, a été établi et validé pour estimer les rayonnements solaires directs et circumsolaires pour des demi-angles d'ouverture dans l'intervalle [0.4°, 5°] à partir de mesures *in-situ* de DNI et de DHI, qui sont quand même bien plus fréquentes que les mesures des propriétés optiques des aérosols.

2.6. Applicabilité du modèle proposé à un autre site de type désertique

L'objectif de cette section est d'apporter une réponse à la troisième question de recherche qui consiste à savoir si le modèle proposé est applicable à un autre site de type désertique, dans des conditions de ciel clair.

Le site de Tamanrasset dans le désert du sud de l'Algérie a été jugé adéquat pour tester cette applicabilité. La géolocalisation de Tamanrasset est 22.7903°N et 5.5292°E et correspond à une altitude au-dessus du niveau moyen de la mer de 1385 m. Les mesures pyranométriques *in-situ* sont issues de la station de Tamanrasset (TAM) du *Baseline Surface Radiation Network* (BSRN), sur la période allant de septembre 2006 à février 2009 (McArthur, 2005 ; Ohmura *et al.*, 1998). Cette période a été sélectionnée pour son recouvrement avec des données AERONET « *Level 2.0* » sur le site. Les mesures de GHI, DHI et DNI sont disponibles avec une résolution temporelle de 1 min. Le GHI est mesuré avec un pyranomètre de type *Eppley Precision Spectral Pyranometer* (PSP, *cf.* section 2.3.2), le DHI par le même type de pyranomètre avec un système d'ombrage de type boule, et le DNI par un pyrhéliomètre de type *Eppley Normal Incidence Pyrheliometer* (NIP) pour lequel ε_S = 1.8°, α = 2.9° et ε_L = 4°. Seules les mesures pyranométriques ayant passé l'ensemble des tests de qualité présenté par Roesch *et al.* (2011a), ont été gardées. Les mesures issues d'AERONET ont été appariées avec des mesures pyranométriques concomitantes, avec une tolérance de ±2.5 min. Le tableau 2.5 liste les jeux de données utilisées pour la suite de cette section.

Tableau 2.5: Jeux de données disponibles pour l'étude sur le site de Tamanrasset, Algérie.

Jeu de données	**Période**	**Nombre de données**	**Types de mesures**
TAM_DS1	sept. 2006 à fév. 2009	21778	*Eppley* PSP : DHI et GHI. *Eppley* NIP : DNI. AERONET DSA (*Level 2.0*) : les AOD monochromatiques (1020 nm, 870 nm, 675 nm, and 440 nm) et le contenu total de la colonne d'air en vapeur d'eau.
TAM_DS2	sept. 2006 to fév. 2009	1627	*Eppley* PSP : DHI and GHI. *Eppley* NIP : DNI. AERONET *Inversion* (*Level 2.0*) : les AOD monochromatiques (1020 nm, 870 nm, 675 nm, and 440 nm) et le contenu total de la colonne d'air en vapeur d'eau, moyennés sur plus ou moins 16 min autour de chaque instant de mesures AERONET *Inversion* (*Level 2.0*).

Les résultats de l'application directe du modèle de calcul de DNI_S développé pour Abu Dhabi au site de Tamanrasset se révèlent très précis. Pour le jeu de données TAM_DS1, l'EQM relative est de 3 %, le biais relatif est de +1 % et le coefficient de détermination R^2 est de 0.994. Pour TAM_DS2, l'EQM relative est aussi de 3 %, le biais relatif est de +2 % et le coefficient de détermination R^2 est identique. Cependant, les erreurs sont plus importantes pour les estimations de CSR et de CSNI. Pour TAM_DS2, l'EQM relative pour le CSR atteint 37 % avec un biais de -22 % et un coefficient de détermination R^2 de 0.970. Pour le CSNI, l'EQM relative est de 30 %, le biais relatif est de -24 % et le coefficient de détermination R^2 est de 0.854.

Une explication possible pour ces erreurs importantes dans l'estimation du CSR et du CSNI est liée aux problèmes de mesures pyranométriques *in-situ* à Abu Dhabi. Les mesures issues du RSI semblent avoir un problème d'étalonnage qui se retrouve dans le calcul des indices de clarté du ciel établis à partir des mesures de DHI et de DNI du RSI. On peut attribuer une plus grande confiance aux mesures pyranométriques de la station BSRN de Tamanrasset, pour plusieurs raisons. Premièrement, les mesures de DNI sont collectées par un pyrhéliomètre – de type Eppley NIP – qui a des paramètres d'ouverture angulaire bien définis, ce qui n'est pas explicitement le cas pour l'instrument RSI. Deuxièmement, les pyranomètres – de type Eppley PSP – et le pyrhéliomètre sont de type thermopile avec une sensitivité allant de 0.285 μm à 2.8 μm alors que le RSI est composé d'une photodiode, de sensibilité spectrale plus réduite, étalonnée vis-à-vis de la température et des effets spectraux sur un site de référence (*Plataforma Solar de Almeria*, Espagne) et utilisée dans un autre lieu. Troisièmement, les mesures de GHI, DHI et de DNI sont collectées par trois instruments différents sur le site de Tamanrasset, alors que le DNI du RSI est calculé à partir des mesures de GHI et de DHI déduites des observations du même appareil. Le test de qualité proposé par Roesch *et al.* (2011a) reposant sur la cohérence entre les trois composantes mesurées du rayonnement est très efficace pour éliminer des mesures erronées. Il est applicable aux mesures de Tamanrasset mais ne l'est pas à celles du RSI.

Les mesures pyranométriques *in-situ* du site de Tamanrasset étant affectées d'un plus grand niveau de confiance, les coefficients des modèles de CST ont été estimés de nouveau en utilisant les mêmes procédures présentées dans la section 2.5.3, mais avec les mesures *in-situ* de Tamanrasset. L'erreur absolue maximale dans la modélisation du CSR est de 0.021 lorsque *SC* est inférieur à 1.74 – ciel très turbide –, pour le demi-angle d'ouverture α de 5°. Pour l'intervalle de *SC* [1.74, 5.09], le MEA est inférieur à 0.008 et pour *SC* supérieur à 5.09 – ciel très clair –, le maximum de MEA est de 0.004.

Les coefficients des équations (2.21) à (2.23) en fonction du demi-angle d'ouverture α exprimé en degré, sont donnés par les polynômes suivants :

$$o_1 = 1.119\,\mathrm{e}^{-5}\,\alpha^6 - 6.298\,\mathrm{e}^{-4}\,\alpha^5 + 9.319\,\mathrm{e}^{-3}\,\alpha^4 - 5.991\,\mathrm{e}^{-2}\,\alpha^3 + 1.698\,\mathrm{e}^{-1}\,\alpha^2 - 5.173\,\mathrm{e}^{-2}\,\alpha + 8.397\,\mathrm{e}^{-3} \quad (2.33)$$

$$\rho_1 = -5.425\,\mathrm{e}^{-4}\,\alpha^6 + 6.949\,\mathrm{e}^{-3}\,\alpha^5 - 2.603\,\mathrm{e}^{-2}\,\alpha^4 - 2.266\,\mathrm{e}^{-2}\,\alpha^3 + 3.628\,\mathrm{e}^{-1}\,\alpha^2 - 2.032\,\mathrm{e}^{-1}\,\alpha - 6.802 \quad (2.34)$$

$$\nu_1 = 8.654\,\mathrm{e}^{-6}\,\alpha^6 - 1.403\,\mathrm{e}^{-4}\,\alpha^5 + 1.192\,\mathrm{e}^{-3}\,\alpha^4 - 7.028\,\mathrm{e}^{-3}\,\alpha^3 + 2.374\,\mathrm{e}^{-2}\,\alpha^2 - 6.402\,\mathrm{e}^{-3}\,\alpha + 9.588\,\mathrm{e}^{-4} \quad (2.35)$$

$$o_2 = -1.083\,\mathrm{e}^{-5}\,\alpha^6 + 1.675\,\mathrm{e}^{-4}\,\alpha^5 - 4.975\,\mathrm{e}^{-4}\,\alpha^4 - 5.398\,\mathrm{e}^{-3}\,\alpha^3 + 4.196\,\mathrm{e}^{-2}\,\alpha^2 - 8.182\,\mathrm{e}^{-3}\,\alpha + 9.819\,\mathrm{e}^{-4} \quad (2.36)$$

$$\rho_2 = -5.660\,\mathrm{e}^{-5}\,\alpha^6 + 1.071\,\mathrm{e}^{-3}\,\alpha^5 - 8.240\,\mathrm{e}^{-3}\,\alpha^4 + 3.228\,\mathrm{e}^{-2}\,\alpha^3 - 5.875\,\mathrm{e}^{-2}\,\alpha^2 + 1.470\,\mathrm{e}^{-2}\,\alpha - 1.538 \quad (2.37)$$

$$o_3 = -1.910\,\mathrm{e}^{-7}\,\alpha^6 + 3.670\,\mathrm{e}^{-6}\,\alpha^5 - 3.272\,\mathrm{e}^{-5}\,\alpha^4 + 1.819\,\mathrm{e}^{-4}\,\alpha^3 - 6.291\,\mathrm{e}^{-4}\,\alpha^2 + 1.668\,\mathrm{e}^{-4}\,\alpha - 2.516\,\mathrm{e}^{-5} \quad (2.38)$$

$$\nu_3 = 2.043\,\mathrm{e}^{-6}\,\alpha^6 - 4.087\,\mathrm{e}^{-5}\,\alpha^5 + 3.778\,\mathrm{e}^{-4}\,\alpha^4 - 2.131\,\mathrm{e}^{-3}\,\alpha^3 + 7.297\,\mathrm{e}^{-3}\,\alpha^2 - 1.860\,\mathrm{e}^{-3}\,\alpha + 2.705\,\mathrm{e}^{-4} \quad (2.39)$$

La validation avec le jeu de données TAM_DS2 de ce modèle montre que les erreurs sont très faibles : la modélisation du CSR présente une EQM relative de 21 %, un biais relatif de −1 % et un coefficient de détermination R^2 of 0.972. La modélisation du CSNI présente une EQM relative de 19 %, un biais relatif de +2 % et un coefficient de détermination R^2 of 0.846. Enfin, la modélisation du DNI_S présente une EQM relative de 3 %, un biais relatif de +1 % et un coefficient de détermination R^2 de 0.994.

Ce modèle a de plus été validé pour le DNI_S avec des données n'ayant pas été utilisées pour l'établissement du modèle, issues du jeu TAM_DS1. L'EQM relative du DNI_S est de 3 %, le biais relatif est de 0 % et le coefficient de détermination R^2 est de 0.994. Avec un biais absolu de moins de 2 W m^{-2} et 72 % des données de TAM_DS1 correspondant à des erreurs de moins de 20 W m^{-2}, la modélisation du DNI_S est particulièrement précise. Ces résultats sont proches des recommandations de précision des instruments de mesures pyranométriques émises par l'Organisation Météorologique Mondiale (*World Meteorological Organization*, WMO) pour lesquelles le biais doit être inférieur à 3 %, et 95 % des mesures doivent présenter des erreurs absolues de moins de 20 W m^{-2}.

L'application au jeu de données DS1 du site d'Abu Dhabi du modèle établi sur Tamanrasset pour estimer le DNI_S, montre que ce dernier présente une EQM relative de 9 %, un biais relatif de -6 % et un coefficient de détermination R^2 de 0.976. Sur le jeu DS3, la modélisation du CSR présente une EQM relative de 23 %, un biais relatif de +13 % et un coefficient de détermination R^2 de 0.960, celle du CSNI présente une EQM relative de 20 %, un biais relatif de +9 % et un coefficient de détermination R^2 de 0.703. Enfin, le DNI_S modélisé présente sur DS3 une EQM relative de 7 %, un biais relatif de -6 % et un coefficient de détermination R^2 de 0.994.

Le nouveau modèle empirique établi sur Tamanrasset est bien plus précis sur le site d'Abu Dhabi que le premier modèle établi sur Abu Dhabi et appliqué sur Tamanrasset. De plus, le modèle établi sur Tamanrasset est bien plus précis que celui d'Abu Dhabi pour des ciels très clairs, lorsque *SC* est supérieur à 5.09 car le nombre d'occurrences de cette condition est bien plus élevé. C'est donc le modèle empirique établi sur Tamanrasset qui est retenu pour estimer, par conditions de ciel clair et sur d'autres sites de type désertique, le DNI_S ainsi que le CSR et le CSNI pour des demi-angles d'ouverture dans l'intervalle [0.4°, 5°]. L'utilisation de ce modèle empirique nécessite cependant des mesures de DNI et de DHI de très bonne qualité sur le site d'intérêt.

Ces résultats apportent une réponse à la troisième question de recherche : oui, le modèle empirique développé à partir des données d'un site désertique particulier peut être utilisé sur un autre site désertique, avec un certain degré de précision.

2.7. Conclusions et perspectives

Un modèle empirique paramétrique simple et rapide est proposé pour améliorer l'estimation des éclairements totaux directs et circumsolaires par condition de ciel clair, dans un environnement désertique. Avec ce modèle, le CSR peut être estimé pour un demi-angle d'ouverture quelconque entre 0.4° et 5°, à partir des mesures de DNI et de DHI sur le site d'intérêt. Ce modèle a pour avantage de ne nécessiter que des mesures de DNI et DHI en entrée. A l'inverse, les modèles de transfert radiatif nécessitent des données précises et spécifiques – et donc rares – sur les propriétés monochromatiques optiques des aérosols pour le calcul du rayonnement direct (AOD) et circumsolaire (AOD, SSA et PFCN des aérosols). Lorsque ces données sont disponibles, le modèle proposé reste nettement plus rapide que, par exemple, le modèle de transfert radiatif libRadtran. Le modèle proposé détermine le CSR qui est ensuite utilisé avec les mesures *in-situ* de DNI, pour évaluer le CSNI et le DNI_S. Ces estimations de CSR, de CSNI et de DNIS pour un demi-angle d'ouverture donné sont en particulier importantes pour la simulation de systèmes de conversion de l'énergie solaire par concentration.

Dans l'article de Blanc *et al.* (2014), il est recommandé d'évaluer le CSR et le *sunshape* en complément des mesures standard de DNI dont il faut d'ailleurs préciser les demi-angles d'ouverture. Le modèle proposé permet l'estimation du CSR et CSNI, sur des sites désertiques, par condition de ciel clair. Le *sunshape* peut être déterminé en utilisant le modèle paramétrique en fonction du CSR proposé par Buie *et al.* (2013).

Ce modèle a été développé et validé sur le site d'Abu Dhabi, EAU. Ce modèle a ensuite été évalué sur le site de Tamanrasset, Algérie. A l'inverse, afin de profiter des mesures pyranométriques de très bonne qualité des stations BSRN et AERONET sur le site de Tamanrasset, les coefficients du modèle empirique ont été réévalués avec les mesures de Tamanrasset. Ce nouveau modèle a ensuite été évalué et validé de nouveau sur Tamanrasset et Abu Dhabi. Compte tenu de la grande qualité des mesures *in-situ* disponible sur Tamanrasset, il est recommandé d'utiliser ce nouveau modèle pour évaluer sur un autre site désertique, pour des conditions de ciel clair, le DNI_S ainsi que le ratio CSR, le CSNI pour un demi-angle d'ouverture quelconque entre 0.4° et 5°.

Dans le développement du modèle empirique proposé, des propriétés monochromatiques optiques des aérosols (AOD, SSA, PFCN) ont été utilisées pour calculer avec libRadtran les éclairements de référence DNI_S, le CSNI ainsi que le ratio CSR. Cependant, des erreurs dans ces propriétés optiques des aérosols induisent des erreurs dans ces références. La correction affine proposée pour les AOD d'AERONET n'a été établie et validée que sur le site d'Abu Dhabi et uniquement pour la longueur d'onde 670 nm. Or, pour le calcul des éclairements totaux par libRadtran, cette même correction affine

a été appliquée pour toutes les longueurs d'onde. Des études supplémentaires sont nécessaires pour vérifier que cette correction est effectivement applicable pour d'autres longueurs d'onde ou non.

Une autre voie d'amélioration concerne les PFCN des aérosols. En effet, une meilleure estimation de ces PFCN pour de plus petits angles de diffusion que ceux proposés par AERONET améliorerait sensiblement les performances de modélisation de libRadtran qui, à son tour, améliorerait le modèle empirique une fois les coefficients réévalués en conséquence.

Le modèle proposé pourrait être étendu en incluant tous les sites abritant en même temps des stations AERONET et BSRN. Dans ce cas, les coefficients pourraient être réévalués et fournis sous forme d'abaques. Ceci pourrait être intéressant dans la mesure où ce modèle pour être applicable à une échelle plus grande en incluant d'autres environnements que celui désertique.

L'ensemble de ce travail a été établi en ne considérant que des situations de ciel clair, sans nuage. Les effets des nuages de type cirrus dans le ciel sont d'intérêt pour les systèmes solaires à concentration car le DNI mesuré peut être relativement élevé mais aussi le CSNI ainsi que le ratio CSR. Reinhardt *et al.* (2014) ont proposé un modèle, basé sur libRadtran, pour estimer le CSR à partir des propriétés optiques de nuages de type cirrus évalué à partir des images du satellite *Meteosat Second Generation* (MSG). La prise en compte des nuages de type cirrus dans le modèle empirique proposé est donc possible *a priori* et pourrait faire l'objet de recherches futures.

Chapter 3 - Basics

In this chapter the downwelling solar radiation received at ground level is introduced. The chapter is organized as follows:

- the common angles referred to in this work are presented in Sect. 3.1,
- Sect. 3.2 deals with the background on the extraterrestrial solar radiation,
- an introduction to the radiative transfer in the atmosphere is presented in Sect. 3.3,
- followed by the solar radiation components reaching the surface of the Earth in Sect. 3.4,
- finally, parameterizations of the diffuse radiance are presented in Sect. 3.5.

Many symbols and acronyms are used in this thesis. In the framework of the Task 46 "Solar Resource Assessment and Forecasting" of the Solar Heating and Cooling (SHC) program of the International Energy Agency (IEA) a panel of experts have reached a consensus for using similar symbols and acronyms in their works. In addition, an article was published in the Solar Energy journal by these experts reaching an agreement on the definition of the DNI with emphasis on the CSNI issue (Blanc *et al.*, 2014). Therefore, whenever possible the same symbols and acronyms used in the work of Blanc *et al.* (2014) and IEA SHC Task 46 will be used from hereinafter.

3.1. Sun-Earth geometry

A schematic of the common angles with respect to the zenith and the horizontal surface, *i.e.* surface of the Earth in this context, is shown in Fig. 3.1.

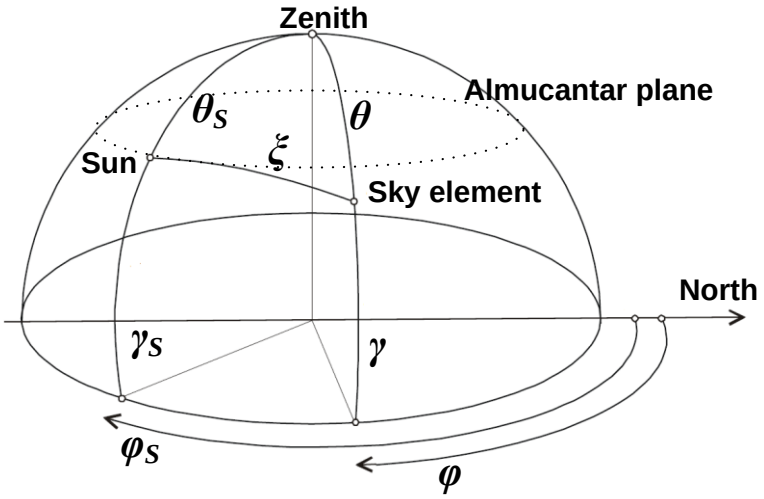


Fig. 3.1: Schematic showing the angular positions of the Sun and any arbitrary sky element (modified after CIE, 2002).

Definitions:

i. The zenith is the point in the sky normal to an observer at ground level, *i.e.* the horizontal plane.

ii. The solar zenith angle θ_S is the angle between the direction of the solar disc and the local vertical. It ranges from 0 when the Sun is at the zenith to $\pi/2$ when the Sun is at the horizon.

iii. The solar elevation angle γ_S is the complementary of the solar zenith angle θ_S, *i.e.* $\gamma_S = \pi/2 - \theta_S$. It ranges from 0 when the Sun is at the horizon to $\pi/2$ when the Sun is at the zenith.

iv. The solar azimuth angle φ_S is the angle between the projection of the direction of the Sun on the horizontal plane and a reference point. The reference point is the north direction following ISO standard. It ranges from 0 to 2π, in a clockwise direction from north: 0 corresponds to north; $\pi/2$ to east; π to south; and $3\pi/2$ to west.

v. The element zenith angle θ is the angle between an arbitrary element in the sky and the zenith. It ranges from 0 for a sky element at the zenith to $\pi/2$ for a sky element at the horizon.

vi. The element elevation angle γ is the complementary of the element zenith angle θ, *i.e.* $\gamma = \pi/2 - \theta$. It ranges from 0 for a sky element at the horizon to $\pi/2$ for a sky element at the zenith.

vii. The element azimuth angle φ is the angle between the projection of the direction of the sky element on the horizontal plane and a reference point. It ranges from 0 to 2π, in a clockwise direction from north: 0 corresponds to north; $\pi/2$ to east; π to south; and $3\pi/2$ to west.

viii. The scattering angle ξ is the angular distance between the center of the solar disc and an arbitrary element in the sky.

ix. The almucantar plane is the plane around the Sun which is parallel to the horizon, where the zenith angle θ of any sky element on the almucantar plane is equal to the solar zenith angle θ_S. The angle between the Sun and any point on the almucantar plane is presented in terms of the scattering angle ξ.

In this work the solar zenith and solar azimuth angles were computed by the SG2 algorithm of Blanc and Wald (2012), which has a reported maximum absolute error of 0.005° for the solar azimuth angle and 0.002° for the solar zenith angle in the period 1980 to 2030. The scattering angle is computed as:

$$\xi = \arccos(\cos(\theta_S)\cos(\theta) + \sin(\theta_S)\sin(\theta)\cos(\varphi - \varphi_S)) \quad (3.1)$$

Other important definitions are:

i. The normal irradiance at the top of the atmosphere $E_{0,n}$, which is the extraterrestrial irradiance incident on a plane normal to the solar rays. It can be computed with a satisfactory level of accuracy as:

$$E_{0,n}(t) = (r_0 / r(t))^2 E_{SC} \quad (3.2)$$

where E_{SC} is the solar constant set to 1367 Wm^{-2}, t is the time, r is the actual Sun-Earth distance in astronomical units (AU) and r_0 is the mean Sun-Earth distance having a value of 1 AU (equivalent to 149597870691 m ± 6 m) (Blanc and Wald, 2012). The extraterrestrial irradiance annually varies by ± 3.3% from the solar constant, being highest at the winter solstice and lowest at the summer solstice for the Northern hemisphere.

ii. The relative optical air mass m is the ratio of the absolute air mass the solar rays travel through to the absolute air mass travelled if the Sun were at the zenith (Kasten and Young, 1989). The smaller the θ_S, the smaller m. When the Sun is at the zenith, *i.e.* $\theta_S = 0$, the pressure corrected relative optical air mass has a value of 1, for an observer at mean sea level. It is computed as:

$$m = \frac{\exp(-Z/8435.2)}{\cos(\theta_S) + 0.50572(96.07995 - \theta_S)^{-1.6364}} \quad (3.3)$$

where θ_S is expressed in deg in this expression, $\exp(-Z/8435.2)$ is the pressure correction term where Z is the altitude of the observer above mean sea level expressed in meters and 8435.2 m is the scale height of the Rayleigh atmosphere near the surface of the Earth (Remund *et al.*, 2003; Rigollier *et al.*, 2000).

3.2. The solar radiation at top of atmosphere

The term "solar radiation" refers to the electromagnetic radiation emitted by the Sun. This electromagnetic radiation lies mostly in the ultraviolet, visible and near to short-wavelength infrared regions of the electromagnetic spectrum. Fig. 3.2 exhibits the spectral distribution of the extraterrestrial radiation as a function of wavelength at the mean Sun-Earth distance (Gueymard, 2004), *i.e.* the monochromatic irradiance outside of the atmosphere of the Earth received on a plane normal to the Sun. The extraterrestrial monochromatic irradiance is the power received per unit area per unit wavelength, normally presented in units of W m^{-2} μm^{-1}. The extraterrestrial irradiance for a defined wavelength interval $E_{0,n}(\lambda_1, \lambda_2)$ is the power per unit area, having SI units of W m^{-2}:

$$E_{0,n}(\lambda_1, \lambda_2) = \int_{\lambda_1}^{\lambda_2} E_{0,n,\lambda} d\lambda \quad (3.4)$$

where $E_{0,n,\lambda}$ is the normal extraterrestrial monochromatic irradiance and λ is the wavelength. Ideally for the broadband radiation the limits of the integration should be for all wavelengths, *i.e.* [0, ∞]. Practically, it is reasonable to assume that all radiation emitted by the Sun is in the interval [0.3 μm, 4.0 μm] and zero for all other wavelengths, because 98% of the radiation emitted by the Sun

is contained in this wavelength interval (Wald, 2007). For a given instant, $E_{0,n}(t)$ is the normal broadband irradiance, also known as the normal total irradiance:

$$E_{0,n}(t) = \int_{0.3\mu m}^{4.0\mu m} E_{0,n,\lambda}(t) d\lambda \tag{3.5}$$

The solar constant E_{SC} is the average of $E_{0,n}(t)$ over one year and corresponds to $E_{0,n}(t)$ for a distance of 1 AU.

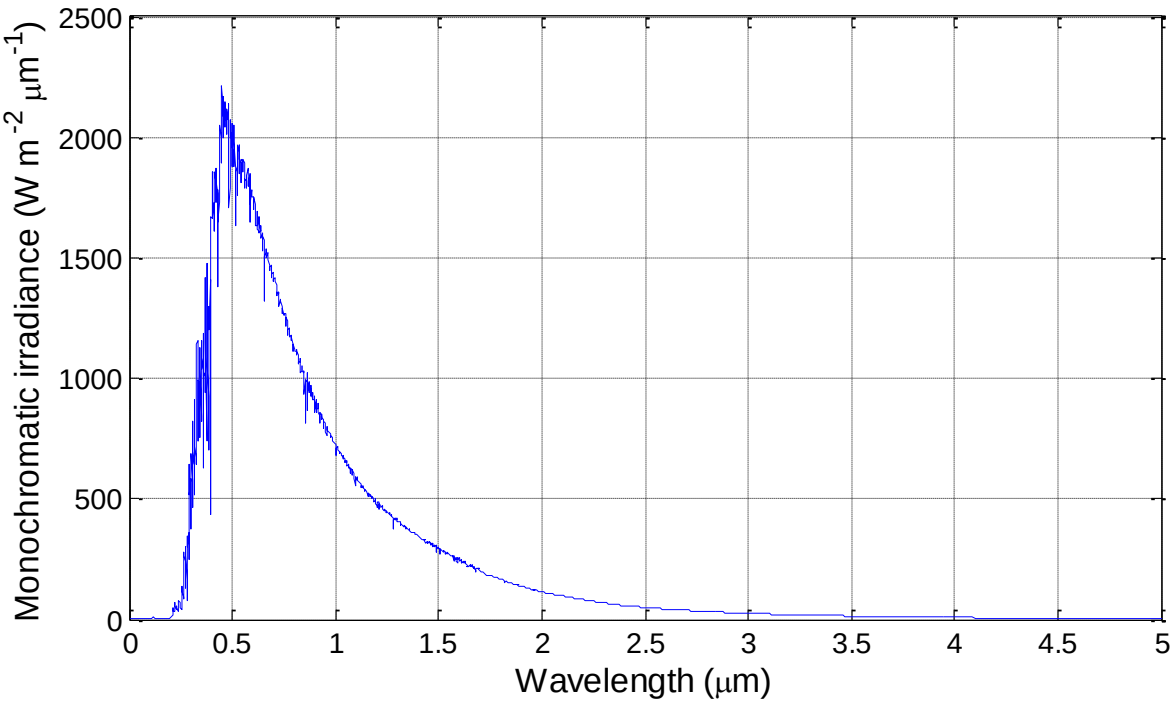


Fig. 3.2: .The spectral distribution of the extraterrestrial irradiance received on a plane normal to the Sun at the mean Sun-Earth distance in the interval [0 μm, 5.0 μm], adapted from Gueymard (2004).

3.3. Radiative transfer in the atmosphere

3.3.1. Scattering, multiple scattering and absorption

As the solar radiation travels through the atmosphere it is attenuated due to scattering and absorption processes caused by the constituents encountered during its path (Wald, 2007). Therefore, knowledge of the optical properties of the atmosphere is necessary to model the attenuation of the solar radiation received at the surface of the Earth.

Scattering of the solar radiation occurs when a particle in the path of the solar rays abstracts energy from the solar rays and reradiates that energy in all directions. Fig. 3.3 shows a schematic of the typical Rayleigh and Mie scattering patterns. Rayleigh scattering occurs when the incident radiation is scattered by the smaller constituents of the atmosphere, *i.e.* the air molecules. The probability of the wave being

scattered in a forward or backward direction is equal, and the scattering probability to the sides is smaller (*cf.* Fig. 3.3(a)). Rayleigh scattering affects the shorter wavelength more prominently than the longer ones because the scattering is proportional to λ^{-4} (Liou, 2002; Wald, 2007). The Rayleigh scattering explains the blue skies in clean and dry atmospheres, because the shortwave solar radiation (*i.e.* blue region of the spectrum) encounters the most scattering and hence the sky is perceived as blue. A clean and dry atmosphere is referred to as a Rayleigh atmosphere (Wald, 2007).

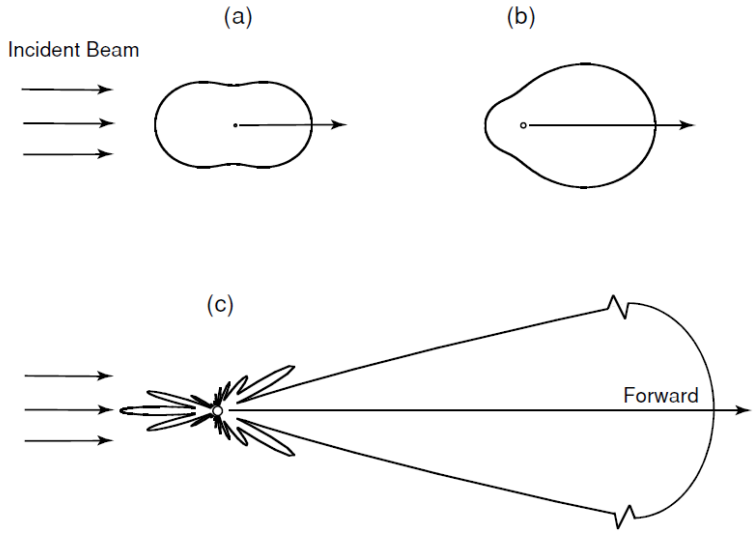


Fig. 3.3: Typical angular patterns of the scattered radiation due to spherical aerosols of sizes: 10^{-4} μm (a); 0.1 μm (b) and 1.0 μm (c) for visible light of wavelength 0.5 μm. Figure copied from Liou (2002).

Mie scattering is the result of the incident radiation being scattered by the larger particles in the atmosphere having sizes between [0.1 μm, 1 μm] (Buie *et al.*, 2003), *e.g.* dust and ice crystals such as cirrus. Unlike Rayleigh scattering, it is less dependent on the wavelength, and it favors a forward scattering direction (*cf.* Fig. 3.3(b, c)).

Multiple scattering occurs when a ray has been scattered from its original direction and is scattered again. It may happen that it is scattered back to that same direction as illustrated in Fig. 3.4.

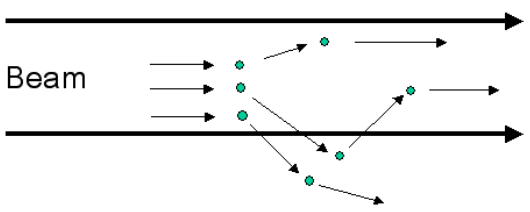


Fig. 3.4: The multiple scattering phenomenon. Figure copied from Wald (2007).

The absorption of solar radiation may occur at specific wavelengths (Liou, 2002; Wald, 2007). It is mainly caused by ozone, water vapor and carbon dioxide. Fig. 3.5 illustrates the wavelengths in which significant Rayleigh scattering and gaseous absorption occur.

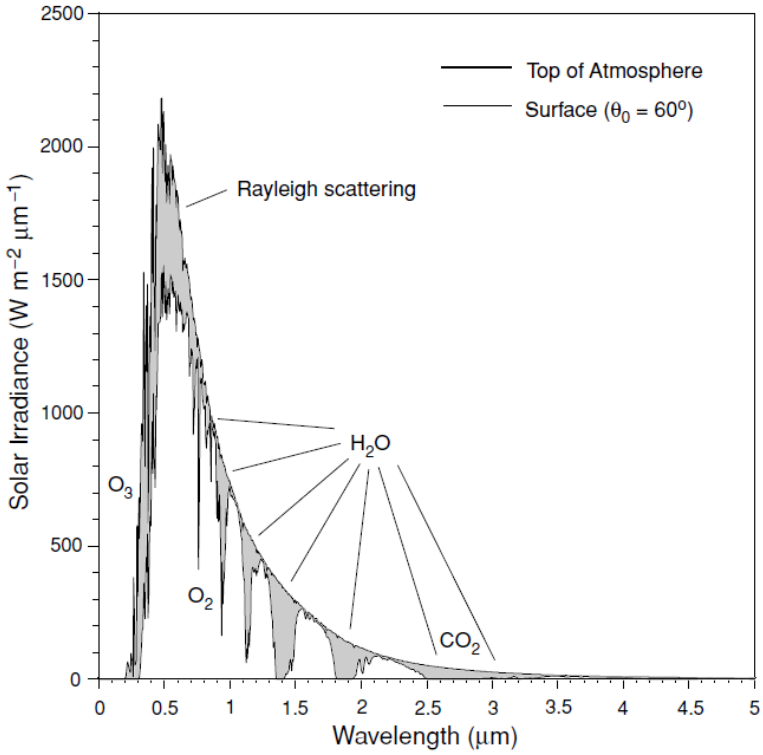


Fig. 3.5: Spectral distribution of the irradiance showing the spectral bands which encounter the most Rayleigh scattering and gaseous absorption, assuming a cloud-free atmosphere with no aerosols and a solar zenith angle of 60°. Figure copied from Liou (2002).

3.3.2. The radiative transfer equation

The radiative transfer equation is a mathematical representation of the attenuation of radiation as it passes through a medium; in this case it would correspond to the absorption and scattering processes encountered by the solar radiation as it travels through the atmosphere. The equations describing the radiative transfer for the remainder of this section are taken from the works of Liou (2002) and Stamnes *et al.* (2000).

First, the concepts of the solid angle and the radiance need to be presented. The solid angle, shown in Fig. 3.6, is the ratio of the area projected on a spherical surface to the square of the radius. It has units of steradian (sr) and is computed as:

$$\Omega = S / r_s^2 \tag{3.6}$$

where Ω is the solid angle, S is the area and r_s is the radius of the sphere. In the case of the solid angle of the Sun as seen by an observer on Earth, r_s would be the Sun-Earth distance and S would be πr_{Sun}^2 (r_{Sun} is the radius of the Sun).

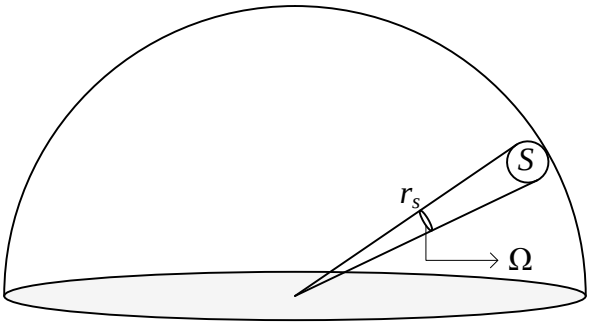


Fig. 3.6: A schematic of the solid angle.

The differential solid angle is defined as:

$$d\Omega = \sin(\theta) d\theta d\varphi \tag{3.7}$$

where θ is the zenith angle measured to the center of the formed cone and φ is the azimuth angle. If the convention is such that the plane is normal to the Sun (*i.e.* the Sun is at the zenith of the new frame), then to be consistent with the angles presented in Fig. 3.1 the Eq. (3.7) becomes:

$$d\Omega = \sin(\xi) d\xi d\varphi_n \tag{3.8}$$

where ξ is the scattering angle and φ_n is the azimuth angle in the plane normal to the direction of the Sun.

The radiance is the flux passing through a cone defined by its solid angle. It is presented in units of W m^{-2} sr^{-1} for broadband radiance and units of W m^{-2} μm^{-1} sr^{-1} for monochromatic radiance. Defining the frame such that the plane is normal to the Sun, then the monochromatic radiance L_λ in the direction defined by the scattering angle and its relative azimuth angle is related to the monochromatic irradiance E_λ as:

$$L_\lambda = \frac{dE_\lambda}{\cos(\xi) d\Omega} \tag{3.9}$$

where the differential solid angle is defined in Eq. (3.8).

Considering the monochromatic irradiance confined within a solid angle traversing through a medium, part of its energy is lost to scattering and absorption processes to become $L_\lambda + dL_\lambda$. dL_λ is presented as:

$$dL_\lambda = -\beta_{ext,\lambda} L_\lambda ds \tag{3.10}$$

where $\beta_{ext,\lambda}$ is the monochromatic extinction coefficient due to scattering and absorption processes measured in m^{-1} and ds is the length the radiance traversed through the medium. The extinction coefficient is defined as:

$$\beta_{ext,\lambda} = \beta_{scat,\lambda} + \beta_{abs,\lambda} \tag{3.11}$$

where $\beta_{scat,\lambda}$ is the monochromatic extinction coefficient due to scattering processes and $\beta_{abs,\lambda}$ is the monochromatic extinction coefficient due to absorption processes.

The monochromatic radiance can increase due to forward and multiple scattering effects, defined by the source term *J*. Then the general form of the radiative transfer equation is presented as:

$$\frac{dL_\lambda}{\beta_{ext,\lambda} ds} = -L_\lambda + J \tag{3.12}$$

The emission of photons within the medium also contributes to the source term, but this phenomenon is negligible in the useful solar spectrum.

Considering a plane-parallel atmosphere, *i.e.* an atmosphere of parallel homogeneous layers where the radiance and atmospheric variables can only vary along the vertical, Eq. (3.12) becomes:

$$\cos(\theta)\frac{dL_\lambda(z,\theta,\varphi)}{\beta_{ext,\lambda} dz} = -L_\lambda(z,\theta,\varphi) + J(z,\theta,\varphi) \tag{3.13}$$

where *z* is the distance travelled in the atmosphere in a normal direction and $dz = ds\cos(\theta)$. The monochromatic total optical depth is defined as:

$$d\tau_\lambda = \beta_{ext,\lambda} dz \tag{3.14}$$

Rewriting the terms in Eq. (3.13) as a function of the monochromatic total optical depth rather than the altitude above ground level, it follows that:

$$\cos(\theta)\frac{dL_\lambda(\tau_\lambda,\theta,\varphi)}{d\tau_\lambda} = -L_\lambda(\tau_\lambda,\theta,\varphi) + J(\tau_\lambda,\theta,\varphi) \tag{3.15}$$

Solving Eq. (3.15) for the downwelling direct radiance component, and assuming no forward or multiple scattering effects (*i.e.* the source term drops), no dependence on the azimuth angle and that the zenith angle is the solar zenith angle, then Eq. (3.15) simplifies into the Beer-Bouguer-Lambert law as:

$$\frac{dL_\lambda}{L_\lambda} = -d\tau_\lambda / \cos(\theta_S) \tag{3.16}$$

$$\ln\left(\frac{L_\lambda(\tau_\lambda)}{L_\lambda(0)}\right) = -\tau_\lambda / \cos(\theta_S) \tag{3.17}$$

$$L_\lambda = L_{0,\lambda}\exp(-\tau_\lambda / \cos(\theta_S)) \tag{3.18}$$

where L_λ is the monochromatic direct radiance after the direct extraterrestrial radiance $L_{0,\lambda}$ has passed through an atmosphere with a monochromatic total optical depth of τ_λ. In the meteorology and solar energy fields the $1/\cos(\theta_S)$ term is usually referred to as the pressure corrected relative optical air mass, presented earlier in Eq. (3.3). Therefore, similar to the direct radiance, the direct irradiance could be presented as:

$$B_{n,\lambda} = E_{0,n,\lambda} \exp(-\tau_\lambda m) \tag{3.19}$$

$$B_\lambda = \cos\theta_S E_{0,n,\lambda} \exp(-\tau_\lambda m) \tag{3.20}$$

where $B_{n,\lambda}$ is the monochromatic DNI (received on a plane normal to the solar disc) and B_λ is the direct irradiance received on a horizontal plane. Whether these beam irradiance quantities refer to the direct irradiance from the solar disc only or including the irradiance from the circumsolar region to some extent mainly depends on how the monochromatic total optical depth is presented. If the monochromatic total optical depth is derived from measurements within the extent of the solar disc only, then the direct irradiances in Eqs. (3.19) and (3.20) would correspond to the irradiances from the solar disc only.

Solving the radiative transfer equation becomes more complex for the diffuse monochromatic radiance. To simplify, in the circumsolar region the multiple scattering effects can be neglected (Box and Deepak, 1978; Dubovik *et al.*, 2000; Kocifaj and Gueymard, 2011; Thomalla *et al.*, 1983). Then for the small scattering angles within the circumsolar region, the monochromatic diffuse radiance received at the surface of the Earth in the direction defined by the scattering angle is expressed as (Dubovik and King, 2000; Liou, 2002;, Wilbert *et al.*, 2013):

$$L_\lambda(\xi) = E_{0,n,\lambda} m \exp(-\tau_\lambda m) P_\lambda(\xi) \omega_\lambda \tau_\lambda / (4\pi) \tag{3.21}$$

where ω_λ is the monochromatic SSA and P_λ is the monochromatic scattering PFCN. The monochromatic total optical depth τ_λ, SSA and PFCN are investigated further in the Sect. 3.5.

3.4. The solar radiation components reaching the surface of the Earth

Ideally, the DNI is the radiant flux collected by a 1 m^2 surface normal to the direction of the Sun within the extent of the solar disc only, *i.e.* the DNI_S. However, according to the definition by the WMO (WMO, 2010), the DNI is the radiation: "*measured by means of pyrheliometers, the receiving surfaces of which are arranged to be normal to the solar direction. By means of apertures, only the radiation from the sun and a narrow annulus of sky is measured, the latter radiation component is sometimes referred to as circumsolar radiation or aureole radiation. In modern instruments, this extends out to a half-angle of about 2.5° on some models, and to about 5° from the sun's centre (corresponding, respectively, to 5 x 10^{-3} and 5 x 10^{-2} sr)*".

This definition is in agreement with the ISO definition presented in Sect. 1.1. Then again, many CST applications require more information on the DNI because the aperture half-angles of the measurement instruments are different than those of the CST systems. Blanc *et al.* (2014) recommend that in addition to the conventional DNI measurements, the half-angle of the measurement instrument should be reported along with the sunshape and the circumsolar contribution, which could be provided in terms of the CSR at different half-angles.

From the monochromatic radiance, the monochromatic DNI_S can be computed as (Blanc *et al.*, 2014; Buie *et al.*, 2003; Wilbert *et al.*, 2013):

$$B_{n,\lambda}^{Sun} = \int_0^{2\pi} \int_0^{\delta_S} L_\lambda(\xi, \varphi_n) \cos(\xi) \sin(\xi) d\xi d\varphi_n \tag{3.22}$$

where δ_S is the angular radius of the Sun corrected with respect to the Sun-Earth distance. For small ξ of the solar and circumsolar regions the deviation from 1 of the $\cos(\xi)$ term can be considered negligible. Also, under the assumption of radial symmetry of the sky radiance in the vicinity of the Sun under cloud-free conditions, Eq. (3.22) simplifies to:

$$B_{n,\lambda}^{Sun} = 2\pi \int_0^{\delta_S} L_\lambda(\xi) \sin(\xi) d\xi \tag{3.23}$$

The monochromatic DNI incident for a defined aperture half-angle, *i.e.* including the CSNI for the defined aperture half-angle, is computed as:

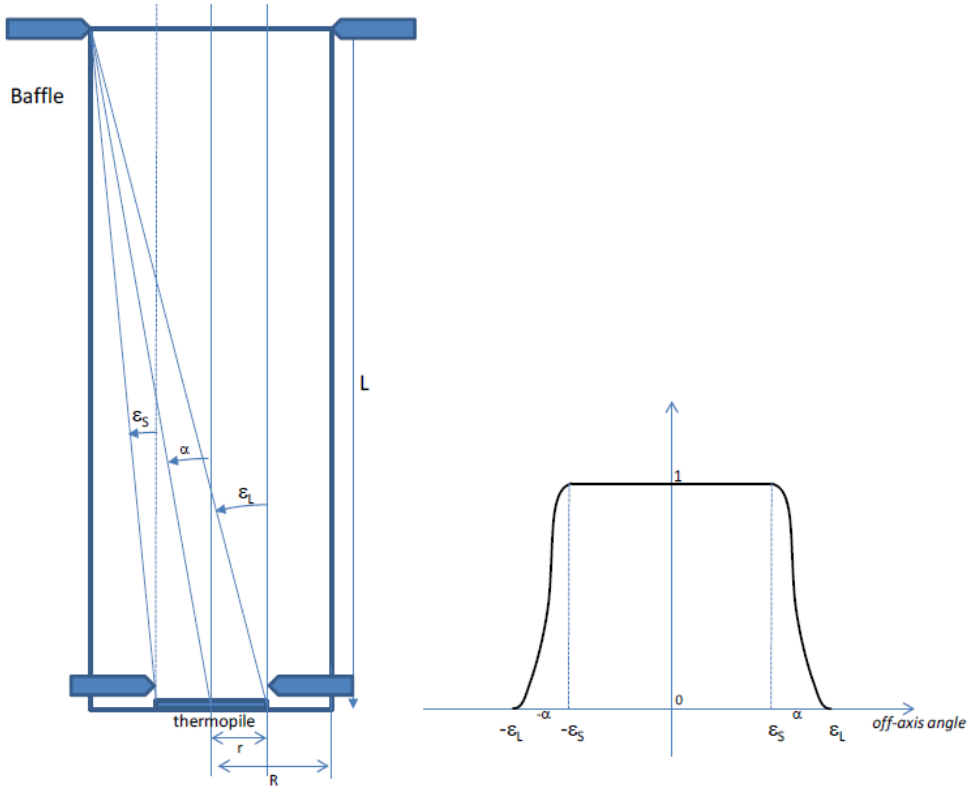
$$B_{n,\lambda}(\alpha) = 2\pi \int_0^{\alpha} L_\lambda(\xi) \sin(\xi) d\xi \tag{3.24}$$

where $B_{n,\lambda}(\alpha)$ is the DNI received for the defined aperture half-angle of α.

For a more precise representation of the DNI measured by a pyrheliometer, the penumbra function should be considered in Eq. (3.24). The penumbra function, also known as the acceptance function, is the sensitivity of the pyrheliometer to the radiation intercepted within its aperture (Blanc *et al.*, 2014; Gueymard, 1995). For pyrheliometers having circular openings it can be, as a first approximation, defined by three angles: the slope angle, the aperture half-angle, and the limit angle. The aperture half-angle is approximately the average of the limit and slope angles. The slope and limit angles are respectively the minimum and maximum viewing half-angles, in which for beam radiation incident at angles less than the slope angle there will be a full response from the sensor and null response for beam radiation incident at angles greater than limit angle. For beam radiation incident between the slope and limit angles a continuous monotonic transition occurs from 1 to 0, which is described by the geometric penumbra function of the instrument. Table 3.1 lists the viewing half-angles of the more common pyrheliometers and Fig. 3.7 presents a schematic of the viewing half-angles and the penumbra function.

Table 3.1: Acceptance half-angles of common pyrheliometers (adapted from Blanc *et al.*, 2014).

Pyrheliometer/CST system	ε_S (°)	α (°)	ε_L (°)
Abbott, silver disk – pyrheliometer	0.8	2.9	4.9
Eko, MS-56 – pyrheliometer	1.0	2.5	4.0
Eppley, AHF (Cavity) – pyrheliometer	0.8	2.5	4.2
Eppley, NIP – pyrheliometer	1.8	2.9	4.0
Eppley, sNIP – pyrheliometer	0.8	2.5	4.2
Hukseflux, DR01, DR02 – pyrheliometer	1.0	2.5	4.0
Kipp and Zonen, CH1, CHP1, SHP1 – pyrheliometer	1.0	2.5	4.0
Kipp and Zonen L-F (Linke-Feussner) – pyrheliometer	1.0	5.1	9.1
Middleton, DN5, DN5-E – pyrheliometer	1.0	2.5	4.0



(a) (b)

Fig. 3.7: Schematic showing the viewing half-angles of pyrheliometers (a), where α is the aperture half-angle, ε_S is the slope angle and ε_L is the limit angle. The penumbra function with respect to the viewing half-angles is also shown (b). Figure copied from Blanc *et al.* (2014).

The penumbra function is presented in the SMARTS description (Gueymard, 1995), following the derivation by Pastiels (1959). The penumbra function is expressed as a function of the scattering angle in the interval between the slope angle and the limit angle:

$$p(\xi) = \frac{a^2(q - \sin(q)) + h - \sin(h)}{2\pi} \tag{3.25}$$

$$h = 2\arccos(y_1 - y_2) \tag{3.26}$$

$$q = 2\arccos((y_1 + y_2)/a) \tag{3.27}$$

$$y_1 = b\tan(\xi)/2 \tag{3.28}$$

$$y_2 = (a^2 - 1)/(2b\tan(\xi)) \tag{3.29}$$

$$a = (\tan(\varepsilon_L) + \tan(\varepsilon_S))/(\tan(\varepsilon_L) - \tan(\varepsilon_S)) \tag{3.30}$$

$$b = 2/(\tan(\varepsilon_L) - \tan(\varepsilon_S)) \tag{3.31}$$

where p is the penumbra function, ε_S is the slope angle and ε_L is the limit angle. It is important to make the distinction between the PFCN which has a symbol of P and the penumbra function which has a symbol of p.

The monochromatic DNI intercepted by a pyrheliometer with all three viewing half-angles is:

$$B_{n,\lambda}(\varepsilon_L) = 2\pi\int_0^{\varepsilon_L} p(\xi)L_\lambda(\xi)\sin(\xi)d\xi \tag{3.32}$$

where $p(\xi)$ is 1 for $\xi < \varepsilon_S$ and 0 for $\xi > \varepsilon_L$.

If the viewing half-angles of the instrument are known, then the monochromatic CSNI:

$$CS_{n,\lambda}(\delta_S, \varepsilon_L) = 2\pi\int_{\delta_S}^{\varepsilon_L} p(\xi)L_\lambda(\xi)\sin(\xi)d\xi \tag{3.33}$$

If only the aperture half-angle is known, then the monochromatic CSNI is:

$$CS_{n,\lambda}(\delta_S, \alpha) = 2\pi\int_{\delta_S}^{\alpha} L_\lambda(\xi)\sin(\xi)d\xi \tag{3.34}$$

Provided that $\varepsilon_S > \delta_S$, the monochromatic CSNI, DNI and DNI_S for defined slope, limit and aperture half-angles are related together:

$$B_{n,\lambda}(\varepsilon_L) = CS_{n,\lambda}(\delta_S, \varepsilon_L) + B_{n,\lambda}^{Sun} \tag{3.35}$$

Similarly, the monochromatic CSNI, DNI and DNI_S for a defined aperture half-angle are related together:

$$B_{n,\lambda}(\alpha) = CS_{n,\lambda}(\delta_S, \alpha) + B_{n,\lambda}^{Sun} \tag{3.36}$$

The monochromatic CSR for a defined aperture half-angle is then:

$$CSR_\lambda(\alpha) = \frac{CS_{n,\lambda}(\delta_S, \alpha)}{CS_{n,\lambda}(\delta_S, \alpha) + B_{n,\lambda}^{Sun}} \tag{3.37}$$

Similarly, the monochromatic CSR for defined slope, limit and aperture half-angles is:

$$CSR_{\lambda}(\varepsilon_L) = \frac{CS_{n,\lambda}(\delta_S, \varepsilon_L)}{CS_{n,\lambda}(\delta_S, \varepsilon_L) + B_{n,\lambda}^{Sun}} \tag{3.38}$$

Similar equations, written without the λ subscript, hold for broadband radiance and irradiance.

The broadband GHI, *G*, is:

$$G = \int_0^{2\pi} \int_0^{\pi/2} L(\theta, \varphi) \cos(\theta) \sin(\theta) d\theta d\varphi \tag{3.39}$$

The broadband DHI, *D*, is:

$$D = \int_0^{2\pi} \int_0^{\pi/2} L(\theta, \varphi) \cos(\theta) \sin(\theta) (1 - (\xi(\theta, \varphi) < \alpha)) d\theta d\varphi \tag{3.40}$$

The relationship between the broadband GHI, DNI and DHI is:

$$G = B_n(\alpha) \cos(\theta_S) + D \tag{3.41}$$

Ideally, the DHI should exclude the diffuse irradiance from the circumsolar region defined by the aperture half-angle in the DNI observations.

Several indices computed from the broadband irradiances and describing the state of the atmosphere are introduced herein (Lefevre *et al.*, 2013). The clearness index *KT*, also called the global transmissivity of the atmosphere, is defined as:

$$KT = G / (E_{0,n} \cos(\theta_S)) \tag{3.42}$$

Similarly the direct normal clearness index KT_{B_n} is defined as:

$$KT_{B_n} = B_n(\alpha) / E_{0,n} \tag{3.43}$$

The diffuse fraction K_D is the fraction of DHI in GHI:

$$K_D = D / G \tag{3.44}$$

The corrected clearness index *KT'* has less dependence on the solar zenith angle than the clearness index of Eq. (3.42) and is defined as (Perez *et al.*, 1990b):

$$KT' = \frac{KT}{1.031 \exp(-1.4/(0.9 + 9.4/m)) + 0.1} \tag{3.45}$$

Another empirical index has been proposed by Perez et al. (1993), named the sky clearness index, and is computed as:

$$SC = \left[(D + B_n)/D + 1.041\theta_S{}^3\right] / \left[1 + 1.041\theta_S{}^3\right] \quad (3.46)$$

where SC is the sky clearness index and θ_S is in radians.

3.5. Parameterization of the diffuse radiance

The angular distribution of the diffuse radiance needs to be known to compute the circumsolar radiation contribution in the DNI presented in Eqs. (3.24) and (3.32), and to compute the CSNI directly in Eqs. (3.33) and (3.34). The SAM instrument measures both the direct and diffuse monochromatic radiances, but not the broadband values (*cf.* Sect. 4.4). The broadband direct and diffuse radiances can also be measured by special telescopes (Noring *et al.*, 1991), but such measurements are very scarce. Those available from the LBL RDB were collected at only 11 sites in the USA during the years 1976 to 1981.

Both the monochromatic and broadband diffuse radiances are modelled by radiative transfer solvers available in libRadtran (Mayer and Kylling, 2005; Mayer *et al.*, 2012). The RTM SMARTS can directly model the CSNI for scattering angles up to 10°, but does not provide the diffuse radiance as an output (Gueymard, 1995, 2001).

When modelling the diffuse radiance in the vicinity of the solar disc it is essential to know the variables affecting it. Rewriting Eq. (3.21), it could be computed with a certain level of accuracy for an observer at ground level as:

$$L_\lambda(\xi) = E_{0,n,\lambda} m \exp(-\tau_\lambda m) P_\lambda(\xi) \omega_\lambda \tau_\lambda / (4\pi) \quad (3.47)$$

$E_{0,n,\lambda}$ and m are well described in the literature (*cf.* Sects. 3.1 and 3.2). The remaining variables are key for accurate estimates of the diffuse radiance in the circumsolar region and they are important inputs to be specified in the RTMs for accurate modelling, namely:

- The monochromatic scattering PFCN $P_\lambda(\xi)$, which is a measure of the angular distribution of the scattered energy,
- The monochromatic SSA ω_λ, which is a measure of the amount of energy attenuation due to scattering effects,
- The monochromatic total optical depth τ_λ, which is a measure of the attenuation due to the interaction of the radiation with the constituents of the atmosphere.

In Eq. (3.47) the monochromatic total vertical optical depth of the atmosphere could be presented as (Dubovik and King, 2000):

$$\tau_\lambda = \tau_{a,\lambda}^{scat} + \tau_{a,\lambda}^{abs} + \tau_{r,\lambda}^{scat} + \tau_{g,\lambda}^{abs} \quad (3.48)$$

where $\tau_{a,\lambda}^{scat}$ is the optical depth due aerosol scattering, $\tau_{a,\lambda}^{abs}$ that due to aerosol absorption, $\tau_{r,\lambda}^{scat}$ that due to the scattering of air molecules (*i.e.* Rayleigh scattering) and $\tau_{g,\lambda}^{abs}$ that due to gaseous absorption (*i.e.* water vapor, ozone, carbon dioxide).

For an observer at ground level, ω_λ in Eq. (3.47) is (Dubovik and King, 2000):

$$\omega_\lambda = (\tau_{a,\lambda}^{scat} + \tau_{r,\lambda}^{scat}) / \tau_\lambda = \tau_\lambda^{scat} / \tau_\lambda \tag{3.49}$$

The monochromatic aerosol SSA $\omega_{a,\lambda}$ is (Dubovik and King, 2000):

$$\omega_{a,\lambda} = \tau_{a,\lambda}^{scat} / (\tau_{a,\lambda}^{scat} + \tau_{a,\lambda}^{abs}) = \tau_{a,\lambda}^{scat} / \tau_{a,\lambda} \tag{3.50}$$

$P_\lambda(\xi)$ is computed as:

$$P_\lambda(\xi) = (\tau_{a,\lambda}^{scat} / \tau_\lambda^{scat}) P_{a,\lambda}(\xi) + (\tau_{r,\lambda}^{scat} / \tau_\lambda^{scat}) P_{r,\lambda}(\xi) \tag{3.51}$$

where $P_{a,\lambda}(\xi)$ is the monochromatic aerosol PFCN and $P_{r,\lambda}(\xi)$ the monochromatic Rayleigh PFCN.

The inversion products from AERONET (*cf.* Sect. 4.3) include values of $\omega_{a,\lambda}$ and $P_{a,\lambda}(\xi)$, namely at the wavelengths: 1020 nm, 870 nm, 675 nm, and 440 nm. These channels were carefully selected to avoid gaseous absorption (Dubovik and King, 2000; Holben *et al.*, 1998). The optical depth due to Rayleigh scattering and the Rayleigh PFCN are well explained in the literature (Bodhaine *et al.*, 1999). Therefore, the unknown variables significantly affecting the monochromatic diffuse radiance are $\tau_{a,\lambda}$, $\omega_{a,\lambda}$ and $P_{a,\lambda}(\xi)$. A sensitivity analysis of these variables on L_λ is presented in Sect. 5.1.

The monochromatic AOD $\tau_{a,\lambda}$ can be retrieved from several sources, *i.e.* ground observations from, for example, the AERONET stations or by chemical transport models (*e.g.* Inness *et al.*, 2013). From the AERONET products, less samples of $\omega_{a,\lambda}$ and $P_{a,\lambda}(\xi)$ are available as opposed to $\tau_{a,\lambda}$, because the inversion algorithm requires scattering angles greater than 100° to retrieve them with sufficient accuracy (Dubovik *et al.*, 2002). Sect. 4.6 presents an overview of the available ground observations over the selected test area.

The monochromatic SSA $\omega_{a,\lambda}$ is a single value for each observation at a given location and time. However, that is not the case for $P_{a,\lambda}(\xi)$ because it is a function of the scattering angle ξ. The simple and more common approximation of this function of ξ is the Henyey-Greenstein (HG) PFCN, which is based on only one parameter as opposed to the aerosol PFCN being presented at many scattering angles (Henyey and Greenstein, 1941; Liou, 2002). The HG PFCN (P_{HG}) is computed as:

$$P_{HG}(\xi, g) = (1 - g^2) / (1 + g^2 - 2g\cos(\xi))^{1.5} \tag{3.52}$$

where g is the asymmetry parameter or asymmetry factor. To compute the monochromatic HG PFCN, g is replaced by g_λ. The HG PFCN could be expanded as a series of Legendre polynomials as (Liou, 2002; Mayer *et al.*, 2012):

$$P_{HG}(\xi, g) = \sum_{l=0}^{\infty}(2l+1)g^{l}\, p_{l}(\cos(\xi)) \tag{3.53}$$

where g^l is the l'th moment and p_l is the l'th Legendre polynomial as a function of cos(ξ). The advantage of the HG PFCN is that it is described by one parameter, the disadvantage is that it is not accurate for scattering patterns which are strongly peaked in the forward direction (Liou, 2002). When considering the distribution of the radiance in the circumsolar region a PFCN which accurately represents the strong peaks in the forward direction must be considered.

Libraries of the optical properties of aerosols are usually available in RTMs, *e.g.* the OPAC (Optical Properties of Aerosols and Clouds) library of Hess *et al.* (1998) in libRadtran or the Shettle and Fenn (1979) aerosol optical properties in SMARTS. The accuracies of the HG PFCN and the libraries of aerosol optical properties available in the RTMs when modelling the diffuse radiance of the circumsolar region are investigated in Chapter 6.

Chapter 4 - Study area and ground measurements

In this chapter the ground measurements from different sources which are used in the context of this work are presented:

- Sect. 4.1 describes the main study area,
- the solar irradiance ground measurements are presented in Sect. 4.2,
- Sect. 4.3 presents the measurements of the aerosol optical properties available from the AERONET station,
- in Sect. 4.4 the available ground measurements of monochromatic beam and circumsolar radiances are presented,
- in Sect. 4.5 comparisons between the AERONET and SAM observations are performed,
- finally, in Sect. 4.6 the different data sets are presented and are given unique acronyms.

4.1. Study area

The environment of interest in this thesis is a desert environment under cloud-free conditions. The UAE is a country which exhibits such characteristics, where the surrounding environment is mostly desert and there are modest cloud occurrences in the sky. Indeed, the measurements made by the AERONET station in Abu Dhabi, UAE reveals 75% cloud-free and quality assured cases in the direction of the Sun, by comparing Level 1.0 with Level 2.0 AERONET products (*cf.* Sect. 4.3). The direction of the Sun and its vicinity are the main interest in this thesis because the main focus is on the beam and circumsolar radiation. Partly cloudy skies, where the clouds do not obstruct either the solar disc or circumsolar regions, do not affect the beam and circumsolar radiation. Also, the skies of the UAE exhibit frequent cloud-free but turbid skies, due to natural and anthropogenic dust emissions (Gherboudj and Ghedira, 2014), making it an interesting location in the context of circumsolar radiation.

Masdar City is located in the suburbs of Abu Dhabi, shown in Figs. 4.1 and 4.2. The environment of Masdar City could be described as near-coastal, desert and urban. The altitude of Masdar City above mean sea level is only 7 m, and it is located at 24.420°N and 54.613°E. Solar irradiance, AERONET, and solar and circumsolar radiance ground observations are available at Masdar City making it a site of particular interest in the context of this work. A description of the available ground measurements will follow in the subsequent sections.



Fig. 4.1: The surrounding environment of Masdar City, Abu Dhabi, UAE (image from Google Earth).

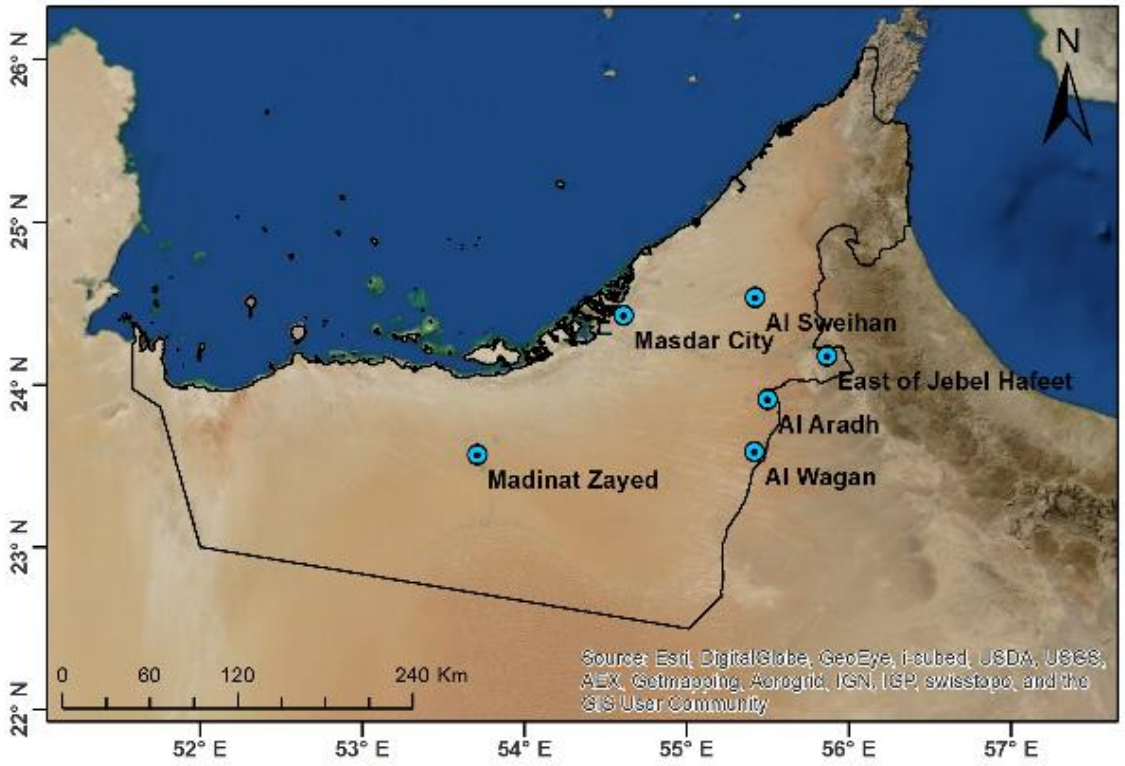


Fig. 4.2: A map of the whole UAE showing Masdar City.

4.2. Solar irradiance ground measurements

The operation and maintenance costs of the instruments located at Masdar City were covered by Masdar Clean Energy, who owns them. The company CSP Services installed the stations, performed their calibrations and provided the measurements at a 10 min temporal step (Geuder *et al.*, 2014).

The broadband irradiances were measured using a RSI, shown in Fig. 4.3. The RSI is a silicon photodiode, the LI-COR LI-200 Pyranometer, integrated with a rotating shadowband. This pyranometer has a spectral range from 400 nm to 1100 nm, and was calibrated against an Eppley Precision Spectral Pyranometer under natural daylight conditions (http://www.licor.com/env/products/light/pyranometers). CSP services then performed another calibration to the RSI measured irradiances with respect to a high precision meteorological station at Plataforma Solar de Almeria, Spain, and it has checked that such a calibration is suitable for other sites in the MENA region (Geuder *et al.*, 2014).



Fig. 4.3: The rotating shadowband irradiometer. In this picture the shadowband is still and below the horizon of the photodiode. © Yehia Eissa, 2012.

During acquisition, the GHI is measured when the shadowband is stationary below the horizon of the photodiode and the DHI is measured when the rotating shadowband blocks the entire solar disc from the photodiode. The shadowband rotates once per minute. The DNI received on a plane normal to the Sun rays is then computed from the DHI, GHI and the solar zenith angle (*cf.* Eq. (3.41)). The irradiances were provided at a 10 min temporal step (Geuder *et al.* 2008, 2014). It is assumed the solar irradiance measurements underwent a quality check procedure by CSP Services before dissemination, because all observations pass the quality checks of Roesch *et al.* (2011a, b).

The time period of interest is between June 2012 and May 2013, which there was an overlap of the SAM, AERONET and RSI measurements. The RSI measurements during this time period have no gaps, and the ambient temperature (T_{amb}) and relative humidity (RH) collected in parallel by a Campbell Scientific CS215 probe are also reported.

One disadvantage of the RSI computed DNI is that the RSI does not have clearly defined values of the viewing half-angles, as is the case with pyrheliometers. Wilbert *et al.* (2012b) reported viewing half-angles of the RSI close to those of the common pyrheliometers (*cf.* Table 3.1), with a slope angle of 1.1°, an aperture half-angle of 2.86° and a limit angle of 4.6°.

In the works of Vignola (1999, 2006) several errors of the RSI instrument measurements were examined, namely the systematic errors due to spectral changes within the photodiode spectral response from changes in the air mass, the temperature and the changes in sky color from blue under clear-sky conditions to white under cloudy conditions. It was uncertain *a priori* whether the calibrations performed by CSP Services on the RSI measurements are in fact realistic of the climate conditions of the UAE or not. Fortunately, there are some other stations in the UAE which have coinciding RSI and pyrheliometer measurements for DNI intercomparisons. The pyrheliometer measurements are considered as the reference values because the pyrheliometer thermopile has a spectral range which better matches that of the broadband solar radiation.

At Al Aradh station (Fig. 4.2), in addition to the RSI measurements the DNI measurements were collected in parallel by the Kipp and Zonen CHP1 pyrheliometer (http://www.kippzonen.com), a thermopile covering the spectral range from 200 nm to 4000 nm. At a 10 min temporal step, the intercomparison between Al Aradh RSI DNI and CHP1 DNI measurements available from the year 2010 for DNI values greater than 200 W m^{-2} exhibit a root mean square error (RMSE) of 3% of the mean value of the CHP1 DNI and a relative bias of 0%. The errors between the two instruments are very low, and it is therefore assumed that they have similar viewing half-angles and that the RSI calibration is suitable over this site.

However, over the Madinat Zayed station (Fig. 4.2), RSI DNI and CHP1 DNI measurements collected in parallel do not exhibit the same range of deviation. For coinciding samples in the year 2012 a relative RMSE of 3% and a relative bias of −2% were observed, where the RSI was underestimating with respect to the CHP1 (Eissa *et al.*, 2015). The errors of the RSI DNI when compared to the CHP1 DNI over both Al Aradh and Madinat Zayed are still within the reported accuracy of the RSI instrument, which according to the information provided from CSP Services with the measurements is within ± 4.1% for the DNI. The accuracy of the RSI DNI observations needs to be considered when commenting on the modelled broadband DNI values later in Sect. 6.4.

4.3. AERONET measurements

Ground measurements from the AERONET program are available over the UAE from 16 stations (Holben *et al.*, 1998). The majority of the measurements were collected during the UAE Unified Aerosol Experiment which started in the year 2004, providing a remarkably increased availability of AERONET data in the Middle East (Reid *et al.*, 2005). For coinciding solar irradiance measurements, the AERONET station at Masdar City which was installed after the UAE Unified Aerosol Experiment is of interest as it was installed in June 2012 and the measurements are still ongoing.

At the AERONET station the CIMEL CE-318 Sun photometer, shown in Fig. 4.4, collects measurements at ground level which are then converted into aerosol optical properties and are available for public access (http://aeronet.gsfc.nasa.gov). The AERONET Version 2 Direct Sun Algorithm (DSA) products include the aerosol optical depth at eight wavelengths, the solar zenith angle and the total column content in water vapor. The products could be downloaded in any of three levels. The Level 1.0 DSA product is neither cloud-screened nor quality assured. The Level 1.5 DSA product is cloud-screened but not quality assured. The Level 2.0 DSA product is both cloud-screened and quality assured. The cloud-screening algorithm used on the AERONET data set only filters out the cloud contaminated observations in the direction of the Sun (Smirnov *et al.*, 2000).



Fig. 4.4: The Cimel 318 Sun photometer used in the AERONET stations (image from: http://www.cimel.fr/?instrument=photometre-multi-bandes-soleilciel).

The CIMEL CE-318 Sun photometer has an aperture half-angle of 0.6° (Holben *et al.*, 1998), and over Masdar City the monochromatic AOD is provided at: 1640 nm, 1020 nm, 870 nm, 675 nm, 500 nm, 440 nm, 380 nm, and 340 nm. In this work only the Level 2.0 DSA product is used to ensure cloud-free

and quality assured observations. Currently, the Level 2.0 DSA product from the Masdar City station is only available in the time period from June 2012 to May 2013, and they make up 10285 observations.

Also, available from AERONET are the Version 2 Inversion products. They include the monochromatic radiance measurements as a function of the scattering angle in the almucantar plane, measured at the wavelengths greater than 440 nm. The measurements in the almucantar plane are carried out at an air mass of 4, 3, 2 and 1.7 in the morning and the afternoon and hourly between 9:00 and 15:00 true solar time (Holben *et al.*, 1998). In the near vicinity of the solar disc the almucantar measurements are provided over Masdar City at scattering angles ξ of: ±3°; ±3.5°; ±4°; ±5°; ±6°. The measurements exceed scattering angles of 6°, but for the sake of the discussion on circumsolar radiation the cutoff is made at 6°. In Masdar City for the time period from June 2012 to May 2013 there are 2241 profiles of the diffuse radiance notably at 675 nm in the almucantar plane, all in Level 2.0. The wavelength of 675 nm is of specific interest in this study because it coincides with the radiance measurements of the SAM instrument that is presented in Sect. 4.4.

At four different wavelengths (1020 nm, 870 nm, 675 nm, and 440 nm), the AERONET Version 2 Inversion products also include $\tau_{a,\lambda}$, $\omega_{a,\lambda}$, $P_{a,\lambda}(\xi)$ and g_λ (Dubovik and King, 2000; Holben *et al.*, 1998). The Inversion products do not have the same time stamps as the DSA products, as the Inversion products were derived from the almucantar radiance measurements. The monochromatic AOD available with the Inversion products is in fact extracted from the DSA monochromatic AOD by averaging the Level 1.5 or 2.0 AOD data values (priority is for the Level 2.0) in the interval ± 16 min of the retrieval time (http://aeronet.gsfc.nasa.gov/new_web/Documents/Almucantar_Retrieval_Info.pdf). From the Inversion products for the time period June 2012 to May 2013 there are 1068 observations of $P_{a,\lambda}(\xi)$ and g_λ, and their corresponding $\tau_{a,\lambda}$, of which only 491 observations include $\omega_{a,\lambda}$.

4.4. Beam and circumsolar radiance ground measurements

The beam and circumsolar radiance ground measurements over this study area were collected using the SAM instrument installed in Masdar City (DeVore *et al.*, 2012a). The SAM instrument measures the monochromatic beam and circumsolar radiance for scattering angles up to ± 8° vertically and horizontally. The monochromatic radiance is measured at 670 nm with a full spectral width at half-maximum of 10 nm. The system comprises two cameras. One directly measures the radiance within the solar disc. The solar aureole image is formed on a screen with a beam dump for the solar disc region and this image is captured by the other camera facing the screen (*cf.* Fig. 4.5). The angular resolution of the radiance measurements at Masdar City is 0.0217°. A gap exists between the two cameras to avoid superimposition of the solar disc radiance scattered on the screen with the image of the circumsolar region on that screen (Wilbert *et al.*, 2013). DeVore *et al.* (2012b) suggest that radiance measurements

less than 0.64° measured by the solar aureole camera are noisy and should be excluded. The SAM measurements are collected at a frequency of 4 or 5 times per minute.

The relative error of the beam radiance is reported to be lower than 1% for aerosol optical depths less than 0.6, while that of the aureole radiance is reported to be between 5% and 15% (Stair and DeVore, 2012).

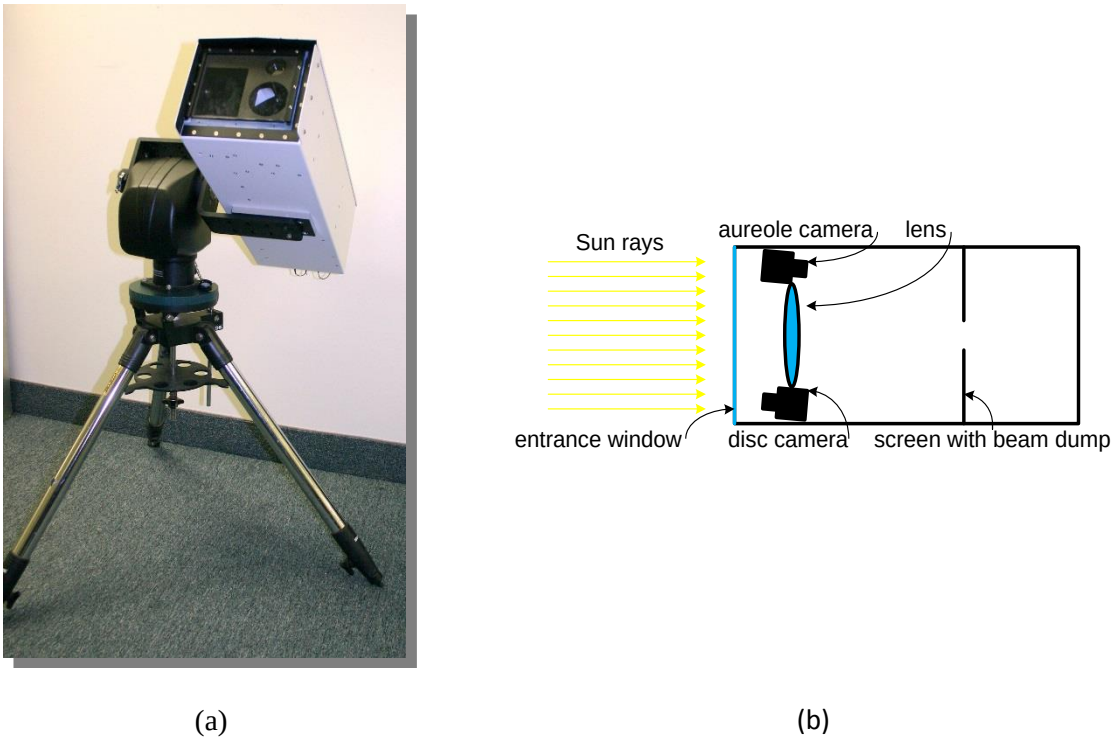


Fig. 4.5: A picture of the SAM instrument (Stair and DeVore, 2012) (a) and a schematic of the SAM instrument modified after Wilbert *et al.* (2012a) (b).

The data downloaded over Masdar City from the website (http://www.visidyne.com) covers the period from January 2012 until September 2013. There are four main files for each day (LePage *et al.*, 2008). One file contains the radial profiles (*i.e.* azimuthally averaged) of the solar radiance throughout the whole day. A second file contains the horizontal beam and circumsolar radiance measurements throughout the whole day, scanning the Sun in the east and west directions with respect to the center of the Sun. A third file contains the vertical beam and circumsolar radiance measurements throughout the whole day, scanning the Sun in the north and south directions with respect to the center of the Sun. The reported angular resolution for the horizontal and vertical measurements is also 0.0217°. The last file includes the derived monochromatic AOD at 670 nm and the solar zenith angle.

The SAM instrument is a fairly new instrument. The oldest reference found was that of DeVore *et al.* (2007) who reported examples of the SAM measurements collected in 2006. However, no article has been found which clearly defines a quality control procedure for the SAM measurements. There are

also several gaps in the downloaded data. Therefore, a set of quality check procedures are defined herein to retain only the high quality measurements. The proposed quality checks are:

i. The radial, horizontal and vertical solar radiance profiles SAM measurements are matched to the derived monochromatic AOD observations which have the same time stamps. The remaining observations are 229561 from originally 244609 solar radiance profiles.

ii. Any azimuthally averaged solar radiance profile with negative values in the solar disc region is removed. The remaining observations are 222742.

iii. The monochromatic radiance of the azimuthally averaged solar radiance profile should decrease with an increasing angular displacement in the solar disc region, *i.e.* the condition $dL_\lambda(\xi)/d\xi < 0$ must be fulfilled. This procedure is similar to that by Buie *et al.* (2003) when performing the quality checks on the LBL RDB sunshapes. The remaining observations were 222714.

iv. According to Buie *et al.* (2003) and Neumann *et al.* (2002) the variations in sunshape is low for CSRs ranging between 0.05 and 0.4. When comparing the CSR 0 and CSR 40 sunshapes proposed by Neumann *et al.* (2002) a relative RMSE of 4% is observed taking the CSR 0 sunshape as the reference. The RMSE was constructed from the relative intensity of each sunshape at the different scattering angles. To this end, each of the SAM radiance measurements in the solar disc region were normalized between 0 and 1. In the solar disc region a mean normalized solar radiance profile was generated from all the available measurements, which was then matched to the closest actual normalized profile in terms of Euclidean distance. Then the relative RMSE was computed for each normalized solar radiance profile with respect to the real mean normalized profile. The 90^{th} percentile of the RMSE was chosen as the cutoff; it also coincides with a relative RMSE of 4%. Fig. 4.6 shows the normalized solar radiance profiles which pass this quality check and those which did not. 200443 profiles pass this quality check.

v. As pointed out by Noring *et al.* (1991), the circumsolar radiances and the scattering angle exhibit a linear relation in the log-log space. Therefore, the correlation coefficient in the log-log space was computed between the circumsolar radiances of the azimuthally averaged solar radiance profile and the scattering angles in the interval [0.64°, 6°]. Any radial profile exhibiting a correlation coefficient less than 0.990 was eliminated. The number of remaining observations was 191812.

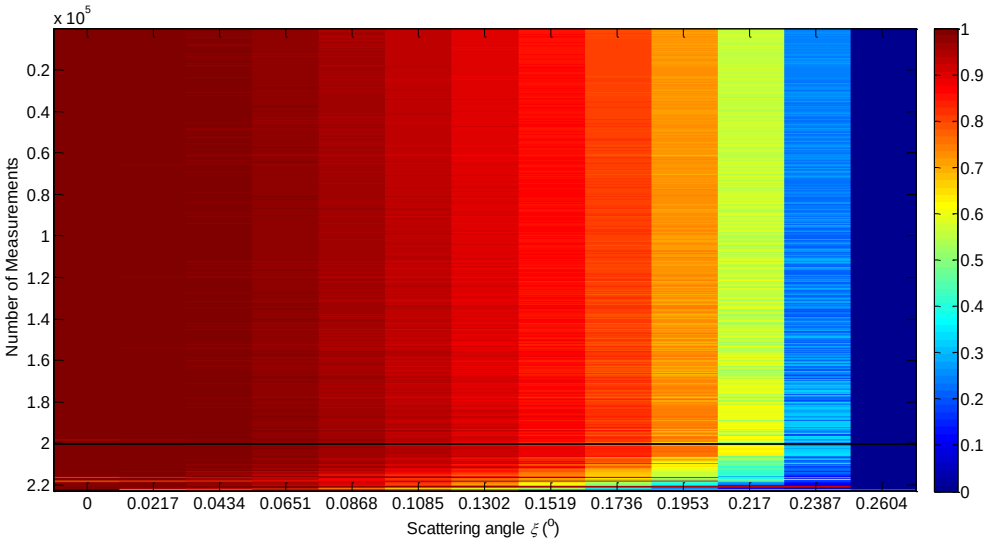


Fig. 4.6: The 222714 solar radiance profiles normalized between [0, 1] in the Sun disc region. They are sorted out in terms of the RMSE with respect to the real mean normalized solar radiance profile. The black line represents the cutoff, profiles below it are eliminated.

4.5. Comparisons between SAM and AERONET observations

Comparing between the same measurements from different instruments is a way to crosscheck the measurements. Both SAM measurements and AERONET Inversion products include the monochromatic radiance measurements in the near vicinity of the solar disc and the derived monochromatic AOD. Comparing them is a way to remove outliers from measurements from either instruments. In the discussion on the modelling of the monochromatic DNI_S and CSNI by means of RTMs in Chapter 6, the aerosol optical properties are usually from the AERONET observations and the SAM measurements are kept as the reference values. The objective in this case is not to validate the RTM modelled values with those of SAM but to monitor the accuracy of the RTM to model the monochromatic DNI_S and CSNI given a set of inputs. The validations will be carried out later for the broadband DNI_S and CSNI, when the modelled irradiance values will be validated against measurements of the broadband DNI.

The AERONET almucantar radiance measurements were matched to the SAM horizontal monochromatic radiance measurements in terms of time stamp. In the matching process the measurements between the two different instruments had to be at most 1 min apart and the solar zenith angle reported by the two instruments had to match: the bias between the matched solar zenith angles was found to be 0.00° and the maximum absolute error in angle for all observations was 0.22°.

To compare the AERONET and SAM radiance measurements, the SAM values were aggregated to match the 1.2° field of view of the CIMEL 318 Sun photometer. After matching the measurements, 1117 AERONET and SAM profiles remained. Ideally for the 1117 profiles there should be 11170

radiance measurements corresponding to the scattering angles of AERONET in the almucantar plane (±3°; ±3.5°; ±4°; ±5°; ±6°). Instead there is a lower number of observations due to missing measurements in the almucantar radiance measurements from AERONET which could occur at any of the scattering angles. If the deviation between the matched samples was greater than three times the standard deviation of the discrepancies the samples were filtered out (253 samples matched this criteria). This test is meant to filter out extreme cases which could occur if one instrument is shaded by clouds while the other is not.

Fig. 4.7 exhibits the density scatter plot (or 2-D histogram) of the SAM and AERONET radiance measurements. Red dots correspond to regions with high densities of samples and the dark blue ones to those with very low densities of samples. The relative RMSE is 18%, the relative bias is 0% and the coefficient of determination (R^2) is high at 0.894. The observations are well-scattered around the 1:1 line and the slope of the robust affine regression is 0.98. Generally the results are good, implying reliable measurements from both instruments. The AERONET measurements were collected at 675 nm while those of SAM were collected at 670 nm. This may induce minor errors in this comparison. Also shown in Fig. 4.7 are the mean value of the observables on the x-axis, the correlation coefficient (CC), the 1:1 line, the least-squares (LS) affine regression, and the first axis of inertia, also known as the first component in principal component analysis (PCA).

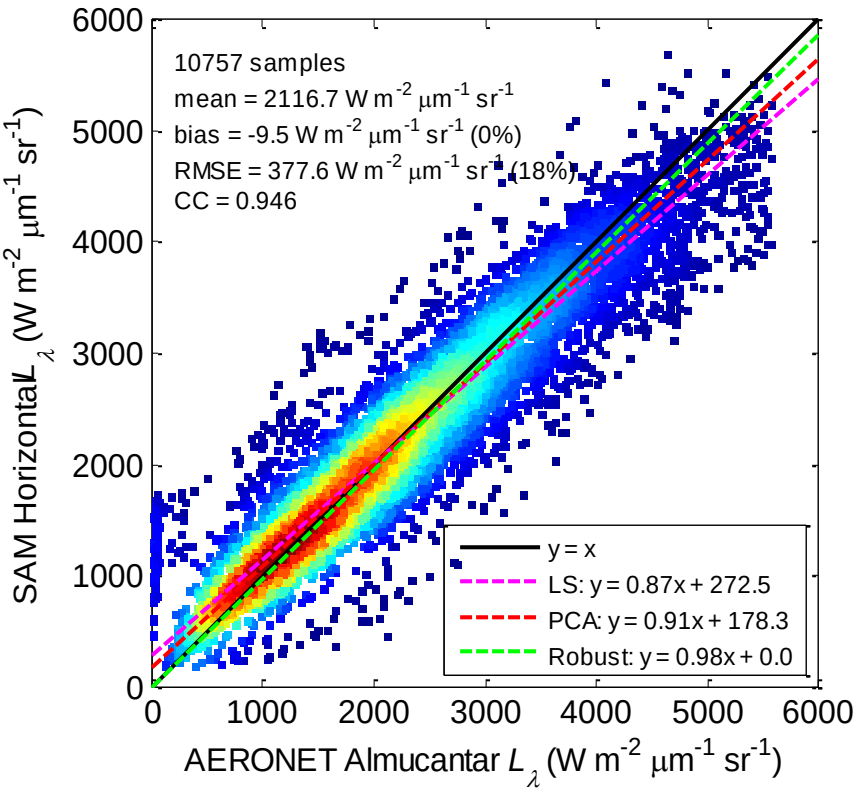


Fig. 4.7: Scatter density plot between the SAM and AERONET monochromatic radiance L_λ measurements.

For the comparison between the SAM and AERONET monochromatic AOD, the difference in spectral filter of each instrument is accounted for by using the Ångström law (Ångström, 1964) as:

$$\tau_{a,\lambda} = b\lambda^{-a} \tag{4.1}$$

$$\ln(\tau_{a,\lambda}) = \ln(b) - a\ln(\lambda) \tag{4.2}$$

where b is the AOD at 1000 nm and a is the Ångström parameter. 5130 pairs of coincident observations remain, where the maximum difference in time stamp of both instruments is 1 min. Fig. 4.8 exhibits the density scatter plot of the SAM versus AERONET AOD at 670 nm. The relative RMSE is 18% and the relative bias is +9% meaning that the SAM monochromatic AOD is greater in average than the AERONET AOD. The R^2 value is high at 0.962. Due to the high range of values it is difficult to observe the region with the highest density of samples. Fig. 4.9 displays the same plot but the limits of the axes have changed to have a maximum value of 0.8 in order to better examine the regions with higher sample densities.

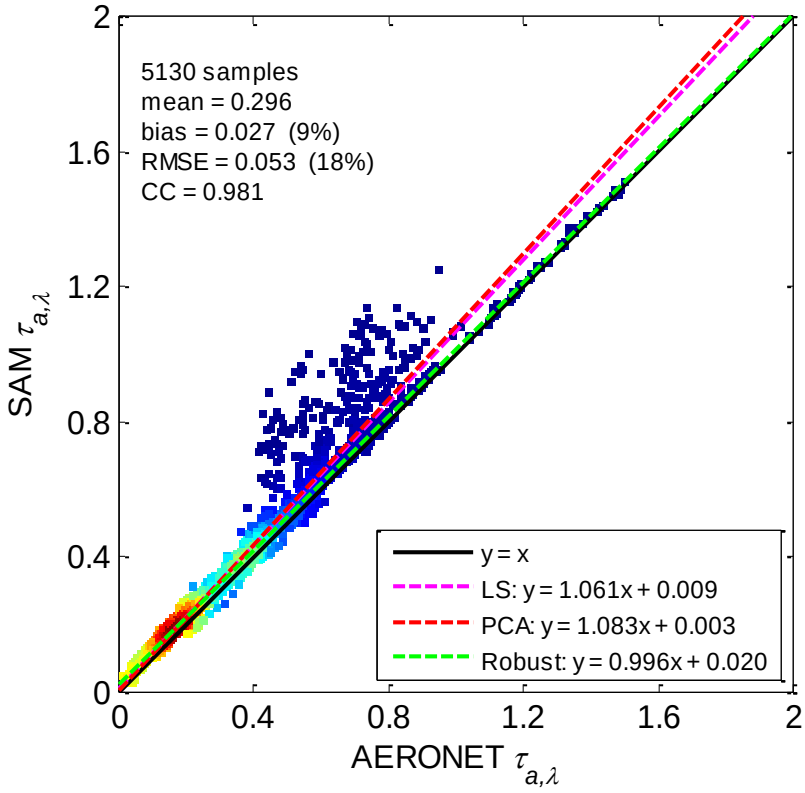


Fig. 4.8: Scatter density plot between the SAM and AERONET monochromatic AOD ($\tau_{a,\lambda}$) at 670 nm.

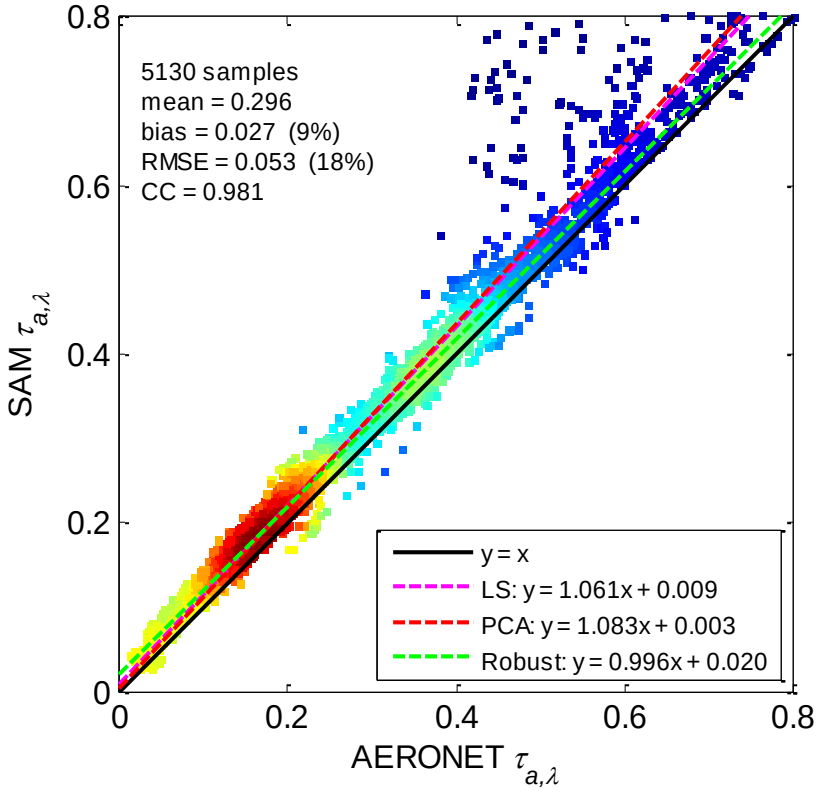


Fig. 4.9: Scatter density plot between the SAM and AERONET monochromatic AOD ($\tau_{a,\lambda}$) at 670 nm, same samples as in Fig. 4.8 but the axes are limited to 0.8 for a better view.

There are some outliers present in Figs. 4.8 and 4.9. To eliminate such outliers the reported accuracy (± 0.03) of the SAM monochromatic AOD retrievals is accounted for (DeVore *et al.*, 2012a), which is greater than the reported accuracy (± 0.01 for $\lambda \geq 440$ nm) for the AERONET AOD retrievals (Holben *et al.*, 1998). Therefore, any coinciding SAM and AERONET retrievals of the monochromatic AOD which do not agree within ± 0.03 of each other were eliminated, keeping 3766 observations. This number is quite large: 73% of the observations agree in both instruments. This means in particular that one may use the SAM $\tau_{a,\lambda}$ confidently. The scatter density plot of such remaining observations is shown in Fig. 4.10 (only values up to 0.8 are shown). Of course, the relative RMSE is less than previously at 6% and the R^2 value is very high 0.998. The relative bias is +5%, indicating a clear overestimation of the SAM $\tau_{a,\lambda}$ compared to that from AERONET.

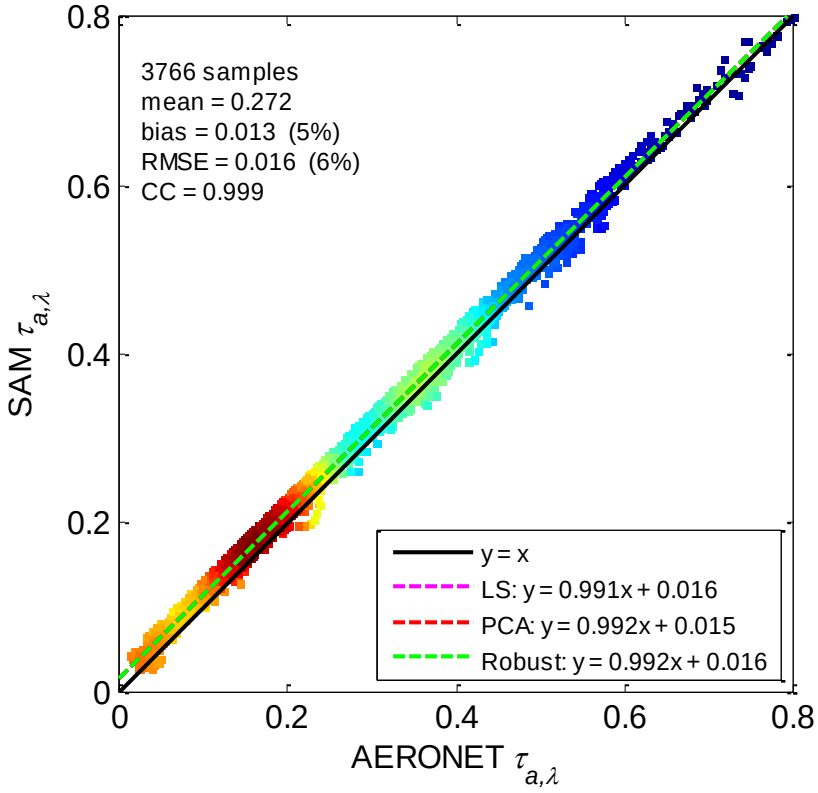


Fig. 4.10: Scatter density plot between the SAM and AERONET monochromatic AOD ($\tau_{a,\lambda}$) at 670 nm after accounting for the accuracy of the SAM retrievals, the axes are limited to 0.8 for a better view.

The main interest of Fig. 4.10 is that it better demonstrates that the overestimation of the SAM monochromatic AOD is due to the field of view of the different instruments. Indeed, the AERONET Sun photometer has an aperture half-angle of 0.6°. This implies that the circumsolar radiation from the edge of the solar disc up to a scattering angle of 0.6° is intercepted within the aperture of the Sun photometer, which would imply an underestimation in the AERONET AOD, because the measured irradiance is greater than that within the extent of the solar disc alone. On the contrary, due to the finer resolution of the SAM instrument the AOD is retrieved within the extent of the solar disc only (DeVore *et al.*, 2012a).

4.6. The data sets available over the study area

In Sects. 4.2, 4.3 and 4.4 three different instruments were presented. To avoid any confusion in the subsequent sections the different data sets are given unique acronyms. Table 4.1 lists the different data sets, their unique acronyms, the available data and the time period of the data.

Table 4.1: The different data sets available over Abu Dhabi, UAE.

Data set	Time period	Samples	Observables
DS1	June 2012 to May 2013	10285	RSI: DNI, DHI and GHI. CS215: T_{amb} and RH. AERONET DSA Level 2.0: monochromatic AOD and total column content in water vapor.
DS2	June 2012 to April 2013	3723	RSI: DNI, DHI and GHI. CS215: T_{amb} and RH. AERONET DSA Level 2.0: monochromatic AOD and total column content in water vapor. SAM: monochromatic AOD, and horizontal, vertical and azimuthally averaged solar radiance profiles.
DS3	June 2012 to May 2013	1068	RSI: DNI, DHI and GHI. CS215: T_{amb} and RH. AERONET Version 2 Inversion products in Level 2.0: monochromatic AOD and total column content in water vapor (from the DSA Level 2.0, averaged ± 16 min of Inversion product retrievals), monochromatic aerosol PFCN, monochromatic asymmetry parameter.
DS4	June 2012 to May 2013	491	Same as DS3 but including: AERONET Version 2 Inversion products in Level 2.0: monochromatic SSA.
DS5	June 2012 to April 2013	425	Same as DS3, but including: SAM: monochromatic AOD, and horizontal, vertical and azimuthally averaged solar radiance profiles.
DS6	June 2012 to April 2013	138	Same as DS4, but including: SAM: monochromatic AOD, and horizontal, vertical and azimuthally averaged solar radiance profiles.

Chapter 5 - Modelling the beam and circumsolar radiation

This chapter deals with the first research question: what are the key aerosol optical properties required under cloud-free conditions in a desert environment for an accurate estimate of the beam and circumsolar radiation? It is organized as:

- firstly, in Sect. 5.1.1 the sensitivity of the diffuse radiance in the very near vicinity of the solar disc based on the aerosol optical properties is conducted to know the variables of significance,
- followed by a discussion on the AOD in Sect. 5.1.2, which is an important variable for modelling both the diffuse radiance and beam irradiance,
- in Sect. 5.1.3 a discussion on the aerosol SSA is presented,
- followed by a discussion on an accurate representation of the aerosol PFCN in Sect. 5.1.4,
- Sect. 5.1.5 discusses the aerosol optical properties with respect to the first research question,
- finally, Sect. 5.2 presents the parameterizations of the libRadtran (Sect. 5.2.1) and SMARTS (Sect. 5.2.2) RTMs to model the beam and circumsolar radiation.

5.1. The aerosol optical properties

5.1.1. Sensitivity of the radiance

A sensitivity analysis was conducted to better understand which variables mostly affect the diffuse radiance in the very near vicinity of the solar disc. This analysis provides an insight on the errors of the modelled radiance with respect to errors in inputs. The Eq. (3.47), recalled as Eq. (5.1) for convenience, as an approximation without the multiple scattering effects reveals that in the very near vicinity of the solar disc the monochromatic diffuse radiance L_λ as a function of the scattering angle ξ is dependent on the monochromatic extraterrestrial irradiance received on a plane normal to the Sun rays $E_{0,n,\lambda}$, the pressure corrected relative optical air mass m, the monochromatic total optical depth τ_λ, the monochromatic scattering PFCN $P_\lambda(\xi)$ and the monochromatic SSA ω_λ.

$$L_\lambda(\xi) = E_{0,n,\lambda} m \exp(-\tau_\lambda m) P_\lambda(\xi) \omega_\lambda \tau_\lambda / (4\pi) \tag{5.1}$$

As discussed in Sect. 3.5, $E_{0,n,\lambda}$ and m are well defined in the literature and can be precisely computed with no significant uncertainty. Therefore, the uncertainty associated with modelling the monochromatic radiance is associated mainly with the uncertainties in τ_λ, $P_\lambda(\xi)$ and ω_λ. In this sensitivity analysis an atmosphere dominated only by aerosols is assumed, since the variability of the aerosol optical properties contributes the most to the radiance (Dubovik and King, 2000). In an atmosphere dominated by aerosols Eq. (5.1) can be written as:

$$L_\lambda(\xi) = f(P_{a,\lambda}(\xi), \omega_{a,\lambda}, \tau_{a,\lambda}) \tag{5.2}$$

The data set DS4 was used (*cf.* Table 4.1) in this sensitivity analysis. It includes 491 observations. At 675 nm the observations of $\tau_{a,\lambda}$, $P_{a,\lambda}(\xi)$ and $\omega_{a,\lambda}$ are exploited. The sensitivity analysis was conducted for each variable separately, *i.e.* by varying only the variable in question and keeping the others constant. The temporal standard deviations of each variable were computed. For all of the 491 observations, the relative absolute error in the monochromatic radiance was computed for each variable in the interval $[-1\sigma, +1\sigma]$, where σ is the standard deviation of the corresponding variable. For the sensitivity of each variable only the variable and the corresponding interval need to be known, everything else cancels out, except for m when considering $\tau_{a,\lambda}$. $P_{a,\lambda}$ is a function of ξ, therefore the sensitivity of the radiance on $P_{a,\lambda}$ was conducted at the three ξ available from AERONET which are less than 6°, *i.e.* 0°, 1.71°, and 3.93°.

Results of the sensitivity of the monochromatic diffuse radiance on the three main variables are presented in Fig. 5.1. Over this study area, it is clear that $\omega_{a,\lambda}$ has the least influence on the errors involved in computing the monochromatic radiance. The maximum relative absolute error in this case is close to 2%, which occurs when the error in $\omega_{a,\lambda} \pm 1\sigma$ of all the 491 reference values. Indeed, the relative standard deviation (*i.e.* the standard deviation normalized by the mean of the observations) of $\omega_{a,\lambda}$ is 2%, whereas $\omega_{a,\lambda}$ is linearly proportional to the monochromatic radiance. On the contrary, $\tau_{a,\lambda}$ has the greatest influence on the computation of the radiance. Relative absolute errors up to 100% could be observed in several cases in the interval $\pm 1\sigma$ of all the 491 reference values. Finally, the errors due to $P_{a,\lambda} \pm 1\sigma$ of all the 491 reference values cause a maximum relative absolute error of 43% in the monochromatic radiance computation for the three considered scattering angles ξ. Table 5.1 lists the mean, standard deviation and relative standard deviation for $\tau_{a,\lambda}$, $P_{a,\lambda}(\xi)$ and $\omega_{a,\lambda}$.

Table 5.1: The mean, standard deviation and relative standard deviation for $\tau_{a,\lambda}$, $P_{a,\lambda}(\xi)$ and $\omega_{a,\lambda}$ for the 491 samples of data set DS4.

Variable	**mean**	**standard deviation**	**relative standard deviation (%)**
$\tau_{a,\lambda}$	0.501	0.209	42
$P_{a,\lambda}(0°)$	179.6	31.9	18
$P_{a,\lambda}(1.71°)$	127.6	19.2	15
$P_{a,\lambda}(3.93°)$	62.7	8.9	14
$\omega_{a,\lambda}$	0.954	0.019	2

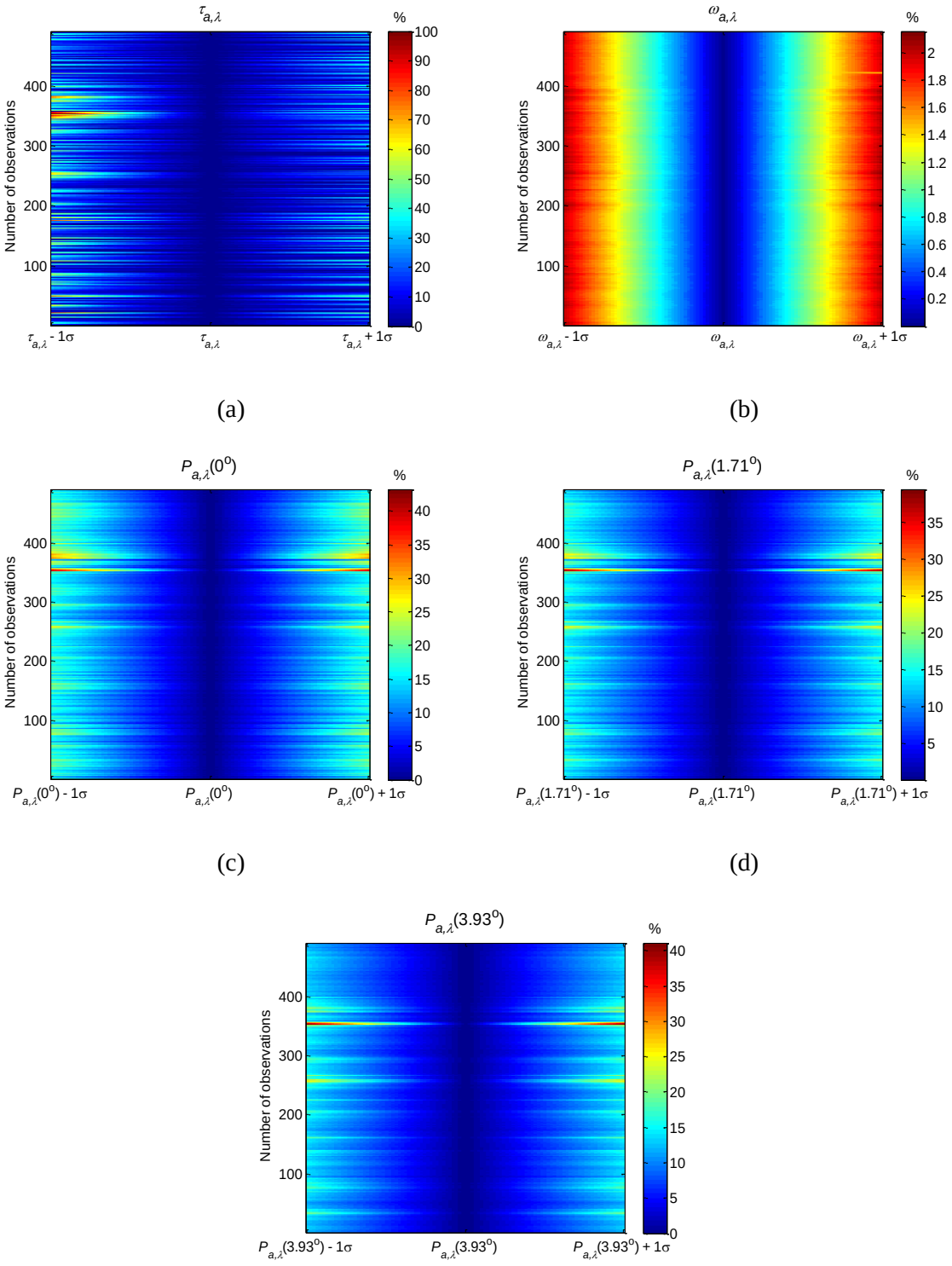


Fig. 5.1: Relative absolute errors induced in the monochromatic radiance by varying $\tau_{a,\lambda}$ (a), $\omega_{a,\lambda}$, (b) and $P_{a,\lambda}(\xi)$ (c, d and e) for three scattering angles ξ. In each plot only the variable in question was varied.

The uncertainties in $\tau_{a,\lambda}$ induce the greatest errors in the radiance. Fortunately, $\tau_{a,\lambda}$ can be retrieved from a number of sources with various uncertainties. It can be obtained from any of the AERONET measurement stations. In general, at the AERONET stations observations of $\tau_{a,\lambda}$ are retrieved much more often than $\omega_{a,\lambda}$ and $P_{a,\lambda}$ (*cf.* Sect. 4.3). $\tau_{a,\lambda}$ can also be retrieved at coarser spatial and temporal resolutions from numerical weather and chemical transport models. For example, the MACC reanalysis data set which provides since 2004 till the current day, every 3 hours, $\tau_{a,\lambda}$ notably at 550 nm and 1240 nm globally at a 1.125° spatial resolution (Inness *et al.*, 2013). Uncertainties in the MACC $\tau_{a,\lambda}$ vary for different locations (Eissa *et al.*, 2015; Oumbe *et al.*, 2013).

Over the study area, the errors involved from the variations of $\omega_{a,\lambda}$ are not great. Therefore, the main uncertainties in modelling the radiance are expected to be due to the uncertainties in $\tau_{a,\lambda}$ and $P_{a,\lambda}$. In the study period there exists 10285 observations of $\tau_{a,\lambda}$ as opposed to 1068 observations of $P_{a,\lambda}$ (by comparing data sets DS1 and DS3). Therefore, in the absence of measurements of $P_{a,\lambda}$ models to accurately estimate the CSNI would be of great interest.

5.1.2. The aerosol optical depth

$\tau_{a,\lambda}$ is critical for an accurate modelling of both the monochromatic diffuse radiance and the monochromatic DNI_S. The monochromatic DNI_S is related to τ_λ by the Beer-Bouguer-Lambert law (*cf.* Eq. (3.19)) as:

$$B_{n,\lambda}^{Sun} = E_{0,n,\lambda} \exp(-\tau_\lambda m) \tag{5.3}$$

Normally in desert regions $\tau_{a,\lambda}$ would be the greatest contributor to τ_λ. However, if the AERONET $\tau_{a,\lambda}$ DSA product is used as an input to the RTMs to compute the monochromatic DNI_S a correction is needed due to the field of view of the AERONET Sun photometer, which has an aperture half-angle of 0.6° (Holben *et al.*, 1998).

Indeed, this underestimation of the AERONET AOD has been observed in the previous chapter when comparing the AERONET and SAM AODs at 670 nm. Fig. 4.10 exhibits an overestimation of 5% of AERONET $\tau_{a,\lambda}$ by SAM $\tau_{a,\lambda}$. This bias is too large to be neglected.

To demonstrate the errors induced on the monochromatic DNI_S by errors in $\tau_{a,\lambda}$ in an aerosol only atmosphere, it is assumed that the actual $\tau_{a,\lambda}$ is presented by the robust affine regression shown in Fig. 4.10 and presented in Eq. (5.4). This is illustrated in Fig. 5.2, where for varying θ_S and $\tau_{a,\lambda}$ the relative error in monochromatic DNI_S is shown in colors and computed as shown in Eq. (5.5), where $\tau_{a,\lambda}$(corrected) in Eq. (5.5) is presented by Eq. (5.4).

$$\tau_{a,\lambda}(\text{SAM}) = 0.992\tau_{a,\lambda}(\text{AERONET}) + 0.016 \tag{5.4}$$

$$\text{relative error} = [\exp(-\tau_{a,\lambda} m) - \exp(-\tau_{a,\lambda}(\text{corrected}) m)]/\exp(-\tau_{a,\lambda}(\text{corrected}) m) \tag{5.5}$$

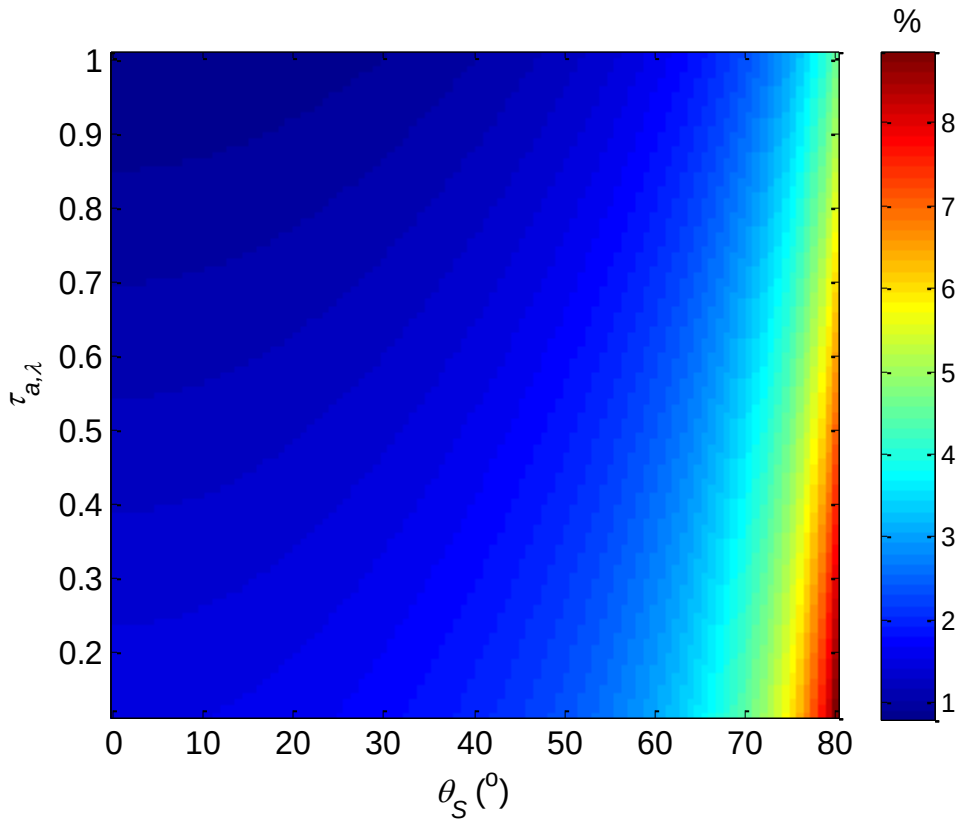


Fig. 5.2: Relative error in monochromatic DNI_S when varying $\tau_{a,\lambda}$ and θ_S.

The relative errors in monochromatic DNI_S, illustrated in Fig. 5.2, are too large to ignore, especially when the aim is an accurate assessment of the beam and circumsolar radiation. Therefore, a correction of the AERONET AOD at 670 nm is proposed based on the SAM reference values. The 3766 samples present in Fig. 4.10 were randomly split in two subsets:

- 80% of the samples were used to correct the AERONET AOD at 670 nm with respect to the SAM values *via* a robust fit,
- the remaining 20% of the samples were used to test the correction and compute the errors.

Fig. 5.3 exhibits the 80% of the samples which were used to correct the AERONET values. The coefficients of the robust affine regression are the same as those presented in Eq. (5.4).

Applying the correction of Eq. (5.4) on the testing samples and comparing with the reference SAM values, the relative bias of the corrected AERONET $\tau_{a,\lambda}$ is 0%, the relative RMSE is 3% and the R^2 value is 0.998. Therefore, it is assumed that this correction works well for the samples having different time stamps over the same location. The test results are presented in Fig. 5.4.

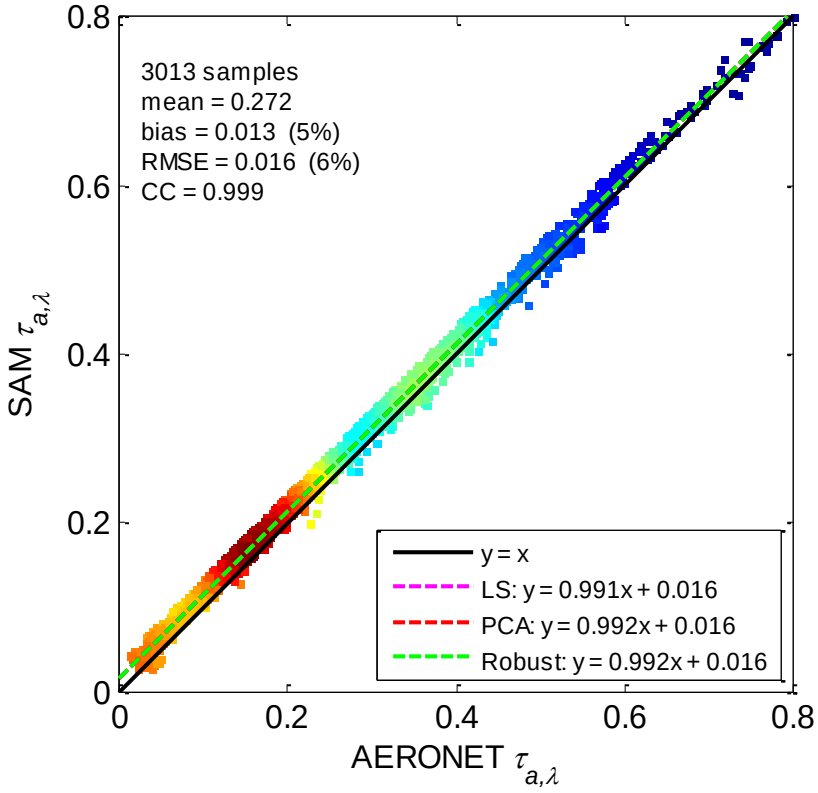


Fig. 5.3: Scatter density plot of the fitting subset of the matched SAM versus AERONET AOD at 670 nm. Axes are limited to 0.8 for a better view.

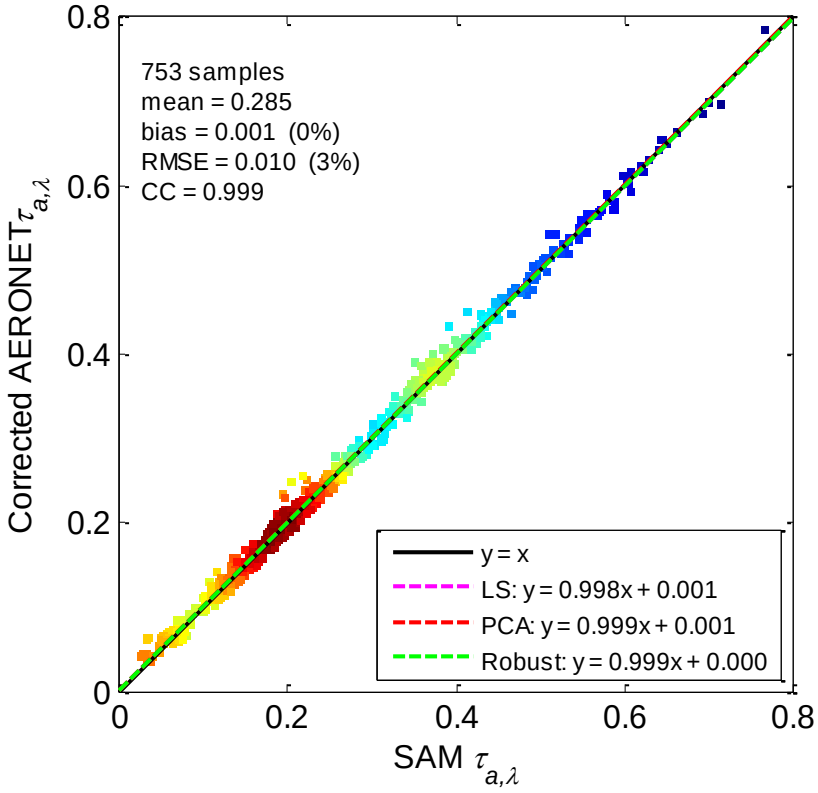


Fig. 5.4: Scatter density plot of the testing subset of the corrected AERONET versus SAM AOD at 670 nm. Axes are limited to 0.8 for a better view.

To conclude, an accurate $\tau_{a,\lambda}$ which has been derived within the extent of the solar disc only is necessary for an accurate estimate of the monochromatic DNI_S. An accurate $\tau_{a,\lambda}$ is also vital for an accurate assessment of the monochromatic diffuse radiance as shown in Sect. 5.1.1. Therefore, it is proposed that the correction of Eq. (5.4) is applied before using the AERONET $\tau_{a,\lambda}$.

5.1.3. The aerosol single scattering albedo

$\omega_{a,\lambda}$ affects the modelling of the monochromatic diffuse radiance. The errors induced by applying deviations on $\omega_{a,\lambda}$ are not as pronounced as those induced by applying deviations on $\tau_{a,\lambda}$ or $P_{a,\lambda}$, as shown previously in Fig. 5.1. To illustrate this, the histogram of the AERONET $\omega_{a,\lambda}$ at 675 nm from the data set DS4 is shown in Fig. 5.5. The mean value, the limits of the mean ± 1σ and the mean ± 2σ area also shown in the figure.

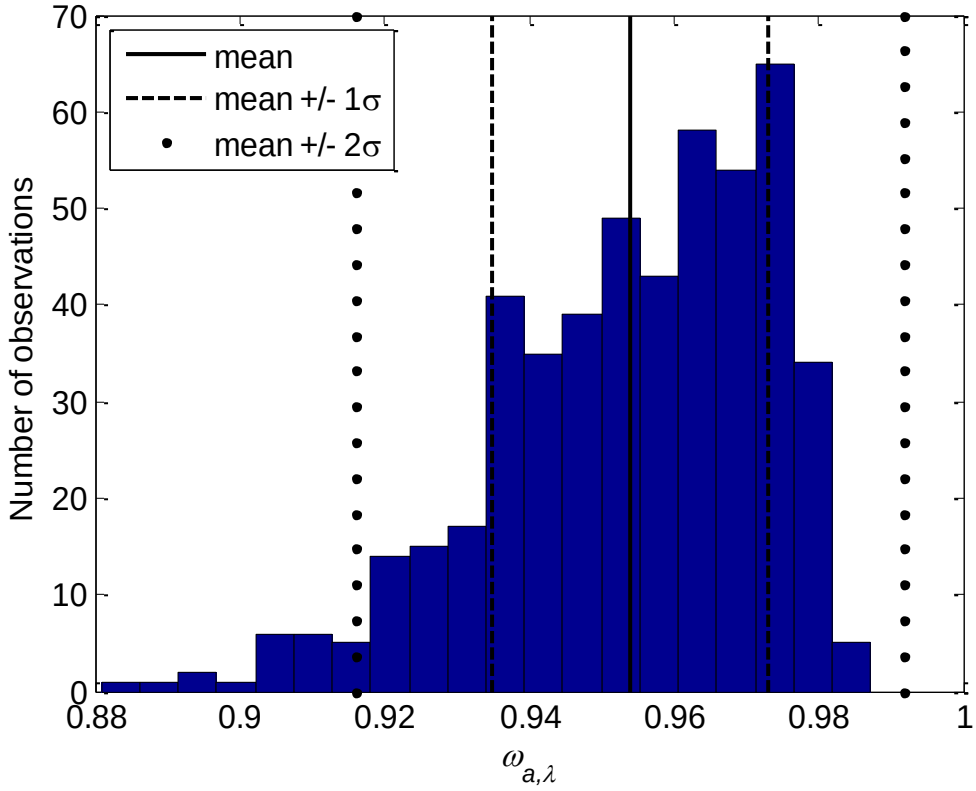


Fig. 5.5: Histogram of the AERONET $\omega_{a,\lambda}$ at 675 nm. The solid black line depicts the mean value, the black dashed line the mean value ± 1σ and the black dotted line the mean ± 2σ, where σ is the standard deviation.

Due to the low temporal variability of $\omega_{a,\lambda}$ and its low sensitivity to the sky radiance, and hence a low number of observations, a mean value may be sufficient over the study area. If using a mean representative value over the site, then the maximum relative errors in diffuse radiance would be ± 2% if the actual $\omega_{a,\lambda}$ deviates by ± 1σ and ± 4% if the actual $\omega_{a,\lambda}$ deviates by ± 2σ. These errors are small compared to the errors on the monochromatic diffuse radiance induced by errors in $\tau_{a,\lambda}$ and $P_{a,\lambda}$. To retain the highest possible number of observations, in this work the mean of the AERONET $\omega_{a,\lambda}$ was used.

5.1.4. The aerosol phase function

An accurate representation of the sharp peaks of $P_{a,\lambda}$ is very important for an accurate estimate of the circumsolar diffuse monochromatic radiance. The simple and more common representation of $P_{a,\lambda}$ is the HG PFCN, which is based on only one parameter rather than being represented as a function of many scattering angles (Henyey and Greenstein, 1941; Liou, 2002). The HG PFCN as a function of the asymmetry parameter g and its expansion as a series of Legendre polynomials were presented earlier in

Eqs. (3.52) and (3.53). However, there is still the problem that the HG PFCN does not properly reproduce the scattering patterns which are strongly peaked in the forward direction (Liou, 2002).

Irvine (1965) and Kattawar (1975) propose a two term HG (TTHG) PFCN to better depict the PFCNs with sharp peaks. The TTHG PFCN has also been used in the application of light scattering in seawater by Haltrin (2002), and optical properties of clouds in the atmosphere by Key *et al.* (2002). However, no literature has been found on direct application of the TTHG PFCN to model the circumsolar radiation under turbid cloud-free skies.

The TTHG PFCN is presented as a superposition of two HG PFCNs, and it is more capable of accurately representing the sharp peak of the PFCN at the small scattering angles. The TTHG PFCN is computed as (Haltrin, 2002; Kattawar, 1975):

$$P_{TTHG}(\xi, c_1, c_2, c_3) = c_1 P_{HG}(\xi, c_2) + (1 - c_1) P_{HG}(\xi, c_3) \tag{5.6}$$

where c_1, c_2 and c_3 are three parameters describing the TTHG PFCN and P_{HG} is the HG PFCN computed by Eq. (3.52). The TTHG PFCN can be expanded as a series of Legendre polynomials as:

$$P_{TTHG}(\xi, c_1, c_2, c_3) = \sum_{l=0}^{\infty} (2l+1)(c_1 {c_2}^l + (1 - c_1){c_3}^l)\, p_l(\cos(\xi)) \tag{5.7}$$

where $(c_1 {c_2}^l + (1 - c_1){c_3}^l)$ is the l'th moment and p_l is the l'th Legendre polynomial as a function of $\cos(\xi)$.

$P_{a,\lambda}$ from AERONET is provided as a function of the scattering angle ξ in the interval [0°, 180°]. However, for a user-defined monochromatic aerosol PFCN in libRadtran one needs to define its respective Legendre moments. One way to retrieve the Legendre moments of the PFCN is by calling the *pmom* tool in libRadtran.

The problem with this method is that it takes hundreds of Legendre moments to describe the PFCN with a sufficient accuracy. One advantage of using the TTHG PFCN is that it is described by only three parameters. One would still need to compute hundreds of Legendre moments before passing it on to libRadtran, but this is a simple computation as shown in Eq. (5.7). Another advantage is that in the case of developing a model to estimate the monochromatic aerosol PFCN, it is easier to try and estimate the three parameters of Eq. (5.6) rather than estimating hundreds of Legendre moments. Therefore, in this work the AERONET $P_{a,\lambda}$ was used to fit the three parameters of Eq. (5.6) using the nonlinear least-squares Levenberg-Marquardt method (Marquardt, 1963).

To illustrate the improvement of using the TTHG PFCN as opposed to the HG PFCN, Fig. 5.6 presents one $P_{a,\lambda}$ at 675 nm from AERONET, its HG and TTHG representation. For the small scattering angle $\xi < 6°$, it is evident that the HG representation of this monochromatic aerosol PFCN is very bad, whilst the TTHG representation is very good. There is a deficiency in the TTHG –and the HG– PFCNs for

scattering angles greater than 70°, but for the sake of the discussion on circumsolar radiation such large scattering angles are of no interest.

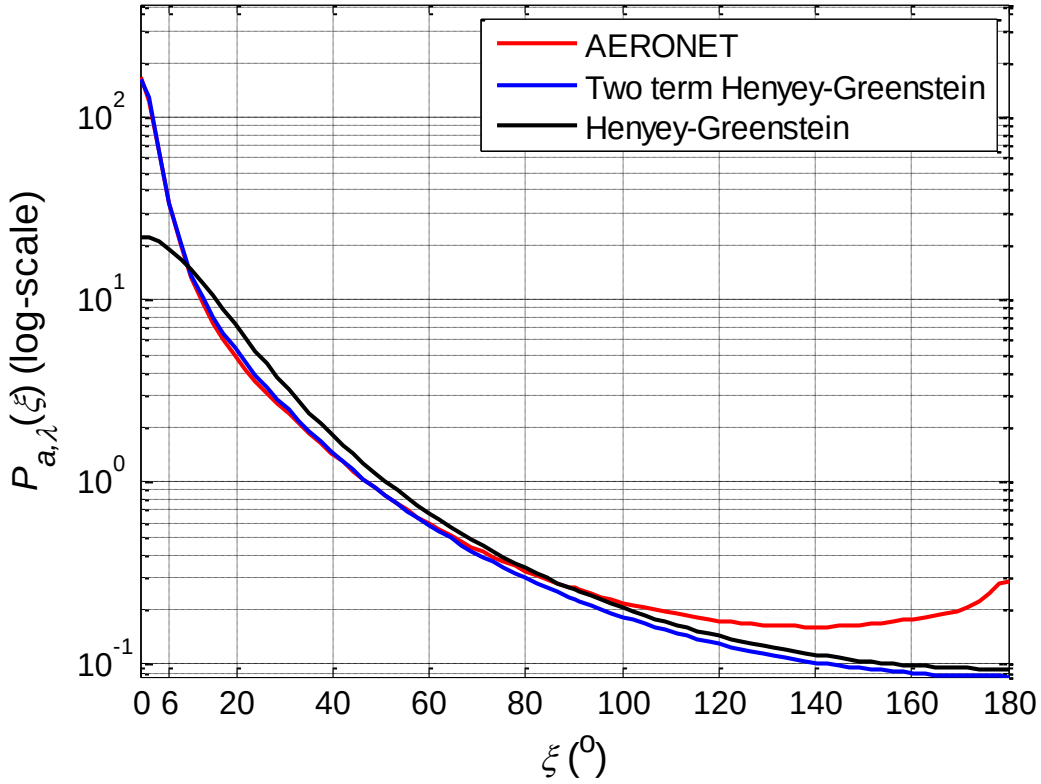


Fig. 5.6: An arbitrary AERONET $P_{a,\lambda}$ as a function of the scattering angle ξ at 675 nm, its HG PFCN representation and its TTHG PFCN representation.

5.1.5. Discussion on the aerosol optical properties

To answer the first research question, with regards to the modelling of the monochromatic diffuse radiance in the very near vicinity of the solar disc, it is apparent that $\tau_{a,\lambda}$, $P_{a,\lambda}(\xi)$ and $\omega_{a,\lambda}$ are the variables of significance. Their effects on the modelling of the monochromatic diffuse radiance are not the same. Assuming a constant $\omega_{a,\lambda}$ is sufficient over this study area, because the errors induced from its temporal deviations from the reference value are much less pronounced than those of $\tau_{a,\lambda}$ and $P_{a,\lambda}(\xi)$. It is these two variables which need to be available with a high accuracy for an accurate estimation of the monochromatic diffuse radiance in the very near vicinity of the solar disc.

As for the same research question but for variables affecting the monochromatic DNI_S, according to the Beer-Bouguer-Lambert law they are $E_{0,n,\lambda}$, m and τ_λ. As said before, these first two variables are well defined in the literature and can be precisely computed with no significant uncertainty. The most significant contributor to τ_λ under cloud-free skies is $\tau_{a,\lambda}$. However, the AERONET $\tau_{a,\lambda}$ observations need a correction for a more accurate estimate of the DNI_S. Such a correction is proposed in Sect. 5.1.2.

5.2. Parameterizations of the radiative transfer models

The RTMs are valuable for two main reasons in this work. First one is to assess the accuracy of the inputs used to parameterize the RTM, by comparing the RTM modelled values with respect to the reference values. The errors in the RTM modelled values could be highly attributed to errors in the inputs, as the RTMs are physical models. The flexibility of the RTM to define the inputs may be a factor in the accuracy of the modelled values. The second and more practical advantage is that the broadband DNI_S and CSNI at any geographic location could be modelled by the RTM if the right set of inputs is available. For that matter, not only the broadband and monochromatic irradiance could be computed, but also the irradiance between any specified wavelength interval. This could be, for example, useful for the CPV systems, which are only nonlinearly sensitive to the solar radiation in specific wavelength intervals depending on the technology.

The parameterizations of libRadtran and SMARTS are presented in the remainder of this section.

5.2.1. libRadtran

Before getting into details, it is important to note that libRadtran version 1.7 was used in this work. Towards the end of this work the libRadtran version 2.0 beta was released (Mayer *et al.*, 2014). Therefore, several option names in the new libRadtran might be different from those explained here.

The most popular solver of the radiative transfer equation is DISORT (DIScrete-ordinate-method Radiative Transfer, Stamnes *et al.*, 1988, 2000), which is included in the *uvspec* tool in libRadtran (Mayer and Kylling, 2005; Mayer *et al.*, 2012). The DISORT solver according to Mayer *et al.* (2012) is "*probably the most versatile, well-tested and mostly used 1D radiative transfer solver on this planet*". It solves the radiative transfer equation in 1-D geometry assuming a plane-parallel atmosphere and allows accurate calculations of the radiance and irradiance.

There are two main drawbacks when modelling the beam and circumsolar radiation using the DISORT solver, which have also been identified by Reinhardt (2013). The first drawback is that the solver DISORT assumes the Sun is a Dirac function, *i.e.* a point source. Realistically, the Sun is not a point source. It is in fact an extended source, with an angular radius of 0.266° at the mean Sun-Earth distance as viewed from the surface of the Earth. Stamnes *et al.* (2000) raised this concern in their report on the DISORT solver, and they demonstrate that the error in DNI_S modelled from the Sun as a Dirac function is very negligible when compared to the beam irradiance modelled from the Sun with a finite size. For example, even if θ_S is large at 80° and τ_λ at an arbitrary wavelength is 0.4, the relative error in the monochromatic beam irradiance at the arbitrary wavelength is still very negligible ~ 0%. The error is

even more negligible for smaller θ_S. Therefore, in the context of this work the assumption of the Sun as a Dirac function by the DISORT solver is not of a major concern.

The second drawback is that DISORT cannot reproduce the extremely strong peaks of some scattering PFCNs, thus affecting the modelling of the radiance under such conditions (Reinhardt, 2013). An alternative is the radiative transfer solver MYSTIC (Monte Carlo code for the phYSically correct Tracing of photons In Cloudy atmospheres), which is also a solver in the *uvspec* tool in libRadtran (Emde and Mayer, 2007; Mayer, 2009; Mayer *et al.*, 2012). It has several advantages over DISORT. It assumes 3-D geometry, it assumes the Sun is an extended source and it more accurately handles the extremely peaked scattering PFCNs. However, the advantage of MYSTIC over DISORT is only visible under cirrus cloudy conditions. Assuming a desert type aerosol and the Sun as a Dirac function, Reinhardt (2013) found that in the modelling case of the diffuse radiance for ξ less than 2° the relative difference between the DISORT and MYSTIC modelled radiance is less than 1%. This is not true under cirrus cloudy conditions, but this is out of the scope of this thesis. In the framework of this thesis, a similar simulation was performed under cloud-free conditions, for a wavelength of 675 nm and assuming a desert type aerosol at different θ_S (5° to 85° in steps of 5°) and different $\tau_{a,\lambda}$ (0.01 to 1.96 in steps of 0.05), the deviations between the DISORT and MYSTIC modelled monochromatic radiances in the near vicinity of the Sun have a relative bias of 0% and a relative RMSE of 1%.

Many of the features of the MYSTIC solver are unavailable in the public version of libRadtran. The MYSTIC solver in libRadtran version 1.7 assumes a 1-D geometry instead of 3-D and assumes the Sun as a Dirac function instead of an extended source. It is significantly slower than the DISORT solver, can only compute the radiance in one direction at a time where DISORT can compute the radiance in multiple directions, and it cannot be used with the *aerosol_files* option in libRadtran in contrary to DISORT. In the *aerosol_files* option the user can define the extinction coefficient, the aerosol SSA and the moments of the aerosol PFCN at different wavelengths for different layers in the atmosphere. This option will prove to be very valuable when computing the broadband radiances and irradiances as will be illustrated in Sect. 6.4.

The drawbacks of the MYSTIC solver available in the public version of libRadtran outweigh its advantages in terms of flexibility of inputs and computational times. Therefore, in the context of this thesis DISORT was the chosen solver.

The set of inputs needed to solve the radiative transfer equation in libRadtran for the monochromatic radiance and irradiance is:

i. The solar zenith angle θ_S
ii. The specified wavelength λ to compute the monochromatic radiance/irradiance
iii. The AOD $\tau_{a,\lambda}$ at the wavelength specified in point (ii)

iv. The atmospheric profile (*i.e.* the vertical profile of the temperature, pressure, density and volume mixing ratios for gases). In this thesis the mid-latitude summer atmospheric profile from Anderson *et al.* (1986) was selected
v. The total column content in water vapor
vi. The altitude of the site above mean sea level
vii. The altitude of the sensor above ground level
viii. The radiative transfer equation solver, DISORT in this case
ix. The aerosol SSA $\omega_{a,\lambda}$ at the wavelength specified in point (ii)
x. The moments of the aerosol PFCN $P_{a,\lambda}$ at the wavelength specified in point (ii)
xi. The sky element zenith angle θ
xii. The sky element azimuth angle φ
xiii. The extraterrestrial spectrum, *atlas_plus_modtran* was selected
xiv. The day of the year (*i.e.* 1 to 365 or 366 for a leap year), to correct for the Sun-Earth distance
xv. The number of streams to be used in DISORT 16 in this case, *i.e.* the number of directions at which the radiance is computed

The solar zenith angle θ_S was computed by the SG2 algorithm of Blanc and Wald (2012). The total column content in water vapor is directly available from the AERONET DSA Level 2.0 product. $\omega_{a,\lambda}$ and $P_{a,\lambda}$ are extracted from the AERONET Inversion products for the closest wavelength to the reference value, *i.e.* 675 nm from AERONET as opposed to the 670 nm of the SAM reference measurements. As explained in Sect. 5.1.3, a mean $\omega_{a,\lambda}$ was used to retain a greater number of samples. In this case the value of $\omega_{a,\lambda}$ at 675 nm over the study area in Abu Dhabi was found to be 0.954. The moments of $P_{a,\lambda}$ were computed from the TTHG representation as explained in Sect. 5.1.4. $\tau_{a,\lambda}$ at the specified wavelength was computed as explained earlier in Sect. 4.5 and then corrected as explained in Sect. 5.1.2. Finally, the sky element zenith and azimuth angles were defined in the intervals $[\theta_S - 6°, \theta_S + 6°]$ and $[\varphi_S - 6°, \varphi_S + 6°]$, respectively, at intervals of 0.0217°. Note that in libRadtran the sky element zenith angle needs to be defined as $-\cos(\theta)$ for computations of the downwelling radiation for a sensor looking upwards.

In libRadtran if the asymmetry parameter is defined (and not the moments of the aerosol PFCN), then an HG PFCN is assumed. Another option, if $\omega_{a,\lambda}$ or $P_{a,\lambda}$ are not available as inputs, is that they could be retrieved from the OPAC library in libRadtran by specifying the aerosol type (Hess *et al.*, 1998; Mayer and Kylling, 2005).

5.2.2. SMARTS

In the RTM SMARTS the inputs are extracted from 17 "cards" defined by the user (Gueymard, 2006). The defined inputs for these 17 cards in order are:

1. COMNT: a line of text, does not affect the computations
2. ISPR: the pressure at the site, in this case defined by the latitude, the altitude of the site above mean sea level and the altitude of the sensor above ground level
3. IATMOS: the atmospheric profile, in this case chosen as mid-latitude summer (same as that defined in libRadtran)
4. IH20: the total column content in water vapor, available from the AERONET DSA Level 2.0 product
5. IO3: the total column content in ozone, chosen the default value from the selected atmospheric profile
6. IGAS: gaseous absorption and atmospheric pollution, the default value was chosen
7. qCO2: the concentration of carbon dioxide, the default value of 370 ppmv was selected
    a. ISPCTR: the extraterrestrial spectrum, selected as MODTRAN (Spctrm_4.dat which is the one closest to that used in libRadtran)
8. AEROS: the aerosol model. Once it was selected as 'DESERT_MAX' and once it was user-defined as:
    a. ALPHA1 (Ångström wavelength exponent for wavelength less than 500 nm), ALPHA2 (Ångström wavelength exponent for wavelength greater than 500 nm), OMEGAL (the aerosol SSA ω_a), and GG (the asymmetry parameter g)
9. ITURB: turbidity data input, selected as the AOD $\tau_{a,\lambda}$ at 550 nm
10. IALBDX: the albedo, selected as the broadband albedo and set to 0.3
11. WLMN, WLMX, SUNCOR, SOLARC: for the broadband irradiance they respectively correspond to the minimum wavelength (set to 280 nm), the maximum wavelength (set to 4000 nm), the Sun-Earth distance correction, and the solar constant (set to 1367 W m^{-2})
12. IPRT: to print broadband and monochromatic results to the output file
    a. WPMX, WPMX, INTVL: minimum wavelength for monochromatic irradiance (set to 670 nm), maximum wavelength for monochromatic irradiance (also set to 670 nm), interval (set to an arbitrary value of 1 nm, since only one wavelength is specified)
13. ICIRC: option to compute the circumsolar irradiance
    a. SLOPE, APERT, LIMIT: slope angle ε_S of the instrument (set to 0 in SMARTS if it is not available), aperture half-angle α of the instrument, limit angle ε_L of the instrument (set to 0 in SMARTS if it is not available)
14. ISCAN: option not used and set to 0
15. ILLUM: option not used and set to 0
16. IUV: option not used and set to 0
17. IMASS: option for solar position and air mass m
    a. ZENIT, AZIM: respectively the solar zenith angle θ_S and the solar azimuth angle φ_S

According to the SMARTS manual (Gueymard, 2006), the aerosol model 'DESERT_MAX' corresponds to the extremely turbid conditions which could be due to sand storms. However, no further details were found on this aerosol model.

For the inputs to SMARTS the $\tau_{a,\lambda}$ at 550 nm was computed from the AERONET $\tau_{a,\lambda}$ observations using the method described earlier in Sect. 4.5. In the case where the aerosol model was user-defined, the Ångström wavelength exponents ALPHA1 and ALPHA2 were computed also as explained in Sect. 4.5. Even though SMARTS requires the broadband asymmetry parameter g and the broadband aerosol SSA ω_a, such broadband values were not available. Therefore, g_λ at 675 nm from the AERONET Inversion product was used, whereas for $\omega_{a,\lambda}$ at 675 nm the mean value was used.

There are several problems concerning a fair comparison between the results of libRadtran and SMARTS. One is that SMARTS does not give the flexibility to input $\tau_{a,\lambda}$ at a user-defined wavelength, the only two options available are either at 500 nm or 550 nm, whereas this flexibility is available in libRadtran. Also, SMARTS does not offer the flexibility of a user-defined $P_{a,\lambda}$, while that option is available in libRadtran given that the PFCN could be expanded as a series of Legendre polynomials. The difference in the parameterizations of libRadtran and SMARTS will be considered when discussing the results in Chapter 6.

Chapter 6 - Modelling the beam and circumsolar radiation: results and model

In this chapter the monochromatic DNI_S and CSNI modelled by libRadtran and SMARTS are compared with the SAM reference values. The term 'compared' is used rather than the term 'validated' because the data sets DS2 and DS5, used for this comparison, were filtered such that the SAM and AERONET monochromatic AOD agree with each other within the reported errors of the SAM instrument in the AOD retrievals. The monochromatic radiance measurements of the SAM instrument and AERONET Sun photometer were also compared to make sure they agree. The objective of this comparison is to assess the ability of each RTM to model the monochromatic DNI_S and CSNI given a set of inputs, where the aerosol optical properties are from the AERONET products and the reference values are those from the SAM measurements.

The SAM instrument measures the monochromatic direct and diffuse radiance at 670 nm. Therefore, the reference irradiance values from the SAM radiance measurements were computed using Eqs. (3.23) and (3.34) with Riemann sums. The limits of the integration in Eq. (3.34) for computing the monochromatic CSNI from the modelled diffuse radiance should be from the edge of the solar disc to the defined limit aperture half-angle, 6° in this case. However, due to the gap in the SAM radiance measurements from the edge of the solar disc up to ~ 0.64°, these limits have been changed to the interval [δ = 0.64°, α = 6°].

Depending on the results of the comparison, the RTM exhibiting the more accurate results will be used to model the broadband DNI_S and CSNI. The validations of the broadband DNI_S and CSNI are indirect validations. Indirect in the sense that the DNI_S, and the sum of the DNI_S and the CSNI are validated with respect to reference broadband DNI observations for the same instant. This is because no reference measurements are available of the broadband DNI_S and CSNI separately.

After the validations of the broadband DNI_S and CSNI, an attempt to answer the research question #2 is performed. To recall it, the question is: can a fast and accurate model be developed to estimate the beam and circumsolar radiation (for a defined aperture angle) using observables which are more frequently available than aerosol optical properties? The proposed model to estimate the DNI_S and CSNI at different aperture half-angles is presented and validated.

This chapter is organized as follows:

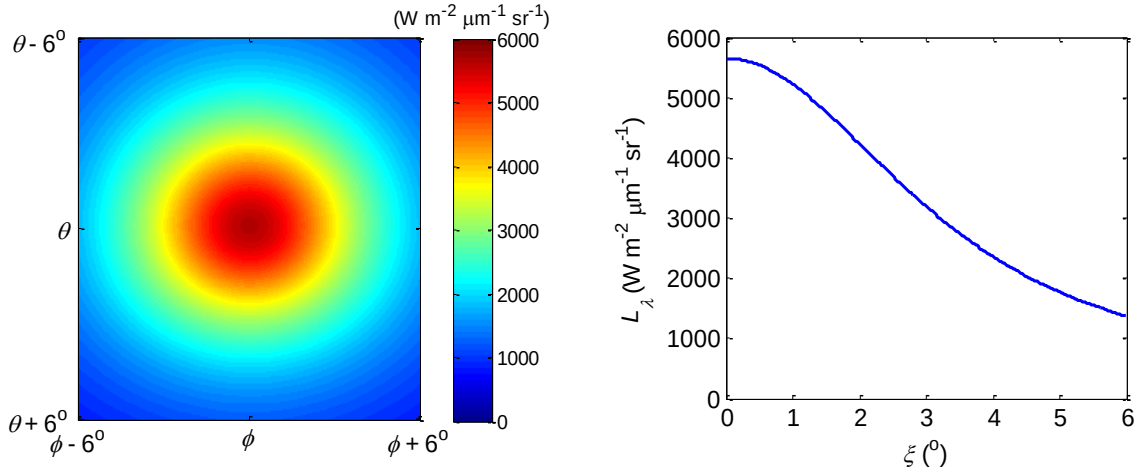
- libRadtran results of modelling the monochromatic DNI_S and CSNI (Sect. 6.1),
- SMARTS results of modelling the monochromatic DNI_S and CSNI (Sect. 6.2),
- comparison between the libRadtran and SMARTS results (Sect. 6.3),
- proposed model for estimating the broadband DNI_S and CSNI (Sect. 6.4),

- and finally a discussion (Sect. 6.5).

The results of both the comparisons and validations are presented in the form of scatter density plots, where the dark red dots in the scatter plots denote high densities of samples and the dark blue ones denote very low densities of samples. The discussions on the results are mainly based on three statistical measures, namely the bias, the RMSE, and the coefficient of determination R^2. The deviations were computed by subtracting the reference value for each sample from the modelled value. Therefore, a positive bias corresponds to an overestimation in the modelled value and *vice versa*.

6.1. Modelling the monochromatic beam and circumsolar irradiances at 670 nm using libRadtran

The RTM libRadtran assumes the Sun is a point source and the direct radiance within the extent of the solar disc is not provided as an output. The output from libRadtran is actually the beam horizontal irradiance from the Sun only; knowing the solar zenith angle θ_S the DNI_S is provided. The diffuse radiance is provided as a 2-D matrix, with each value corresponding to the viewing direction defined by the sky element zenith θ and azimuth φ angles. The scattering angle ξ is then computed for each corresponding modelled diffuse radiance cell and then used to compute the azimuthally averaged solar diffuse radiance profile. Using Riemann sums and Eq. (3.34) the CSNI is then computed from this profile in the interval [$\delta = 0.64°$, $\alpha = 6°$]. The Fig. 6.1 exhibits an example of the monochromatic diffuse radiance modelled by libRadtran and its corresponding azimuthally averaged diffuse solar radiance profile.



(a) (b)

Fig. 6.1: Example of the diffuse radiance L_λ at 670 nm shown in colors at different element zenith θ and azimuth angles φ (a) and its corresponding diffuse solar radiance profile as a function of the scattering angle ξ (b).

The modelling results of the monochromatic DNI_S and CSNI using libRadtran are organized as follows:

- results of the monochromatic DNI_S (Sect. 6.1.1),
- results of the monochromatic CSNI using the HG PFCN (Sect. 6.1.2),
- results of the monochromatic CSNI using the aerosol properties from the OPAC library (Sect. 6.1.3),
- results of the monochromatic CSNI using the TTHG PFCN (Sect. 6.1.4).

In this section all irradiance values are modelled at the wavelength 670 nm, to match that of the reference SAM measurements. In all cases the monochromatic AOD $\tau_{a,\lambda}$ is corrected as explained in Sect. 5.1.2 and a mean value of 0.954 for the monochromatic aerosol SSA $\omega_{a,\lambda}$ is used for all samples as explained in Sect. 5.1.3. All the inputs for libRadtran were discussed earlier in Sect. 5.2.1.

6.1.1. Results of modelling the monochromatic beam irradiance

For the comparisons of the monochromatic DNI_S the data set DS2 was used to retain the greatest number of possible samples, since the presence of the aerosol SSA or the aerosol PFCN is insignificant for the DNI_S modelling. The scatter density plot of the monochromatic DNI_S modelled by libRadtran versus the SAM reference values is shown in Fig. 6.2. Most observations lie around the 1:1 line and the scatter around this line is very low. The relative RMSE and bias are very low: 5% and +1% respectively. R^2 is 0.972, and the slope of the robust affine regression is very close to 1. These results are very good, and mean that if the right set of inputs are available the monochromatic DNI_S could be very accurately modelled by libRadtran.

The outliers which are present in Fig. 6.2, where the libRadtran values are overestimated, correspond to specific days in which most samples exhibit a high overestimation. It is hypothesized that during these days there was some soiling on the entrance window of the SAM instrument.

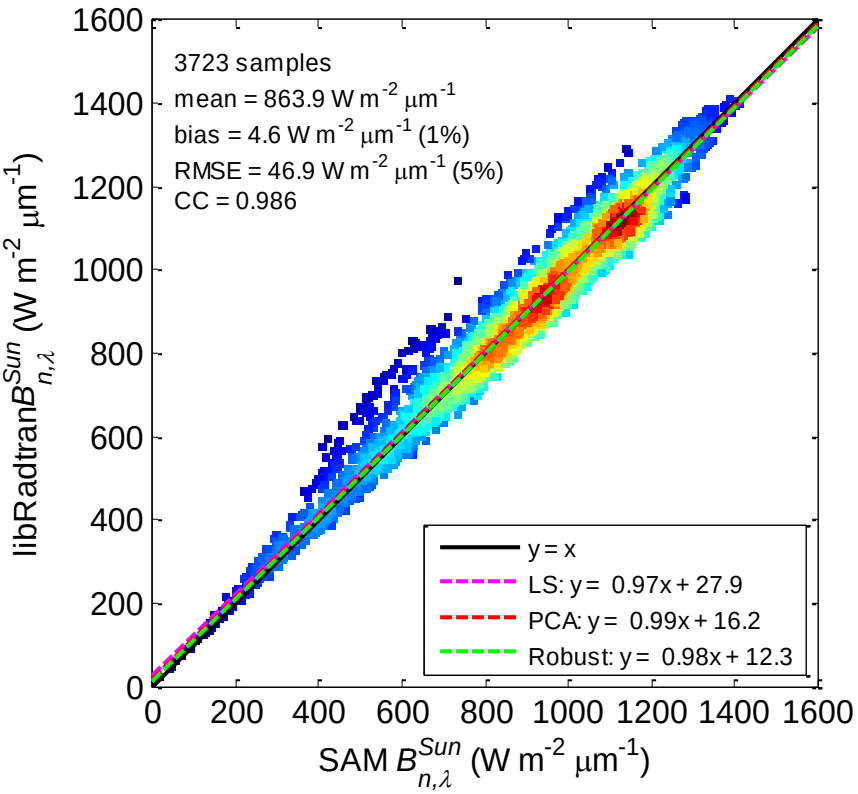


Fig. 6.2: Scatter density plot of the libRadtran DNI_S at 670 nm (libRadtran $B_{n,\lambda}^{Sun}$) versus the reference values from the SAM instrument (SAM $B_{n,\lambda}^{Sun}$).

6.1.2. Results of modelling the monochromatic circumsolar irradiance using the Henyey-Greenstein phase function

The data set DS5 was used for the comparisons of the monochromatic CSNI. In this case the monochromatic aerosol PFCN was modelled by a HG PFCN. In libRadtran the HG PFCN can be defined by either by computing the moments of the HG PFCN and passing the moments in the input file or, more simply, by defining the corresponding monochromatic asymmetry parameter g_λ in the input file. Both approaches give the same results.

The scatter density plot of the monochromatic CSNI modelled by libRadtran versus the ground reference values is shown in Fig. 6.3. It is evident that despite of a relatively high coefficient of determination ($R^2 = 0.721$) there is a very high underestimation of the monochromatic CSNI modelled by libRadtran when the monochromatic aerosol PFCN is represented by the HG PFCN. The statistical indicators exhibit very high errors. The relative RMSE is 81% and the relative bias is −76%. The slope of the robust affine regression is far from 1. These results show that the HG PFCN is a very bad representation of the real aerosol PFCN, especially for the very small scattering angles ξ in the case of strongly peaked forward scattering. The inability of the HG PFCN to represent the aerosol PFCN was

shown earlier in Fig. 5.6. Therefore, based on these results it is not recommended to use the HG PFCN to model the CSNI.

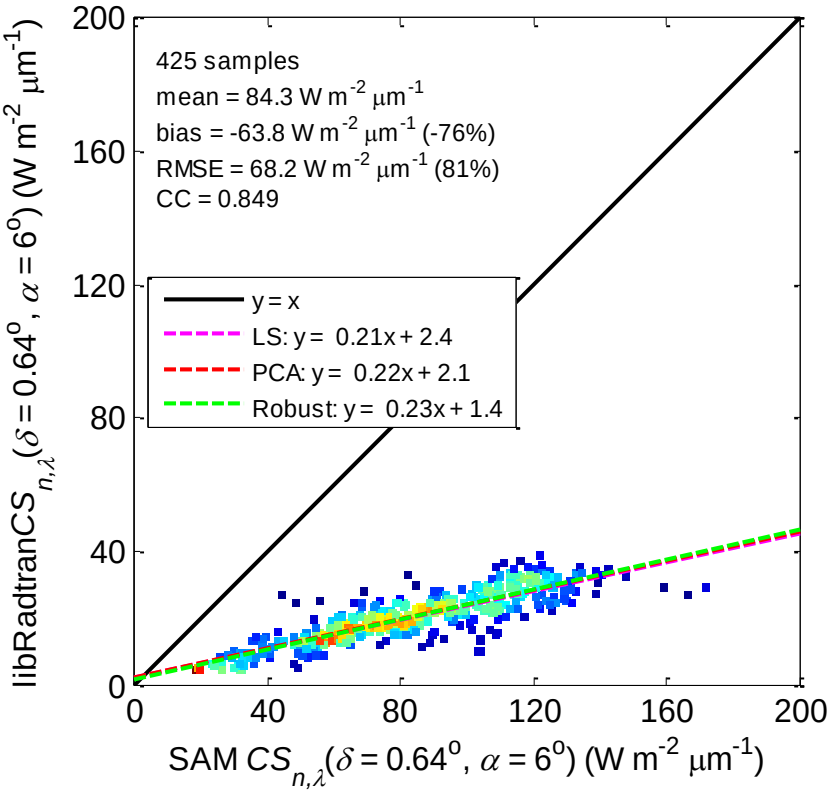


Fig. 6.3: Scatter density plot of the libRadtran CSNI at 670 nm modelled by defining the HG PFCN (libRadtran $CS_{n,\lambda}(\delta = 0.64°, \alpha = 6°)$) versus the reference values from the SAM instrument (SAM $CS_{n,\lambda}(\delta = 0.64°, \alpha = 6°)$).

6.1.3. Results of modelling the monochromatic circumsolar irradiance using the OPAC library aerosol optical properties

In this case, also using the data set DS5, the desert type aerosol was selected from the OPAC library. By calling the OPAC library in libRadtran the PFCN is computed by the Mie theory based on the aerosol properties specified in the OPAC library (Mayer *et al.*, 2012).

The scatter density plot of the monochromatic CSNI modelled by libRadtran versus the ground reference values is shown in Fig. 6.4. Also in this case, it is clear that there is a very high underestimation of the monochromatic CSNI modelled by libRadtran when the monochromatic aerosol PFCN is represented by the desert type aerosol optical properties of the OPAC library. The statistical indicators exhibit very high errors. The relative RMSE is 38% and the relative bias is −31%. R^2 is 0.719 and the slope of the robust affine regression is far from 1. The results are a significant improvement compared to those when using the standard HG PFCN (Fig. 6.3), but still there is a significant underestimation in the modelled values meaning that the properties of the desert type aerosols in the OPAC library are not

realistic over this study area. Therefore, based on the results presented herein over this study area it is not recommended to use the OPAC library to compute the CSNI as the errors are very significant.

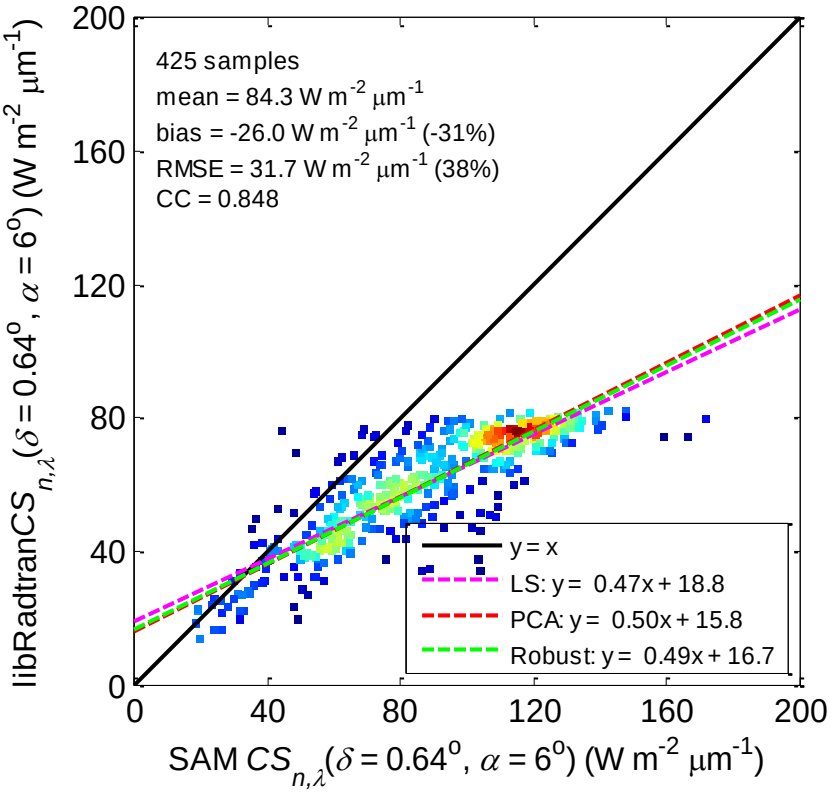


Fig. 6.4: Scatter density plot of the libRadtran CSNI at 670 nm modelled by defining the desert type aerosol in the OPAC library (libRadtran $CS_{n,\lambda}(\delta = 0.64°, \alpha = 6°)$) versus the reference values from the SAM instrument (SAM $CS_{n,\lambda}(\delta = 0.64°, \alpha = 6°)$).

6.1.4. Results of modelling the monochromatic circumsolar irradiance using the two term Henyey-Greenstein phase function

Using the same data set DS5, the monochromatic aerosol PFCN in this case was represented as a TTHG PFCN. The scatter density plot of the monochromatic CSNI modelled by libRadtran versus the ground reference values is shown in Fig. 6.5. It is clear that there is a very significant improvement in the results, when compared to those presented in Figs. 6.3 and 6.4. The relative RMSE is 22%, the relative bias is −19%, R^2 is 0.891, and the slope of the robust affine regression is 0.82. The improvement is attributed to the TTHG PFCN which is able to accurately represent the strong forward scattering peaks in the PFCN, as shown previously in Fig. 5.6. However, there is still a noticeable underestimation in the modelled values, which is discussed further in Sect. 6.3.

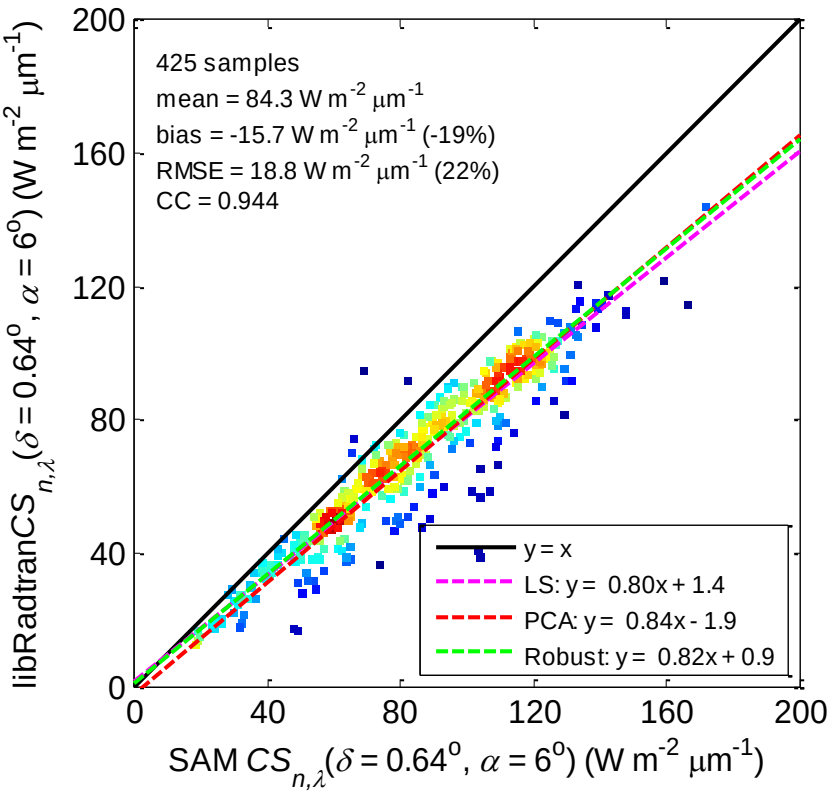


Fig. 6.5: Scatter density plot of the libRadtran CSNI at 670 nm modelled by defining the TTHG PFCN (libRadtran $CS_{n,\lambda}(\delta = 0.64°, \alpha = 6°)$) versus the reference values from the SAM instrument (SAM $CS_{n,\lambda}(\delta = 0.64°, \alpha = 6°)$).

6.2. Modelling the monochromatic beam and circumsolar irradiances at 670 nm using SMARTS

Like libRadtran, the RTM SMARTS also assumes the Sun is a point source. Therefore, the modelled DNI_S is a direct output. Unlike libRadtran, SMARTS directly provides the CSNI for the defined aperture half-angle (up to a maximum of 10°), but does not provide the diffuse radiance. Therefore, in order to compute the CSNI in the interval [$\delta = 0.64°$, $\alpha = 6°$] SMARTS is run twice. Once to compute the CSNI up to the scattering angle of 0.64° and once to compute the CSNI up to the scattering angle of 6°. The CSNI in the limits [$\delta = 0.64°$, $\alpha = 6°$] is computed by subtracting the CSNI at 0.64° from the CSNI at 6°.

The modelling results of the monochromatic DNI_S and CSNI using SMARTS are organized as follows:

- results of the monochromatic DNI_S (Sect. 6.2.1),
- results of the monochromatic CSNI by defining the aerosol SSA ω_a and asymmetry parameter g (Sect. 6.2.2),
- results of the monochromatic CSNI using the 'DESERT_MAX' aerosol properties of SMARTS (Sect. 6.2.3).

In this section all irradiance values are modelled at the wavelength 670 nm, to match that of the reference SAM measurements. Unfortunately, in SMARTS the AOD $\tau_{a,\lambda}$ cannot be defined at any user-defined wavelength. It can only be defined at either 500 nm or 550 nm. In all cases $\tau_{a,\lambda}$ at 550 nm is used as an input and is corrected as explained in Sect. 5.1.2. A mean value of 0.954 for $\omega_{a,\lambda}$ is used for all samples as explained in Sect. 5.1.3. All the other inputs for SMARTS were discussed earlier in Sect. 5.2.2.

6.2.1. Results of modelling the monochromatic beam irradiance

For the monochromatic DNI_S the data set DS2 was used to retain the maximum number of samples. The scatter density plot of the monochromatic DNI_S modelled by SMARTS versus the SAM reference values is shown in Fig. 6.6. Most observations lie around the 1:1 line and the scatter around this line is very low. The statistical indicators exhibit very low errors. The relative RMSE is 5% and the relative bias is +1%. R^2 is 0.974 and the slope of the robust affine regression is very close to 1. These results are very good and the observed relative errors are very close to those modelled by libRadtran.

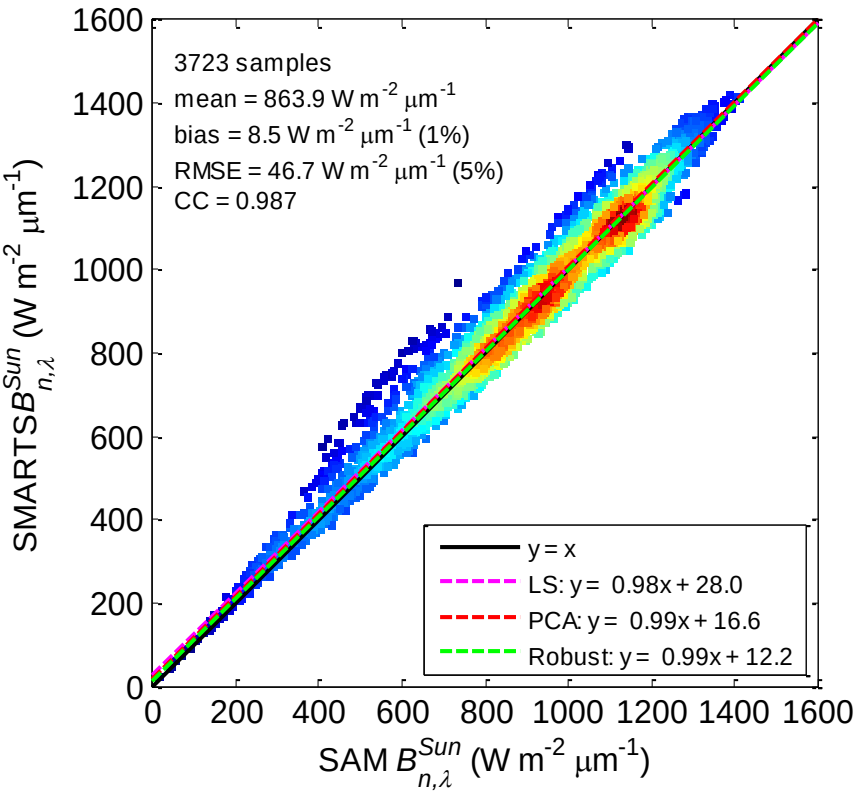


Fig. 6.6: Scatter density plot of the SMARTS DNI_S at 670 nm (SMARTS $B_{n,\lambda}^{Sun}$) versus the reference values from the SAM instrument (SAM $B_{n,\lambda}^{Sun}$).

6.2.2. Results of modelling the monochromatic circumsolar irradiance by user-defined aerosol optical properties

In this case, the monochromatic asymmetry parameter g_λ of data set DS5 was used along with the mean monochromatic aerosol SSA $\omega_{a,\lambda}$. The scatter density plot of the monochromatic CSNI modelled by SMARTS versus the ground reference values is shown in Fig. 6.7. The statistical indicators exhibit very high errors. The relative RMSE is 79% and the relative bias is −73%. R^2 is 0.694 and the slope of the robust affine regression is far from 1.

It is unclear in the SMARTS manual (Gueymard, 2006) which representation of the aerosol PFCN is used in the case where the aerosol model is user-defined, as in this case. As the results are very similar to those of libRadtran when defining the HG PFCN (as shown in Sect. 6.1.2), it is assumed that SMARTS also uses the HG PFCN in the user-defined aerosol model. As pointed out earlier, the HG PFCN is a very bad representation of the aerosol PFCN and its use is not recommended when modelling the CSNI.

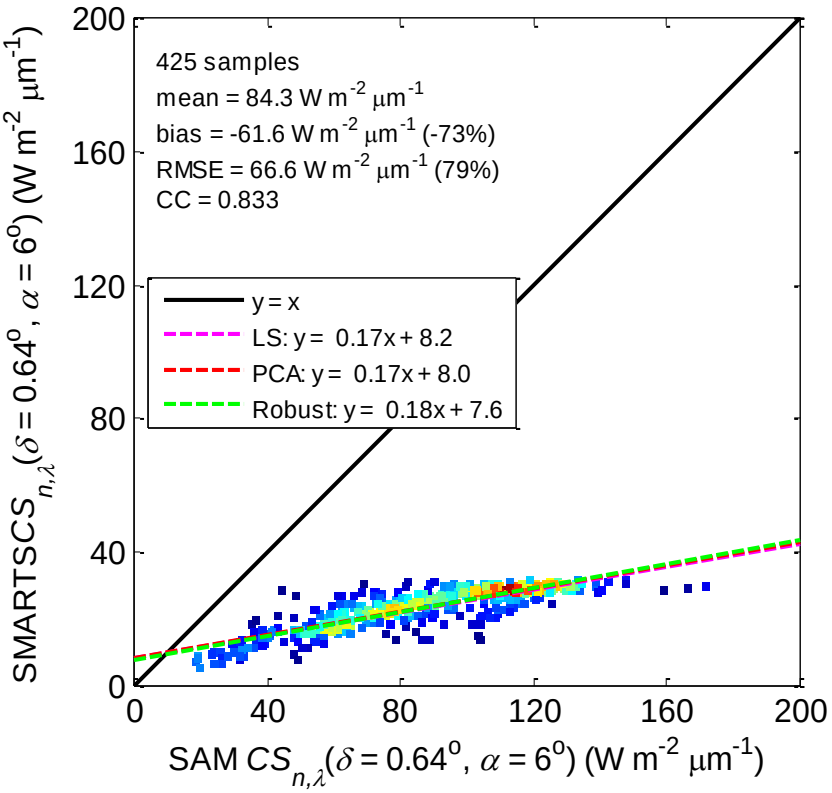


Fig. 6.7: Scatter density plot of the SMARTS CSNI at 670 nm modelled by defining the SSA and asymmetry parameter (SMARTS $CS_{n,\lambda}(\delta = 0.64°, \alpha = 6°)$) versus the reference values from the SAM instrument (SAM $CS_{n,\lambda}(\delta = 0.64°, \alpha = 6°)$).

6.2.3. Results of modelling the monochromatic circumsolar irradiance using the 'DESERT_MAX' aerosol properties

In this case the 'DESERT_MAX' aerosol type in SMARTS was used. Even though the asymmetry parameter and the SSA cannot be defined in this case in SMARTS, the data set DS5 was still the one selected to be able to compare with the previously presented results.

The scatter density plot of the monochromatic CSNI modelled by SMARTS versus the ground reference values is shown in Fig. 6.8. There is still a very high underestimation of the monochromatic CSNI modelled by SMARTS when defining the 'DESERT_MAX' aerosol type. Even though there is an improvement compared to Fig. 6.7, the statistical indicators still exhibit very high errors. The relative RMSE is 54% and the relative bias is −46%. R^2 is 0.570 and the slope of the robust affine regression is far from 1. Over this study area the 'DESERT_MAX' aerosol model in SMARTS does not provide accurate results of the monochromatic CSNI.

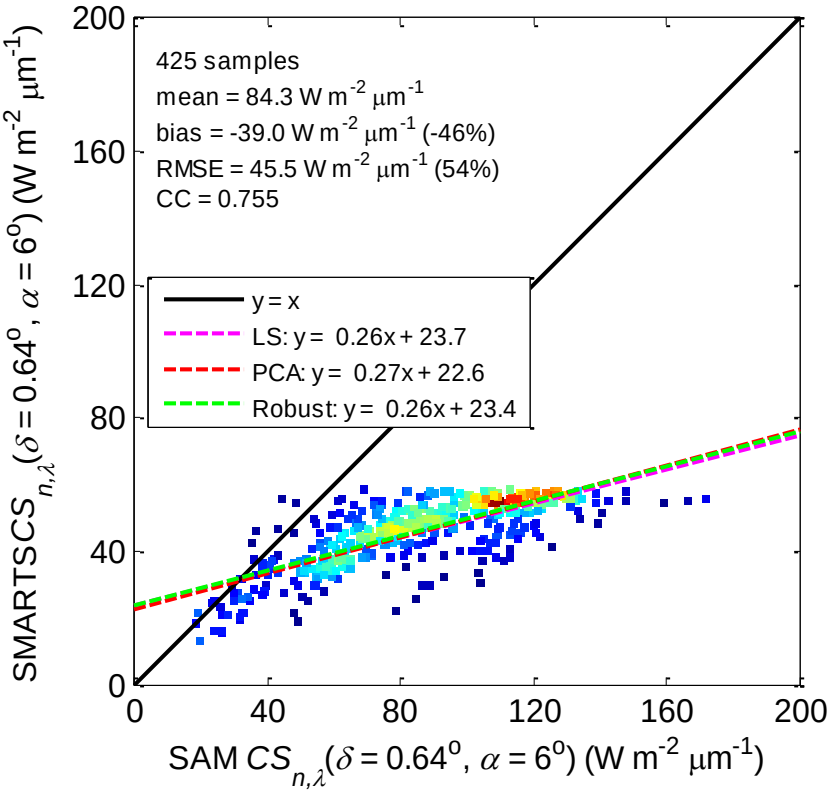


Fig. 6.8: Scatter density plot of the SMARTS CSNI at 670 nm modelled by defining the 'DESERT_MAX' aerosol type (SMARTS $CS_{n,\lambda}(\delta = 0.64°, \alpha = 6°)$) versus the reference values from the SAM instrument (SAM $CS_{n,\lambda}(\delta = 0.64°, \alpha = 6°)$).

6.3. Discussion on the modelled monochromatic beam and circumsolar irradiances

The comparison results of the monochromatic DNI_S and CSNI modelled by the two RTMs are respectively presented in Tables 6.1 and 6.2.

The differences between the two RTMs in the modelling of the monochromatic DNI_S are negligible. The same atmospheric profile (mid-latitude summer) was defined in both models. The very minor difference in the bias between both models may be due to the scaling of the AOD to 670 nm in the SMARTS model, since the AOD at 550 nm was provided as an input. Another cause in the difference in the bias of SMARTS is that the correction applied to the AOD at 550 nm was based on the analysis of the AOD at 670 nm and this correction has not been validated at other wavelengths. In relative terms the bias between both models is the same. Given the accuracy of the SAM instrument in the solar disc region which is less than 1% for AOD less than 0.6, it may be concluded that both models provide very accurate estimates of the monochromatic DNI_S.

Table 6.1: Results of libRadtran and SMARTS for the modelling the monochromatic DNI_S at 670 nm.

RTM	**Aerosol optical properties**	**Data set; # of samples**	**Mean**	**Bias**		**RMSE**		**R^2**
			W m^{-2} μm^{-2}	W m^{-2} μm^{-2}	%	W m^{-2} μm^{-2}	%	
libRadtran	AOD at 670 nm	DS2; 3723	863.9	+4.6	+1	46.9	5	0.972
SMARTS	AOD at 550 nm	DS2; 3723	863.9	+8.5	+1	46.7	5	0.974

The modelling of the monochromatic CSNI is very strongly dependent on the defined aerosol optical properties. The differences in the results by applying different inputs to the RTMs are summarized in Table 6.2. It is clear from the results that the HG PFCN is a very bad representation of the aerosol PFCN and its use is not recommended when modelling the CSNI. A relative bias greater than −70% is observed in both RTMs when the HG PFCN is used.

The 'DESERT_MAX' aerosol type is not explicated in the publications describing the SMARTS model (Gueymard 1995, 2001). It is only included in the SMARTS version 2.9.5 and in its documentation (Gueymard, 2006); no reference is given to describe the properties of the 'DESERT_MAX' aerosol model. It is apparent from the presented results that the aerosol PFCN used in this case is an improvement when compared to the standard HG PFCN in SMARTS and libRadtran. The errors are still high though, even higher than when using the desert type aerosols of the OPAC library in libRadtran. Neither the 'DESERT_MAX' aerosol model in SMARTS nor the desert type aerosol of the OPAC library in libRadtran provide accurate results of the monochromatic CSNI over this study area.

All of the statistical indicators of modelled monochromatic CSNI when using the TTHG PFCN show a very significant improvement when compared to all the other results. There is still an underestimation in the monochromatic CSNI of −19% when using the TTHG PFCN. This bias may partly originate from the reference monochromatic aerosol PFCN $P_{a,\lambda}$. The aperture half-angle of the Sun photometer used in

the AERONET stations is 0.6°, which is relatively large considering that the angular radius of the Sun is 0.266° ± 1.7%, and that the circumsolar region in this context is defined only up to a scattering angle of 6°. In fact, for scattering angles less than 6° the AERONET PFCN is only provided at three scattering angles, namely at: 0°; 1.71°; and 3.93°. Actually the PFCN at those first two scattering angles are extrapolated values, because the almucantar measurements were only collected at $\xi \geq 3°$ over this study area.

Even though the AERONET monochromatic aerosol PFCN and its representation as a TTHG PFCN improve the results of the modelled CSNI, the field of view of the Sun photometer is not narrow enough to accurately represent the aerosol PFCN in the very near vicinity of the solar disc. This is a limitation of using the AERONET Inversion products. However, given the accuracy of the SAM instrument in the aureole region to be ~ 15%, it is concluded that defining the moments of the TTHG PFCN in libRadtran provides remarkably accurate and interesting estimates of the monochromatic CSNI over this study area.

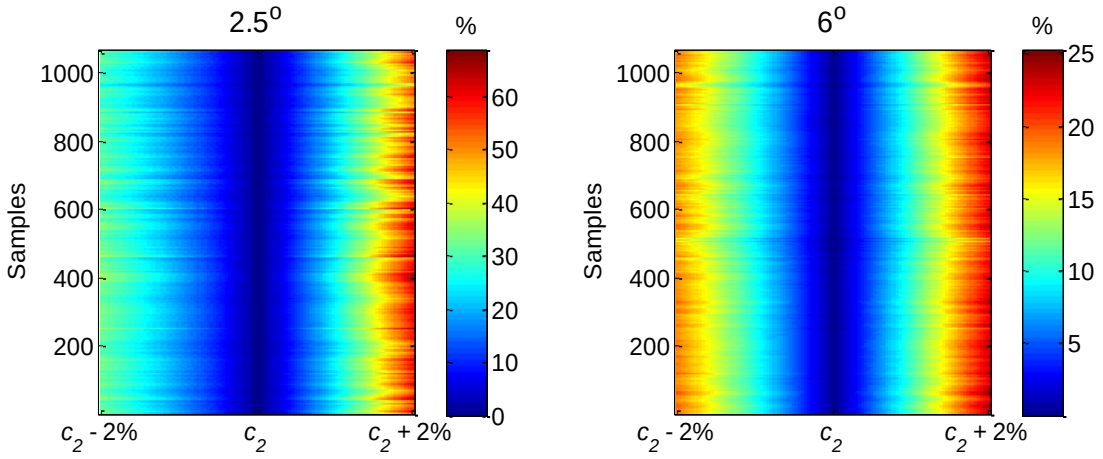
Table 6.2: Results of libRadtran and SMARTS for the monochromatic CSNI at 670 nm.

RTM	**Aerosol optical properties**	**Data set; # of samples**	**Mean**	**Bias**		**RMSE**		**R^2**
			W m^{-2} μm^{-2}	W m^{-2} μm^{-2}	%	W m^{-2} μm^{-2}	%	
libRadtran	AOD at 670 nm; mean SSA; HG PFCN	DS5; 425	84.3	−63.8	−76	68.2	81	0.721
SMARTS	AOD at 550 nm; mean SSA; asymmetry parameter	DS5; 425	84.3	−61.6	−73	66.6	79	0.694
libRadtran	AOD at 670 nm; OPAC desert type aerosol	DS5; 425	84.3	−26.0	−31	31.7	38	0.719
SMARTS	AOD at 550 nm; 'DESERT_MAX' aerosol model	DS5; 425	84.3	−39.0	−46	45.5	54	0.570
libRadtran	AOD at 670 nm; mean SSA; TTHG PFCN	DS5; 425	84.3	−15.7	−19	18.8	22	0.891

A problem of using the AERONET Inversion products is that the number of observations is significantly lower than that of the available AOD observations. For example, over this study area there are 10285 samples in data set DS1 (DSA products), while there are only 1068 samples in data set DS3 (Inversion

products) for the period June 2012 to May 2013. $P_{a,\lambda}$ is only available at θ_S greater than 50°, which poses a problem for modelling the CSNI for smaller θ_S.

An attempt to correlate the three parameters describing the TTHG PFCN to the observable variables describing the state of the atmosphere (*cf.* Sect. 3.4) was not successful, especially because any small error in the c_2 parameter of the TTHG PFCN would induce a very high error in the modelled diffuse radiance and irradiance. To illustrate this, the 1068 samples of the data set DS3 were used to compute the relative absolute error on the CSNI by adding a small deviation to the c_2 parameter. The results are shown in Fig. 6.9, where it is clear that a modest error of only ± 2% in c_2 could cause a relative absolute error of 65% in the modelled CSNI for a half-angle of 2.5° and 25% for a half-angle of 6°.



(a) (b)

Fig. 6.9: The relative absolute error on the monochromatic CSNI (shown in colors) by inducing an error of ± 2% on the c_2 parameter in the TTHG PFCN. The results for an aperture half-angle of 2.5° (a) and those for 6° (b) are shown.

Instead of trying to directly model $P_{a,\lambda}$ another approach is proposed, in which the DNI_S and CSNI are directly estimated from observables which are more frequently available than the precise aerosol optical properties. Such a model is proposed in Sect. 6.4 for estimating the broadband DNI_S and CSNI.

6.4. Proposed method for modelling the broadband beam and circumsolar irradiances using libRadtran

In the previous sections the results were presented for monochromatic DNI_S and CSNI values, whereas for the resource assessment of CSTE systems the broadband DNI_S and CSNI are of interest. Therefore, a model to estimate the broadband DNI_S and CSNI is proposed and validated herein. In Sect. 6.4.1 the method for modelling the broadband irradiances using libRadtran is explained, followed by the validations of such irradiances in Sect. 6.4.2. In Sect. 6.4.3 the proposed model and its validation are presented.

6.4.1. Modelling the broadband beam and circumsolar irradiances using libRadtran

The results of RTM libRadtran modelled monochromatic DNI_S were very good when compared to the SAM reference values. Also, the results of the monochromatic CSNI modelled by libRadtran when using the TTHG PFCN showed a significant improvement when compared to the SAM reference values, as opposed to the CSNI modelled when using the HG PFCN or the aerosol optical properties form the predefined libraries available in the RTMs libRadtran and SMARTS.

The broadband DNI_S is (*cf.* Eqs. (3.4) and (3.19)):

$$B_n^{Sun} = \int_{\lambda_1}^{\lambda_2} B_{n,\lambda}^{Sun} d\lambda \tag{6.1}$$

Ideally, the monochromatic DNI_S should be computed at an infinitesimally small wavelength intervals in Eq. (6.1). However, this is impractical because it is computationally expensive. The k-distribution method and correlated-k approximation of Kato *et al.* (1999) are an efficient means to significantly speed up the computations whilst providing accurate results, as opposed to spectrally resolved computations. It divides the useful solar spectrum, between [0.24 μm, 4.6 μm] in this case, in to 32 wavelength intervals for an approximation of the broadband irradiance. The approach of Kato *et al.* is available in libRadtran.

Inputs to libRadtran to estimate the broadband DNI_S and diffuse radiance in the vicinity of the solar disc are very similar to those presented in Sect. 5.2.1. The appropriate wavelength interval is defined to coincide with that of the approach of Kato *et al.* For a more accurate estimate, it is valuable to define the aerosol optical properties at different wavelengths to minimize the errors in libRadtran when interpolating the aerosol optical properties at each of the 32 wavelength intervals. This is done in libRadtran by defining the aerosol optical properties at different wavelength by using the *aerosol_files* option.

From the AERONET Inversion products $\tau_{a,\lambda}$, $\omega_{a,\lambda}$, and $P_{a,\lambda}$ are available at the following wavelengths: 1020 nm, 870 nm, 675 nm, and 440 nm. Observations of $P_{a,\lambda}$ were represented as TTHG PFCNs and the moments were computed as explained in Sect. 5.1.4.

In libRadtran the defined aerosol optical properties can be interpolated at any wavelength, but not extrapolated. Therefore, the aerosol optical properties must be available at the limits of the defined wavelength interval, in this case [0.25 μm, 4.6 μm]. $\tau_{a,\lambda}$ at the limits were computed using the method explained in Sect. 4.5, where in this case the Ångström parameter was computed for the interval [0.34 μm, 1.64 μm], corresponding the minimum and maximum wavelengths of the $\tau_{a,\lambda}$ observations from the AERONET products. $\tau_{a,\lambda}$ at the different wavelengths were all corrected as discussed in Sect. 5.1.2.

To define $P_{a,\lambda}$ at the limits the Fraunhofer theory is used as explained in Wilbert *et al.* (2013). ξ_2 is defined as:

$$\xi_2 = \xi_2 \lambda_2/\lambda_1 \tag{6.2}$$

where ξ_1 is the scattering angle of the available $P_{a,\lambda}$, λ_1 is the wavelength of the available $P_{a,\lambda}$, and λ_2 is the wavelength defined at the new $P_{a,\lambda}$. The new $P_{a,\lambda}$ is computed as:

$$P(\lambda_2, \xi_2) = P(\lambda_1, \xi_1)\left(\frac{\lambda_1}{\lambda_2}\right)^2 \tag{6.3}$$

To compute $P_{a,\lambda}$ at the limits the closest $P_{a,\lambda}$ in terms of wavelength was used. The problem in Eq. (6.3) is that when computing $P_{a,\lambda}$ at 250 nm the values as a function of ξ will not be available up to ξ = 180°, because $\lambda_2/\lambda_1 < 1$ where in this case λ_1 = 440 nm. To solve this, the missing values of the computed $P_{a,\lambda}$ at 250 nm were extrapolated up to ξ of 180°. This extrapolation will have minimal effects on results of libRadtran, because when modelling the circumsolar diffuse radiance the $P_{a,\lambda}$ is only useful at small ξ.

$\omega_{a,\lambda}$ at the limits of the interval [0.25 μm, 4.6 μm] were adapted from the SMARTS model (Gueymard, 1995), which in turn adapts them from the SRA (Standard Radiation Atmosphere) model (IAMAP, 1986):

$$\omega_{a,\lambda} = \min(0.99, \sum_{i=o}^{i=3} j_i \lambda^i) \qquad \text{for } \lambda < 2\ \mu\text{m} \tag{6.4}$$

$$\omega_{a,\lambda} = 1 - \frac{\upsilon_0 \exp[\upsilon_1(\lambda - \upsilon_2)]}{\{1 + \exp[\upsilon_1(\lambda - \upsilon_2)]\}^2} \qquad \text{for } 2\ \mu\text{m} \le \lambda \le 4\ \mu\text{m} \tag{6.5}$$

where λ is expressed in μm, and the coefficients j and υ are given in Table 6.3 for different aerosol models. The continental aerosol type was selected in this case. The Eq. (6.5) is only valid for wavelengths up to 4 μm, but it was applied to the wavelength 4.6 μm. This induces errors in the results, but considering that < 10% of the broadband radiation is present for wavelengths > 1.6 μm the errors should be minimal.

Table 6.3: Coefficients of Eqs. (6.4) and (6.5) adapted from Gueymard (1995).

	Aerosol type		
	Continental	Urban	Maritime
j_0	$8.4372e^{-1}$	$6.4886e^{-1}$	$9.6635e^{-1}$
j_1	$3.0206e^{-1}$	$1.3465e^{-1}$	$7.3464e^{-2}$
j_2	$-4.7838e^{-1}$	$-3.0166e^{-1}$	$-7.1847e^{-2}$
j_3	$1.5647e^{-1}$	$8.3393e^{-2}$	$1.9774e^{-2}$
υ_0	1.2853	2.9784	2.0006
υ_1	1.4860	$6.1494e^{-1}$	7.1110
υ_2	2.8357	3.3122	3.0136

6.4.2. Validations of the modelled broadband beam and circumsolar irradiances using libRadtran

For the broadband diffuse radiance computations by libRadtran, the sky element zenith and azimuth angles were defined in steps of 0.1° and not the finer steps of 0.0217° for the monochromatic values, in order to speed up the computations with a very low induced error. The outputs from libRadtran are similar to those for the monochromatic values. The broadband diffuse radiance is provided as a 2-D matrix, where the azimuthally averaged diffuse solar radiance profile can be computed as shown previously in Fig. 6.1. The broadband CSNI was computed:

$$CS_n(\delta, \varepsilon_L) = 2\pi \int_{\delta}^{\varepsilon_L} p(\xi) L(\xi) \sin(\xi) d\xi \qquad (6.6)$$

In this case the modelled values were validated with respect to the RSI DNI observations. The penumbra function $p(\xi)$ was computed for the RSI instruments using the viewing half-angles presented in Sect. 4.2. In libRadtran the Sun is assumed to be a point source. Therefore, the limits of integration in Eq. (6.6) for the broadband CSNI were [$\delta = 0°$, $\varepsilon_L = 4.6°$], where 4.6° is the limit angle of the RSI instrument.

No reference measurements of the broadband DNI_S and CSNI are available. The broadband DNI_S and CSNI are compared to the RSI DNI observations for an indirect validation. Ideally if there are no errors in the modelled or reference values, the DNI_S should be underestimated with respect to the RSI DNI, while the DNI_S + CSNI should exhibit no bias with respect to the RSI DNI.

Using the data set DS3, the scatter density plot of the libRadtran DNI_S versus the RSI DNI is shown in Fig. 6.10. Most observations lie around the 1:1 line and the scatter around this line is very low. The statistical indicators exhibit very low errors. The relative RMSE is 5% and the relative bias is +1%. R^2 is 0.992 and the slope of the robust affine regression is very close to 1.

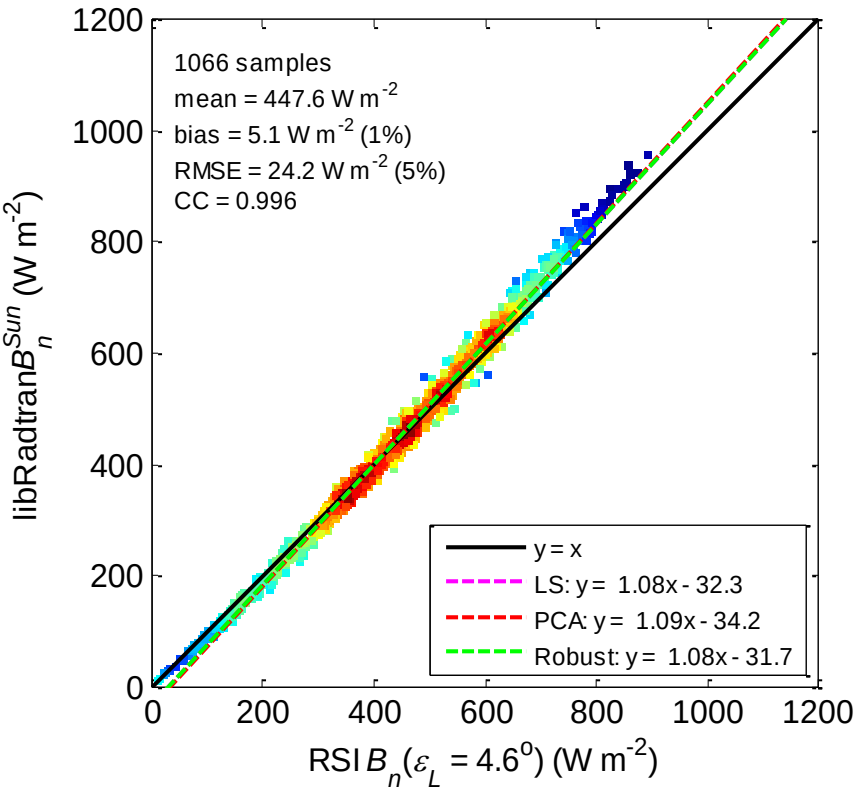


Fig. 6.10: Scatter density plot of the libRadtran broadband DNI_S (libRadtran B_n^{Sun}) versus the reference values from the RSI instrument (RSI $B_n(\varepsilon_L = 4.6°)$).

One observes a positive bias as a whole with a noticeable overestimation of the greatest values, which is unfortunate because ideally there should be an underestimation (or negligible bias in the case of very clear skies) by the libRadtran modelled DNI_S. The bias is still within the reported error of the RSI DNI, being ± 4.1%.

There are several possible causes of the bias. It may be partly due to the inputs to libRadtran. The interpolation of the aerosol optical properties may induce errors in the modelling. The correction applied to $\tau_{a,\lambda}$ was only validated at the wavelength 670 nm; whether it is directly applicable to other wavelengths is an area requiring further research. Miscalibrations of the RSI instrument may be a possible cause of the bias though it underwent two calibrations by the photodiode manufacturer and by CSP Services. In Fig. 6.11 the scatter density plot of the residuals versus the air temperature at the surface is shown. There is a positive bias (libRadtran overestimating) for the lowest temperatures. In this study area the lowest temperatures generally coincide with the highest DNI values. It is not clear as to whether these errors are due to the dependence of the RSI instrument with temperature or due to other calibration errors.

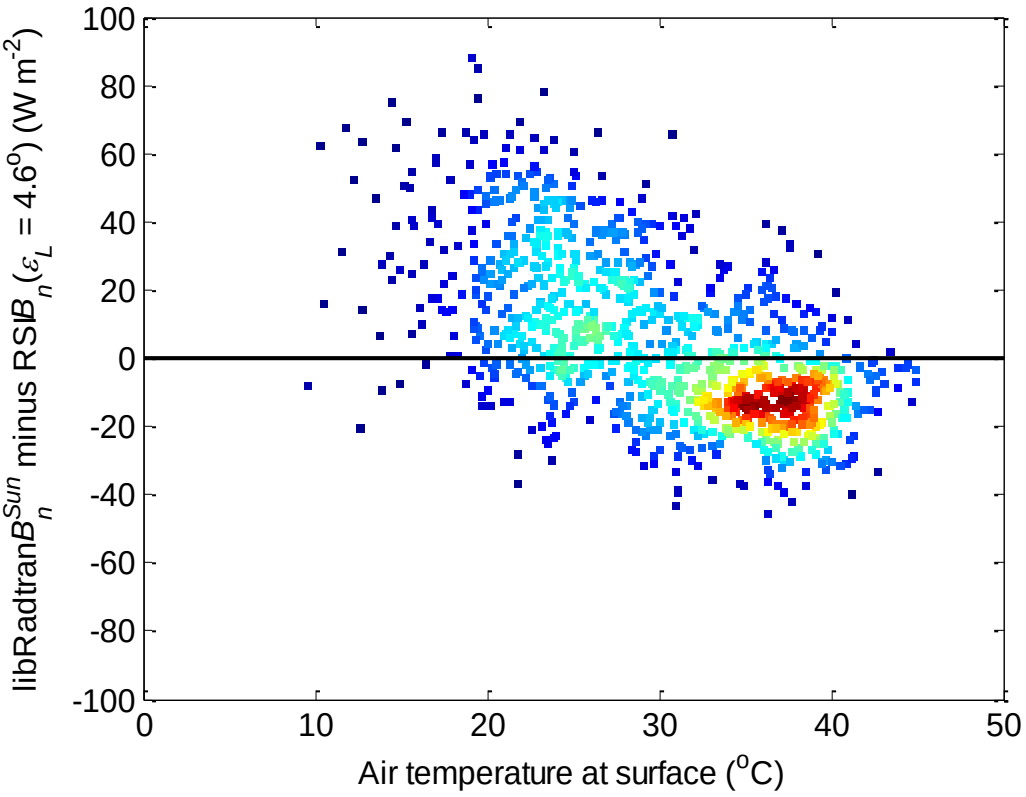


Fig. 6.11: Scatter density plot of the residuals versus the air temperature at surface.

The scatter density plot of the libRadtran DNI (*i.e.* DNI_S + CSNI(δ = 0°, ε_L = 4.6°)) versus the RSI DNI is shown in Fig. 6.12. The relative RMSE is 7% and the relative bias is +5%. R^2 is 0.994 and the slope of the robust affine regression is very close to 1. There is an overestimation for all the modelled values except the smallest ones. As stated earlier, the bias may be due to miscalibrations of the RSI instrument or errors in the inputs to libRadtran. The bias is still very close to the reported error of the RSI DNI.

Compared to the previous case, adding the CSNI to DNI_S increases the overestimation for almost all values. The bias increases from 5.1 W m^{-2} to 22.5 W m^{-2}. This was expected as a positive value (CSNI) was added to DNI_S. However, one may note that the correlation coefficient has increased which demonstrates that adding CSNI contributes to model better the variability of DNI. This is corroborated by the fact that the standard deviation of the deviations for DNI is 21 W m^{-2}, less than that for DNI_S (23.7 W m^{-2}).

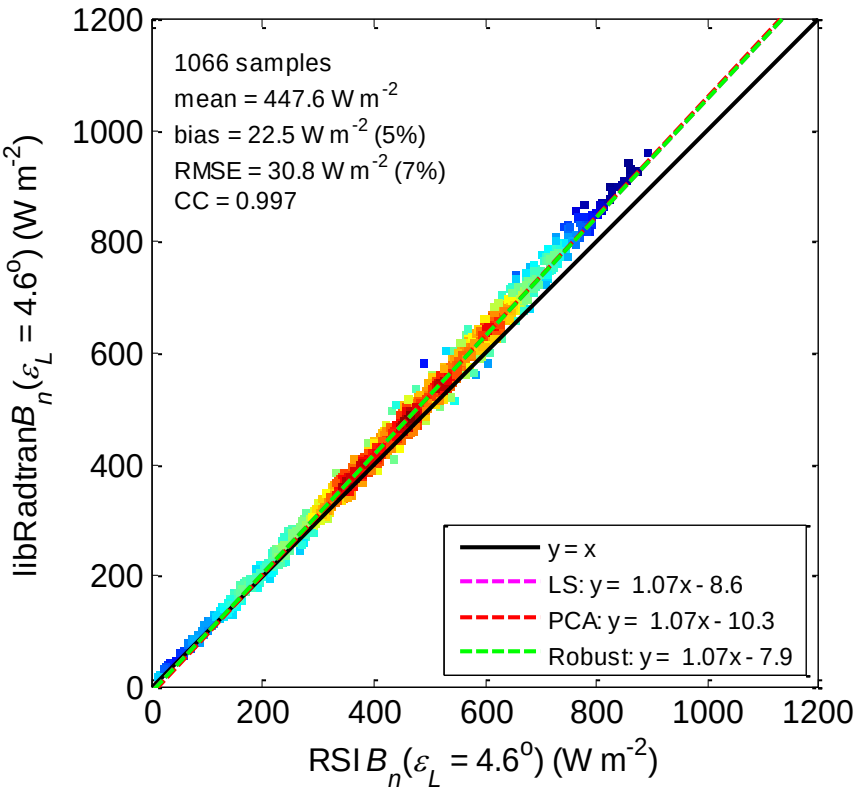


Fig. 6.12: Scatter density plot of the libRadtran broadband DNI for a limit angle of 4.6° (libRadtran $B_n(\varepsilon_L = 4.6°)$) versus the reference values from the RSI instrument (RSI $B_n(\varepsilon_L = 4.6°)$).

By comparing the modelled DNI_S and DNI, the CSNI contributes to 4% of the DNI as an average. Considering that Shams 1, the 100 MW CSTE plant in Abu Dhabi, cost around 600 M$, an overestimation of 4% in the DNI when compared to the DNI_S is a not negligible at all. The cumulative distribution function (CDF) of the modelled CSR is shown in Fig. 6.13. It is apparent that 50% of the observations of the data set DS3 have a CSR > 0.04. This shows that the CSNI for a limit angle of 4.6° is very significant even under cloud-free skies. Therefore, accurate modelling of the CSNI would lead to improved assessments of the DNI resource.

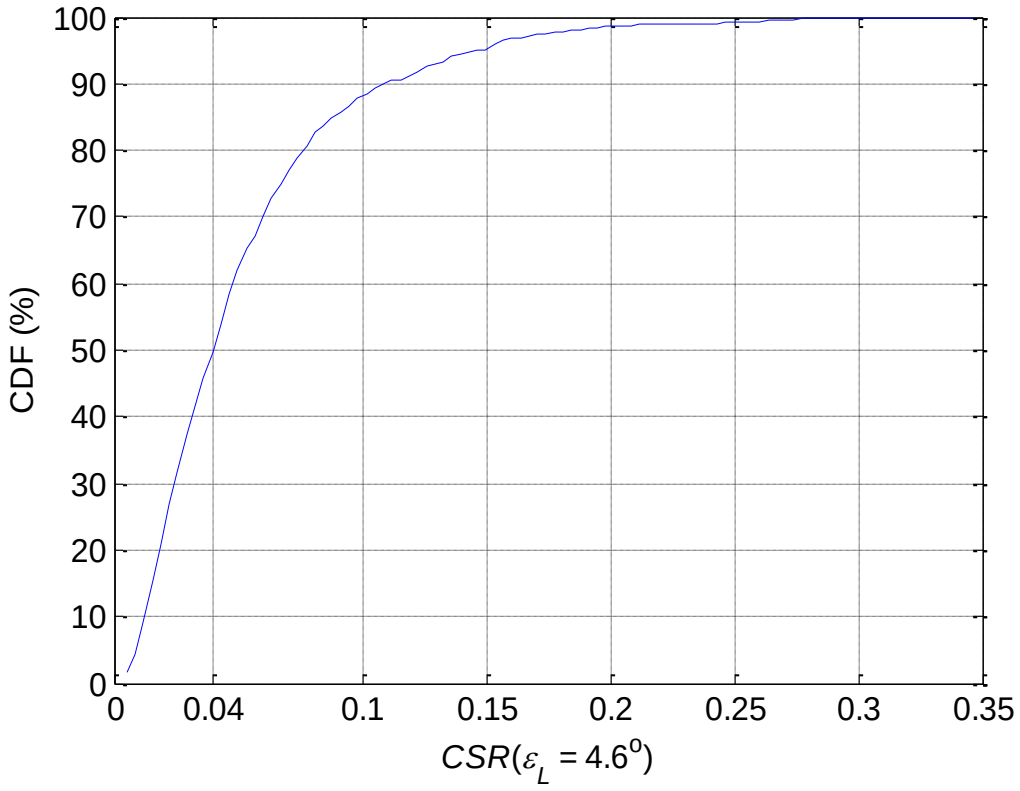


Fig. 6.13: The cumulative distribution function (CDF) of the CSR for a limit angle of 4.6° ($CSR(\varepsilon_L = 4.6°)$).

6.4.3. Empirical model to estimate the broadband beam and circumsolar irradiances

The aerosol optical properties required to model the broadband DNI_S and CSNI are not frequently available over many sites, and if they are available the RTM libRadtran is computationally expensive to run. Therefore, a fast model to estimate the broadband DNI_S and CSNI from variables describing the state of the atmosphere, which can be derived from the more frequently available GHI, DNI and DHI measurements, would be valuable from the point of view of the resource assessments for CSTE systems. In addition, instead of estimating the DNI_S and CSNI separately the model could estimate the CSR, from which the DNI_S and CSNI could be computed.

To start with, and to compare with what is available in the literature, the relationship between the modelled CSR and the ground measured DNI is shown in Fig. 6.14. It is clear that there is a strong relationship, where the highest CSR values occur at the lowest DNI and *vice versa*. A similar curve is available in Blanc *et al.* (2014) though it includes the presence of clouds. A good agreement is found between the two curves under cloud-free conditions.

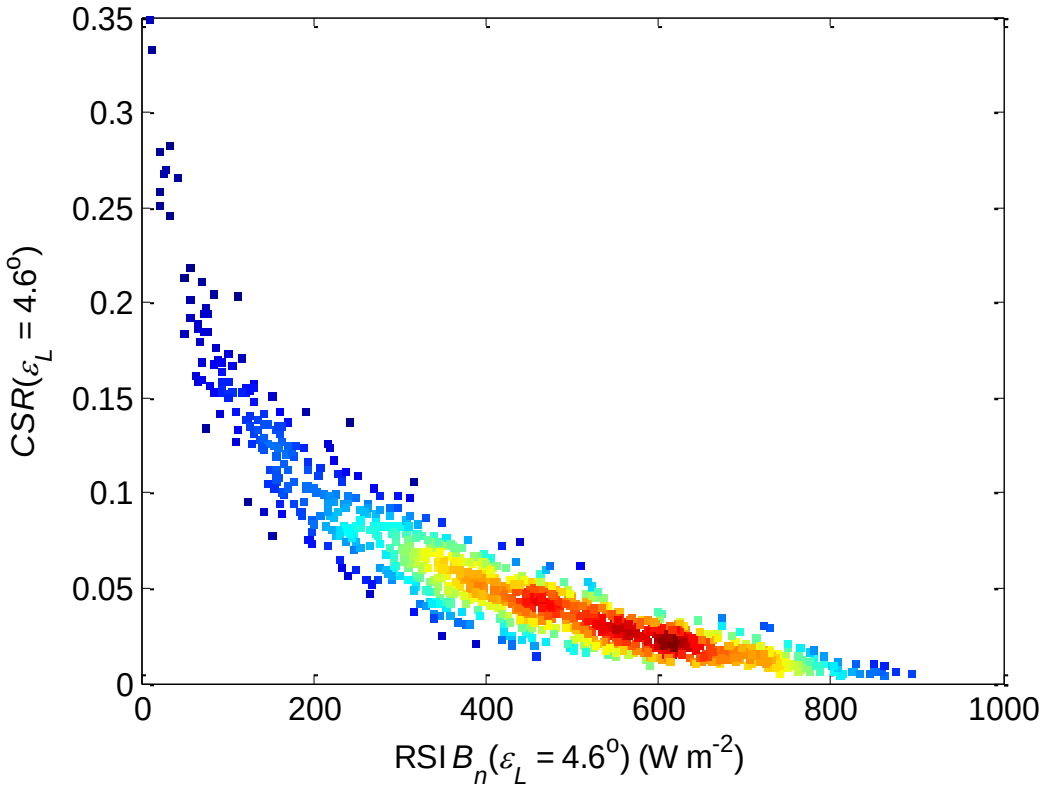


Fig. 6.14: The CSR modelled by libRadtran for a limit angle of 4.6° ($CSR(\varepsilon_L = 4.6°)$) versus the measurements from the RSI instrument (RSI $B_n(\varepsilon_L = 4.6°)$).

One way to develop the model CSR as a function of DNI, may be based on the samples shown in Fig. 6.14. This could be done by dividing the CSR values into three DNI intervals and then fitting a separate function for each interval. The intervals may correspond to the operational DNI of the CSTE systems. The threshold DNI for the CSTE system startup is ~ 300 W m^{-2} (Romero-Alvarez and Zarza, 2007; Zhang *et al.*, 2010), while the maximum threshold is ~ 800 W m^{-2} after which the system may start to defocus the DNI (Wittmann *et al.*, 2009). Therefore, the three intervals could be: DNI < 300 W m^{-2}; 300 W m^{-2} ≤ DNI ≤ 800 W m^{-2}; and DNI > 800 W m^{-2}. The drawback of this technique is that except the DNI, no other information is given on the state of the atmosphere. In the operational DNI range it would be unknown how much the atmospheric composition is affecting the DNI. For example, it would be unknown whether moderate DNI values are due to the larger air mass the Sun rays travel through in a Rayleigh atmosphere or to a turbid atmosphere where the Sun rays travel through a smaller air mass.

Another approach to model the CSR could be by fitting the CSR as a function of any of the variables describing the state of the atmosphere, which are computed from the ground measured irradiances (*cf.* Sect. 3.4). By visually observing the scatter density plots of the CSR versus the clearness index, the direct normal clearness index, the diffuse fraction, the corrected clearness index, and the sky clearness

index; the CSR could be fitted as a function of the sky clearness index. The scatter density plot of the CSR versus sky clearness index is shown in Fig. 6.15.

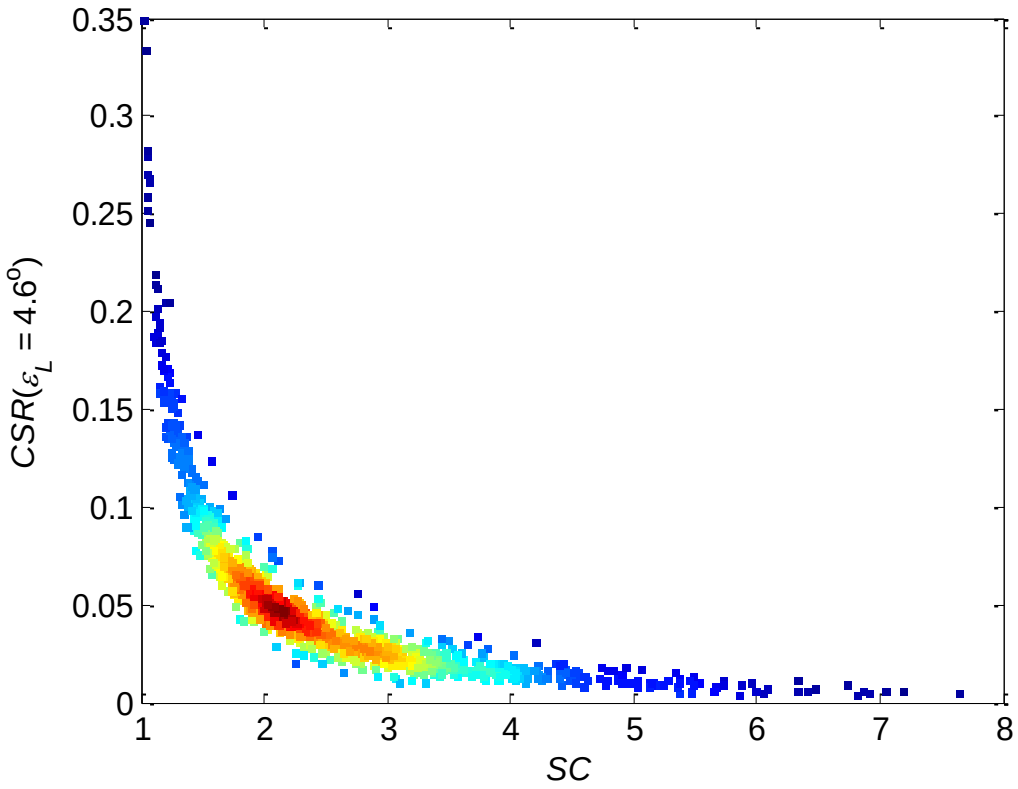


Fig. 6.15: The CSR modelled by libRadtran for a limit angle of 4.6° ($CSR(\varepsilon_L = 4.6°)$) versus the sky clearness index (SC).

As shown in Fig. 6.15 and pointed out by Perez *et al.* (1993) the smallest sky clearness indices SC represent the turbid skies and the largest ones represent the very clear skies, corresponding respectively to high and low CSR values. Instead of fitting only one function for all the range of SC, a more accurate model may be devised by splitting this range into three intervals and fitting a function on each interval. The three intervals were selected by taking the mean of SC in the minimum and maximum DNI thresholds ± 10% of the CSTE systems. The three intervals of SC are: $SC < 1.74$, $1.74 \leq SC \leq 5.09$, and $SC > 5.09$. A power function best fits the first two intervals, while a simple LS affine function is sufficient for the third interval. No constraint was imposed on the continuity of the three functions.

The three functions are:

$$CSR(\varepsilon_L) = o_1 SC^{\rho_1} + \nu_1 \quad \text{for } SC < 1.74 \tag{6.7}$$

$$CSR(\varepsilon_L) = o_2 SC^{\rho_2} \quad \text{for } 1.74 \leq SC \leq 5.09 \tag{6.8}$$

$$CSR(\varepsilon_L) = o_3 SC + \nu_3 \quad \text{for } SC > 5.09 \tag{6.9}$$

where the coefficients are listed in Table 6.4.

Table 6.4: The coefficients of Eqs. (6.7) to (6.9), their 95% confidence intervals (CI) and the MAE for each sky clearness index interval.

Interval	o_i	ρ_i	v_i	**MAE for CSR**
	95% CI	95% CI	95% CI	
$SC < 1.74$	0.2753	−4.902	0.05343	0.010
$i = 1$	[0.2659, 0.2847]	[−5.353, −4.452]	[0.04675, 0.06011]	
$1.74 \leq SC \leq 5.09$	0.1779	−1.788	N/A	0.005
$i = 2$	[0.1700, 0.1859]	[−1.845, −1.732]		
$SC > 5.09$	−0.00200	N/A	0.01954	0.002
$i = 3$	[−0.00312, −0.00088]		[0.01294, 0.02614]	

Due to the low number of observations, the validation of each function is based on the leave-one-out cross validation. For each of the three intervals and repeating for the number of samples in each interval, one sample is left out and the function is fitted with the remaining samples. The error in this case is the absolute error, which is monitored for each independent sample in terms of the CSR. The final reported error is the mean of all the independent sample absolute errors, *i.e.* the mean absolute error (MAE).

In Fig. 6.16 CSR is plotted as a function of *SC*, along with the fitted functions, the 95% prediction bounds of the functions and the 95% prediction bounds of the observations for the three intervals. The 95% prediction bounds of the fitted function means that under the same conditions if the sampling is repeated many times there is a confidence of 95% that the fitted function would lie within these bounds. The prediction bounds on the fitted functions are very narrow, which signals an accurate fit for the given samples, implying a good estimate of the CSR.

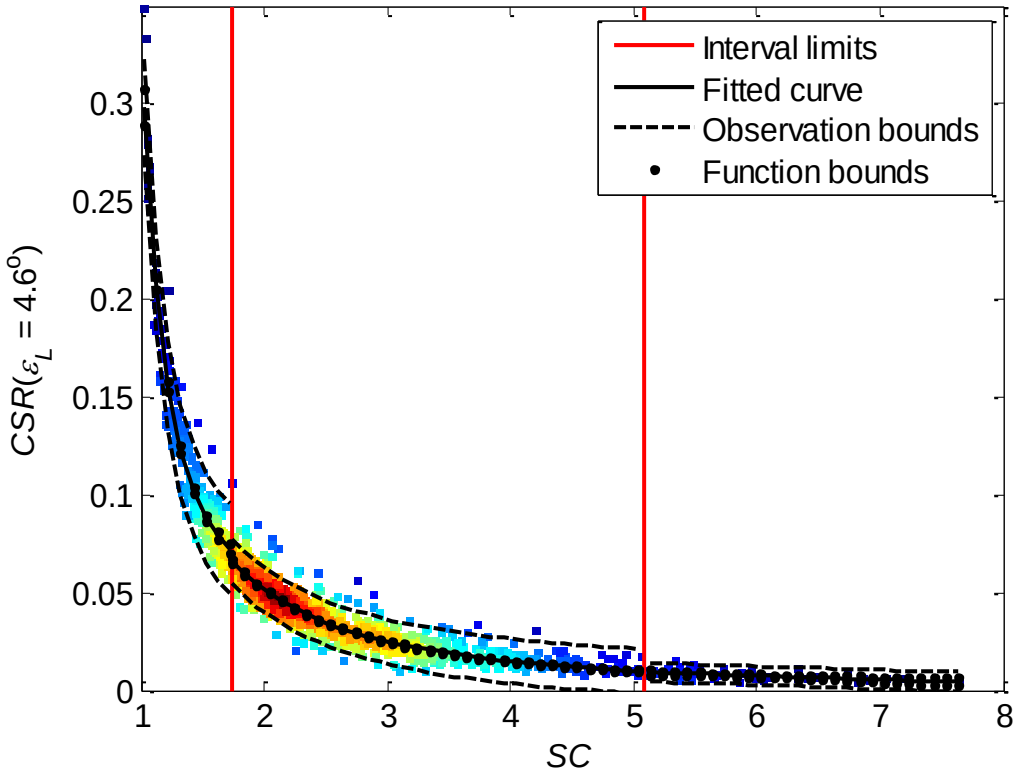


Fig. 6.16: The CSR modelled by libRadtran for a limit angle of 4.6° ($CSR(\varepsilon_L = 4.6°)$) versus the sky clearness index (SC). Also shown are the interval limits, the fitted curve for each interval, the 95% prediction bounds on the functions and on the observations.

Table 6.4 lists the 95% confidence interval of each coefficient and the MAE for each SC interval. The MAE for each interval is very low. The interval with the maximum MAE (0.01) is the first one, which corresponds to the turbid skies with the highest CSR values. The errors are significantly lower for the second (MAE of 0.005) and third (MAE of 0.002) intervals. The 95% confidence intervals of the coefficients are narrow for the first two intervals, not so much for the third interval due to the lower number of observations.

To validate this model, the sky clearness indices SC are derived from DHI and DNI observations from the RSI instrument. The CSR is computed using Eqs. (6.7) to (6.9), and is then compared to the libRadtran CSR. The scatter density plot of this validation is shown in Fig. 6.17. Most observations lie around the 1:1 line and the scatter around this line is very low. The statistical indicators exhibit very low errors. The relative RMSE is 16% and the relative bias is −1%. R^2 is 0.964 and the slope of the robust affine regression is very close to 1. The results are very good over this study area.

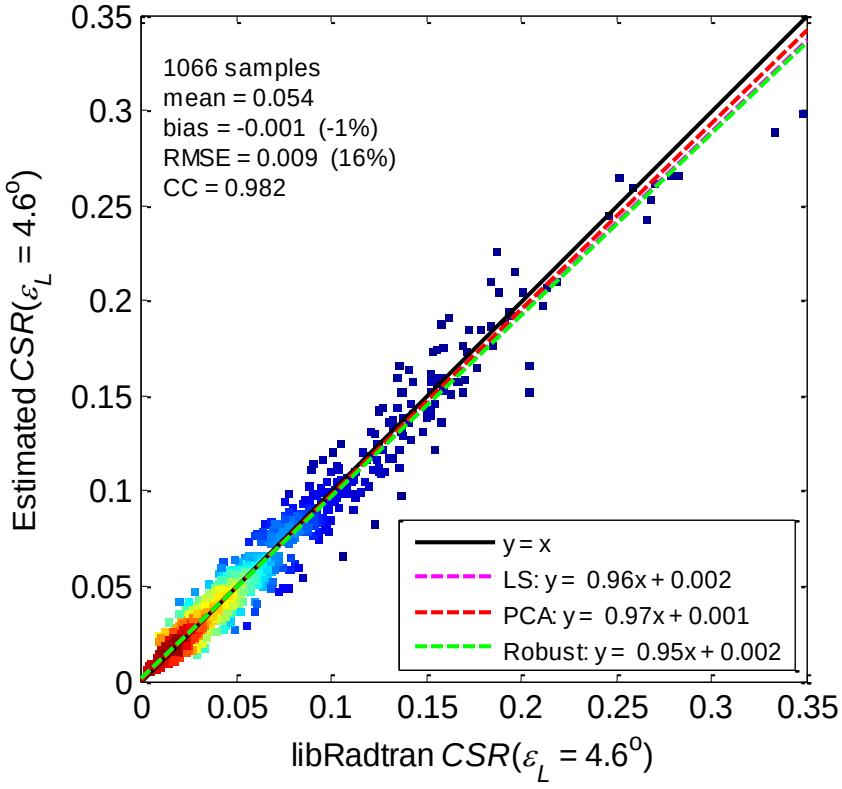


Fig. 6.17: Scatter density plot of the estimated CSR for a limit angle of 4.6° (estimated $CSR(\varepsilon_L = 4.6°)$) versus the reference values modelled by libRadtran (libRadtran $CSR(\varepsilon_L = 4.6°)$).

With the estimated CSR and the ground measured DNI at hand, the estimated CSNI is their product. The difference between the ground measured DNI and the estimated CSNI should yield the estimated DNI_S. Using this approach the scatter density plot between the estimated CSNI and the libRadtran modelled CSNI is shown in Fig. 6.18. The relative RMSE is 18%, the relative bias is −5% and R^2 is 0.726. These results are good, when compared to other models. Using the McClear model to estimate the DNI under cloud-free skies, Eissa *et al.* (2015) report a relative bias ranging from −8% to +1% for seven sites in the UAE, and a relative RMSE ranging from 9% to 13%. Gueymard (2012) reports the validation results of 18 models to estimate the DNI under cloud-free skies at the Solar Village site in Saudi Arabia are presented; the relative bias ranges from −30% to +31% and the relative RMSE from 2% to 33%.

The scatter density plot of the estimated DNI_S versus the libRadtran modelled DNI_S is shown in Fig. 6.19. The relative RMSE is 7%, the relative bias is −5%, R^2 is 0.994, and the slope of the robust affine regression is very close to 1. This bias has been previously observed, and it is suspected that it may be due to miscalibrations of the RSI instrument, with the largest DNI values being underestimated by the RSI instrument.

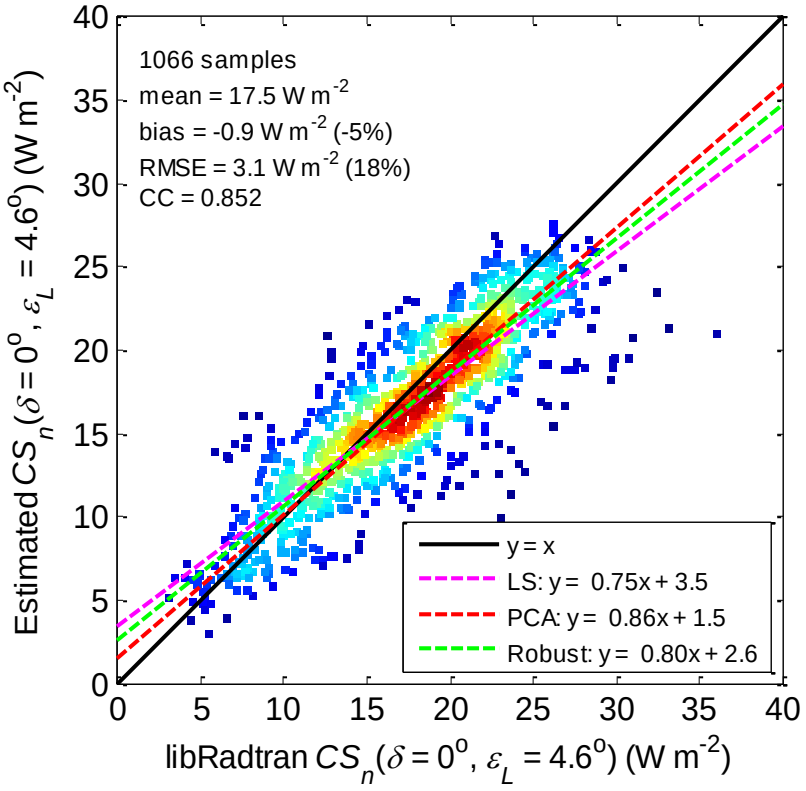


Fig. 6.18: Scatter density plot of the estimated CSNI for a limit angle of 4.6° (estimated $CS_n(\delta = 0°, \varepsilon_L = 4.6°)$) versus the reference values modelled by libRadtran (libRadtran $CS_n(\delta = 0°, \varepsilon_L = 4.6°)$).

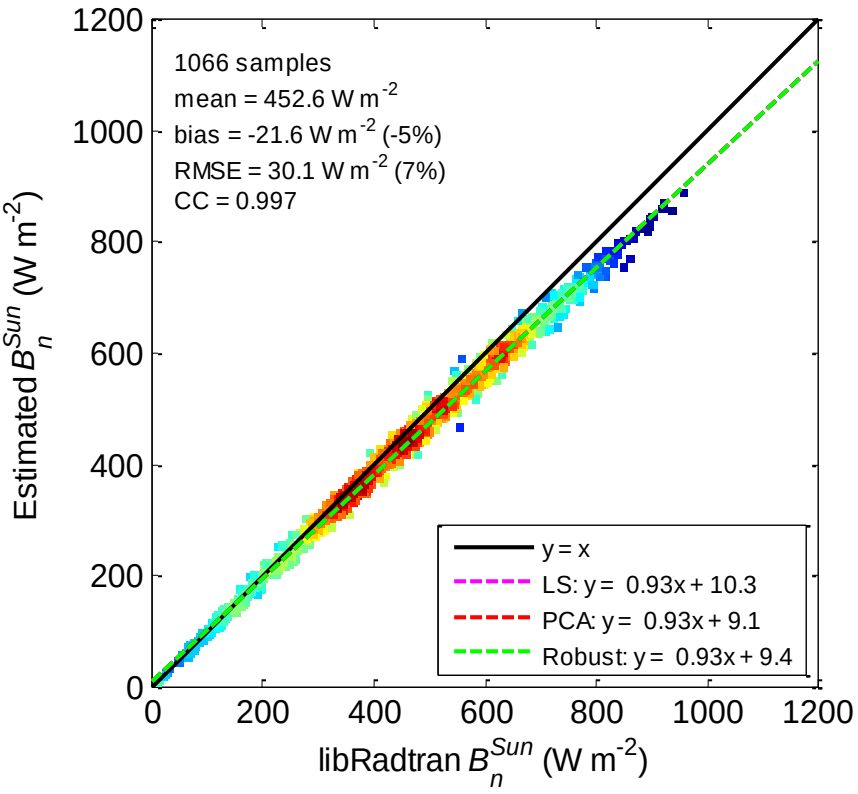


Fig. 6.19: Scatter density plot of the estimated DNI_S (estimated B_n^{Sun}) versus the reference values modelled by libRadtran (libRadtran B_n^{Sun}).

Up to now the proposed model is only valid for the viewing half-angles of the RSI instrument. The aperture half-angles of the common CST systems are generally smaller than those of the RSI instrument. Therefore, the coefficients of Eqs. (6.7) to (6.9) could be fitted to provide the CSR at different aperture half-angles, with *SC* still being computed from the RSI DHI and DNI values. By varying aperture half-angles from 0.4° to 5° in steps of 0.2°, a similar procedure is followed where the libRadtran modelled CSR for each aperture half-angle is fitted as a function of *SC* in each of the three intervals. In this way one can estimate the CSR for any defined aperture half-angle in the interval [0.4°, 5°]. The CSNI for the defined aperture half-angle α in the interval [0.4°, 5°] is:

$$CS_n(\delta = 0°, \alpha) = \frac{CSR(\alpha) B_n^{Sun}}{1 - CSR(\alpha)} \tag{6.10}$$

where the DNI_S is:

$$B_n^{Sun} = B_n^{RSI} - CS_n(\delta = 0°, \varepsilon_L = 4.6°) \approx B_n^{RSI} - CS_n(\delta = 0°, \alpha = 2.86°) \tag{6.11}$$

where B_n^{RSI} is the RSI DNI.

The validation of this model is also performed using the leave-one-out cross validation. The MAE of the CSR for the three *SC* intervals for the different aperture half-angles α is shown in Fig. 6.20. The MAE is low for all cases. The maximum value is 0.015, which occurs in the first interval of *SC*, *i.e.* turbid skies, and when the aperture half-angle is 5°.

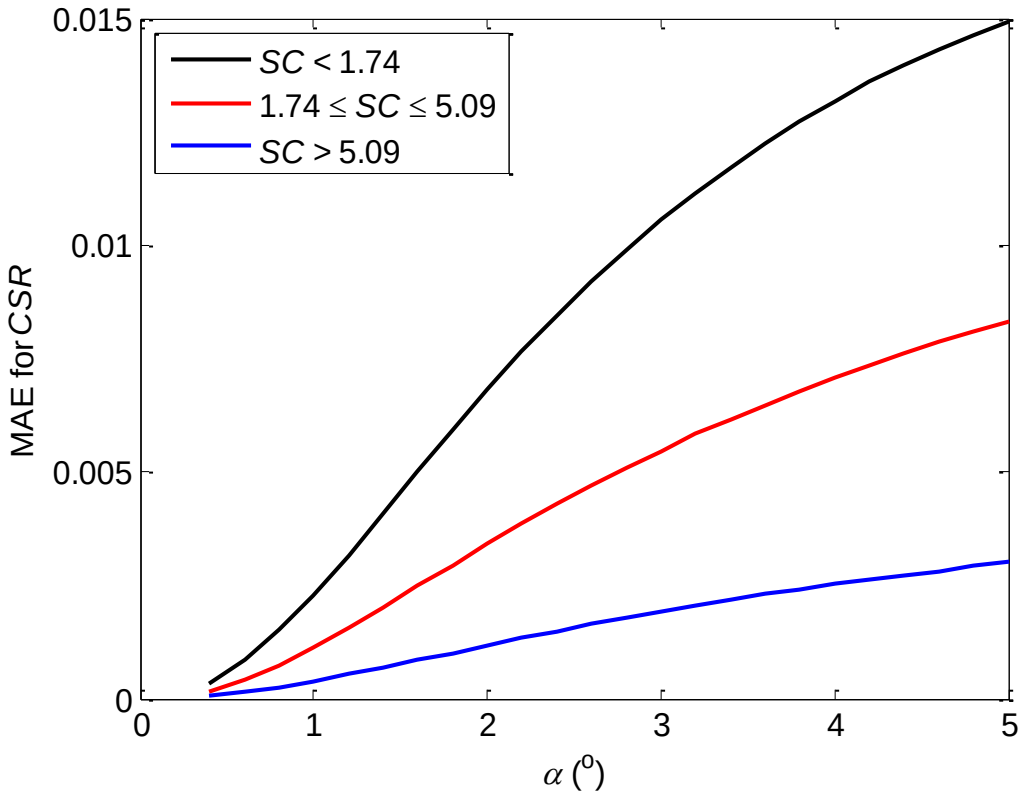


Fig. 6.20: The MAE of the CSR for the different aperture half-angles (α).

The Fig. 6.21 exhibits the coefficients of Eqs. (6.7) to (6.9) plotted as a function of the aperture half-angles. The curves are smooth and can be accurately fitted by 6th order polynomials, also displayed. The 6th degree polynomial fits for each of the coefficients of Eqs. (6.7) to (6.9) are presented in Eqs. (6.12) to (6.18).

$$o_1 = -4.254\,\mathrm{e}^{-6}\,\alpha^6 - 1.987\,\mathrm{e}^{-4}\,\alpha^5 + 4.505\,\mathrm{e}^{-3}\,\alpha^4 - 3.407\,\mathrm{e}^{-2}\,\alpha^3 + 1.095\,\mathrm{e}^{-1}\,\alpha^2 - 2.944\,\mathrm{e}^{-2}\,\alpha + 4.390\,\mathrm{e}^{-3} \quad (6.12)$$

$$\rho_1 = 8.047\,\mathrm{e}^{-5}\,\alpha^6 - 1.076\,\mathrm{e}^{-3}\,\alpha^5 + 1.050\,\mathrm{e}^{-2}\,\alpha^4 - 8.125\,\mathrm{e}^{-2}\,\alpha^3 + 3.040\,\mathrm{e}^{-1}\,\alpha^2 - 7.735\,\mathrm{e}^{-2}\,\alpha - 5.758 \quad (6.13)$$

$$\nu_1 = -8.853\,\mathrm{e}^{-6}\,\alpha^6 + 9.154\,\mathrm{e}^{-5}\,\alpha^5 + 1.462\,\mathrm{e}^{-5}\,\alpha^4 - 3.663\,\mathrm{e}^{-3}\,\alpha^3 + 1.676\,\mathrm{e}^{-2}\,\alpha^2 - 3.563\,\mathrm{e}^{-3}\,\alpha + 4.440\,\mathrm{e}^{-4} \quad (6.14)$$

$$o_2 = -1.393\,\mathrm{e}^{-5}\,\alpha^6 + 1.850\,\mathrm{e}^{-4}\,\alpha^5 - 3.037\,\mathrm{e}^{-4}\,\alpha^4 - 7.126\,\mathrm{e}^{-3}\,\alpha^3 + 4.483\,\mathrm{e}^{-2}\,\alpha^2 - 8.604\,\mathrm{e}^{-3}\,\alpha + 9.833\,\mathrm{e}^{-4} \quad (6.15)$$

$$\rho_2 = -1.897\,\mathrm{e}^{-5}\,\alpha^6 + 4.410\,\mathrm{e}^{-4}\,\alpha^5 - 4.043\,\mathrm{e}^{-3}\,\alpha^4 + 1.785\,\mathrm{e}^{-2}\,\alpha^3 - 3.254\,\mathrm{e}^{-2}\,\alpha^2 + 2.900\,\mathrm{e}^{-3}\,\alpha - 1.742 \quad (6.16)$$

$$o_3 = -4.935\,\mathrm{e}^{-7}\,\alpha^6 + 8.189\,\mathrm{e}^{-6}\,\alpha^5 - 5.965\,\mathrm{e}^{-5}\,\alpha^4 + 2.669\,\mathrm{e}^{-4}\,\alpha^3 - 7.698\,\mathrm{e}^{-4}\,\alpha^2 + 2.406\,\mathrm{e}^{-4}\,\alpha - 4.127\,\mathrm{e}^{-5} \quad (6.17)$$

$$\nu_3 = 3.164\,\mathrm{e}^{-6}\,\alpha^6 - 6.258\,\mathrm{e}^{-5}\,\alpha^5 + 4.881\,\mathrm{e}^{-4}\,\alpha^4 - 2.359\,\mathrm{e}^{-3}\,\alpha^3 + 7.161\,\mathrm{e}^{-3}\,\alpha^2 - 2.062\,\mathrm{e}^{-3}\,\alpha + 3.349\,\mathrm{e}^{-4} \quad (6.18)$$

where the aperture half-angle α is given in deg.

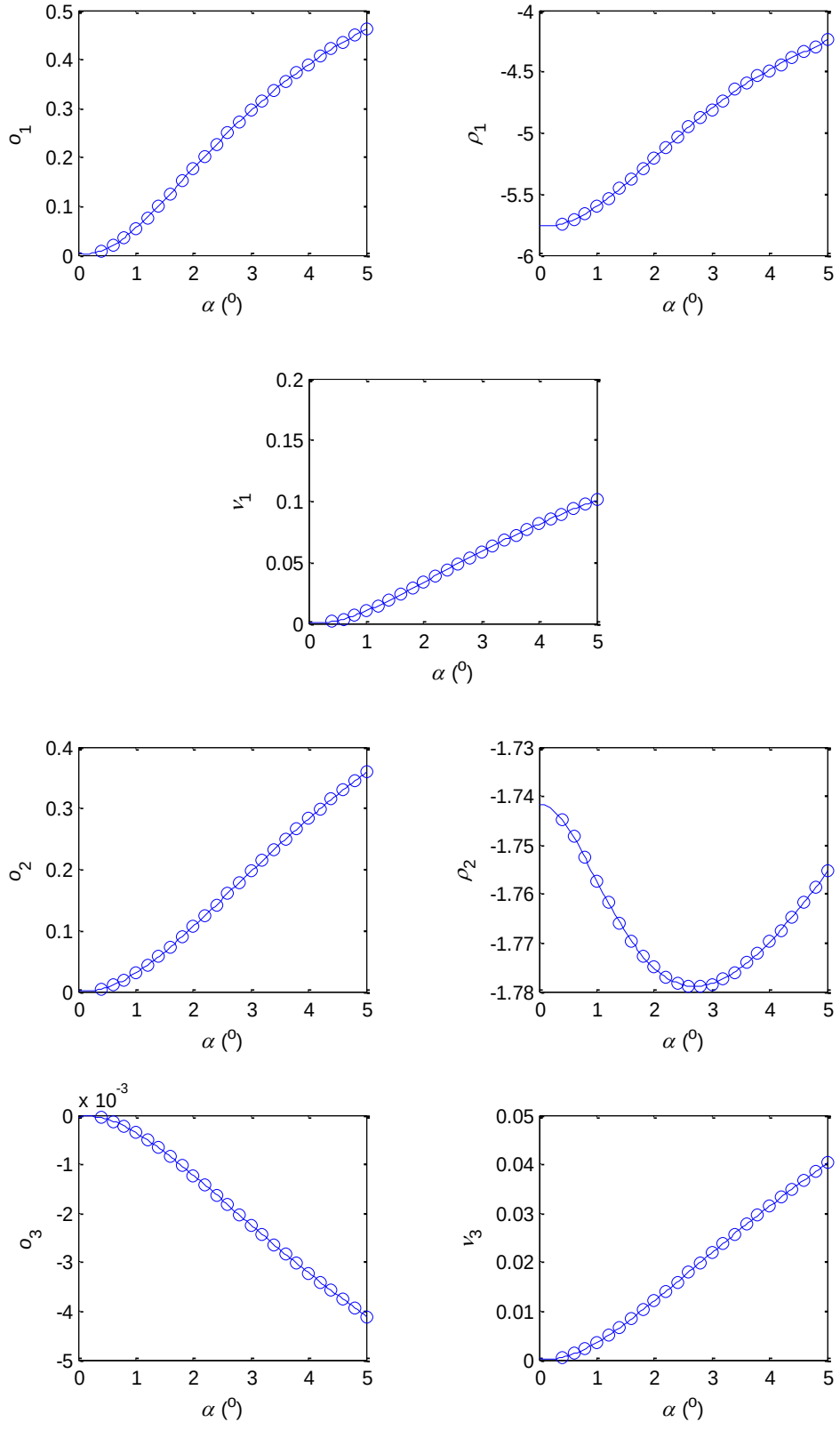


Fig. 6.21: The coefficients of Eqs. (6.7) to (6.9) as a function of the aperture half-angle α (circles) and the 6th order polynomial fit.

Up to now the model has been developed and validated using the data set DS3, which includes the AERONET Inversion products. The model is further validated using observations which were not used in the model development. The data set DS1 comprises the AERONET DSA Level 2.0 $\tau_{a,\lambda}$ values in addition to the RSI measurements, but does not contain the $P_{a,\lambda}$ or $\omega_{a,\lambda}$ values. DS1 is also of interest because it comprises observations at low values of θ_S, which are not present in DS3.

For this validation the CSR is computed using Eqs. (6.7) to (6.9) and (6.12) to (6.18), where *SC* values are computed from the RSI DHI and DNI. The estimated CSNI is computed as the product of the estimated CSR and RSI DNI. The estimated DNI_S is then computed as the difference of the RSI DNI and the estimated CSNI. The performance of the model is assessed based on its ability to estimate the DNI_S, which is validated with respect to the libRadtran modelled DNI_S for the data set DS1.

The scatter density plot of the estimated DNI_S for the data set DS1 versus the libRadtran modelled DNI_S is shown in Fig. 6.22. The relative RMSE is 8%, the relative bias is −5% and R^2 is 0.976. The statistical indicators are very similar to those presented in Fig. 6.19, and the relative bias is the same. This similarity in results demonstrates the ability of the model to estimate the circumsolar radiation for samples other than that used for development. There are some outliers present in Fig. 6.22, where the estimated DNI_S is underestimated with respect the libRadtran DNI_S. These outliers may be due to the presence of scattered clouds, *i.e.* cloud-free instances during the AERONET acquisition but mostly cloudy during the RSI measurements (which are 10 min averages and interpolated to match the AERONET acquisition time).

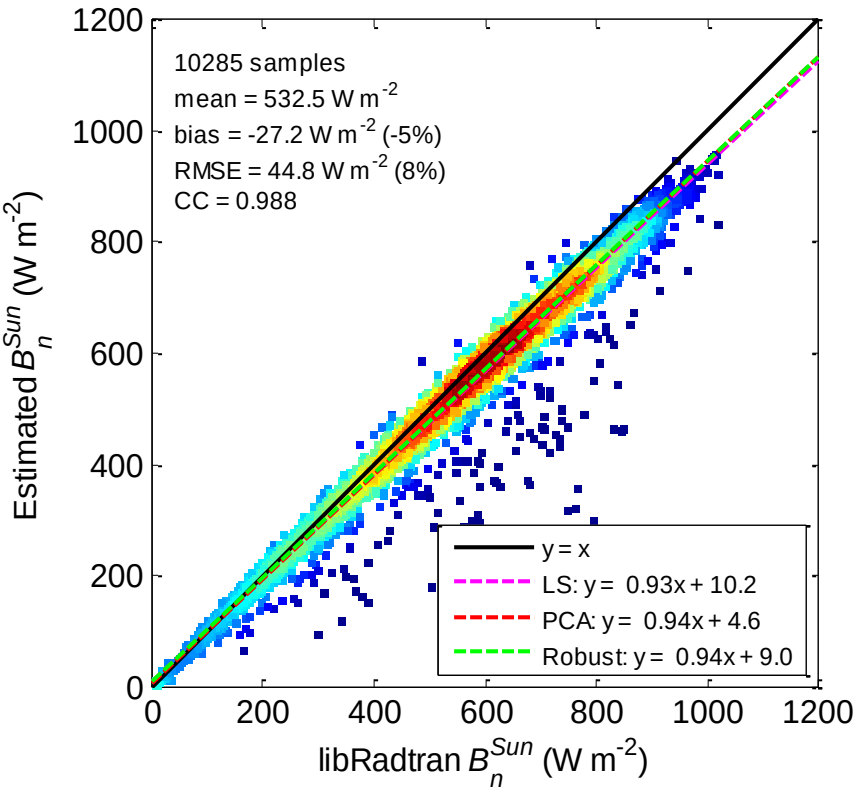


Fig. 6.22: Scatter density plot of the estimated DNI_S (estimated B_n^{Sun}) versus the reference values modelled by libRadtran (libRadtran B_n^{Sun}), for validating the model in time using data set DS1.

The proposed model herein could be applied in a fast manner to estimate the broadband DNI_S and the CSNI incident for any aperture half-angle in the interval [0.4°, 5°] given standard DNI and DHI RSI measurements. The model has been validated using the leave-one-out cross validation and in time using measurements which were not used in its development having a larger interval of θ_S. The two different validation results of the model show similar errors, implying that the model is not overfitted for the data set used for development. This model can be used for the assessment of resource for CST systems for a quick and accurate estimate of the beam and circumsolar radiation for different aperture half-angles. The applicability of the model over a location other than that for which it was developed is studied in Chapter 7.

6.5. Discussion

The results presented in this section have revealed a number of observations to keep in mind when modelling the beam and circumsolar radiation. Firstly, over the studied area and in cloud-free conditions in a desert environment, the circumsolar radiation is non-negligible: 50% of the observations have a CSR greater than 0.04 (*cf.* Fig. 6.13). Therefore, the CSNI component in the standard DNI

measurements should be accounted for, especially by CST systems which normally exhibit an aperture half-angle smaller than that of the DNI measurement sensors.

Another important observation is that when modelling the CSNI the representation of the aerosol PFCN can make very significant differences in the results. Therefore, it is proposed to use the TTHG PFCN representation of the aerosol PFCN when modelling the CSNI with RTMs. It has the advantage of being described by only three parameters, and using the TTHG PFCN significantly improves the results of the CSNI modelling by libRadtran when compared to the HG PFCN, the OPAC PFCN for a desert type aerosol, or the 'DESERT_MAX' PFCN from the SMARTS RTM.

Correcting the AERONET AOD is also crucial, since the aperture half-angle of the AERONET Sun photometer is quite larger than the angular radius of the Sun. The proposed correction yields very good validations of the monochromatic DNI_S modelled by both libRadtran and SMARTS when compared to the SAM reference values. For modelling the monochromatic DNI_S the corrected AOD at the specified wavelength is the key input. For the broadband DNI_S it is recommended to provide the corrected AOD at several wavelength to avoid interpolation errors by the RTM libRadtran. Unfortunately, this cannot be done in SMARTS, as the AOD can be specified at either 500 nm or 550 nm only. The proposed correction has not been validated for the AODs at different wavelengths than 670 nm. This is a limitation of the proposed method and is an area requiring further research.

The drawbacks of modelling the DNI_S and CSNI by libRadtran are: it is computationally expensive and it requires specific aerosol optical properties which are infrequent both temporally and spatially. Therefore, a fast parametric model is proposed to estimate the CSR for any aperture half-angle in the interval [0.4°, 5°]. One still needs ground measurements of the DHI and the DNI to compute the sky clearness index, of which the CSR is a function, but such measurements are much more frequent than the AERONET measurements.

Another approach to model the beam and circumsolar radiation could have been followed. A library of the CSR could have been generated by running libRadtran using the aerosol optical properties available from the AERONET Inversion products. Then the monochromatic AOD observations from the AERONET Inversion products would have been matched, in terms of the Mahalanobis distance, with the AOD observations from the AERONET DSA products. The CSR for the matched observations would have been called from the library, and the DNI_S would have been directly computed from libRadtran using the AERONET DSA AOD after correcting it. Knowing the CSR and the DNI_S the CSNI would have been computed. The drawback of this approach is that it needs the AERONET observations.

To conclude this section, the research question #2 is answered: a fast and accurate model is proposed herein to estimate the beam and circumsolar radiation for aperture angles varying in the interval

[0.4°, 5°] using observables (DNI and DHI measurements) which are more frequently available than the aerosol optical properties.

Chapter 7 - Applicability of the model to another site

The proposed model to estimate the broadband beam and circumsolar radiation, presented in Sect. 6.4, has only been validated over the site for which it was developed, *i.e.* Abu Dhabi, UAE. The validation of this model for a different site exhibiting desert environmental conditions, will indicate as to whether the model is applicable to other sites. The objective of this section is to answer the third research question, as to whether the developed model is applicable over other desert areas under cloud-free conditions or not.

The site of Tamanrasset in Algeria is appropriate for this work. Tamanrasset is a remote city located in the desert southern Algeria. The ground measurements collected at this site are very relevant in the context of this work. The solar radiation station in this site is a Baseline Surface Radiation Network (BSRN) station, implying very high quality data. It coexists with an AERONET station at the site.

Due to the high quality ground measurements of Tamanrasset not only can the parametric model developed over Abu Dhabi be validated, but also the coefficients of the parametric model could be fitted over the site of Tamanrasset. This is valuable because the DNI measurements in Tamanrasset were collected by a pyrheliometer, which has well-defined viewing half-angles as opposed to the RSI.

This section is organized as follows:

- an overview of the study area and the available ground measurements (Sect. 7.1),
- validation of the model developed in Abu Dhabi over Tamanrasset (Sect. 7.2),
- refitting the coefficients of the model over Tamanrasset (Sect. 7.3),
- validation of the model developed in Tamanrasset over Abu Dhabi (Sect. 7.4),
- finally, a discussion (Sect. 7.5).

7.1. The study area and ground measurements

The site of Tamanrasset, Algeria, shown in Fig. 7.1, is located at 22.7903°N and 5.5292°E and has an altitude above mean sea level of 1385 m. In this work the solar irradiance ground measurements from the BSRN station of Tamanrasset for the time period September 2006 to February 2009 were used (Mimouni, 2007). This time period was selected due to the overlap in time with the AERONET Level 2.0 products.

The goal of the BSRN network is to provide long-term high quality measurements of the downwelling surface solar radiation which is frequently sampled (McArthur, 2005; Ohmura *et al.*, 1998). The GHI, DNI and DHI measurements in Tamanrasset are available at a 1 min temporal step. The GHI is measured by an Eppley Precision Spectral Pyranometer, which is a thermopile sensitive in the

wavelength interval [0.285 μm, 2.8 μm]. The DHI is measured by a shaded Eppley Precision Spectral Pyranometer. The DNI is measured by an Eppley Normal Incidence Pyrheliometer (NIP), which has an aperture half-angle of 2.9°, a slope angle of 1.8° and a limit angle of 4° (*cf.* Table 3.1). The uncertainty targets of the BSRN measurements are 2 W m^{-2} for the DNI and 5 W m^{-2} for both the GHI and DHI (McArthur, 2005). Only the irradiance measurements which pass the quality checks presented in Roesch *et al.* (2011a) are used in this study.

The Level 2.0 products of the AERONET station in Tamanrasset are of interest because they are cloud-screened (in the direction of the Sun) and quality assured. From the AERONET Level 2.0 DSA product the total column content in water vapor is available along with the AOD $\tau_{a,\lambda}$ at: 1020 nm, 870 nm, 675 nm, 440 nm, and 380 nm. Available from the Version 2 Inversion products are the aerosol PFCN $P_{a,\lambda}$, aerosol SSA $\omega_{a,\lambda}$ and $\tau_{a,\lambda}$ at: 1020 nm, 870 nm, 675 nm, and 440 nm.

The observations from the AERONET products were matched to the closest solar irradiance measurements in time, such that the difference in the time stamps had to be less than 5 min. Table 7.1 lists the data sets of Tamanrasset used for the remainder of this section.

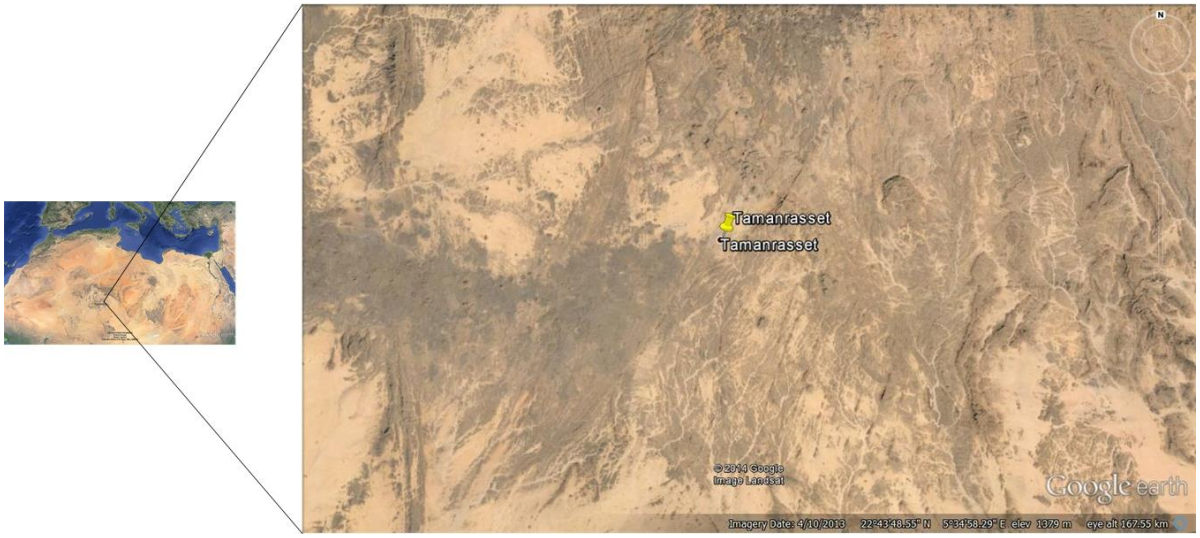


Fig. 7.1: A zoom in on Tamanrasset, Algeria, and its surrounding environment (image from Google Earth).

Table 7.1: The different data sets available over Tamanrasset, Algeria.

Data set	Time period	Samples	Observables
TAM_DS1	Sept, 2006 to Feb. 2009	21778	Eppley PSP: DHI and GHI. Eppley NIP: DNI. AERONET DSA Level 2.0: monochromatic AOD and total column content in water vapor.
TAM_DS2	Sept, 2006 to Feb. 2009	1627	Eppley PSP: DHI and GHI. Eppley NIP: DNI. AERONET Version 2 Inversion products in Level 2.0: monochromatic AOD and total column content in water vapor (from the DSA Level 2.0, averaged ± 16 min of Inversion product retrievals), monochromatic aerosol PFCN, and mean monochromatic SSA (computed from the 186 available samples).

7.2. Validation of the model developed in Abu Dhabi over Tamanrasset

The validation of the model developed in Abu Dhabi is performed over both data sets TAM_DS1 and TAM_DS2.

For the data set TAM_DS1 the validation is performed only in terms of the DNI_S, where the reference DNI_S values are computed by libRadtran (*cf.* Sect. 6.4.1). In this case the CSR for an aperture half-angle of 2.9° is computed by Eqs. (6.7) to (6.9), where the coefficients of the model are computed by Eqs. (6.12) to (6.18). The product of the CSR and ground measured DNI is the CSNI. The estimated DNI_S is then the difference between the measured DNI and the estimated CSNI.

For the data set TAM_DS2 the validation is performed in terms of the CSR, CSNI and DNI_S, where the reference values are from libRadtran. The sky element zenith and azimuth angles for the broadband diffuse radiance computations by libRadtran are defined in steps of 0.1° (*cf.* Sect. 6.4.1). The reference CSNI is computed from the diffuse solar radiance profile by Eq. (3.34), where the limits of integration for the CSNI are defined as [$\delta = 0°$, $\alpha = 2.9°$]. The reference CSR is computed by Eq. (3.37).

7.2.1. Validation of the broadband beam irradiance over Tamanrasset

For data set TAM_DS1, the scatter density plot of the estimated DNI_S versus the reference DNI_S from libRadtran is shown in Fig. 7.2. The scatter along the 1:1 line is very low and the statistical indicators exhibit very low errors. The relative RMSE is 3% and the relative bias is +1%. R^2 is 0.994 and the slope of the robust affine regression is very close to 1. There are a very few outliers for which the DNI_S is underestimated. Such outliers can be attributed to scattered cloudy conditions, where it could have been cloudy during part of the 1 min DNI acquisition but not cloudy during the AERONET acquisition (which are instantaneous measurements).

The constraints set in the development of the McClear model and adapted from the WMO constraints for the radiation measurements, were a bias less than 3 W m^{-2} and 95% of the differences should be less than 20 W m^{-2} when comparing to libRadtran reference values. In this case these constraints are not entirely met, with the bias being 5.1 W m^{-2} and 70% of the samples having an absolute difference less than 20 W m^{-2}. The errors may arise from the AERONET AOD retrievals which have an uncertainty of ± 0.01 for wavelengths greater than 440 nm, while the BSRN DNI measurements have an uncertainty of 2 W m^{-2}. Globally, the results are good and using the model developed in Abu Dhabi over Tamanrasset provides accurate estimates of the DNI_S.

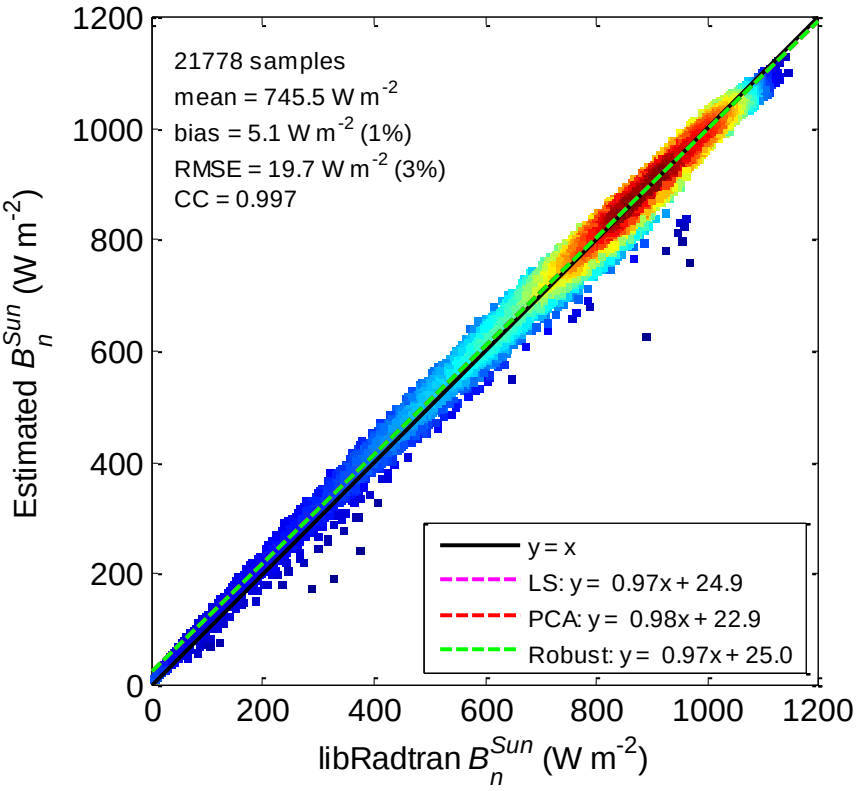


Fig. 7.2: Scatter density plot of the estimated DNI_S (estimated B_n^{Sun}) versus the reference values modelled by libRadtran (libRadtran B_n^{Sun}) using data set TAM_DS1, when using the model developed over Abu Dhabi.

7.2.2. Validation of the circumsolar ratio, and the broadband beam and circumsolar irradiances over Tamanrasset

For data set TAM_DS2, the scatter density plot of the estimated CSR versus the reference CSR computed from libRadtran DNI_S and CSNI is shown in Fig. 7.3. The relative RMSE is 37% and the relative bias is −22%. R^2 is 0.970 and the slope of the robust affine regression is 0.82. The model developed over Abu Dhabi is much less accurate over Tamanrasset for CSR. The difference in the results might be due to the different radiometers available in both sites. In Abu Dhabi the model was developed using sky clearness indices *SC* derived from the RSI DHI and DNI and it is suspected that

there is an underestimation in the RSI DNI values (*cf.* Fig. 6.11). This questions the ability of the model to be applied over other sites which have different ground measurement instruments, such as Tamanrasset. Another reason for the errors may be due to the different characteristics of the two sites. The site of Abu Dhabi experiences more turbid skies than Tamanrasset; this may be observed from the mean reference DNI_S values in Fig. 7.2 (being 745.5 W m^{-2}) and that in Fig. 6.22 (being 532.5 W m^{-2}).

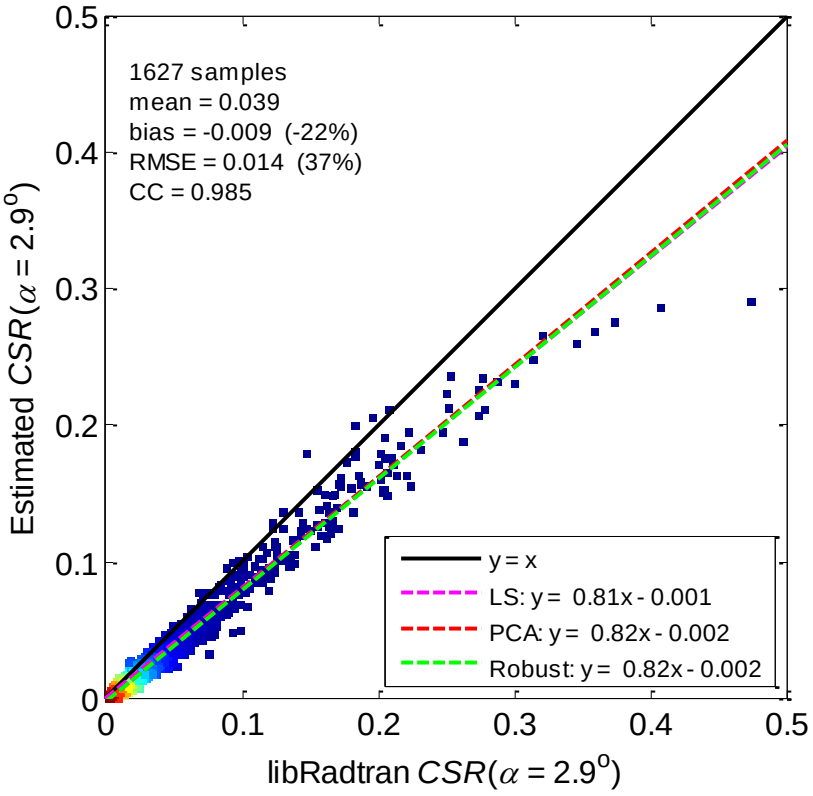


Fig. 7.3: Scatter density plot of the CSR for an aperture half-angle of 2.9° (estimated $CSR(\alpha = 2.9°)$) versus the reference values modelled by libRadtran (libRadtran $CSR(\alpha = 2.9°)$) using data set TAM_DS2, when using the model developed over Abu Dhabi.

The scatter density plot of the estimated CSNI versus the reference libRadtran CSNI is shown in Fig. 7.4. The relative RMSE is 30% and the relative bias is −24%. R^2 is 0.854 and the slope of the robust affine regression is 0.88. The errors can be attributed to the same sources discussed for the validation of the CSR. Another drawback of using the model developed over Abu Dhabi is that there are only a few observations, 42 to be exact for $SC > 5.09$, which correspond to the very clear skies. This poses a challenge when applying the model over different sites exhibiting clearer sky conditions, because the estimated CSR could be less than zero when using the fitted function of this *SC* interval. A CSR less than zero is not possible and any negative estimated CSR is set to zero, while the libRadtran CSNI is not null. Such cases are observed in red in the bottom left of the scatter density plot shown in Fig. 7.4.

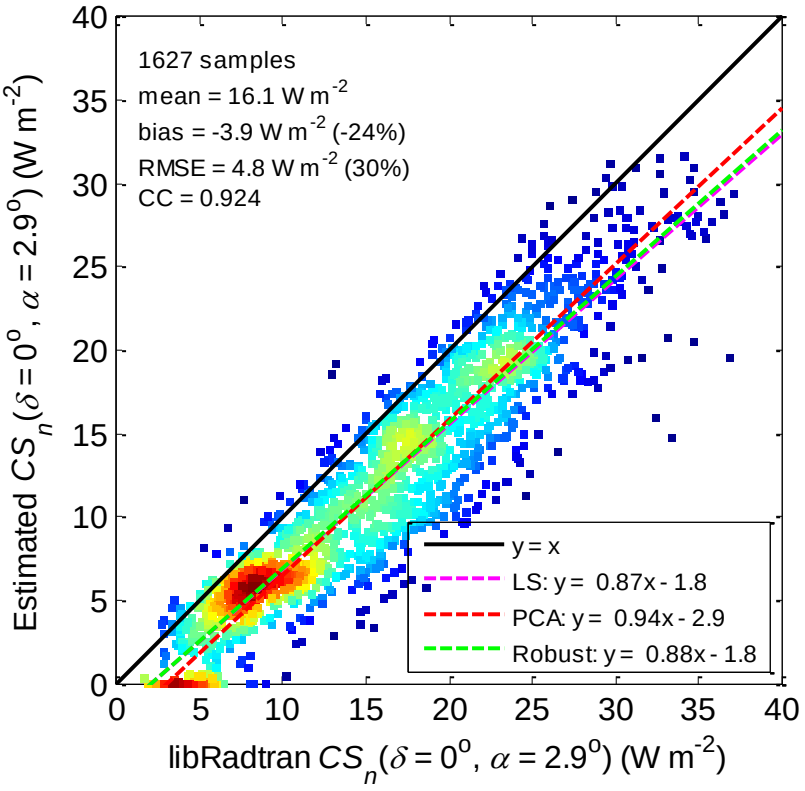


Fig. 7.4: Scatter density plot of the CSNI for an aperture half-angle of 2.9° (estimated $CS_n(\delta = 0°, \alpha = 2.9°)$) versus the reference values modelled by libRadtran (libRadtran $CS_n(\delta = 0°, \alpha = 2.9°)$) using data set TAM_DS2, when using the model developed over Abu Dhabi.

The scatter density plot of the estimated DNI_S versus the reference DNI_S from libRadtran is shown in Fig. 7.5. The scatter along the 1:1 line is very low and the statistical indicators exhibit very low errors. The relative RMSE is 3% and the relative bias is +2%. R^2 is 0.994 and the slope of the robust affine regression is 0.99. The relative errors are very close to those presented in Sect. 7.2.1, and for the estimation of the DNI_S the model developed over Abu Dhabi exhibits accurate results when applied over Tamanrasset.

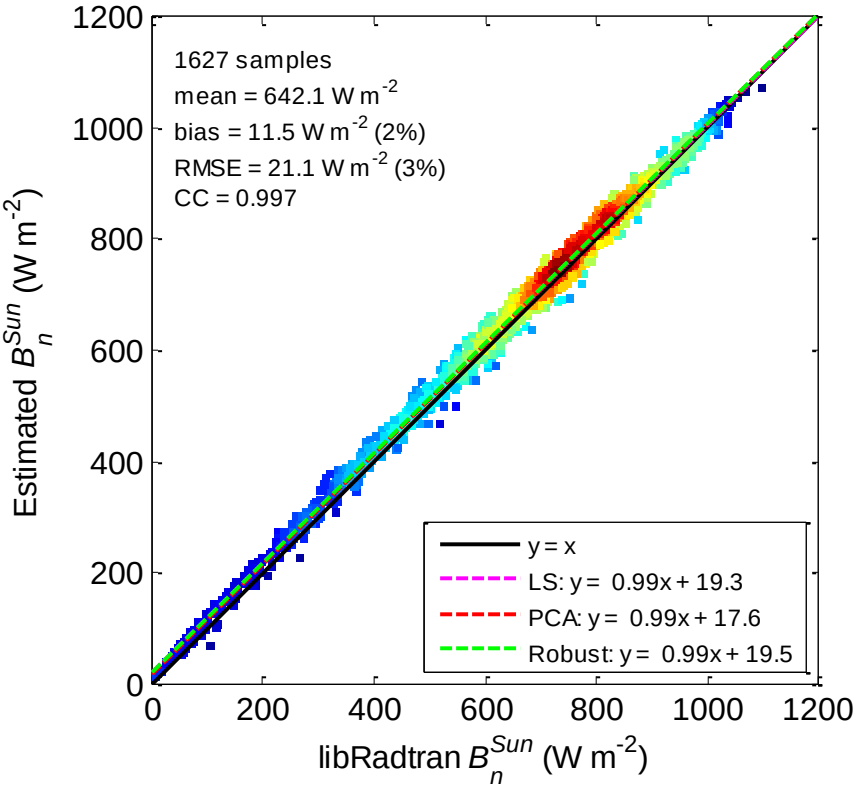


Fig. 7.5: Scatter density plot of the estimated DNI_S (estimated B_n^{Sun}) versus the reference values modelled by libRadtran (libRadtran B_n^{Sun}) using data set TAM_DS2, when using the model developed over Abu Dhabi.

The errors in the validation of the CSR and CSNI are attributed mainly to the different instruments used in each station. To further support this claim, the CSR versus *SC* for both Abu Dhabi (data set DS3) and Tamanrasset (data set TAM_DS2) is plotted in Fig. 7.6. The CSR for each station is computed at a different limit angle, corresponding to the respective limit angle of the instrument at each station. The difference in the aperture half-angle between the RSI and Eppley NIP is less than 0.05°. Therefore, it is expected that the CSR from the two data sets overlap for the same *SC*. This is not the case as shown in Fig. 7.6. The CSR from data set DS3 are shifted to the left when compared to those of data set TAM_DS2. This implies an underestimation in CSR in Tamanrasset when applying the model fitted over Abu Dhabi, as observed in Fig. 7.3.

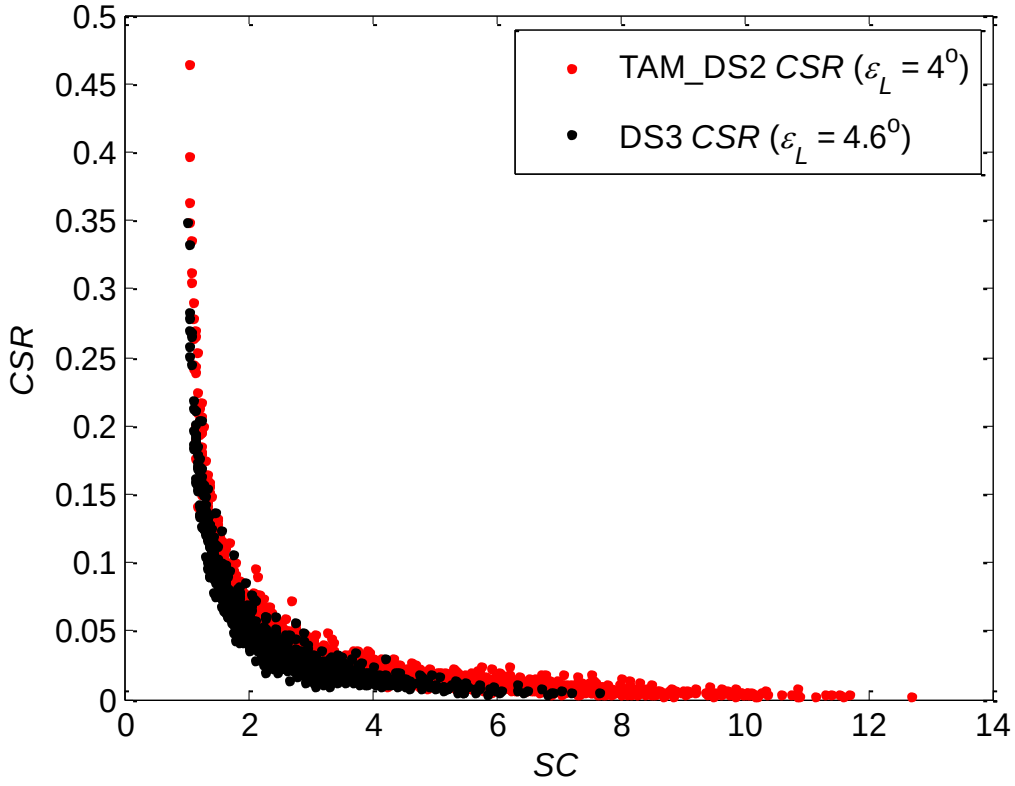


Fig. 7.6: CSR versus the sky clearness index (*SC*) for data set TAM_DS2 and data set DS3.

7.3. Refitting the coefficients of the model over Tamanrasset

The coefficients of the model could be refitted over Tamanrasset using the same methodology presented in Sect. 6.4.3. First the validations of the libRadtran modelled beam and circumsolar irradiances are presented in Sect. 7.3.1 and the model is presented in Sect. 7.3.2.

7.3.1. Validations of the modelled broadband beam and circumsolar irradiances using libRadtran

This section follows the same steps and methods of Sect. 6.4.2. The sky element zenith and azimuth angles were defined in steps of 0.1° for the diffuse radiance computations. The azimuthally averaged diffuse solar radiance profile is computed from the diffuse radiance at the different viewing angles. By accounting for the penumbra function of the Eppley NIP, the broadband CSNI is computed with [δ = 0°, ε_L = 4°].

The validations of the libRadtran modelled CSNI and DNI_S are indirect validations. The modelled DNI_S is validated with respect the Eppley NIP DNI reference measurements, and ideally there should be an underestimation because the Eppley NIP DNI includes the CSNI (from the defined viewing half-angles) while it is not included in the libRadtran modelled DNI_S. The validation of the libRadtran modelled DNI_S + CSNI with respect to the Eppley NIP DNI should ideally exhibit negligible bias.

Using the data set TAM_DS2, the scatter density plot of the libRadtran DNI_S versus the Eppley NIP DNI is shown in Fig. 7.7. The relative RMSE is 5% and the relative bias is −4%. R^2 is 0.994 and the slope of the robust affine regression is very close to 1. Not accounting for the CSNI causes this observed underestimation as expected. It is also evident in Fig. 7.7 that the underestimation is not present for the very high DNI values, due to the very low CSNI under very clear sky conditions. The overestimation of the libRadtran DNI_S for the higher DNI values observed for data set DS3 is not present in Fig. 7.7. This strengthens the claim that there might be a miscalibration in the RSI instrument.

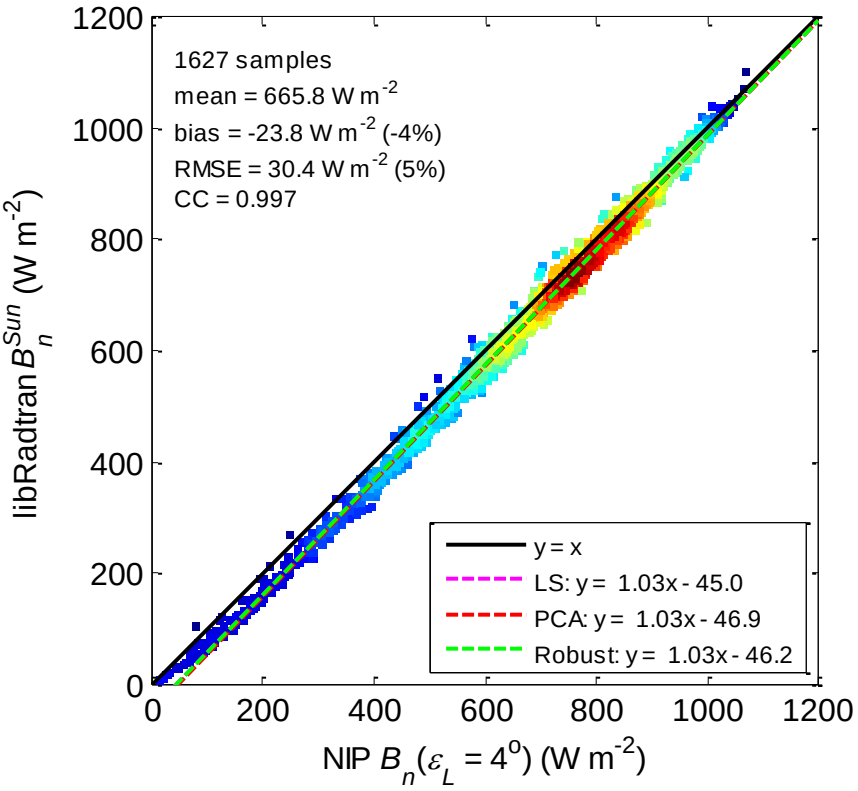


Fig. 7.7: Scatter density plot of the libRadtran broadband DNI_S (libRadtran B_n^{Sun}) versus the reference values from the Eppley NIP (NIP $B_n(\varepsilon_L = 4°)$) using data set TAM_DS2.

The scatter density plot of the libRadtran modelled DNI versus the Eppley NIP DNI is shown in Fig. 7.8. Most samples lie around the 1:1 line and the scatter around the line is very low. The relative RMSE is 3% and the relative bias is −1%. R^2 is 0.994 and the slope of the robust affine regression is 1.01. 69% of the samples have an absolute difference less than 20 W m^{-2}. It is difficult to conclude on whether this very slight underestimation is due to an underestimation in the CSNI or an underestimation in the DNI_S. One source of error can be the misrepresentation of the AERONET $P_{a,\lambda}$ for $\xi < 3°$. The AERONET $P_{a,\lambda}$ is derived from the almucantar radiance measurements which are not collected for $\xi < 3°$. Nonetheless, the results are very good, much better than those of data set DS3 (shown in Fig. 6.12) where the relative RMSE was 7% and the relative bias was +5%. By observing the standard

deviation of the deviations for the results presented in Figs. 7.7 and 7.8, the standard deviation of the deviations decreases by 1.9 W m^{-2} when accounting for the CSNI which implies that the added CSNI is positively contributing to the modelled DNI.

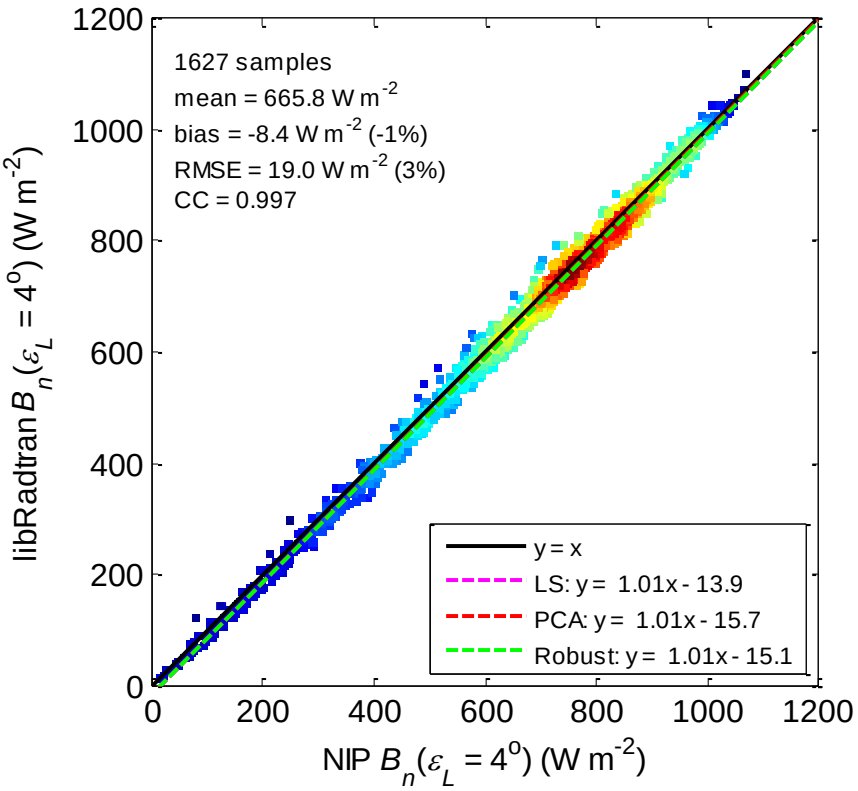


Fig. 7.8: Scatter density plot of the libRadtran broadband DNI for a limit angle of 4° (libRadtran $B_n(\varepsilon_L = 4°)$) versus the reference values from the Eppley NIP (NIP $B_n(\varepsilon_L = 4°)$) using data set TAM_DS2.

The cumulative distribution functions of the CSR for both Abu Dhabi and Tamanrasset are shown in Fig. 7.9. It is apparent that the site of Tamanrasset exhibits more frequently clearer skies than the site of Abu Dhabi. Indeed, only 25% of the observations have a CSR greater than 0.04 in Tamanrasset, whereas 50% of the observations had a CSR greater than 0.04 in Abu Dhabi.

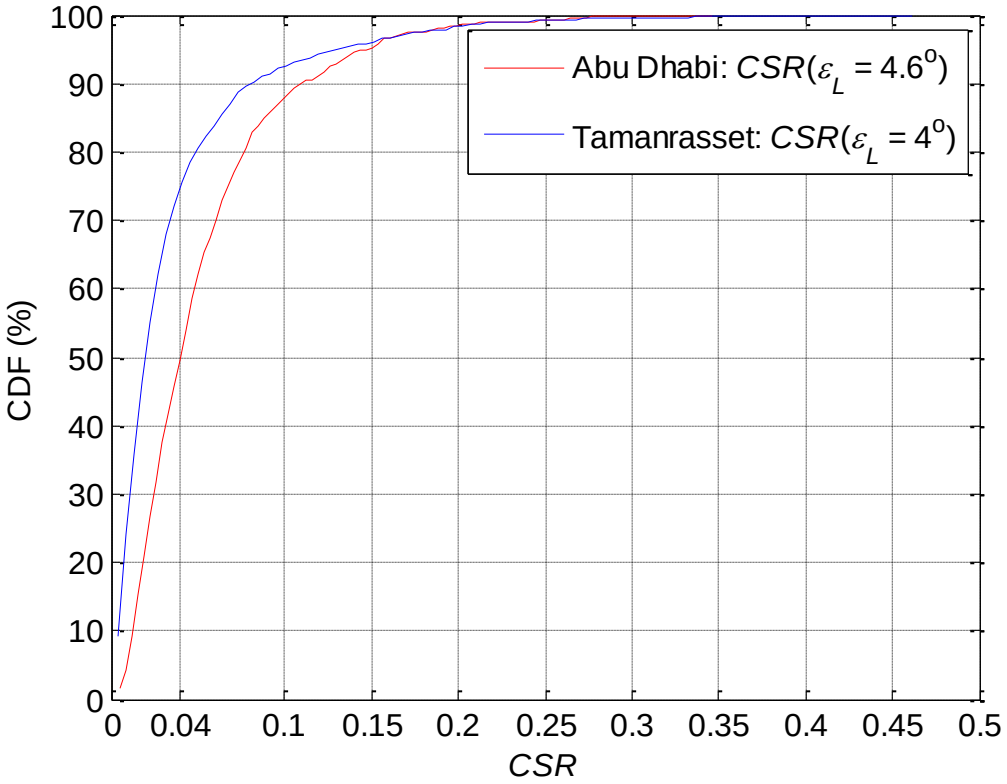


Fig. 7.9: The cumulative distribution function (CDF) of the CSR for a limit angle of 4° ($CSR(\varepsilon_L = 4°)$) in Tamanrasset using data set TAM_DS2 (blue line) and the CSR for a limit angle of 4.6° ($CSR(\varepsilon_L = 4.6°)$) in Abu Dhabi using data set DS3 (red line).

7.3.2. Empirical model to estimate the broadband beam and circumsolar irradiances

The coefficients of the model presented in Sect. 6.4.3 were refitted over the site of Tamanrasset. The three intervals of *SC* and their functions remain the same than those for the model developed over Abu Dhabi. The validations of the three fitted functions are based on the leave-one-out cross validation, where the error is presented in terms of MAE.

In Fig. 7.10 CSR is drawn as a function of *SC*, along with the fitted functions, the 95% prediction bounds of the functions and the 95% prediction bounds of the observations for the three intervals. The 95% prediction bounds on the fitted functions are very narrow, signaling an accurate fit for the given samples. The prediction bounds on the observations are not too wide, implying a good estimate of the CSR for a given *SC*.

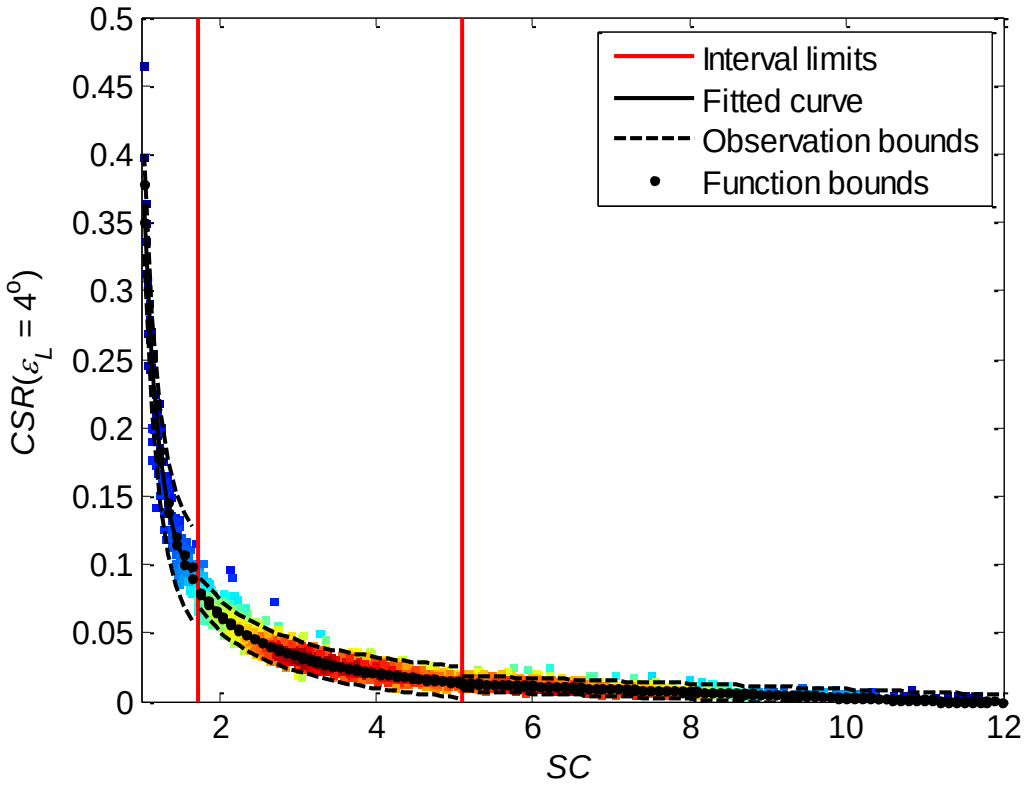


Fig. 7.10: The CSR modelled by libRadtran for a limit angle of 4° ($CSR(\varepsilon_L = 4°)$) versus the sky clearness index (SC) using data set TAM_DS2. Also shown are the interval limits, the fitted curve for each interval, the 95% prediction bounds on the functions and on the observations.

The three functions of the curve shown in Fig. 7.10 take the same form than Eqs. (6.7) to (6.9), and are presented as:

$$CSR(\varepsilon_L) = o_1 SC^{\rho_1} + \nu_1 \qquad \text{for } SC < 1.74 \qquad (7.1)$$

$$CSR(\varepsilon_L) = o_2 SC^{\rho_2} \qquad \text{for } 1.74 \leq SC \leq 5.09 \qquad (7.2)$$

$$CSR(\varepsilon_L) = o_3 SC + \nu_3 \qquad \text{for } SC > 5.09 \qquad (7.3)$$

where the coefficients are listed in Table 7.2. Also listed in Table 7.2 is the 95% confidence interval (CI) of each coefficient and the MAE for each SC interval.

Table 7.2: The coefficients of Eqs. (7.1) to (7.3), their 95% confidence intervals (CI) and the MAE for each sky clearness index interval.

Interval	o_i 95% CI	ρ_i 95% CI	v_i 95% CI	**MAE for CSR**
$SC < 1.74$	0.3654	−5.647	0.07164	0.015
$i = 1$	[0.3466, 0.3841]	[−6.299, −4.996]	[0.06176, 0.08151]	
$1.74 \leq SC \leq 5.09$	0.1924	−1.603	N/A	0.005
$i = 2$	[0.1855, 0.1994]	[−1.642, −1.563]		
$SC > 5.09$	−0.00207	N/A	0.02383	0.002
$i = 3$	[−0.002233, −0.001908]		[0.02266, 0.02499]	

The MAE for the three intervals are very low. The interval with the maximum MAE (0.015) is the first interval, which corresponds to the turbid skies with the highest CSR values. The errors are significantly lower for the second (MAE of 0.005) and third (MAE of 0.002) intervals. The 95% CI of the coefficients are narrow for all intervals. The third interval, in particular, is narrower than the CI of the coefficients presented in Table 6.3 for the same interval. This is due to the larger number of samples exhibiting very clear sky conditions in Tamanrasset. For the first interval only there is a slight overlap in the CIs of the coefficients ρ_1 and v_1 when comparing the fitted coefficients of Tamanrasset and Abu Dhabi. For the second interval there is only a slight overlap of the CI for the coefficient o_2. For the third interval the CIs of the coefficients o_3 and v_3 presented in Table 7.2 overlap with those presented in Table 6.3, but that is only because the coefficients of Table 6.3 have wide CIs due to the low number of observations present in this interval. The difference in the values of the coefficients can be attributed to the different measuring instruments, as shown in Fig. 7.6.

To validate the model over Tamanrasset, the CSR is computed using Eqs. (7.1) to (7.3) and validated against the libRadtran modelled CSR. The scatter density plot of this validation is shown in Fig. 7.11. Most observations lie around the 1:1 line. The relative RMSE is 21% and the relative bias is −1%. R^2 is 0.972 and the slope of the robust affine regression is 0.95. The estimated CSNI is then computed as the product of the estimated CSR and the ground measured DNI. The scatter density plot of the estimated CSNI versus the libRadtran modelled CSNI is shown in Fig. 7.12. The relative RMSE is 19% and the relative bias is +2%. R^2 is 0.846 and the slope of the robust affine regression is 0.95. The validation for the CSNI is good, compared to the DNI estimated by clear-sky models over desert environments (Eissa *et al.*, 2015; Gueymard, 2012). Finally, the estimated DNI_S is computed as the difference between the ground measured DNI and the estimated CSNI. The scatter density plot of the estimated DNI_S versus the libRadtran modelled DNI_S is shown in Fig. 7.13. The scatter around the 1:1 line is very low and 67% of the samples have an absolute difference less than 20 W m^{-2}. The relative

RMSE is 3% and the relative bias is +1%. R^2 is 0.994 and the slope of the robust affine regression is 0.99.

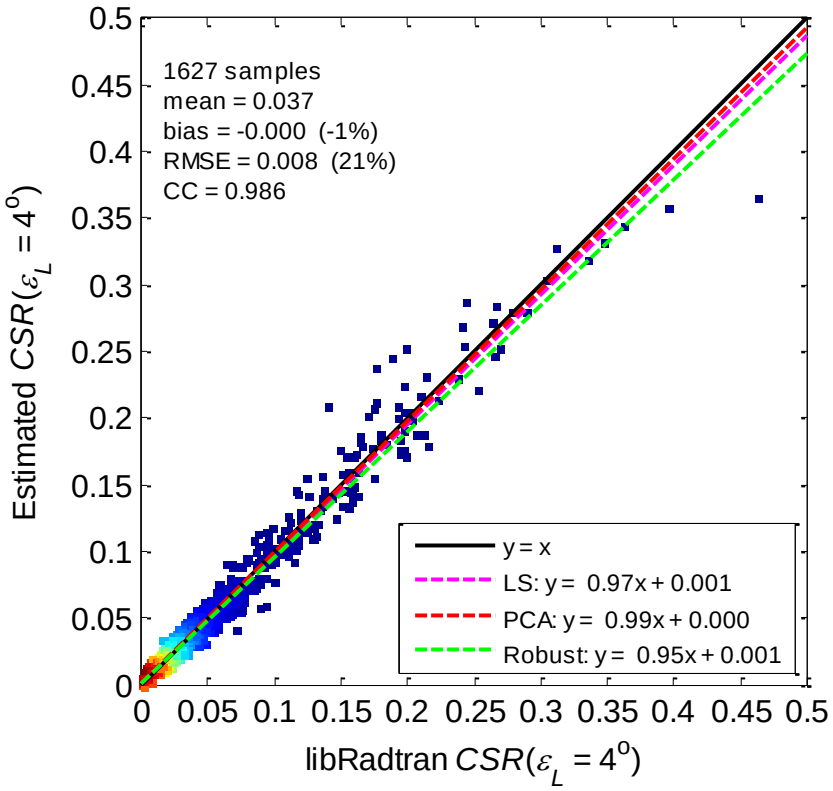


Fig. 7.11: Scatter density plot of the estimated CSR for a limit angle of 4° (estimated $CSR(\varepsilon_L = 4°)$) versus the reference values modelled by libRadtran (libRadtran $CSR(\varepsilon_L = 4°)$) using data set TAM_DS2.

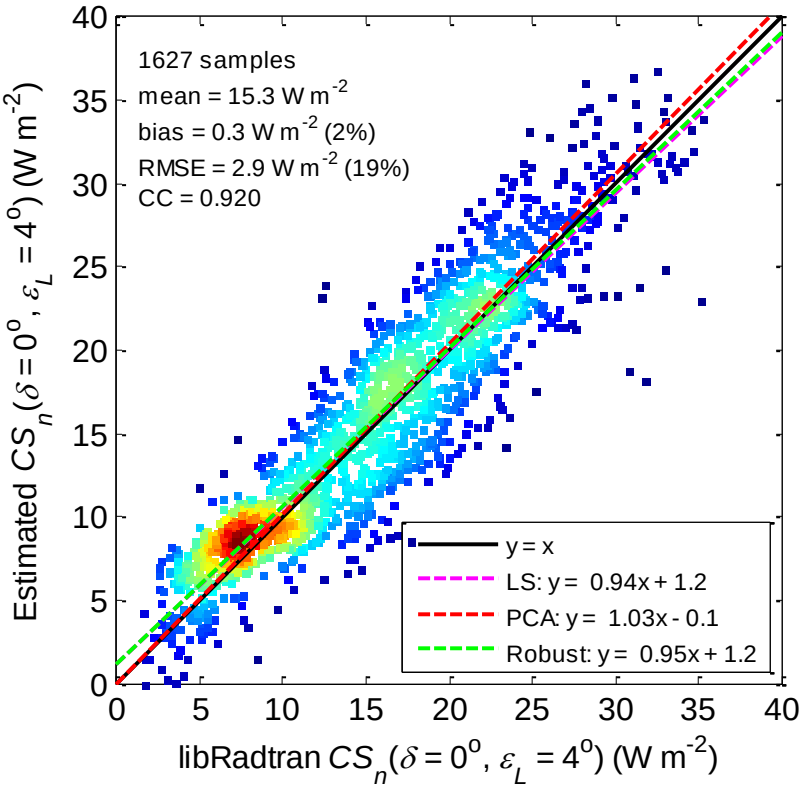


Fig. 7.12: Scatter density plot of the estimated CSNI for a limit angle of 4° (estimated $CS_n(\delta = 0°, \varepsilon_L = 4°)$) versus the reference values modelled by libRadtran (libRadtran $CS_n(\delta = 0°, \varepsilon_L = 4°)$) using data set TAM_DS2.

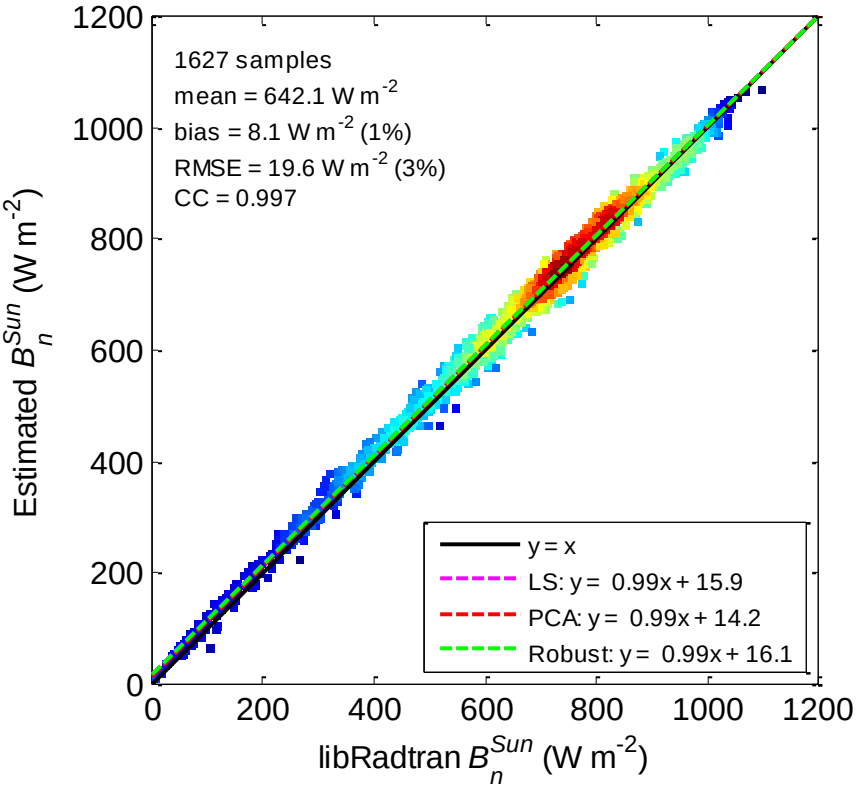


Fig. 7.13: Scatter density plot of the estimated DNI_S (estimated B_n^{Sun}) versus the reference values modelled by libRadtran (libRadtran B_n^{Sun}) using data set TAM_DS2.

The coefficients of Eqs. (7.1) to (7.3) presented in Table 7.2 are only valid for the viewing half-angles of the Eppley NIP. Similar to the model presented in Sect. 6.4.3, the coefficients can be presented as a function of the aperture half-angle α to estimate the CSR. In this case Eqs. (7.1) to (7.3) are presented as a function of α and not the limit angle ε_L. This is done by modelling the CSR from libRadtran for α ranging from 0.4° to 5° in steps of 0.2° and refitting the coefficients of the model for each CSR.

The validation of this method is also performed by the leave-one-out cross validation. The MAE of the CSR for the three defined *SC* intervals for the different α is presented in Fig. 7.14. The maximum MAE occurs when $SC < 1.74$ (*i.e.* turbid skies) and $\alpha = 5°$. The maximum MAE for the *SC* interval [1.74, 5.09] is 0.008, while for $SC > 5.09$ (*i.e.* the very clear skies) the maximum MAE is 0.004.

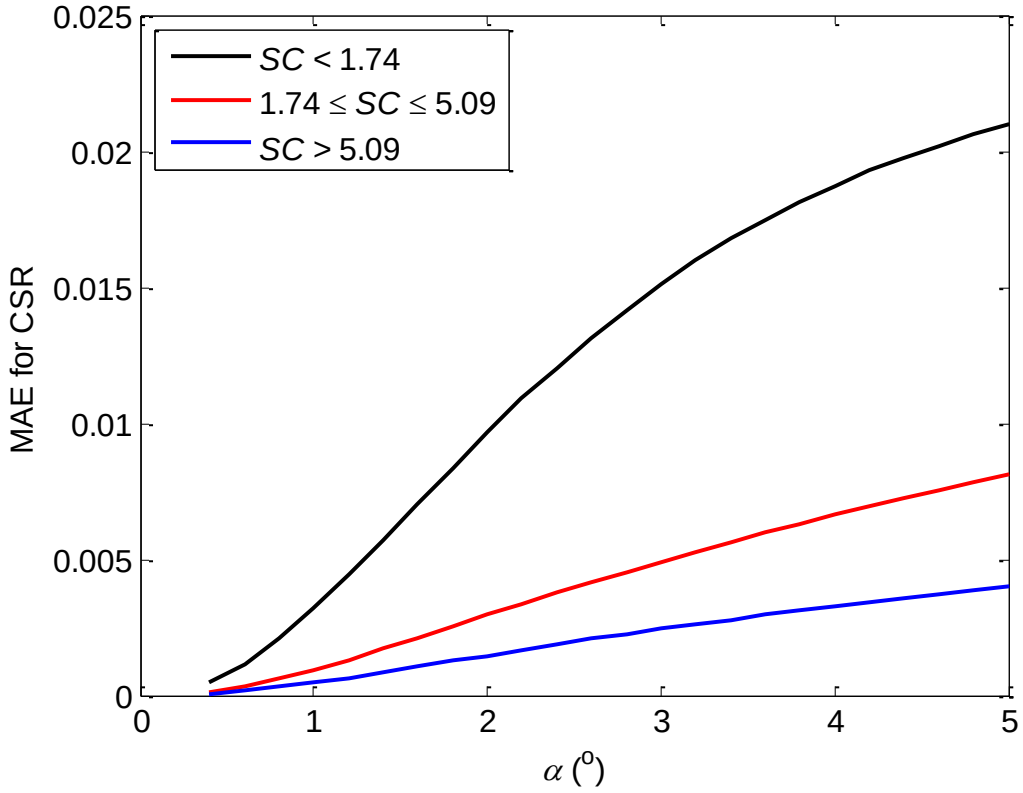


Fig. 7.14: The MAE of the CSR for the different aperture half-angles (α).

The coefficients of Eqs. (7.1) to (7.3) are provided as a function of α using a 6th degree polynomial fit, presented in Eqs. (7.4) to (7.10). The Fig. 7.15 exhibits the coefficients for the different α and their respective 6th degree polynomial fit.

$$o_1 = 1.119\,\mathrm{e}^{-5}\,\alpha^6 - 6.298\,\mathrm{e}^{-4}\,\alpha^5 + 9.319\,\mathrm{e}^{-3}\,\alpha^4 - 5.991\,\mathrm{e}^{-2}\,\alpha^3 + 1.698\,\mathrm{e}^{-1}\,\alpha^2 - 5.173\,\mathrm{e}^{-2}\,\alpha + 8.397\,\mathrm{e}^{-3} \quad (7.4)$$

$$\rho_1 = -5.425\,\mathrm{e}^{-4}\,\alpha^6 + 6.949\,\mathrm{e}^{-3}\,\alpha^5 - 2.603\,\mathrm{e}^{-2}\,\alpha^4 - 2.266\,\mathrm{e}^{-2}\,\alpha^3 + 3.628\,\mathrm{e}^{-1}\,\alpha^2 - 2.032\,\mathrm{e}^{-1}\,\alpha - 6.802 \quad (7.5)$$

$$\nu_1 = 8.654\,\mathrm{e}^{-6}\,\alpha^6 - 1.403\,\mathrm{e}^{-4}\,\alpha^5 + 1.192\,\mathrm{e}^{-3}\,\alpha^4 - 7.028\,\mathrm{e}^{-3}\,\alpha^3 + 2.374\,\mathrm{e}^{-2}\,\alpha^2 - 6.402\,\mathrm{e}^{-3}\,\alpha + 9.588\,\mathrm{e}^{-4} \quad (7.6)$$

$$o_2 = -1.083\,\mathrm{e}^{-5}\,\alpha^6 + 1.675\,\mathrm{e}^{-4}\,\alpha^5 - 4.975\,\mathrm{e}^{-4}\,\alpha^4 - 5.398\,\mathrm{e}^{-3}\,\alpha^3 + 4.196\,\mathrm{e}^{-2}\,\alpha^2 - 8.182\,\mathrm{e}^{-3}\,\alpha + 9.819\,\mathrm{e}^{-4} \quad (7.7)$$

$$\rho_2 = -5.660\,\mathrm{e}^{-5}\,\alpha^6 + 1.071\,\mathrm{e}^{-3}\,\alpha^5 - 8.240\,\mathrm{e}^{-3}\,\alpha^4 + 3.228\,\mathrm{e}^{-2}\,\alpha^3 - 5.875\,\mathrm{e}^{-2}\,\alpha^2 + 1.470\,\mathrm{e}^{-2}\,\alpha - 1.538 \quad (7.8)$$

$$o_3 = -1.910\,\mathrm{e}^{-7}\,\alpha^6 + 3.670\,\mathrm{e}^{-6}\,\alpha^5 - 3.272\,\mathrm{e}^{-5}\,\alpha^4 + 1.819\,\mathrm{e}^{-4}\,\alpha^3 - 6.291\,\mathrm{e}^{-4}\,\alpha^2 + 1.668\,\mathrm{e}^{-4}\,\alpha - 2.516\,\mathrm{e}^{-5} \quad (7.9)$$

$$v_3 = 2.043\,\mathrm{e}^{-6}\,\alpha^6 - 4.087\,\mathrm{e}^{-5}\,\alpha^5 + 3.778\,\mathrm{e}^{-4}\,\alpha^4 - 2.131\,\mathrm{e}^{-3}\,\alpha^3 + 7.297\,\mathrm{e}^{-3}\,\alpha^2 - 1.860\,\mathrm{e}^{-3}\,\alpha + 2.705\,\mathrm{e}^{-4} \quad (7.10)$$

where the aperture half-angle α is given in deg.

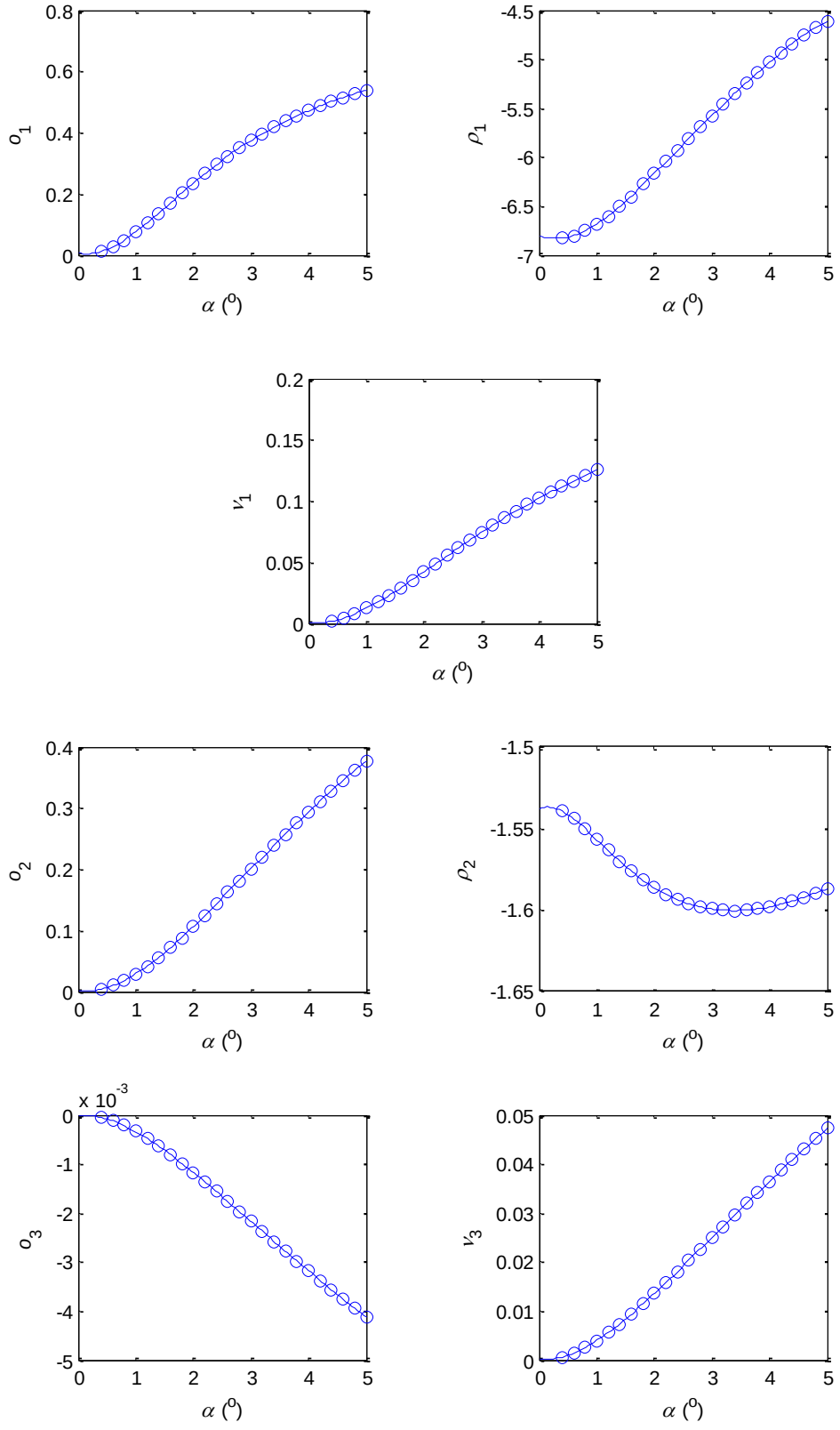


Fig. 7.15: The coefficients of Eqs. (7.1) to (7.3) as a function of the aperture half-angle α (circles) and the 6th order polynomial fit.

The model fitted over Tamanrasset using data set TAM_DS2 is now validated for the DNI_S modelled by libRadtran using data set TAM_DS1. The scatter density plot of the estimated DNI_S for the data set TAM_DS1 versus the libRadtran modelled DNI_S is shown in Fig. 7.16. The scatter around the 1:1 line is very low. The relative RMSE is 3% and the relative bias is 0%. R^2 is 0.994 and the slope of the robust affine regression is 0.98. The estimates are very accurate. The bias is less than 2 W m^{-2} and 72% of the samples exhibit an absolute difference less than 20 W m^{-2}.

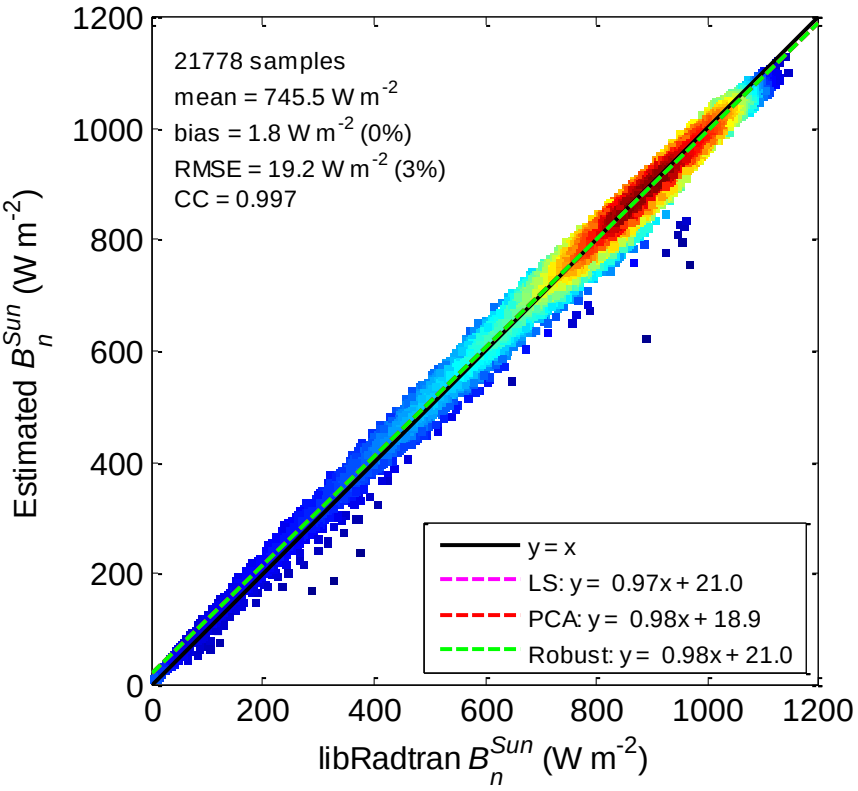


Fig. 7.16: Scatter density plot of the estimated DNI_S (estimated B_n^{Sun}) versus the reference values modelled by libRadtran (libRadtran B_n^{Sun}), for validating the model in time using data set TAM_DS1.

7.4. Validation of the model developed in Tamanrasset over Abu Dhabi

The validation of the model developed in Tamanrasset is performed over data sets DS1 and DS3 from Abu Dhabi.

For the data set DS1 the validation is performed only in terms of the DNI_S, where the reference values are modelled by libRadtran. In this case the CSR for α = 2.86° was computed by Eqs. (7.1) to (7.3), where the coefficients of the model are computed by Eqs. (7.4) to (7.10). The product of the CSR and the ground measured DNI is the estimated CSNI. The estimated DNI_S is then the difference between the measured DNI and the estimated CSNI.

For the data set DS3 the validation is performed in terms of CSR, CSNI and DNI_S, where the reference values are modelled by libRadtran.

7.4.1. Validation of the broadband beam irradiance over Abu Dhabi

For the data set DS1, the scatter density plot of the estimated DNI_S versus the libRadtran modelled DNI_S is shown in Fig. 7.17. The relative RMSE is 9% and the relative bias is −6%. R^2 is 0.976 and the slope of the robust affine regression is 0.94. As pointed out earlier, this bias is attributed to the RSI DNI which was used in computing the estimated DNI_S. The outliers shown in Fig. 7.17 have already been discussed in Sect. 6.4.3.

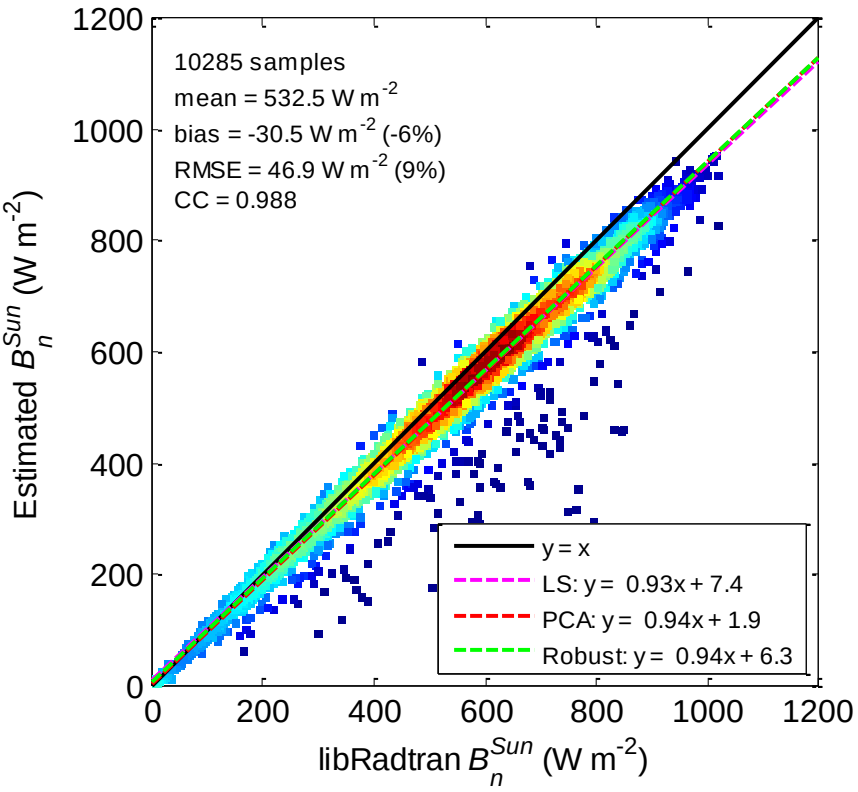


Fig. 7.17: Scatter density plot of the estimated DNI_S (estimated B_n^{Sun}) versus the reference values modelled by libRadtran (libRadtran B_n^{Sun}) using data set DS1, when using the model developed over Tamanrasset.

The results of the model developed in Tamanrasset over Abu Dhabi are very close to the results of the model developed in Abu Dhabi and applied over Abu Dhabi (Fig. 6.22), having a relative RMSE of 8% and a relative bias of −5%. Therefore, the model developed in Tamanrasset could be safely applied to estimate the DNI_S over Abu Dhabi.

7.4.2. Validation of the circumsolar ratio, and the broadband beam and circumsolar irradiances over Abu Dhabi

For the data set DS3, the scatter density plot of the estimated CSR versus the libRadtran CSR is shown in Fig. 7.18. The relative RMSE is 23% and the relative bias is +13%. R^2 is 0.960 and the slope of the robust affine regression is very close to 1. The scatter density plot of the estimated CSNI versus the libRadtran CSNI is shown in Fig. 7.19. The relative RMSE is 20% and the relative bias is +9%. R^2 is 0.702 and the slope of the robust affine regression is 0.78. Finally, the scatter density plot of the estimated DNI_S versus the libRadtran DNI_S is shown in Fig. 7.20. The relative RMSE is 7% and the relative bias is −6%. R^2 is 0.994 and the slope of the robust affine regression is 0.93.

As would be expected the results are less accurate than those when applying the model developed in Abu Dhabi over Abu Dhabi, presented in Sect. 6.4.3. Nevertheless, the results show that the model developed over Tamanrasset is applicable, with a certain degree of uncertainty, over Abu Dhabi. The overestimation of the CSR and CSNI could be attributed to *SC* being computed from DNI and DHI measured using different instruments. As shown previously in Fig. 7.6 the CSR at Tamanrasset generally has higher values than the CSR at Abu Dhabi for the same *SC* values. The underestimation of the DNI_S is attributed to an underestimation of the RSI DNI.

An advantage of using the modelled developed in Tamanrasset to other sites rather than the model developed in Abu Dhabi is that the coefficients of the model are fitted for a larger number of cloud-free conditions. Specifically in the interval $SC > 5.09$, which corresponds to very clear skies, where more samples are available in Tamanrasset than Abu Dhabi. For example, when applying the model of Abu Dhabi over Tamanrasset negative CSR values are observed in the interval $SC > 5.09$ and then set to zero as shown in Figs. 7.3 and 7.4. On the contrary, when applying the model of Tamanrasset over Abu Dhabi there are no negative CSR values.

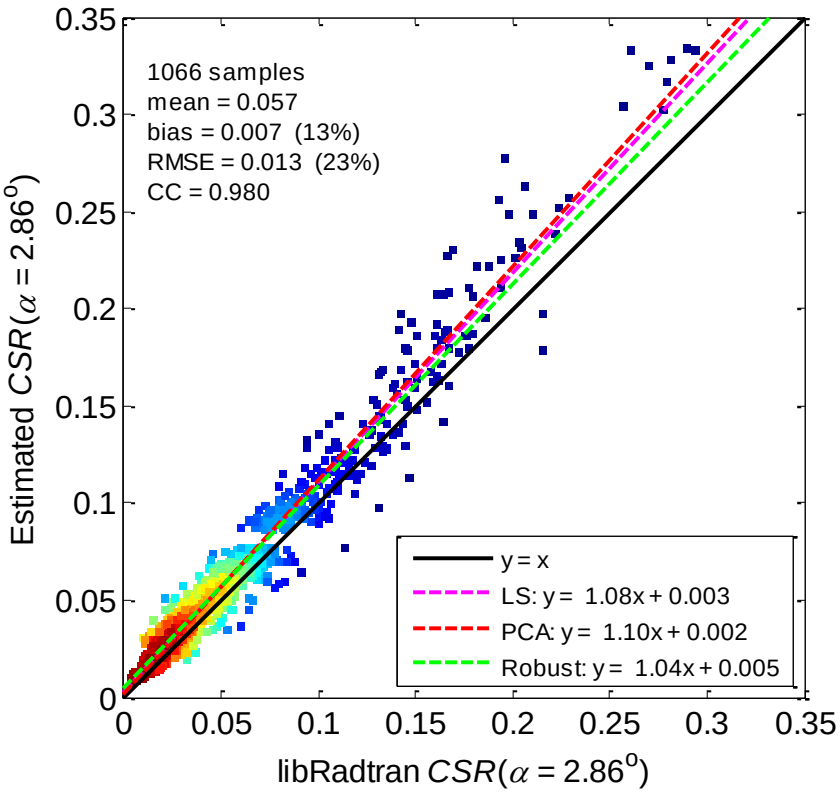


Fig. 7.18: Scatter density plot of the CSR for an aperture half-angle of 2.86° (estimated $CSR(\alpha = 2.86°)$) versus the reference values modelled by libRadtran (libRadtran $CSR(\alpha = 2.86°)$) using data set DS3, when using the model developed over Tamanrasset.

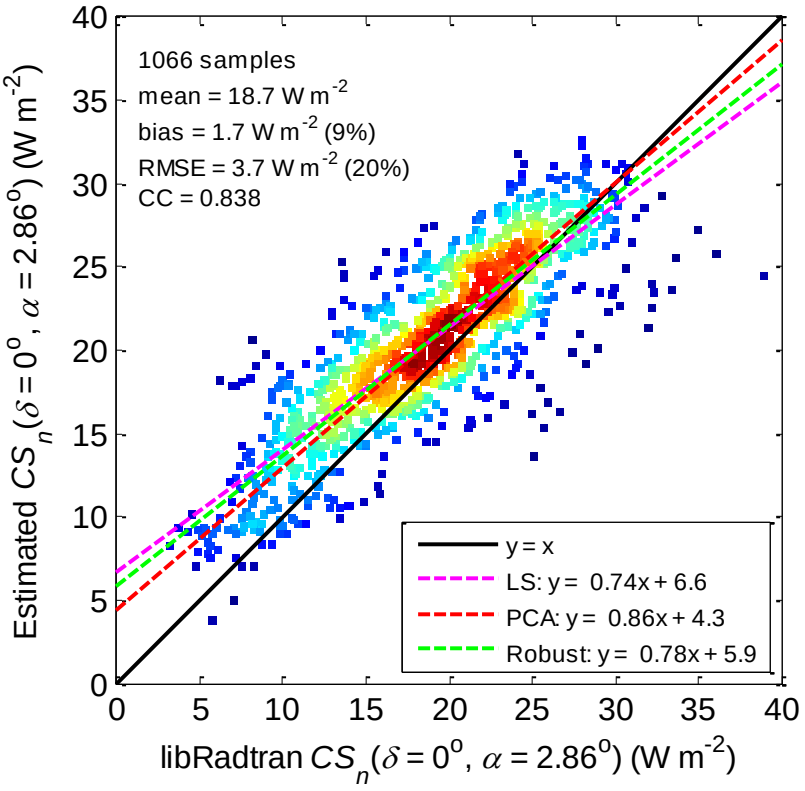


Fig. 7.19: Scatter density plot of the CSNI for an aperture half-angle of 2.86° (estimated $CS_n(\delta = 0°, \alpha = 2.86°)$) versus the reference values modelled by libRadtran (libRadtran $CS_n(\delta = 0°, \alpha = 2.86°)$) using data set DS3, when using the model developed over Tamanrasset.

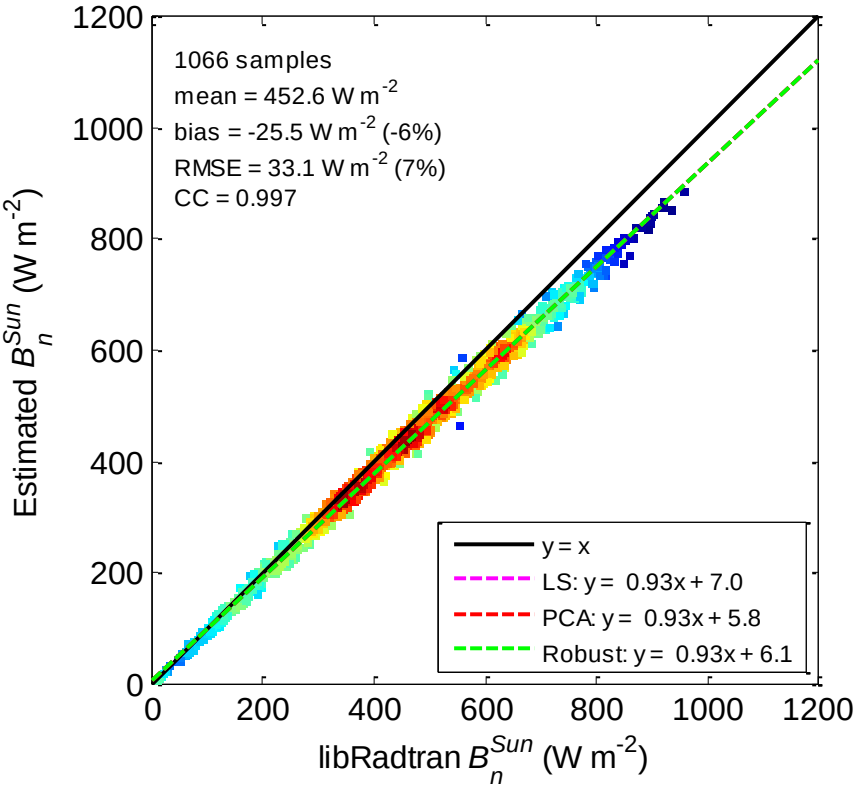


Fig. 7.20: Scatter density plot of the estimated DNI_S (estimated B_n^{Sun}) versus the reference values modelled by libRadtran (libRadtran B_n^{Sun}) using data set DS3, when using the model developed over Tamanrasset.

7.5. Discussion

Referring back to the third research question: *if a model can be devised to estimate the beam and circumsolar radiation for different aperture angles using observables which are more frequently available than aerosol optical properties is it applicable over other desert areas under cloud-free conditions or is it limited to the site for which is was developed?* The answer is yes with a certain degree of accuracy. Applying the model developed in Abu Dhabi over the site of Tamanrasset, the DNI_S can be very accurately estimated, with a relative RMSE of 3% and a relative bias of +1% for data set TAM_DS1 and a relative RMSE of 3% and a relative bias of +2% for data set TAM_DS2. The errors are higher, however, for the CSR and CSNI estimations. For the data set TAM_DS2, the estimated CSR exhibits a relative RMSE of 37% and a relative bias of −22%, while the estimated CSNI exhibits a relative RMSE of 30% and a relative bias of −24%.

The high errors in the estimated CSR and CSNI are suspected to arise from the actual model which was developed over Abu Dhabi. The RSI measurements from Abu Dhabi seem to have a miscalibration, which in turn affects the sky clearness indices computed from the RSI DHI and DNI. The CSR versus the sky clearness index for both Abu Dhabi and Tamanrasset is presented in Fig. 7.6, where a shift is

present in the Abu Dhabi data when compared to the Tamanrasset data. A higher confidence in data is assumed for the Tamanrasset solar irradiance ground measurements from the BSRN station for several reasons. Firstly, the DNI measurements are collected by an Eppley NIP, which has well-defined viewing half-angles as opposed to the RSI. Secondly, the Eppley NIP is a thermopile sensitive in the interval [0.285 μm, 2.8 μm] whereas the RSI is a photodiode and in this case was calibrated with respect to temperature and spectral effects in a place (Plataforma Solar de Almeria, Spain) and used elsewhere. Thirdly, in Tamanrasset the GHI, DNI and DHI are collected by three different instruments. This makes the quality check of Roesch *et al.* (2011a), which compares the measured GHI with the GHI computed from the DNI and DHI, more effective in removing any erroneous data. This quality check is not efficient for the RSI measurements because the GHI and DHI are measured by the same instrument and the DNI is actually computed from them. Finally, in the validations of the libRadtran modelled DNI and DNI_S with respect to the ground measured DNI in Tamanrasset the results do not exhibit the bias present in Abu Dhabi where the highest modelled DNI values were overestimated. This puts more confidence in the ground measurements available in Tamanrasset.

The validation of the model developed over Tamanrasset using data set TAM_DS2 exhibit very low errors in estimating the CSR (relative RMSE of 21% and relative bias of −1%), the CSNI (relative RMSE of 19% and relative bias of +2%) and the DNI_S (relative RMSE of 3% and relative bias of +1%). These errors are very low, especially for the DNI_S where 67% of the samples have an absolute difference less than 20 W m^{-2}. The model is further validated for the DNI_S for samples which were not used in fitting the model coefficients, using the data set TAM_DS1. In this case the relative RMSE is 3% and the relative bias is 0%. The bias is less than 2 W m^{-2} and 72% of the samples have an absolute difference less than 20 W m^{-2}. In fact, the bias reaches the target set in the development of the McClear model which is adapted from the WMO constraints for coinciding DNI measurements.

Application of the model developed in Tamanrasset over Abu Dhabi to estimate the DNI_S using data set DS1 exhibits a relative RMSE of 9% and a relative bias of −6%. For data set DS3 the errors comprise of: relative RMSE of 23% and relative bias of +13% for the CSR, relative RMSE of 20% and relative bias of +9% for the CSNI, relative RMSE of 7% and relative bias of −6% for the DNI_S. Due to the more accurate results in estimating the CSR by using the model developed in Tamanrasset and applied over Abu Dhabi as opposed to the model developed in Abu Dhabi and applied over Tamanrasset and the fact that it is more accurate for the very clear skies when $SC > 5.09$, it is recommended to use this model in other sites to estimate the CSR and CSNI for any aperture half-angle in the interval [0.4°, 5°] and the DNI_S. This can be done only if high quality DNI and DHI measurements are available at the site in question.

Chapter 8 - Conclusions and perspectives

A fast and simple parametric model is proposed for an improved assessment of the broadband beam and circumsolar radiation under cloud-free conditions in a desert environment. With this model the CSR can be estimated for any aperture half-angle between 0.4° and 5°, provided DNI and DHI measurements are available at the site in question. This is valuable because only the DNI and DHI are required, as opposed to the specific aerosol optical properties required as inputs to RTMs for an accurate assessment of the beam radiation (the AOD) and the circumsolar radiation (the AOD, aerosol SSA and aerosol PFCN) which are less frequently available. If such specific aerosol optical properties were available, the proposed model is significantly faster than the RTM libRadtran. Using the proposed model, the CSNI and DNI_S are computed from the estimated CSR and ground measured DNI. The DNI_S estimations along with the CSR and CSNI for a defined aperture half-angle are useful for CST systems.

In the work of Blanc *et al.* (2014) it is recommended to report the viewing half-angles of the radiometer, the CSR and the sunshape in addition to the standard DNI measurements. The model proposed herein estimates the CSR and CSNI. The sunshape can then be retrieved using the parametric model of Buie *et al.* (2013) with the CSR as input.

This model has been developed and validated over Abu Dhabi, UAE. The model developed over Abu Dhabi was also validated over Tamanrasset, Algeria. Inversely in order to benefit from the high quality solar irradiance ground measurements at Tamanrasset, the coefficients of the model were refitted using the data of Tamanrasset and validated over both Tamanrasset and Abu Dhabi.

The validation results for data set DS3 of Abu Dhabi, for the model developed over Abu Dhabi, exhibit very low errors in estimating the CSR (relative RMSE of 16% and relative bias of −1%), the CSNI (relative RMSE of 18% and relative bias of −5%) and the DNI_S (relative RMSE of 7% and relative bias of −5%). Using the data set DS1 of Abu Dhabi to validate the DNI_S, the relative RMSE is 8% and the relative bias is −5%.

Applying the model developed in Abu Dhabi over Tamanrasset, the DNI_S can be very accurately estimated, with a relative RMSE of 3% and a relative bias of +1% for data set TAM_DS1 and a relative RMSE of 3% and a relative bias of +2% for data set TAM_DS2. The errors are greater, however, for the CSR and CSNI estimations. For the data set TAM_DS2, the estimated CSR exhibits a relative RMSE of 37% and a relative bias of −22%, while the estimated CSNI exhibits a relative RMSE of 30% and a relative bias of −24%. The errors are notably due to a miscalibration in the RSI DHI and DNI from Abu Dhabi, which were used to compute the sky clearness index which in turn was used to fit the coefficients of the model.

The validation results over Tamanrasset (data set TAM_DS2), for the model developed over Tamanrasset, exhibit very low errors in estimating the CSR (relative RMSE of 21% and relative bias of −1%), the CSNI (relative RMSE of 19% and relative bias of +2%) and the DNI_S (relative RMSE of 3% and relative bias of +1%). Using the data set TAM_DS1 to validate the DNI_S, the relative RMSE is 3% and the relative bias is 0%. Application of the model developed in Tamanrasset over Abu Dhabi to estimate the DNI_S using data set DS1 exhibits a relative RMSE of 9% and a relative bias of −6%. For data set DS3 the errors comprise of: relative RMSE of 23% and relative bias of +13% for the CSR, relative RMSE of 20% and relative bias of +9% for the CSNI, relative RMSE of 7% and relative bias of −6% for the DNI_S. Due to a higher confidence in the solar irradiance ground measurements available at Tamanrasset, it is recommended to use this specific model in other sites to estimate the CSR and CSNI for any aperture half-angle in the interval [0.4°, 5°] and the DNI_S.

In the development of the proposed model the aerosol optical properties were used as inputs to compute the reference DNI_S, CSNI and CSR by the RTM libRadtran, but any errors in such properties would generate an error in the reference values. The correction which has been applied to the AOD, has only been validated over the site of Abu Dhabi and this correction was only applied at the wavelength of 670 nm. In the modelling of the broadband radiances and irradiances by libRadtran the same correction was applied to all the AODs at the different wavelengths. This is an area requiring further research, because it is not certain whether the applied correction is applicable for the AOD at different wavelengths or not. Also, the aerosol PFCN retrieved from the AERONET Inversion products is available at scattering angles less than 3°. However, the AERONET almucantar radiance measurements from both Tamanrasset and Abu Dhabi are not provided at scattering angles less than 3°. As the aerosol PFCN is derived from the almucantar radiance measurements this suggests that the PFCN values provided at the smaller scattering angles are extrapolated values, which may induce errors in the results. Also, the aperture half-angle of the AERONET Sun photometer is relatively large (α = 0.6°) to capture the aerosol PFCN at a fine angular resolution. A better representation of the aerosol PFCN at small scattering angles with a finer angular resolution may improve the modelling results by libRadtran, which in turn would improve the performance of the model after refitting the coefficients.

Another factor which may limit the application of the model is the availability of high quality DNI and DHI ground measurements. Even though they are more frequently available than the aerosol optical properties from the AERONET stations, they might not be available at a specific site of interest. And if such measurements were available, they are not necessarily available for public access. In such situations the McClear model could be used, which is a physical model based on the RTM libRadtran to estimate the downwelling surface solar irradiances under cloud-free conditions. The AOD values used in McClear are from the reanalysis data set of atmospheric composition available worldwide from 2004 provided by the MACC project (Benedetti *et al.*, 2009; Inness *et al.*, 2013; Schroedter-Homscheidt *et al.*, 2013). The McClear model is available as a Web service, *i.e.* an application that can be invoked

via the Web. An interface has been developed to launch McClear within a standard Web browser *via* the catalogue of products on the MACC Web site (http://www.gmes-atmosphere.eu). The DNI estimates of McClear are in fact the DNI_S as no information on the CSNI is provided. Therefore, the model proposed herein can be applied using the McClear DNI_S and DHI estimates to compute the sky clearness index, from which the CSR and CSNI are computed. However, the results of the CSR and CSNI need to be carefully analyzed, because in this case it is the DNI_S which would be used in the computation of the sky clearness index. In addition, there are other errors induced in the McClear irradiance estimates due to errors in the AOD used as an input to the model (Benedictow *et al.*, 2014; Eissa *et al.*, 2015). The capability of using McClear irradiance estimates for information on the CSNI and CSR is an area requiring further research.

The proposed model may be extended to include all sites which have AERONET and BSRN stations present. In this case the coefficients of the model would be refitted over each of these sites and then provided in look-up-tables. This is of interest because the model may be more applicable on a global scale, comprising different environmental conditions and not just desert.

Another approach to estimate the CSR may be done by generating a library of CSR values modelled by libRadtran for the available data from the AERONET Inversions products. The data from the AERONET DSA products could then be matched to those of the AERONET Inversion products in terms of Mahalanobis distance, and then match the corresponding CSR from the library. The DNI_S may be directly modelled by libRadtran from the AOD data from the AERONET DSA products after correcting it, and the CSNI is computed from the DNI_S and CSR. This approach may prove valuable in sites with a large data set of AERONET observations.

All the work presented in this thesis accounted for cloud-free conditions only. The presence of cirrus clouds in the sky is also of interest for CST systems because the DNI may still be relatively high, but so would the CSNI and CSR. Reinhardt *et al.* (2014) propose a model to estimate the CSR from cirrus cloud properties retrieved from the Meteosat Second Generation satellite data. The inclusion of cirrus cloudy conditions to the proposed model is of interest and is another area requiring further research.

References

Al Jaber, S.A., 2013. MENA energy transition strategy: A call for leadership in energy innovation. Energy Strategy Reviews 2, 5–7. doi: http://dx.doi.org/10.1016/j.esr.2012.11.009.

Anderson, G.P., Clough, S.A., Kneizys, F.X., Chetwynd, J.H., Shettle, E.P., 1986. AFGL atmospheric constituent profiles (0-120km). Tech. Rep. AFGL-TR-86-0110, Air Force Geophys. Lab., Hanscom Air Force Base, Bedford, Mass., USA. http://www.dtic.mil/cgi-bin/GetTRDoc?AD=ADA175173 (last access: 6 March 2014).

Ångström, A., 1964. The parameters of atmospheric turbidity. Tellus 16, 64–75. doi: http://dx.doi.org/10.1111/j.2153-3490.1964.tb00144.x.

Benedetti, A., Morcrette, J.-J., Boucher, O., Dethof, A., Engelen, R.J., Fisher, M., Flentje, H., Huneeus, N., Jones, L., Kaiser, J.W., Kinne, S., Mangold, A., Razinger, M., Simmons, A.J., Suttie, M., 2009. Aerosol analysis and forecast in the European Centre for Medium-Range Weather Forecasts Integrated Forecast System: 2. Data assimilation. Journal of Geophysical Research 114, D13205. doi: http://dx.doi.org/10.1029/2008JD011115.

Benedictow, A., Blechschmidt, A.M., Bouarar, I., Botek, E., Chabrillat, S., Christophe, Y., Cuevas, E., Clark, H., Flentje, H., Gaudel, A., Griesfeller, J., Huijnen, V., Huneeus, N., Jones, L., Kapsomenakis, J., Kinne, S., Langerock, B., Lefever, K., Razinger, M., Richter, A., Schulz, M., Thomas, W., Thouret, V., Vrekoussis, M., Wagner, A., Zerefos, C., 2014. Validation report of the MACC reanalysis of global atmospheric composition: Period 2003-2012. Tech. Rep., MACC-II Project. https://www.gmes-atmosphere.eu/documents/maccii/deliverables/val/MACCII_VAL_DEL_D_83.6_REAreport04_20140729.pdf (last access: 11 September 2014).

Blanc, P., Espinar, B., Geuder, N., Gueymard, C.A., Meyer, R., Pitz-Paal, R., Reinhardt, B., Renne, D., Sengupta, M., Wald, L., Wilbert, S., 2014. Direct normal irradiance related definitions and applications: the circumsolar issue. Solar Energy 110, 561–577. doi: http://dx.doi.org/10.1016/j.solener.2014.10.001.

Blanc, P., Wald, L., 2012. The SG2 algorithm for a fast and accurate computation of the position of the Sun for multi-decadal time period. Solar Energy 86, 3072–3083. doi: http://dx.doi.org/10.1016/j.solener.2012.07.018.

Bodhaine, B.A., Wood, N.B., Dutton, E.G., Slusser, J.R., 1999. On Rayleigh optical depth calculations. Journal of Atmospheric and Oceanic Technology 16, 1854–1861. doi: http://dx.doi.org/10.1175/1520-0426(1999)016<1854:ORODC>2.0.CO;2.

Box, M.A., Deepak, A., 1978. Single and multiple scattering contributions to circumsolar radiation. Applied Optic 17, 3794–3797. doi: http://dx.doi.org/10.1364/AO.17.003794.

Brand, B., Zingerle, J., 2011. The renewable energy targets of the Maghreb countries: Impact on electricity supply and conventional power markets. Energy Policy 39, 4411–4419. doi: http://dx.doi.org/10.1016/j.enpol.2010.10.010.

Brunger, A.P., Hooper, F.C., 1993. Anisotropic sky radiance model based on narrow field of view measurements of shortwave radiance. Solar Energy 51, 53–64. doi: http://dx.doi.org/10.1016/0038-092X(93)90042-M.

Bryden, J., Riahi, L., Zissler, R., 2013. MENA renewables status report. Report for REN21. http://www.ren21.net/Portals/0/documents/activities/Regional%20Reports/MENA_2013_lowres.pdf (last access: 1 October 2014).

Buie, D., Monger, A.G., Dey, C.J., 2003. Sunshape distributions for terrestrial solar simulations. Solar Energy 74, 113–122. doi: http://dx.doi.org/10.1016/S0038-092X(03)00125-7.

CIE, 2002. Spatial distribution of daylight - CIE standard general sky. Commission Internationale de l'Eclarage.

DeVore, J.G., Stair, A.T., McClatchey, R., 2007. SAM (sun and aureole measurement): Examples from April 06 IOP at SGP. Poster presentation available on the Atmospheric Radiation Measurement (ARM) Program website http://www.arm.gov/publications/proceedings/conf17/poster/P00021.pdf (7 October 2014).

DeVore, J.G., Stair Jr., A.T., LePage, A., Villanucci, D., 2012a. Using scattering calculations to compare MODIS retrievals of thin cirrus optical properties with SAM solar disk and aureole radiance measurements. Journal of Geophysical Research 117, D01204. doi: http://dx.doi.org/10.1029/2011JD015858.

DeVore, J.G., Villanucci, D., LePage, A., 2012b. Aureolegraph internal scattering correction. Applied Optics 51, 7891–7899. doi: http://dx.doi.org/10.1364/AO.51.007891.

Dubovik, O., Holben, B., Eck, T.F., Smirnov, A., Kaufman, Y.J., King, M.D., Tanre, D., Slutsker, I., 2002. Variability of absorption and optical properties of key aerosol types observed in worldwide locations. Journal of the Atmospheric Sciences 59, 590–608. doi: http://dx.doi.org/10.1175/1520-0469(2002)059<0590:VOAAOP>2.0.CO;2.

Dubovik, O., King, M.D., 2000. A flexible inversion algorithm for retrieval of aerosol optical properties from Sun and sky radiance measurements. Journal of Geophysical Research 105, 20673–20696. doi: http://dx.doi.org/10.1029/2000JD900282.

Dubovik, O., Smirnov, A., Holben, B.N., King, M.D., Kaufman, Y.J., Eck, T.F., Slutsker, I., 2000. Accuracy assessments of aerosol optical properties retrieved from Aerosol Robotic Network (AERONET) Sun and sky radiance measurements. Journal of Geophysical Research 105, 9791–9806. doi: http://dx.doi.org/10.1029/2000JD900040.

Eissa, Y., Munawwar, S., Oumbe, A., Blanc, P., Ghedira, H., Wald, L., Bru, H., Goffe, D., 2015. Validating the downwelling solar irradiances estimated by the McClear model under cloud-free skies in the United Arab Emirates. Solar Energy 114, 17–31. doi: http://dx.doi.org/10.1016/j.solener.2015.01.017.

Emde, C., Mayer, B., 2007. Simulation of solar radiation during a total eclipse: a challenge for radiative transfer. Atmospheric Chemistry and Physics 7, 2259–2270. doi: http://dx.doi.org/10.5194/acp-7-2259-2007.

Emilio, M., Kuhn, J.R., Bush, R.I., Scholl, I.F., 2012. Measuring the solar radius from space during the 2003 and 2006 Mercury transits. The Astrophysical Journal 750, 135–142. doi: http://dx.doi.org/10.1088/0004-637X/750/2/135.

Geuder, N., Affolter, R., Kraas, B., Wilbert, S., 2014. Long-term behavior, accuracy and drift of LI-200 pyranometers as radiation sensors in Rotating Shadowband Irradiometers (RSI). Proceedings of SolarPACES 2013, Las Vegas, USA. Energy Procedia 49, 2330–2339. doi: http://dx.doi.org/10.1016/j.egypro.2014.03.247.

Geuder, N., Pulvermuller, B., Vorbrugg, O., 2008. Corrections for rotating shadowband pyranometers for solar resource assessment. Proceedings of SPIE, San Diego, USA. http://dx.doi.org/10.1117/12.797472.

Gherboudj, I., Ghedira, H., 2014. Spatiotemporal assessment of dust loading over the United Arab Emirates. International Journal of Climatology. doi: http://dx.doi.org/10.1002/joc.3909.

Grether, D.F., Hunt, A., Evans, D., Wahlig, M., 1978. Measurement of circumsolar radiation - Status Report, in: 3rd Annual Solar Heating & Cooling R&D Contractors' Meeting. Washington D.C. https://publications.lbl.gov/islandora/object/ir%3A107077 (last access: 12 March 2014).

Griffiths, S., 2013. Strategic considerations for deployment of solar photovoltaics in the Middle East and North Africa. Energy Strategy Reviews 2, 125–131. doi: http://dx.doi.org/10.1016/j.esr.2012.11.001.

Gueymard, C.A., 1995. SMARTS, A Simple Model of the Atmospheric Radiative Transfer of Sunshine: Algorithms and performance assessment. Professional paper FSEC-PF-270-95. Florida Solar Energy Center, 1679 Clearlake Rd., Cocoa, FL 32922. http://rredc.nrel.gov/solar/models/SMARTS/relatedrefs/SMARTS2_report.pdf (last access: 12 March 2014).

Gueymard, C.A., 2001. Parameterized transmittance model for direct beam and circumsolar spectral irradiance. Solar Energy 71, 325–346. doi: http://dx.doi.org/10.1016/S0038-092X(01)00054-8.

Gueymard, C.A., 2004. The sun's total and spectral irradiance for solar energy applications and solar radiation models. Solar Energy 76, 423–453. doi: http://dx.doi.org/10.1016/j.solener.2003.08.039.

Gueymard, C.A., 2006. SMARTS code, version 2.9.5: User's manual. http://rredc.nrel.gov/solar/models/smarts/relatedrefs/smarts295_users_manual_pc.pdf (last access 8 October 2014).

Gueymard, C.A., 2009. Direct and indirect uncertainties in the prediction of tilted irradiance for solar engineering applications. Solar Energy 83, 432–444. doi: http://dx.doi.org/10.1016/j.solener.2008.11.004.

Gueymard, C.A., 2010. Spectral Circumsolar Contribution to CPV. Proceedings of International Conference on Concentrating Photovoltaic Systems (CPV-6), Freiburg, Germany, April 7–9.

Gueymard, C.A., 2012. Clear-sky irradiance predictions for solar resource mapping and large-scale applications: Improved validation methodology and detailed performance analysis of 18 broadband radiative models. Solar Energy 86, 2145–2169. doi: http://dx.doi.org/10.1016/j.solener.2011.11.011.

Haltrin, V.I., 2002. One-parameter two-term Henyey-Greenstein phase function for light scattering in seawater. Applied Optics 41, 1022–1028. doi: http://dx.doi.org/10.1364/AO.41.001022.

Henyey, L.G., Greenstein, J.L., 1941. Diffuse radiation in the galaxy. Astrophysical Journal 93, 70–83. http://adsabs.harvard.edu/full/1941ApJ....93...70H (last access: 12 March 2014).

Hess, M., Koepke, P., Schult, I., 1998. Optical Properties of Aerosols and Clouds: The software package OPAC. Bulletin of the American Meteorological Society 79, 831–844. doi: http://dx.doi.org/10.1175/1520-0477(1998)079<0831:OPOAAC>2.0.CO;2.

Holben, B.N., Eck, T.F., Slutsker, I., Tanre, D., Buis, J.P., Setzer, A., Vermote, E., Reagan, J.A., Kaufman, Y.J., Nakajima, T., Lavenu, F., Jankowiak, I., Smirnov, A., 1998. AERONET — A federated instrument network and data archive for aerosol characterization. Remote Sensing of Environment 66, 1–16. doi: http://dx.doi.org/10.1016/S0034-4257(98)00031-5.

IAMAP, 1986. A preliminary cloudless standard atmosphere for radiation computation. Rep. WCP-112, WMO/TD-No. 24, World Meteorological Organization.

Igawa, N., Koga, Y., Matsuzawa, T., Nakamura, H., 2004. Models of sky radiance distribution and sky luminance distribution. Solar Energy 77, 137–157. doi: http://dx.doi.org/10.1016/j.solener.2004.04.016.

Ineichen, P., 2006. Comparison of eight clear sky broadband models against 16 independent data banks. Solar Energy 80, 468–478. doi: http://dx.doi.org/10.1016/j.solener.2005.04.018.

Ineichen, P., Molineaux, B., Perez, R., 1994. Sky luminance data validation: Comparison of seven models with four data banks. Solar Energy 52, 337–346. doi: http://dx.doi.org/10.1016/0038-092X(94)90140-6.

Inness, A., Baier, F., Benedetti, A., Bouarar, I., Chabrillat, S., Clark, H., Clerbaux, C., Coheur, P., Engelen, R.J., Errera, Q., Flemming, J., George, M., Granier, C., Hadji-Lazaro, J., Huijnen, V., Hurtmans, D., Jones, L., Kaiser, J.W., Kapsomenakis, J., Lefever, K., Leitão, J., Razinger, M., Richter, A., Schultz, M.G., Simmons, a. J., Suttie, M., Stein, O., Thépaut, J.-N., Thouret, V., Vrekoussis, M., Zerefos, C., 2013. The MACC reanalysis: an 8 yr data set of atmospheric composition. Atmospheric Chemistry and Physics 13, 4073–4109. doi: http://dx.doi.org/10.5194/acp-13-4073-2013.

Irvine, W.M., 1965. Multiple scattering by large particles. Astrophysical Journal 142, 1563–1575. http://adsabs.harvard.edu/full/1965ApJ...142.1563I (last access: 8 October 2014).

ISO-9488, 1999. Solar energy – Vocabulary. ISO, Geneva, Switzerland.

Jilinski, E.G., Puliaev, S.P., Penna, J.L., Andrei, A.H., Sinceac, V., Chollet, F., Delmas, C., 1998. Solar diameter observations with the Astrolabe at Observatório Nacional - Rio de Janeiro. Astronomy and Astrophysics 130, 317–321. doi: http://dx.doi.org/10.1051/aas:1998228.

Kasten, F., Young, A.T., 1989. Revised optical air mass tables and approximation formula. Applied Optics 28, 4735–4738. doi: http://dx.doi.org/10.1364/AO.28.004735.

Kato, S., Ackerman, T.P., Mather, J.H., Clothiaux, E.E., 1999. The k-distribution method and correlated-k approximation for a shortwave radiative transfer model. Journal of Quantitative Spectroscopy and Radiative Transfer. 62, 109–121. doi: http://dx.doi.org/10.1016/S0022-4073(98)00075-2.

Kattawar, G.W., 1975. A three-parameter analytic phase function for multiple scattering calculations. Journal of Quantitative Spectroscopy and Radiative Transfer 15, 839–849. doi: http://dx.doi.org/10.1016/0022-4073(75)90095-3.

Key, J.R., Yang, P., Baum, B.A., Nasiri, S.L., 2002. Parameterization of shortwave ice cloud optical properties for various particle habits. Journal of Geophysical Research 107 (D13), 1–10. doi: http://dx.doi.org/10.1029/2001JD000742.

Kocifaj, M., Gueymard, C.A., 2011. Theoretical evaluation of errors in aerosol optical depth retrievals from ground-based direct-sun measurements due to circumsolar and related effects. Atmospheric Environment 45, 1050–1058. http://dx.doi.org/10.1016/j.atmosenv.2010.07.054.

Kuravi, S., Trahan, J., Goswami, D.Y., Rahman, M.M., Stefanakos, E.K., 2013. Thermal energy storage technologies and systems for concentrating solar power plants. Progress in Energy and Combustion Science 39, 285–319. doi: http://dx.doi.org/10.1016/j.pecs.2013.02.001.

Kurtz, S., 2012. Opportunities and challenges for development of a mature concentrating photovoltaic power industry. NREL Technical Report, NREL/TP-5200-43208. http://www.nrel.gov/docs/fy13osti/43208.pdf (last access: 12 March 2014).

Lee, C.-Y., Chou, P.-C., Chiang, C.-M., Lin, C.-F., 2009. Sun tracking systems: a review. Sensors 9, 3875–3890. doi: http://dx.doi.org/10.3390/s90503875.

Lefevre, M., Oumbe, A., Blanc, P., Espinar, B., Gschwind, B., Qu, Z., Wald, L., Schroedter-Homscheidt, M., Hoyer-Klick, C., Arola, A., Benedetti, A., Kaiser, J.W., Morcrette, J.-J., 2013. McClear : a new model estimating downwelling solar radiation at ground level in clear-sky conditions. Atmospheric Measurement Techniques 6, 2403–2418. doi: http://dx.doi.org/10.5194/amt-6-2403-2013.

LePage, A., Kras, S., DeVore, J.G., 2008. Description of SAM (sun and aureole measurement) sensor data collected in support of CLASIC and CHAPS. Available at http://www.visidyne.com/SAM/VI-5311(SamClasic+ChapsData).j-2.pdf (last access 7 October 2014).

Liou, K.N., 2002. An introduction to atmospheric radiation, Second edition. Academic Press.

Marquardt, D., 1963. An Algorithm for least-squares estimation of nonlinear parameters. Journal of the Society for Industrial and Applied Mathematics 11, 431–441. doi: http://dx.doi.org/10.1137/0111030.

Mayer, B., 2009. Radiative transfer in the cloudy atmosphere. The European Physical Journal Conferences 1, 75–99. doi: http://dx.doi.org/10.1140/epjconf/e2009-00912-1.

Mayer, B., Kylling, A., 2005. Technical note: The libRadtran software package for radiative transfer calculations - description and examples of use. Atmospheric Chemistry and Physics 5, 1855–1877. doi: http://dx.doi.org/10.5194/acp-5-1855-2005.

Mayer, B., Kylling, A., Emde, C., Hamann, U., Buras, R., 2012. libRadtran user's guide. http://www.libradtran.org/doc/libRadtran.pdf (last access: 12 March 2014).

Mayer, B., Kylling, A., Emde, C., Buras, R., Hamann, U., Gasteiger, J., Richter, B., 2014. libRadtran user's guide. http://www.libradtran.org/doc/libRadtran.pdf (last access: 8 October 2014).

McArthur, L.J.B., 2005. Baseline surface radiation network (BSRN): Operations manual. Technical Report, WCRP-121, WMO/TD-No. 1274. http://www.wmo.int/pages/prog/gcos/documents/gruanmanuals/WCRP/WCRP21_TD1274_BSRN.pdf (last access: 21 October 2014).

Mimouni, Mohamed, 2007. Horizon at station Tamanrasset. National Meteorological Office of Algeria. doi: http://dx.doi.org/10.1594/PANGAEA.669526.

Neumann, A., Witzke, A., Jones, S.A., Schmitt, G., 2002. Representative terrestrial solar brightness profiles. Journal of Solar Energy Engineering 124, 198–204. doi: http://dx.doi.org/10.1115/1.1464880.

Noring, J.E., Grether, D.F., Hunt, A.J., 1991. Circumsolar radiation data: the Lawrence Berkeley Laboratory Reduced Data Base. Berkeley, California. doi: http://dx.doi.org/10.2172/10109904.

Ohmura, A., Dutton, E.G., Forgan, B., Fröhlich, C., Gilgen, H., Hegner, H., Heimo, A., König-Langlo, G., McArthur, B., Müller, G., Philipona, R., Pinker, R., Whitlock, C.H., Dehne, K., Wild, M., 1998. Baseline Surface Radiation Network (BSRN/WCRP): New precision radiometry for climate research. Bulletin of the American Meteorological Society 79, 2115–2136. doi: http://dx.doi.org/10.1175/1520-0477(1998)079<2115:BSRNBW>2.0.CO;2.

Oumbe, A., Bru, H., Hassar, Z., Blanc, P., Wald, L., Eissa, Y., Marpu, P., Gherboudj, I., Ghedira, H., Goffe, D., 2013. On the improvement of MACC aerosol spatial resolution for irradiance estimation in the United Arab Emirates. 2013 ISES Solar World Congress, 3–7 November 2013, Cancun, Mexico.

Parida, B., Iniyan, S., Goic, R., 2011. A review of solar photovoltaic technologies. Renewable and Sustainable Energy Reviews 15, 1625–1636. doi: http://dx.doi.org/10.1016/j.rser.2010.11.032.

Pastiels, R., 1959. Contribution à l'étude du problème des méthodes actinométriques. Institut Royal Météorologique de Belgique, Publ. A11.

Perez, R., Ineichen, P., Seals, R., Michalsky, J., Stewart, R., 1990a. Modeling daylight availability and irradiance components from direct and global irradiance. Solar Energy 44, 271–289. doi: http://dx.doi.org/10.1016/0038-092X(90)90055-H.

Perez, R., Ineichen, P., Seals, R., Zelenka, A., 1990b. Making full use of the clearness index for parameterizing hourly insolation conditions. Solar Energy 45, 111–114. doi: http://dx.doi.org/10.1016/0038-092X(90)90036-C.

Perez, R., Seals, R., Michalsky, J., 1993. All-weather model for sky luminance distribution - Preliminary configuration and validation. Solar Energy 50, 235–245. doi: http://dx.doi.org/10.1016/0038-092X(93)90017-I.

Rabl, A., Bendt, P., 1982. Effect of circumsolar radiation on performance of focusing collectors. Journal of Solar Energy Engineering 104, 237–250. doi: http://dx.doi.org/10.1115/1.3266308.

Reid, J., Piketh, S., Kahn, R., Bruintjes, R., Holben, B., 2005. A summary of first year activities of the United Arab Emirates Unified Aerosol Experiment: UAE2. Tech. Rep., NRL/MR/7534--05-8899. http://uae2.gsfc.nasa.gov/MR8899UAE2.pdf (last access: 6 March 2014).

Reinhardt, B., 2013. On the retrieval of circumsolar radiation from satellite observations and weather model output. Dissertation, LMU München: Faculty of Physics. http://edoc.ub.uni-muenchen.de/16438/1/Reinhardt_Bernhard.pdf (last access: 8 October 2014).

Reinhardt, B., Buras, R., Bugliaro, L., Wilbert, S., Mayer, B., 2014. Determination of circumsolar radiation from Meteosat Second Generation. Atmospheric Measurement Techniques 7, 823–838. doi: http://dx.doi.org/10.5194/amt-7-823-2014.

Remund, J., Wald, L., Lefevre, M., Ranchin, T., Page, J., 2003. World-wide Linke turbidity information. CD-ROM published by International Solar Energy Society, Proceedings of ISES Solar World Congress, 16–19 June, Goteborg, Sweden.

REN21, 2013. Renewables 2013 global status report. REN21 Secretariat, Paris. http://www.ren21.net/ren21activities/globalstatusreport.aspx (last access: 12 March 2014).

Richter, C., Teske, S., Short, R., 2009. Concentrating solar power - global outlook 09. Report published by Greenpeace International, SolarPACES and ESTELA. http://www.greenpeace.org/international/Global/international/planet-2/report/2009/5/concentrating-solar-power-2009.pdf (last access: 12 March 2014).

Rigollier, C., Bauer, O., Wald, L., 2000. On the clear sky model of the ESRA — European Solar Radiation Atlas — with respect to the Heliosat method. Solar Energy 68, 33–48. doi: http://dx.doi.org/10.1016/S0038-092X(99)00055-9.

Roesch, A., Wild, M., Ohmura, A., Dutton, E.G., Long, C.N., Zhang, T., 2011a. Assessment of BSRN radiation records for the computation of monthly means. Atmospheric Measurement Techniques 4, 339–354. doi: http://dx.doi.org/10.5194/amt-4-339-2011.

Roesch, A., Wild, M., Ohmura, A., Dutton, E.G., Long, C.N., Zhang, T., 2011b. Corrigendum to "Assessment of BSRN radiation records for the computation of monthly means" published in Atmos. Meas. Tech., 4, 339–354, 2011. Atmospheric Measurement Techniques 4, 973. doi: http://dx.doi.org/10.5194/amt-4-973-2011.

Romero-alvarez, M., Zarza, E., 2007. Chapter 21: Concentrating solar thermal power, in: Handbook of Energy Efficiency and Renewable Energy. pp. 21–1:21–92. CRC Press 2007. http://dx.doi.org/10.1201/9781420003482.ch21.

Schillings, C., Mannstein, H., Meyer, R., 2004. Operational method for deriving high resolution direct normal irradiance from satellite data. Solar Energy 76, 475–484. doi: http://dx.doi.org/10.1016/j.solener.2003.07.038.

Schroedter-Homscheidt, M., Oumbe, A., Benedetti, A., Morcrette, J.-J., 2013. Aerosols for concentrating solar electricity production forecasts: Requirement quantification and ECMWF/MACC aerosol forecast assessment. Bulletin of the American Meteorological Society 94, 903–914. doi: http://dx.doi.org/10.1175/BAMS-D-11-00259.1.

Shaw, G.F., Deehr, C.S., 1974. Relationship between circumsolar sky brightness and atmospheric aerosols. U.S. Environmental Protection Agency Technical Report, EPA-650/4-75-012.

Shettle, E.P., Fenn, R.W., 1979. Models for the aerosols of the lower atmosphere and the effects of humidity variations on their optical properties. Tech. Rep. AFGL-TR-79-0214, Air Force

Geophys. Lab., Hanscom Air Force Basem Bedford, Mass., USA. http://www.dtic.mil/cgi-bin/GetTRDoc?Location=U2&doc=GetTRDoc.pdf&AD=ADA085951 (last access: 2 October 2014).

Singh, G.K., 2013. Solar power generation by PV (photovoltaic) technology: A review. Energy 53, 1–13. doi: http://dx.doi.org/10.1016/j.energy.2013.02.057.

Smirnov, A., Holben, B.N., Eck, T.F., Dubovik, O., Slutsker, I., 2000. Cloud-screening and quality control algorithms for the AERONET database. Remote Sensing of Environment 73, 337–349. doi: http://dx.doi.org/10.1016/S0034-4257(00)00109-7.

Stair, A.T., DeVore, J.G., 2012. Sun and Aureole Measurements: A sensor for cloud optical properties and circumsolar radiation. Brochure available on www.visidyne.com/SAM/7_VI-5493(SAM%20Trifold).ppt (last access: 7 October 2014).

Stamnes, K., Tsay, S.C., Wiscombe, W., Jayaweera, K., 1988. Numerically stable algorithm for discrete-ordinate-method radiative transfer in multiple scattering and emitting layered media. Applied Optics 27, 2502–2509. doi: http://dx.doi.org/10.1364/AO.27.002502.

Stamnes, K., Tsay, S.C., Wiscombe, W., Laszlo, I., 2000. DISORT, a general-purpose Fortran program for Discrete-Ordinate-Method Radiative Transfer in scattering and emitting layered media: Documentation of methodology. Tech. rep., Dept. of Physics and Engineering Physics, Stevens Institute of Technology, Hoboken, NJ 07030. http://www.met.reading.ac.uk/~qb717363/adient/rfm-disort/DISORT_documentation.pdf (last access: 4 October 2014).

Thomalla, E., Köpke, P., Müller, H., Quenzel, H., 1983. Circumsolar radiation calculated for various atmospheric conditions. Solar Energy 30, 575–587. doi: http://dx.doi.org/10.1016/0038-092X(83)90069-5.

Vignola, F., 1999. Solar cell based pyranometers: Evaluation of the diffuse response. Proceedings of the 1999 ASES Annual Conference. http://solardat.uoregon.edu/download/Papers/SolarCellBasedPyranometers--EvaluationoftheDiffuseResponse.pdf (last access 7 October 2014).

Vignola, F., 2006. Removing systematic errors from rotating shadowband pyranometer data. Proceedings of the 35th ASES Annual Conference, 9-13 July 2006, Denver, CO, USA. http://solardat.uoregon.edu/download/Papers/RemovingSystematicErrorsfromRotatingShadowbandPyranometerData.pdf (last access 7 October 2014).

Wald, L., 2007. Solar radiation energy (fundamentals). In: Julian Blanco, Sixto Malato (Eds.). Solar Energy Conversion and Photoenergy Systems, in Encyclopedia of Life Support Systems (EOLSS), Developed under the Auspices of the UNESCO, Eolss Publishers, Oxford, UK, http://www.eolss.net.

Wilbert, S., Pitz-Paal, R., Jaus, J., 2012a. Circumsolar radiation and beam irradiance measurements for focusing collectors. COST WIRE ES1002 Workshop on Remote Sensing Measurements for Renewable Energy, 22-23 May 2012, Risoe, Denmark. http://www.wire1002.ch/fileadmin/user_upload/Major_events/WS_Risoe_2012/Extended_abstracts/Wilbert.pdf (last access: 12 March 2014).

Wilbert, S., Pitz-Paal, R., Müller, S., 2012b. Rotating shadowband irradiometers and circumsolar radiation. Cost Wire Workshop Payerne, Payerne.

Wilbert, S., Reinhardt, B., DeVore, J.G., Röger, M., Pitz-Paal, R., Gueymard, C.A., Buras, R., 2013. Measurement of solar radiance profiles with the sun and aureole measurement system. Journal of Solar Energy Engineering 135, 041002. doi: http://dx.doi.org/10.1115/1.4024244.

Wittmann, M., Hirsch, T., Eck, M., 2009. Some aspects on parabolic trough field operation with oil as a heat transfer fluid. Proceedings of SolarPACES 2009, 15-18 September 2009, Berlin, Germany. http://elib.dlr.de/62502/1/14805_Wittmann_Some_Aspects_on_Parabolic_Trough_Field_Operation.pdf (last access: 15 October 2014).

WMO, 2010. Guide to meteorological instruments and methods of observation. World Meteorological Organization, WMO-No 8 (2010 update), 7th edn., Geneva, Switzerland. http://library.wmo.int/pmb_ged/wmo_8_en-2012.pdf (last access: 21 January 2015).

Zhang, Y., Smith, S.J., Kyle, G.P., Stackhouse Jr., P.W., 2010. Modeling the potential for thermal concentrating solar power technologies. Energy Policy 38, 7884–7897. doi: http://dx.doi.org/10.1016/j.enpol.2010.09.008.

Nomenclature

Acronyms	
AERONET	Aerosol robotic network
AOD	Aerosol optical depth
BSRN	Baseline surface radiation network
CC	Correlation coefficient
CDF	Cumulative distribution function
CI	Confidence interval
CPV	Concentrated photovoltaics
CSNI	Circumsolar normal irradiance
CSR	Circumsolar ratio
CST	Concentrated solar technologies
CSTE	Concentrated solar thermal electric
DHI	Diffuse horizontal irradiance
DISORT	Discrete-ordinate-method radiative transfer
DLR	German aerospace agency
DNI	Direct normal irradiance
DNI_S	Direct normal irradiance from the solar disc only
DSA	Direct sun algorithm
GHI	Global horizontal irradiance
GNI	Global normal irradiance
GTI	Global tilted irradiance
HG	Henyey-Greenstein
IEA	International Energy Agency
LBL	Lawrence Berkeley Laboratory
LS	Least-squares
MACC	Monitoring atmospheric composition and climate
MAE	Mean absolute error
MENA	Middle East and North Africa region
MYSTIC	Monte Carlo code for the physically correct tracing of photons in cloudy atmospheres
NIP	Normal incidence pyrheliometer
OPAC	Optical properties of aerosols and clouds
PCA	Principal component analysis
PFCN	Phase function
PV	Photovoltaic
R^2	Coefficient of determination
RDB	Reduced data base
RH	Relative humidity
RMSE	Root mean square error
RSI	Rotating shadowband irradiometer
RTM	Radiative transfer model
SAM	Sun and aureole measurement system
SHC	Solar heating and cooling
SMARTS	Simple model of the atmospheric radiative transfer of sunshine
SRA	Standard radiation atmosphere
SSA	Single scattering albedo
T_{amb}	Ambient temperature
TTHG	Two term Henyey-Greenstein
UAE	United Arab Emirates
WMO	World Meteorological Organization

Symbols	
a	The Ångström parameter (unitless)
b	In Ångström's law, it represents the aerosol optical depth at 1 μm (unitless)
B_n	Broadband direct normal irradiance (W m^{-2})
$B_{n,\lambda}$	Monochromatic direct normal irradiance (W m^{-2} μm^{-1})
B_n^{Sun}	Direct normal irradiance from the solar disc only (W m^{-2})
$B_{n,\lambda}^{Sun}$	Monochromatic direct normal irradiance from the solar disc only (W m^{-2} μm^{-1})
B_λ	Monochromatic direct horizontal irradiance (W m^{-2} μm^{-1})
c_1, c_2, c_3	Parameters of the two term Henyey-Greenstein phase function (unitless)
CS_n	Circumsolar normal irradiance (W m^{-2})
$CS_{n,\lambda}$	Monochromatic circumsolar normal irradiance (W m^{-2} μm^{-1})
CSR	Circumsolar ratio (unitless)
CSR_λ	Monochromatic circumsolar ratio (unitless)
D	Broadband diffuse horizontal irradiance (W m^{-2})
$E_{0,n}$	Broadband extraterrestrial irradiance received on a plane normal to the Sun (W m^{-2})
$E_{0,n,\lambda}$	Monochromatic extraterrestrial irradiance received on a plane normal to the Sun (W m^{-2} μm^{-1})
E_{SC}	Solar constant, set to 1367 W m^{-2}
G	Broadband global horizontal irradiance (W m^{-2})
g	Asymmetry parameter (unitless)
g_λ	Monochromatic asymmetry parameter (unitless)
J	Source function in radiative transfer equation
j, υ	Coefficients of the SRA model to compute the single scattering albedo (unitless)
K_D	Diffuse fraction (unitless)
KT	Clearness index (unitless)
KT'	Corrected clearness index (unitless)
KT_{Bn}	Direct normal clearness index (unitless)
L_λ	Monochromatic radiance (W m^{-2} μm^{-1} sr^{-1})
m	Pressure corrected relative optical air mass (unitless)
p	Penumbra function (unitless)
$P_{a,\lambda}$	Monochromatic aerosol phase function (unitless)
P_{HG}	Henyey-Greenstein phase function (unitless)
p_l	l'th Legendre polynomial (unitless)
$P_{r,\lambda}$	Monochromatic Rayleigh phase function (unitless)
P_{TTHG}	Two term Henyey-Greenstein phase function (unitless)
P_λ	Monochromatic phase function (unitless)
r	Actual Sun-Earth distance (AU)
r_0	Mean Sun-Earth distance, 1 AU
r_s	Distance to the element radius of the sphere (m)
S	Area of a spherical surface (m^2)
SC	Sky clearness index
t	Time
Z	Altitude of a site above mean sea level (m)
z	Vertical distance travelled in the atmosphere (m)
α	Aperture half-angle (rad or deg)
$\beta_{ext,\lambda}$	Monochromatic extinction coefficient due to scattering and absorption (m^{-1})
$\beta_{ext,\lambda}^{abs}$	Monochromatic extinction coefficient due to absorption (m^{-1})
$\beta_{ext,\lambda}^{scat}$	Monochromatic extinction coefficient due to scattering (m^{-1})
γ	Elevation of an arbitrary sky element (rad or deg)
γ_S	Solar elevation angle (rad or deg)
δ	Inner angular limit of the circumsolar region (rad or deg)
δ_S	Angular radius of the Sun corrected with respect the Sun-Earth distance (rad or deg)
ε_L	Limit half-angle of pyrheliometer (rad or deg)
ε_S	Slope half-angle of pyrheliometer (rad or deg)
θ	Zenith angle of an arbitrary sky element (rad or deg)

θ_S	Solar zenith angle (rad or deg)
λ	Wavelength (μm or nm)
v, o, ρ	Coefficients of the proposed model to compute the circumsolar ratio (unitless)
ξ	Scattering angle (rad or deg)
σ	Standard deviation (same units as parameter in question)
$\tau_{a,\lambda}$	Monochromatic optical depth due to aerosol absorption and scattering (unitless)
$\tau_{a,\lambda}^{abs}$	Monochromatic optical depth due to aerosol absorption (unitless)
$\tau_{a,\lambda}^{scat}$	Monochromatic optical depth due to aerosol scattering (unitless)
$\tau_{g,\lambda}^{abs}$	Monochromatic optical depth due to gaseous absorption (unitless)
$\tau_{r,\lambda}^{scat}$	Monochromatic optical depth due to Rayleigh scattering (unitless)
τ_{λ}	Monochromatic total optical depth (unitless)
τ_{λ}^{scat}	Monochromatic optical depth due to scattering (unitless)
φ	Azimuth angle of an arbitrary sky element (rad or deg)
φ_n	Azimuth angle on a plane normal to the Sun (rad or deg)
φ_S	Solar azimuth angle (rad or deg)
Ω	Solid angle (sr)
$\omega_{a,\lambda}$	Monochromatic aerosol single scattering albedo (unitless)
ω_{λ}	Monochromatic single scattering albedo (unitless)

List of figures

Fig. #	Caption	Page #
1.1	Picture of the parabolic troughs of Shams 1, a CSTE power plant located in the UAE. © Yehia Eissa, 2012.	2
1.2	The radiation intercepted by a pyrheliometer normal to the Sun. The small disc on the left represents the solar disc and the large disc on the left represents the circumsolar region having a half-angle of 2.5°. The solid angle Ω is explained further in Sect. 3.3.2.	3
1.3	The circumsolar region under clear sky conditions (a) and cirrus cloud conditions (b). The solar disc is shaded by the shading ball (Wilbert *et al.*, 2012a).	4
1.4	A picture of the SAM instrument in Abu Dhabi (image from: http://www.visidyne.com/SAM/SAM_DATA_MAS_files/image002.jpg) (a) and a schematic of the SAM instrument modified after Wilbert *et al.* (2012a) (b).	7
2.1	Diagramme de dispersion entre le CSR modélisé par libRadtran pour un angle limite de 4.6° ($CSR(\varepsilon_L = 4.6°)$) et l'indice de clarté du ciel (SC), associé aux bornes à 95 % des observations. Les limites des trois intervalles pour la modélisation sont représentées en rouge. Pour chacun de ces intervalles, sont représentées la modélisation ainsi que les bornes à 95 % associées.	29
3.1	Schematic showing the angular positions of the Sun and any arbitrary sky element (modified after CIE, 2002).	37
3.2	The spectral distribution of the extraterrestrial irradiance received on a plane normal to the Sun at the mean Sun-Earth distance in the interval [0 μm, 5.0 μm], adapted from Gueymard (2004).	40
3.3	Typical angular patterns of the scattered radiation due to spherical aerosols of sizes: 10^{-4} μm (a); 0.1 μm (b) and 1.0 μm (c) for visible light of wavelength 0.5 μm. Figure copied from Liou (2002).	41
3.4	The multiple scattering phenomenon. Figure copied from Wald (2007).	41
3.5	Spectral distribution of the irradiance showing the spectral bands which encounter the most Rayleigh scattering and gaseous absorption, assuming a cloud-free atmosphere with no aerosols and a solar zenith angle of 60°. Figure copied from Liou (2002).	42
3.6	A schematic of the solid angle.	43
3.7	Schematic showing the viewing half-angles of pyrheliometers (a), where α is the aperture half-angle, ε_S is the slope angle and ε_L is the limit angle. The penumbra function with respect to the viewing half-angles is also shown (b). Figure copied from Blanc *et al.* (2014).	47
4.1	The surrounding environment of Masdar City, Abu Dhabi, UAE (image from Google Earth).	54
4.2	A map of the whole UAE showing Masdar City.	54
4.3	The rotating shadowband irradiometer. In this picture the shadowband is still and below the horizon of the photodiode. © Yehia Eissa, 2012.	55

4.4	The Cimel 318 Sun photometer used in the AERONET stations (image from: http://www.cimel.fr/?instrument=photometre-multi-bandes-soleilciel).	57
4.5	A picture of the SAM instrument (Stair and DeVore, 2012) (a) and a schematic of the SAM instrument modified after Wilbert *et al.* (2012a) (b).	59
4.6	The 222714 solar radiance profiles normalized between [0, 1] in the Sun disc region. They are sorted out in terms of the RMSE with respect to the real mean normalized solar radiance profile. The black line represents the cutoff, profiles below it are eliminated.	61
4.7	Scatter density plot between the SAM and AERONET monochromatic radiance L_λ measurements.	63
4.8	Scatter density plot between the SAM and AERONET monochromatic AOD ($\tau_{a,\lambda}$) at 670 nm.	64
4.9	Scatter density plot between the SAM and AERONET monochromatic AOD ($\tau_{a,\lambda}$) at 670 nm, same samples as in Fig. 4.8 but the axes are limited to 0.8 for a better view.	65
4.10	Scatter density plot between the SAM and AERONET monochromatic AOD ($\tau_{a,\lambda}$) at 670 nm after accounting for the accuracy of the SAM retrievals, the axes are limited to 0.8 for a better view.	66
5.1	Relative absolute errors induced in the monochromatic radiance by varying $\tau_{a,\lambda}$ (a), $\omega_{a,\lambda}$, (b) and $P_{a,\lambda}(\xi)$ (c, d and e) for three scattering angles ξ. In each plot only the variable in question was varied.	70
5.2	Relative error in monochromatic DNI_S when varying $\tau_{a,\lambda}$ and θ_S.	72
5.3	Scatter density plot of the fitting subset of the matched SAM versus AERONET AOD at 670 nm. Axes are limited to 0.8 for a better view.	73
5.4	Scatter density plot of the testing subset of the corrected AERONET versus SAM AOD at 670 nm. Axes are limited to 0.8 for a better view.	74
5.5	Histogram of the AERONET $\omega_{a,\lambda}$ at 675 nm. The solid black line depicts the mean value, the black dashed line the mean value ± 1σ and the black dotted line the mean ± 2σ, where σ is the standard deviation.	75
5.6	An arbitrary AERONET $P_{a,\lambda}$ as a function of the scattering angle ξ at 675 nm, its HG PFCN representation and its TTHG PFCN representation.	77
6.1	Example of the diffuse radiance L_λ at 670 nm shown in colors at different element zenith and azimuth angles (a) and its corresponding diffuse solar radiance profile as a function of the scattering angle ξ (b).	84
6.2	Scatter density plot of the libRadtran DNI_S at 670 nm (libRadtran $B_{n,\lambda}^{Sun}$) versus the reference values from the SAM instrument (SAM $B_{n,\lambda}^{Sun}$).	86
6.3	Scatter density plot of the libRadtran CSNI at 670 nm modelled by defining the HG PFCN (libRadtran $CS_{n,\lambda}(\delta = 0.64°, \alpha = 6°)$) versus the reference values from the SAM instrument (SAM $CS_{n,\lambda}(\delta = 0.64°, \alpha = 6°)$).	87
6.4	Scatter density plot of the libRadtran CSNI at 670 nm modelled by defining the desert type aerosol in the OPAC library (libRadtran $CS_{n,\lambda}(\delta = 0.64°, \alpha = 6°)$) versus the reference values from the SAM instrument (SAM $CS_{n,\lambda}(\delta = 0.64°, \alpha = 6°)$).	88
6.5	Scatter density plot of the libRadtran CSNI at 670 nm modelled by defining the TTHG PFCN (libRadtran $CS_{n,\lambda}(\delta = 0.64°, \alpha = 6°)$) versus the reference values from the SAM instrument (SAM $CS_{n,\lambda}(\delta = 0.64°, \alpha = 6°)$).	89

6.6	Scatter density plot of the SMARTS DNI_S at 670 nm (SMARTS $B_{n,\lambda}^{Sun}$) versus the reference values from the SAM instrument (SAM $B_{n,\lambda}^{Sun}$).	90
6.7	Scatter density plot of the SMARTS CSNI at 670 nm modelled by defining the SSA and asymmetry parameter (SMARTS $CS_{n,\lambda}(\delta = 0.64°, \alpha = 6°)$) versus the reference values from the SAM instrument (SAM $CS_{n,\lambda}(\delta = 0.64°, \alpha = 6°)$).	91
6.8	Scatter density plot of the SMARTS CSNI at 670 nm modelled by defining the 'DESERT_MAX' aerosol type (SMARTS $CS_{n,\lambda}(\delta = 0.64°, \alpha = 6°)$) versus the reference values from the SAM instrument (SAM $CS_{n,\lambda}(\delta = 0.64°, \alpha = 6°)$).	92
6.9	The relative absolute error on the monochromatic CSNI (shown in colors) by inducing an error of ± 2% on the c_2 parameter in the TTHG PFCN. The results for an aperture half-angle of 2.5° (a) and those for 6° (b) are shown.	95
6.10	Scatter density plot of the libRadtran broadband DNI_S (libRadtran B_n^{Sun}) versus the reference values from the RSI instrument (RSI $B_n(\varepsilon_L = 4.6°)$).	99
6.11	Scatter density plot of the residuals versus the air temperature at surface.	100
6.12	Scatter density plot of the libRadtran broadband DNI for a limit angle of 4.6° (libRadtran $B_n(\varepsilon_L = 4.6°)$) versus the reference values from the RSI instrument (RSI $B_n(\varepsilon_L = 4.6°)$).	101
6.13	The cumulative distribution function (CDF) of the CSR for a limit angle of 4.6° ($CSR(\varepsilon_L = 4.6°)$).	102
6.14	The CSR modelled by libRadtran for a limit angle of 4.6° ($CSR(\varepsilon_L = 4.6°)$) versus the measurements from the RSI instrument (RSI $B_n(\varepsilon_L = 4.6°)$).	103
6.15	The CSR modelled by libRadtran for a limit angle of 4.6° ($CSR(\varepsilon_L = 4.6°)$) versus the sky clearness index (SC).	104
6.16	The CSR modelled by libRadtran for a limit angle of 4.6° ($CSR(\varepsilon_L = 4.6°)$) versus the sky clearness index (SC). Also shown are the interval limits, the fitted curve for each interval, the 95% prediction bounds on the functions and on the observations.	106
6.17	Scatter density plot of the estimated CSR for a limit angle of 4.6° (estimated $CSR(\varepsilon_L = 4.6°)$) versus the reference values modelled by libRadtran (libRadtran $CSR(\varepsilon_L = 4.6°)$).	107
6.18	Scatter density plot of the estimated CSNI for a limit angle of 4.6° (estimated $CS_n(\delta = 0°, \varepsilon_L = 4.6°)$) versus the reference values modelled by libRadtran (libRadtran $CS_n(\delta = 0°, \varepsilon_L = 4.6°)$).	108
6.19	Scatter density plot of the estimated DNI_S (Estimated B_n^{Sun}) versus the reference values modelled by libRadtran (libRadtran B_n^{Sun}).	109
6.20	The MAE of the CSR for the different aperture half-angles (α).	110
6.21	The coefficients of Eqs. (6.7) to (6.9) as a function of the aperture half-angle α (circles) and the 6^{th} order polynomial fit.	112
6.22	Scatter density plot of the estimated DNI_S (Estimated B_n^{Sun}) versus the reference values modelled by libRadtran (libRadtran B_n^{Sun}), for validating the model in time using data set DS1.	114
7.1	A zoom in on Tamanrasset, Algeria, and its surrounding environment (image from Google Earth).	118
7.2	Scatter density plot of the estimated DNI_S (estimated B_n^{Sun}) versus the reference values modelled by libRadtran (libRadtran B_n^{Sun}) using data set TAM_DS1, when using the model developed over Abu Dhabi.	120

7.3 Scatter density plot of the CSR for an aperture half-angle of 2.9° (estimated $CSR(\alpha = 2.9°)$) versus the reference values modelled by libRadtran (libRadtran $CSR(\alpha = 2.9°)$) using data set TAM_DS2, when using the model developed over Abu Dhabi. 121

7.4 Scatter density plot of the CSNI for an aperture half-angle of 2.9° (estimated $CS_n(\delta = 0°, \alpha = 2.9°)$) versus the reference values modelled by libRadtran (libRadtran $CS_n(\delta = 0°, \alpha = 2.9°)$) using data set TAM_DS2, when using the model developed over Abu Dhabi. 122

7.5 Scatter density plot of the estimated DNI_S (estimated B_n^{Sun}) versus the reference values modelled by libRadtran (libRadtran B_n^{Sun}) using data set TAM_DS2, when using the model developed over Abu Dhabi. 123

7.6 CSR versus the sky clearness index (*SC*) for data set TAM_DS2 and data set DS3. 124

7.7 Scatter density plot of the libRadtran broadband DNI_S (libRadtran B_n^{Sun}) versus the reference values from the Eppley NIP (NIP $B_n(\varepsilon_L = 4°)$) using data set TAM_DS2. 125

7.8 Scatter density plot of the libRadtran broadband DNI for a limit angle of 4° (libRadtran $B_n(\varepsilon_L = 4°)$) versus the reference values from the Eppley NIP (NIP $B_n(\varepsilon_L = 4°)$) using data set TAM_DS2. 126

7.9 The cumulative distribution function (CDF) of the CSR for a limit angle of 4° ($CSR(\varepsilon_L = 4°)$) in Tamanrasset using data set TAM_DS2 (blue line) and the CSR for a limit angle of 4.6° ($CSR(\varepsilon_L = 4.6°)$) in Abu Dhabi using data set DS3 (red line). 127

7.10 The CSR modelled by libRadtran for a limit angle of 4° ($CSR(\varepsilon_L = 4°)$) versus the sky clearness index (*SC*) using data set TAM_DS2. Also shown are the interval limits, the fitted curve for each interval, the 95% prediction bounds on the functions and on the observations. 128

7.11 Scatter density plot of the estimated CSR for a limit angle of 4° (estimated $CSR(\varepsilon_L = 4°)$) versus the reference values modelled by libRadtran (libRadtran $CSR(\varepsilon_L = 4°)$) using data set TAM_DS2. 130

7.12 Scatter density plot of the estimated CSNI for a limit angle of 4° (estimated $CS_n(\delta = 0°, \varepsilon_L = 4°)$) versus the reference values modelled by libRadtran (libRadtran $CS_n(\delta = 0°, \varepsilon_L = 4°)$) using data set TAM_DS2. 131

7.13 Scatter density plot of the estimated DNI_S (estimated B_n^{Sun}) versus the reference values modelled by libRadtran (libRadtran B_n^{Sun}) using data set TAM_DS2. 132

7.14 The MAE of the CSR for the different aperture half-angles (α). 133

7.15 The coefficients of Eqs. (7.1) to (7.3) as a function of the aperture half-angle α (circles) and the 6th order polynomial fit. 135

7.16 Scatter density plot of the estimated DNI_S (estimated B_n^{Sun}) versus the reference values modelled by libRadtran (libRadtran B_n^{Sun}), for validating the model in time using data set TAM_DS1. 136

7.17 Scatter density plot of the estimated DNI_S (estimated B_n^{Sun}) versus the reference values modelled by libRadtran (libRadtran B_n^{Sun}) using data set DS1, when using the model developed over Tamanrasset. 137

7.18 Scatter density plot of the CSR for an aperture half-angle of 2.86° (estimated $CSR(\alpha = 2.86°)$) versus the reference values modelled by libRadtran (libRadtran 139

	$CSR(\alpha = 2.86°)$) using data set DS3, when using the model developed over Tamanrasset.	
7.19	Scatter density plot of the CSNI for an aperture half-angle of 2.86° (estimated $CS_n(\delta = 0°, \alpha = 2.86°)$) versus the reference values modelled by libRadtran (libRadtran $CS_n(\delta = 0°, \alpha = 2.86°)$) using data set DS3, when using the model developed over Tamanrasset.	140
7.20	Scatter density plot of the estimated DNI_S (estimated B_n^{Sun}) versus the reference values modelled by libRadtran (libRadtran B_n^{Sun}) using data set DS3, when using the model developed over Tamanrasset.	141

List of tables

Table #	Caption	Page #
1.1	Aperture half-angles of current pyrheliometers and CST systems (adapted from Blanc *et al.*, 2014).	3
2.1	Les différents jeux de données disponibles pour la thèse sur le site d'Abu Dhabi (EAU).	19
2.2	Comparaison des estimations de DNI_S monochromatique à 670 nm avec les mesures *in-situ* issues de SAM (DS2) (EQM : erreur quadratique moyenne).	25
2.3	Comparaison des estimations de CSNI monochromatique à 670 nm avec les mesures *in-situ* issues de SAM (DS5) (EQM : erreur quadratique moyenne).	26
2.4	Les coefficients des équations (2.21) à (2.23), leurs intervalles de confiance (IC) à 95 % et les moyennes des erreurs absolues (MEA) du CSR modélisé pour chacun des trois intervalles.	29
2.5	Jeux de données disponibles pour l'étude sur le site de Tamanrasset, Algérie.	32
3.1	Acceptance half-angles of common pyrheliometers (adapted from Blanc *et al.*, 2014).	47
4.1	The different data sets available over Abu Dhabi, UAE.	67
5.1	The mean, standard deviation and relative standard deviation for $\tau_{a,\lambda}$, $P_{a,\lambda}(\zeta)$ and $\omega_{a,\lambda}$ for the 491 samples of data set DS4.	69
6.1	Results of libRadtran and SMARTS for the modelling the monochromatic DNI_S at 670 nm.	93
6.2	Results of libRadtran and SMARTS for the monochromatic CSNI at 670 nm.	94
6.3	Coefficients of Eqs. (6.4) and (6.5) adapted from Gueymard (1995).	98
6.4	The coefficients of Eqs. (6.7) to (6.9), their 95% confidence intervals (CI) and the MAE for each sky clearness index interval.	105
7.1	The different data sets available over Tamanrasset, Algeria.	119
7.2	The coefficients of Eqs. (7.1) to (7.3), their 95% confidence intervals (CI) and the MAE for each sky clearness index interval.	129

Modélisation des rayonnements direct et circumsolaire par ciel clair en environnement désertique

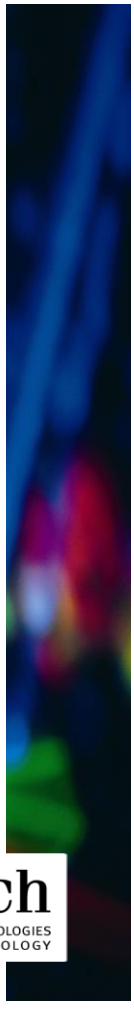
RESUME : Les mesures de l'éclairement solaire direct reçu au sol en incidence normale (DNI) par des pyrhéliomètres ou instruments équivalents incluent l'éclairement provenant de l'angle solide du disque solaire (DNI_S) et celui provenant d'une région angulaire circumsolaire plus large, appelé éclairement circumsolaire (CSNI). Les instruments ont des demi-angles d'ouverture équivalents variant entre 2,5° et 5°, soit un ordre de grandeur plus grand que le demi-angle du disque solaire. Quant aux demi-angles des systèmes de production d'énergie concentrant les rayons solaires, ils sont plus grands que le demi-angle du disque solaire, et plus petits que ceux des instruments. Par consequent, le CSNI doit être connu pour une estimation précise du DNI. Cette thèse contribue à la connaissance et à la modélisation des éclairements direct et circumsolaire en milieu désertique par conditions de ciel clair. Après avoir déterminé les propiétés optiques des aérosols les plus influentes, le modèle numérique de transfert radiatif libRadtran a été utilisé pour modéliser le CSNI et le DNI_S. Un modèle paramétrique simplifié et très rapide a été développé qui reproduit les résultats de libRadtran. Il estime le ratio circumsolaire (CSR), soit le rapport entre le CSNI et la somme du CSNI et du DNI_S, à partir de mesures standards du DNI et de l'éclairement diffus. A partir du DNI mesuré et de CSR modélisé, le CSNI et le DNI_S peuvent être estimés pour tout demi-angle entre 0,4° et 5°. Le modèle a été validé pour deux stations de mesure, dans les Emirats Arabes Unis et en Algérie.

Mots clés : Aerosols; atmosphère; circumsolaire; direct; rayonnement solaire; turbidité

Modelling the beam and circumsolar radiation under cloud-free conditions in desert environment

ABSTRACT : Routine measurements of the broadband direct normal irradiance (DNI), *i.e.* beam irradiance at normal incidence, by means of pyrheliometers or equivalent pyranometric systems include the irradiance originating from within the extent of the solar disc (DNI_S) and that from a larger circumsolar region, called the circumsolar normal irradiance (CSNI). Such instruments have equivalent aperture half-angles between 2.5° and 5° which are one order of magnitude greater than the angular radius of the solar disc. The equivalent aperture half-angles of the concentrated solar powered systems are greater than the angular radius of the solar disc, but smaller than that of the measuring systems. Therefore, information on the CSNI should be provided for an improved assessment of the DNI. The objective of this PhD thesis is to contribute to an improved assessment of the beam and circumsolar radiation under cloud-free conditions in a desert environment. After selecting the aerosol optical properties of significance, the radiative transfer model libRadtran was used to model the CSNI and DNI_S. A fast and simple parametric model which mimics the libRadtran values is proposed. This model uses standard measurements of the DNI and the diffuse horizontal irradiance as inputs to estimate the circumsolar ratio (CSR) for any aperture half-angle between 0.4° and 5°. The CSR is the ratio of the CSNI to the sum of the CSNI and the DNI_S. Knowing the CSR and having the measured DNI, the CSNI and the DNI_S can be computed.

Keywords : Aerosols; atmosphere; beam; circumsolar; solar radiation; turbidity



MINES ParisTech

ParisTech
INSTITUT DES SCIENCES ET TECHNOLOGIES
PARIS INSTITUTE OF TECHNOLOGY